



TEL AVIV UNIVERSITY

RAYMOND AND BEVERLY SACKLER FACULTY OF EXACT SCIENCES
SCHOOL OF PHYSICS AND ASTRONOMY

Double parton scattering in four-jet events in pp collisions at $\sqrt{s} = 7$ TeV with the ATLAS experiment at the LHC

Thesis submitted to the senate of Tel Aviv University
towards the degree "Doctor of Philosophy"

by

Iftach Sadeh

January 2013

Thesis supervisors,
Prof. **Halina Abramowicz** and
Prof. **Aharon Levy**.

The research for this thesis has been carried out in
the Particle Physics Department of Tel Aviv University, under
the supervision of Prof. **Halina Abramowicz** and Prof. **Aharon Levy**.

Abstract

The dijet double-differential cross section is measured as a function of the dijet invariant mass, using data taken during 2010 and during 2011 with the ATLAS experiment at the LHC, with a center-of-mass energy, $\sqrt{s} = 7$ TeV. The measurements are sensitive to invariant masses between 70 GeV and 4.27 TeV with center-of-mass jet rapidities up to 3.5. A novel technique to correct jets for pile-up (additional proton-proton collisions) in the 2011 data is developed and subsequently used in the measurement. The data are found to be consistent over 12 orders of magnitude with fixed-order NLO pQCD predictions provided by NLOJET++. The results constitute a stringent test of pQCD, in an energy regime previously unexplored.

The dijet analysis is a confidence building step for the extraction of the signal of hard double parton scattering in four-jet events, and subsequent extraction of the effective overlap area between the interacting protons, expressed in terms of the variable, σ_{eff} . The measurement of double parton scattering is performed using the 2010 ATLAS data. The rate of double parton scattering events is estimated using a neural network. A clear signal is observed, under the assumption that the double parton scattering signal can be represented by a random combination of exclusive dijet production. The fraction of double parton scattering candidate events is determined to be $f_{\text{DPS}} = 0.081 \pm 0.004$ (stat.) $^{+0.025}_{-0.014}$ (syst.) in the analyzed phase-space of four-jet topologies. Combined with the measurement of the dijet and four-jet cross sections in the appropriate phase-space regions, the effective cross section is found to be $\sigma_{\text{eff}} = 16.0^{+0.5}_{-0.8}$ (stat.) $^{+1.9}_{-3.5}$ (syst.) mb. This result is consistent within the quoted uncertainties with previous measurements of σ_{eff} at center-of-mass energies between 63 GeV and 7 TeV, using several final states.

Acknowledgements

It is with immense gratitude that I acknowledge my supervisors, Prof. Halina Abramowicz and Prof. Aharon Levy, not only for teaching me physics, but for making me feel like part of the family. This thesis is a tribute to their steadfast encouragement, guidance and support, making the course of my studies a pleasure which is difficult to leave behind. I could not have hoped for a better pair of physicists, or for a more caring pair of people, to be a student of.

I consider it an honor to have worked on the double parton scattering analysis with my colleague and friend, Orel Gueta. Defeats and victories, late night insights and countless discussions, have all culminated in a measurement to be proud of. Great thanks is also owed to Dr. Arthur Moraes, for inspiring us with his ideas about multiple interactions, and for keeping faith when all seemed lost. In addition, the shared experience of Dr. Frank Krauss and of Dr. Eleanor Dobson has been instrumental in the success of the analysis, and is much appreciated. On the theoretical side of things, the fruitful discussions with Prof. Yuri Dokshitzer, Prof. Mark Strikman, Prof. Leonid Frankfurt and Prof. Evgeny Levin were of great help in formulating the strategy of the analysis.

I would like to show special appreciation to Dr. Sven Menke and Dr. Teresa Barillari for the stimulating discussions on all things calorimeter (and then some), and to Prof. Allen Caldwell in addition. They have made my visits to the Max-Planck-Institut für Physik in Munich an experience to remember, intellectually and otherwise.

Several people have contributed greatly to my understanding of the workings of the ATLAS experiment, be it in terms of performance or of physics. The debates with Dr. Ariel Schwartzman and Dr. Peter Loch have been of great help in my development of a pile-up correction using the jet area/median method. To start me off on the invariant mass measurement, the guidance of Dr. Christopher Meyer via many hours of discussions and a multitude of emails, has been invaluable. I would like to thank Dr. Pavol Strizenec for starting me off on ATLAS software. I would also like to Acknowledge Dr. Eric Feng and Dr. Serguei Yanush, for developing the software framework for calculation of the non-perturbative corrections to the invariant mass theoretical predictions.

I am grateful to my colleagues and the members of the group at Tel Aviv University, Prof. Gideon Alexander, Prof. Erez Etzion, Prof. Abner Soffer, Dr. Gideon Bella, Dr. Sergey Kananov, Dr. Zhenya Gurvich, Dr. Ronen Ingber, Amir Stern, Rina Schwartz and Itamar Levy, for allowing me to bounce ideas off of, for the stimulating discussions, and for the pleasure of their company.

Finally, completing this thesis would not have been possible without the love and support of my family. As with everything else which is good in my life, it all starts and ends with them. Thank you for being you.

Preface

The goal of this thesis is the study of double-parton scattering (DPS) in four-jet events with the ATLAS experiment. In order to extract DPS in this channel, a good understanding of the reconstruction and calibration of jets is needed. A comprehensive framework exists in ATLAS for this purpose, featuring two main calibration schemes, referred to as the electromagnetic (EM) and the local-hadron (LCW) calibrations. These rely on extensive test-beam and simulation campaigns, which are the result of the efforts of a large number of individual researchers and analysis subgroups.

Test-beam data taken during 2004 served to test the detector performance and to validate the description of the data by simulations. Due to changing software models, these data became incompatible with current ATLAS reconstruction tools. In order to maintain future access, the information had to be made *persistent*, i.e., compatible with all future software. The first project which had been undertaken by the author of this thesis in ATLAS, was persistification of the test-beam data. This was followed by continued support and maintenance of the ATLAS calorimeter reconstruction software, as part of the operational contribution of the author to the experiment.

One of the major challenges in the calibration of jets in ATLAS, is the existence of *pile-up*, additional proton-proton (pp) collisions, which coincide with the hard scattering of interest. The effects of pile-up on final states which involve jets are complicated. Pile-up tends to both bias the energy of jets which originate from the hard interaction, and to introduce additional jets which originate from the extraneous pp collisions. The current pile-up subtraction method in ATLAS involves a simulation-based scheme; it affects an average correction for jet energies, based on the instantaneous luminosity and on the number of reconstructed vertices in an event. An alternate, event-by-event-based correction, has been developed by the author for the LCW calibration scheme. In the new correction, referred to as the *jet area/median method*, the area of a given jet and the “local” energy-density, are used in order to subtract pile-up energy from the jet. The method takes advantage both of the average response of the calorimeter to pile-up energy, and of the observed energy in the vicinity of the jet of interest. The median method is completely data-driven. Consequently, compared to the nominal pile-up correction, the uncertainties on the energy correction associated with the simulation of pile-up were reduced.

The new pile-up correction was developed by the author, initially by using the ATLAS detector simulation. It was subsequently validated by the author with the 2011 ATLAS dataset, in which the rate of pile-up is high. The validation included *in-situ* measurements of several observables, one of which was the invariant mass of dijets, the system of the two jets with the highest transverse momentum in an event. The author also performed measurements of the dijet double-differential cross section for different center-of-mass jet rapidities, as a function of the invariant mass of dijets. The invariant mass spectra had previously been measured in ATLAS using the 2010 data. The new measurements, performed for the first time on the 2011 data, were found to be compatible with the previous observations, showing that the pile-up corrections were under control. In addition, the measurement using the larger dataset recorded during 2011, served to extend the experimental reach to higher values of the invariant mass.

Using the improved jet calibration, events with four-jets in the final state were investigated as part of the DPS analysis. It was shown by the author that the deterioration of the energy resolution due to pile-up distorted greatly the observables of the measurement. The scope of the measurement had, therefore, to be limited. As this is a first measurement of double parton scattering in this channel in ATLAS, it was decided to choose a conservative approach and to limit the systematic uncertainties as much as possible. The analysis, therefore, used only single-vertex events from the 2010 dataset, for which pile-up corrections are small.

Several strategies of the DPS analysis were explored by the author. For instance, the author attempted to measure the fraction of DPS events, by exploiting the sum of the pair-wise transverse momentum balance between different jet-pair combinations in a four-jet event, as previously done by the CDF collaboration. The problem with this type of approach was the absence of an appropriate simulation sample, in which DPS events within the required phase-space were generated. In order to avoid dependence on simulated DPS events, and in addition, to increase the robustness of the analysis, the author decided to utilize a neural network. Two input samples were prepared by the author for the neural network. The first consisted of simulated events in which multiple-interactions were switched off. The second, which stood for the DPS signal, was comprised of overlaid simulated dijet events. Utilizing the neural network, the fraction of double parton scattering events was extracted from the data, and the effective cross section for DPS was subsequently measured. The result was found to be compatible with previous measurements which had used several final states, at center-of-mass energies between 63 GeV and 7 TeV.

Table of Contents

Table of Contents	7
1 Introduction	9
2 Theoretical background	13
2.1 The Standard Model of particle physics	13
2.2 Quantum Chromodynamics	13
2.3 Full description of a hard pp collision	20
2.3.1 The hard scattering	20
2.3.2 Non-perturbative effects	20
2.4 Double parton scattering	26
3 The ATLAS experiment at the LHC	29
3.1 The Large Hadron Collider	29
3.2 The ATLAS detector	29
4 Monte Carlo simulation	33
4.1 Event generators	33
4.2 Simulation of the ATLAS detector	34
4.3 Bunch train structure and overlapping events	35
5 Jet reconstruction and calibration	37
5.1 Jet reconstruction algorithms	37
5.2 Inputs to jet reconstruction	38
5.2.1 Calorimeter jets	38
5.2.2 Other types of jets	40
5.3 Jet energy calibration	41
5.4 Jet quality selection	44
5.5 Systematic uncertainties on the kinematic properties of jets	45
5.5.1 Jet energy scale uncertainties	45
5.5.2 Jet energy and angular resolution	48
6 Data selection	53
6.1 Dataset	53
6.2 Trigger and luminosity	53
6.2.1 Description of the trigger	53
6.2.2 Trigger efficiency	54
6.2.3 Luminosity calculation using a two-trigger selection scheme	56
7 The jet area/median method for pile-up subtraction	59

7.1	Pile-up in ATLAS	59
7.1.1	In- and out-of-time pile-up	59
7.1.2	The jet offset pile-up correction	62
7.2	A pile-up correction using the jet area/median method	65
7.2.1	Parametrization of the average pile-up energy	66
7.2.2	Pile-up subtraction with the median	68
7.2.3	Performance of the median correction in MC	70
7.3	Systematic checks of the median correction	74
7.3.1	Stability in MC for different parameters of the jet algorithm	74
7.3.2	Stability in data	77
7.3.3	Associated systematic uncertainty of the jet energy scale	81
7.4	In-situ measurements	83
7.4.1	Dijet balance	83
7.4.2	Jet p_t and dijet invariant mass spectra	84
7.5	Summary of the performance of the median pile-up correction	86
8	Dijet mass distribution	88
8.1	Cross section definition	88
8.2	Theoretical Predictions	89
8.2.1	NLO calculation	89
8.2.2	Non-perturbative corrections	90
8.2.3	Uncertainties on the NLO prediction	92
8.3	Bias and resolution in the invariant mass	92
8.4	Unfolding	96
8.5	Systematic uncertainties	99
8.5.1	Systematic uncertainty on the jet energy scale	101
8.5.2	Other sources of uncertainty	101
8.5.3	Total systematic uncertainty	103
8.6	Results	104
9	Hard double parton scattering in four-jet events	107
9.1	Strategy of the analysis	108
9.2	Measurement of the ratio of dijet and four-jet cross sections	111
9.3	Extraction of the fraction of DPS events using a neural network	113
9.3.1	Input samples to the neural network	113
9.3.2	Input variables to the neural network	116
9.3.3	Training and output of the neural network	121
9.4	Systematic and statistical uncertainties	124
9.5	Results and summary of the measurement	127
10	Summary	129
A	Additional figures and tables	130
A.1	Jet reconstruction and calibration	130
A.2	Data selection	131
A.3	The jet area/median method for pile-up subtraction	137
A.4	Dijet mass distribution	142
A.5	Hard double parton scattering in four-jet events	148
	Bibliography	151

1. Introduction

The Standard Model (SM) [1] is one of the major intellectual achievements of the twentieth century. In the late 1960s and early 1970s, decades of path breaking experiments culminated in the emergence of a comprehensive theory of particle physics. This theory identifies the fundamental constituents of matter and combines the theory of electromagnetic, weak and strong interactions.

Numerous measurements at energy scales from a few eV to several TeV are reproduced by the SM, and many of its predictions, e.g., the existence of the W and Z bosons, have been found to be realised in nature. By now, only the source of electroweak symmetry breaking, which in the SM is attributed to the Higgs mechanism, has not been verified experimentally. A particle with properties consistent with those of the Higgs boson has recently been discovered at the LHC by the ATLAS [2] and CMS [3] experiments; the final piece of the puzzle is therefore within reach.

The Standard Model falls short of being a complete theory of fundamental interactions because it does not incorporate the full theory of gravitation, as described by general relativity; nor does it predict the accelerating expansion of the universe, as possibly described by dark energy. The theory does not contain any viable dark matter particle that possesses all of the required properties deduced from observational cosmology. It also does not correctly account for neutrino oscillations or for the non-zero neutrino masses. Although the SM is believed to be theoretically self-consistent, it has several apparently unnatural properties, giving rise to puzzles like the *strong CP problem* and the *hierarchy problem* [4]. The SM is therefore viewed as an effective field theory that is valid at the lower energy scales where measurements have been performed, but which arises from a more fundamental theory at higher scales. It is therefore expected that a more fundamental theory exists beyond the TeV energy scale that explains the missing features.

Verification of the Higgs mechanism and the search for new physics beyond the SM are two of the primary enterprises in particle physics today. Any experimental search for the Higgs boson or for new interactions or particles, requires a detailed understanding of the strong interactions, described by Quantum Chromodynamics (QCD). It is common to discuss high-energy phenomena involving QCD in terms of partons (quarks and gluons), yet partons are never visible in their own right. Almost immediately after being produced, a quark or gluon fragments and hadronizes, leading to a collimated spray of energetic hadrons, which may be characterized by a *jet* [5]. Since partons interact strongly, jet production is the dominant hard scattering process in the SM. Figure 1.1 shows the production cross section for various processes as a function of the center-of-mass energy of an accelerator. One may compare the production cross section for energetic jets with transverse energy above 100 GeV, with those of other processes (W and Z) involving leptons. At the center-of-mass energy of the LHC, the former is much larger than the latter.

Because of the large cross sections, jet production provides an ideal avenue to probe QCD and parton distribution functions [6–9], which describe the distribution of the momenta of quarks and gluons within a proton. Processes involving jets also serve as large backgrounds in many searches for new physics. Many models predict the production of new heavy and coloured particles at the LHC. These particles are expected to decay into quarks and gluons, which are detected as particle jets. Such models may therefore be tested by measuring the rate of jet production and comparing it

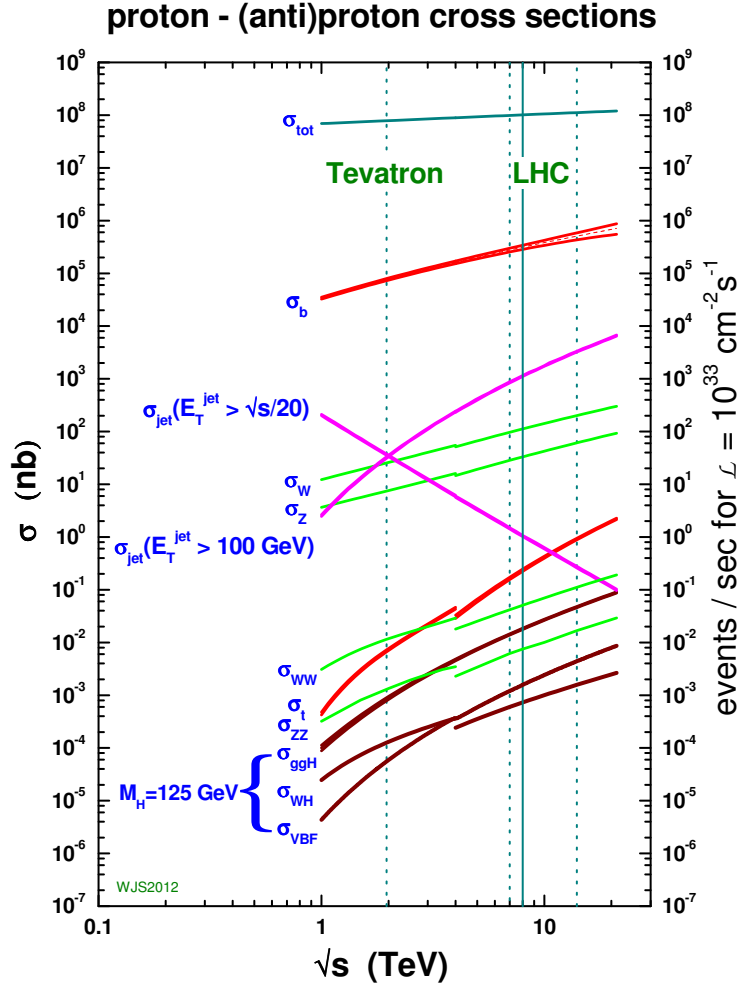


Figure 1.1. Cross sections for different physics processes as a function of center-of-mass energy, \sqrt{s} , assuming the existence of a Higgs boson with a mass of 125 GeV. (Figure by J. Stirling, taken from <http://projects.hepforge.org/mstwpdf/>.)

to the expectations from QCD [10]. Other models, such as quark *compositeness* (the hypothesis that quarks are composed of more fundamental particles), may be realised through *contact interactions* between quarks. Such new phenomena may be discovered by measuring the kinematic distributions of jets [11].

In the most common final state involving jets at the LHC, two jets with high transverse momentum, p_t , emerge from the interaction, as illustrated in figure 1.2a. These *dijet* events are particularly useful for measuring quantities associated with the initial interaction, such as the polar scattering angle in the two-parton center-of-mass frame, and the dijet invariant mass. Precise tests of perturbative QCD (pQCD) at high energies, may therefore be carried out by comparing the theoretical predictions to the experimental distributions. In addition, new physics may manifest itself with e.g., the production of a new massive particle, which subsequently decays into a high-mass dijet system [12]. Final states composed of low- p_t or forward jets are also interesting. These topologies are sensitive to QCD effects which can not be calculated using perturbation theory; as such, their measurement may help to improve the phenomenological models which are currently in use in this regime.

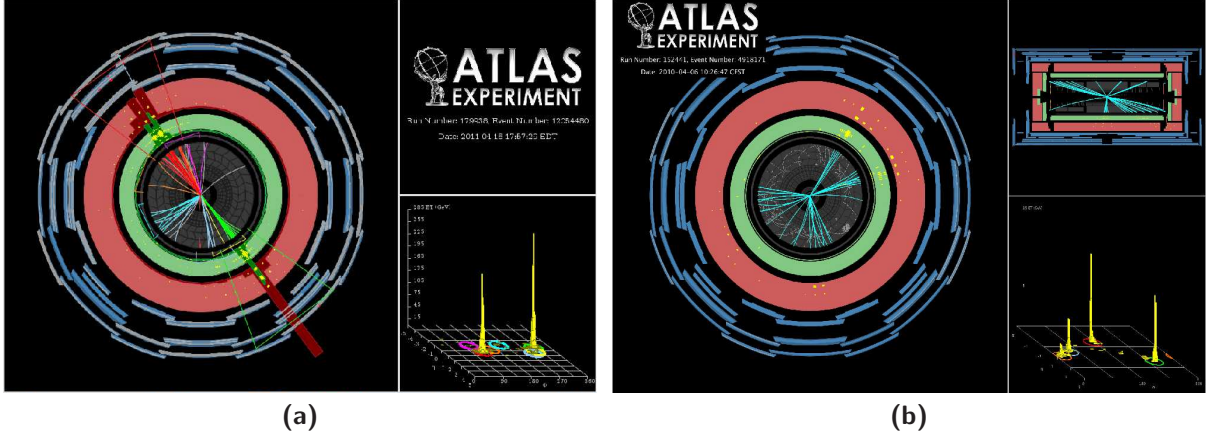


Figure 1.2. (a) Event display of a high-mass (4.04 TeV) dijet event taken in April 2011. The two jets which comprise the dijet system are marked by the colours red and green; these respectively have transverse momenta, $p_t = 1.85$ and 1.84 TeV, pseudo-rapidities, $\eta = 0.32$ and -0.53 and azimuthal angles, $\phi = 2.2$ and -0.92 . Shown are a view along the beam axis (left), and the angular distribution of transverse energy in η and ϕ (bottom right).

(b) Event display of an event with four reconstructed jets, taken in April 2010. The four jets all have $p_t > 50$ GeV, where the highest- p_t jet has transverse momentum of 108 GeV. Depicted points-of-view are along the beam axis (left), parallel to the beam axis (top right), and the angular distribution of transverse energy in η and ϕ (bottom right).

One of the important sources of background for physics searches at the LHC are multiple-parton interactions (MPI). In a generic hadron-hadron collision, several partons in one hadron scatter on counterparts from the other hadron. Most of these interactions are soft, and so generally do not result in high- p_t jets. However, the kinematic reach of the LHC, which extends to high energies and low fractions of proton momenta, enhances the probability of hard MPI relative to past experiments [13]. Hard MPI constitute a source of background for e.g., Higgs production [14, 15], and can possibly influence observed rates of other final states, involving the decay of heavy objects. The existing phenomenology of MPI is based on several simplifying assumptions. Recent interest has produced some advancements [16–22], however, a systematic treatment within QCD remains to be developed.

The simplest case of MPI is that of double parton scattering (DPS). Measurements of DPS at energies between 63 GeV and 1.96 TeV in the four-jet and γ + three-jets channels have previously been performed [23–27]. In addition, a measurement using 7 TeV ATLAS data with W + two-jet production in the final state has recently been released [28]. These have proven helpful in constraining the phenomenological models which describe DPS, and in the development of double parton distribution functions, as e.g., discussed in [17]. An additional channel in which DPS may be measured at the LHC is four-jet production. An ATLAS event display of a four-jet event is presented in figure 1.2b for illustration. A four-jet final state may arise due to a single parton-parton collision, accompanied by additional radiation. Alternatively, it can also originate from two separate parton-parton collisions, each producing a pair of jets. The latter case has distinguishing kinematic characteristics, and so the rate of DPS may be estimated on average. The DPS-rate is related to a so-called effective cross section. The latter holds information about the transverse momentum distributions of partons in the proton, and about the correlations between partons. A measurement of DPS in four-jet events has been performed using a sub-sample of the 2010 ATLAS dataset, and is presented in this thesis.

Outline of the thesis

This thesis presents a measurement of hard double parton scattering in four-jet events. The analysis involves measurement of the dijet and four-jet cross sections, and the extraction of the rate of double parton scattering from the four-jet sample.

In order to measure the individual cross sections, a measurement of the inclusive dijet invariant mass distribution is first performed. Part of the experimental challenge of measurements involving jets in ATLAS, is the calibration of the energy of jets, as these suffer from detector background due to multiple simultaneous pp collisions, referred to as pile-up. A novel method to reduce the pile-up background using jet areas is developed and subsequently utilized to correct the energy of jets. The re-calibrated jets serve as input for the dijet mass distribution analysis of the 2011 ATLAS dataset, for which the pile-up background is severe. The invariant mass measurement serves as a confidence building process for understanding the reconstruction of jets, handling of the trigger and the luminosity. The measurement is also performed on the 2010 dataset, and found to be compatible with the previously published results of ATLAS, and with the present measurement, using the 2011 data.

The 2010 dijet data-sample is also an essential element in the analysis of double parton scattering. In spite of the good understanding of how to handle the 2011 data, the measurement of double parton scattering is limited to the 2010 data, and even to a sub-sample of these data, which include single-vertex events. This choice is dictated by the inherent difficulty in extracting the double parton scattering signal, and by the shortcomings of the available simulation.

Following the short introduction given here, a theoretical overview of the Standard Model and of QCD is presented in [chapter 2](#). The ATLAS experiment is described in [chapter 3](#), followed by a summary of the physics event generators and detector simulation which are used in the analysis in [chapter 4](#). In [chapter 5](#) the concept of a jet is rigorously defined, followed by a discussion of calorimeter jets in the context of the ATLAS detector; this includes a description of the energy calibration of jets and of the systematic uncertainties associated with the calibration. [Chapter 6](#) details the data sample which is used in the analysis, with an emphasis on the trigger selection procedure and on calculation of the luminosity. In [chapter 7](#) the jet areas method to subtract pile-up background is introduced, and the performance of the pile-up correction is estimated in simulation. Several *in-situ* measurements are also used for validation of the performance in data. The new jet energy calibration which is thus developed is used to perform a measurement of the differential dijet invariant mass cross section in [chapter 8](#). In [chapter 9](#), the rate of double parton scattering events is extracted from the data using a neural network, and the effective cross section, σ_{eff} , is measured. A summary of the results is finally given in [chapter 10](#).

2. Theoretical background

2.1. The Standard Model of particle physics

The Standard Model (SM) [29] is the most successful theory describing the properties and interactions (electromagnetic, weak and strong) of the elementary particles. The SM is a gauge quantum field theory based in the symmetry group $SU(3)_C \times SU(2)_L \times U(1)_Y$, where the electroweak sector is based in the $SU(2)_L \times U(1)_Y$ group, and the strong sector is based in the $SU(3)_C$ group.

Interactions in the SM occur via the exchange of integer spin bosons. The mediators of the electromagnetic and strong interactions, the photon and eight gluons respectively, are massless. The weak force acts via the exchange of three massive bosons, the W^\pm and the Z .

The other elementary particles in the SM are half-integer spin fermions, six quarks and six leptons. While both groups interact via the electroweak force, only quarks feel the strong interaction. Electrons (e), muons (μ) and taus (τ) are massive leptons and have electrical charge $Q = -1$. Their associated neutrinos, respectively ν_e , ν_μ and ν_τ , do not have electrical charge. Quarks can be classified depending on their electrical charge; quarks u , c and t have $Q = 2/3$ and quarks d , s and b have $Q = -1/3$. For each particle in the SM, there is an anti-particle with opposite quantum numbers. The fundamental particles of the Standard Model, sorted according to family, generation and mass, are listed in figure 2.1.

The SM formalism is written for massless particles. The Higgs mechanism of spontaneous symmetry breaking is proposed for generating non-zero boson and fermion masses. The symmetry breaking requires the introduction of a new field that leads to the existence of a new massive boson, the Higgs boson. A particle with properties consistent with those of the Higgs boson has recently been discovered at the LHC by the ATLAS [2] and CMS [3] experiments.

Three generations of matter (fermions)			
	I	II	III
mass →	2.4 MeV/c ²	1.27 GeV/c ²	171.2 GeV/c ²
charge →	$\frac{2}{3}$	$\frac{2}{3}$	$\frac{2}{3}$
spin →	$\frac{1}{2}$	$\frac{1}{2}$	$\frac{1}{2}$
name →	u up	c charm	t top
Quarks	4.8 MeV/c ²	104 MeV/c ²	4.2 GeV/c ²
	$-\frac{1}{3}$	$-\frac{1}{3}$	$-\frac{1}{3}$
	$\frac{1}{2}$	$\frac{1}{2}$	$\frac{1}{2}$
	d down	s strange	b bottom
Leptons	<2.2 eV/c ²	<0.17 MeV/c ²	<15.5 MeV/c ²
	0	0	0
	$\frac{1}{2}$	$\frac{1}{2}$	$\frac{1}{2}$
	ν_e electron neutrino	ν_μ muon neutrino	ν_τ tau neutrino
	0.511 MeV/c ²	105.7 MeV/c ²	1.777 GeV/c ²
	-1	-1	-1
	$\frac{1}{2}$	$\frac{1}{2}$	$\frac{1}{2}$
	e electron	μ muon	τ tau
Gauge bosons			
			0
			0
			1
			γ photon
			0
			0
			1
			g gluon
			91.2 GeV/c ²
			0
			1
			Z^0 Z boson
			80.4 GeV/c ²
			± 1
			1
			W^\pm W boson

Figure 2.1. The fundamental particles of the Standard Model, sorted according to family, generation and mass.

2.2. Quantum Chromodynamics

Quantum chromodynamics (QCD) [30] is the theory of strong interactions. Its fundamental constituents are quarks and gluons, which are *confined* in the nucleon but act as free at sufficiently

2. Theoretical background

small scales (and high energies). The latter behaviour is called *asymptotic freedom*. The direct consequence of confinement is that free quarks and gluons are never observed experimentally, and their final state is a collimated shower of hadrons.

The development of QCD was posterior to that of quantum electrodynamics (QED); while the latter was highly successful in the mid-Sixties, no information about the components of the nucleus was available. Strong interactions were commonly described using general principles and the exchange of mesons [31], although the basis for theories that could eventually accommodate QCD had also been developed [32]. A framework called the *Eightfold Way* [33] had been developed to organize subatomic baryons and mesons into octets. Its connection to an underlying point-like structure of hadrons came after the so-called *heroic age* of deep inelastic scattering (DIS) measurements, interpreted using the *parton model* [34]. These experiments and subsequent interpretations showed that the probes scattered against point-like, spin 1/2 constituents of the nucleons that are the quarks. The presence of spin 1 gluons was also inferred using kinematic considerations in terms of the total momentum shared by the quarks. The QCD equivalent of the electromagnetic charge is the colour charge; (anti-)quarks can take three (anti-)colours (red, green and blue, and their counterparts); the eight interacting gluons exist in a superposition of colour and anti-colour states. SU(3) QCD was established as a theoretical framework for strong interactions only following the discovery of asymptotic freedom as a consequence of the renormalisability of the theory [35]. A short overview of these concepts follows.

The lagrangian of QCD, confinement and asymptotic freedom

QCD is the renormalizable gauge field theory that describes the strong interaction between colored particles in the SM, based in the SU(3) symmetric group. The lagrangian of QCD is

$$\mathcal{L}_{\text{QCD}} = \sum_q \bar{\psi}_q (i\gamma^\mu D_\mu - m_q) \psi_q - \frac{1}{4} G_{\alpha\beta}^A G_A^{\alpha\beta}, \quad (2.1)$$

where quarks and anti-quark fields are respectively denoted by ψ_q and $\bar{\psi}_q$, quark mass is denoted by m_q , γ^μ are the Dirac matrices, and D_μ stands for a covariant derivative. The sum runs over the six different flavors of quarks. The gauge invariant gluonic field strength tensor,

$$G_{\alpha\beta}^A = [\partial_\alpha \mathcal{G}_\beta^A - \partial_\beta \mathcal{G}_\alpha^A - g_s f^{ABC} \mathcal{G}_\alpha^B \mathcal{G}_\beta^C], \quad (2.2)$$

is derived from the gluon fields, \mathcal{G}_α^A , where g_s is a coupling constant, f^{ABC} are the structure constants of SU(3), and the indices A, B and C run over the eight color degrees of freedom of the gluon field. The third term originates from the non-abelian character of the SU(3) group. It is responsible for the gluon self-interaction, giving rise to triple and quadruple gluon vertexes. This leads to a strong coupling, $\alpha_s = g_s^2/4\pi$, that is large at low energies and small at high energies (discussed further in the next section). Two consequences follow:

- **confinement** - the color field potential increases linearly with distance. Quarks and gluons can never be observed as free particles, and are always inside hadrons, either as mesons (quark-antiquark) or as baryons (three quarks, each with a different color). If two quarks separate far enough, the field energy increases and new quarks are created, forming colorless hadrons;
- **asymptotic freedom** - at small distances the strength of the strong coupling is low, such that quark and gluons behave as if they were free. This allows the perturbative approach to be used in the regime where $\alpha_s \ll 1$.

Confinement and asymptotic freedom have relevant experimental consequences; quarks and gluons require interactions with high energy probes to be ejected from the nucleon, and they cannot be observed directly. What one detects instead of quarks and gluons are *jets*, which are collimated showers of particles. These particles are the product of a series of steps [36],

- two hadrons collide with a large momentum transfer;
- two *incoming* partons from the hadrons collide and produce the hard process; at leading order this is a $2 \rightarrow 2$ process, for which the cross section is calculable in pQCD. It is assumed that the probabilities of finding partons in the proton, given by the parton density functions (PDFs), are known;
- additional semi-hard or hard interactions may occur between the remaining partons. These arise naturally in that the integrated cross section for hard scattering diverges for low transverse momentum; the cross section becomes bigger than the total cross section, unless multiple-parton interactions (MPI) are invoked. The remaining partons are referred to as *outgoing* partons;
- the incoming and outgoing partons may radiate, due to their having electromagnetic and color charges, as described using pQCD;
- when partons are sufficiently “far” from each other, *hadronisation* takes place. That is, confinement comes into play and additional color charges (quark/anti-quark pairs) are created such that all free partons combine into hadrons. Many of these hadrons are unstable and decay further at various timescales; they or their decay products may be observed in a detector.

The products of the collision that are not directly identified with the hard scattering (hadron remnants, products of soft multiple parton interactions and radiation) are conventionally defined as the *underlying event* (UE).

Each of the steps described here is subject to modeling, and is accompanied by uncertainties that are hard to quantify. Various Monte Carlo (MC) generators [37–41] adopt different approaches, in particular for the treatment of MPI and the UE. A detailed discussion is given in [section 2.3](#).

Renormalisation

Gluons in QCD are massless, the theory therefore results in divergences of theoretical cross section calculations. A *renormalisation* procedure is necessary in order to allow the theory to give meaningful (non infinite) results that can be compared to experimental measurements. This is achieved by effectively subtracting these infinities through counter-terms embedded in so-called bare parameters that are not measurable. The renormalisation procedure introduces a correction to the renormalised parameter, depending on the renormalisation scale, μ_R , (interpreted as the scale at which the subtraction is made), and on the physical scale at which the measurement is made; the latter is taken as the squared momentum transfer, Q^2 , in the following. Imposing the independence of the final result in all orders of perturbation theory from the renormalisation scale, allows one to derive an explicit form for the renormalised parameter. As an example of a renormalised parameter, the strong coupling constant in the one loop approximation (first order in perturbation theory) is

$$\alpha_s(Q^2) = \frac{\alpha_s(\mu_R^2)}{1 + (\beta_1/4\pi) \alpha_s(\mu_R^2) \ln(Q^2/\mu_R^2)} = \frac{4\pi}{\beta_1 \ln(Q^2/\Lambda_{\text{QCD}}^2)}, \quad (2.3)$$

where

$$\Lambda_{\text{QCD}} = \mu_R \exp\left(-\frac{2\pi}{\beta_1 \alpha_s(\mu_R^2)}\right) \quad (2.4)$$

2. Theoretical background

sets the scale of the coupling. The parameter β_1 is a constant, computed by Gross Wilczek and Politzer [42–44]; it is the first term in the *beta function* of the strong coupling constant,

$$\beta(\alpha_s) = -\sqrt{4\pi\alpha_s(\mu^2)} \left(\frac{\alpha_s}{4\pi} \beta_1 + \left(\frac{\alpha_s}{4\pi} \right)^2 \beta_2 + \dots \right), \quad (2.5)$$

which encodes the dependence of α_s on the energy scale.

The coupling constant, initially scale-invariant, becomes a function of the scale of the process, commonly referred to as a *running coupling constant*. The current theoretical and experimental results for the running α_s [45] are shown in figure 2.2. Contrary to QED, where the coupling

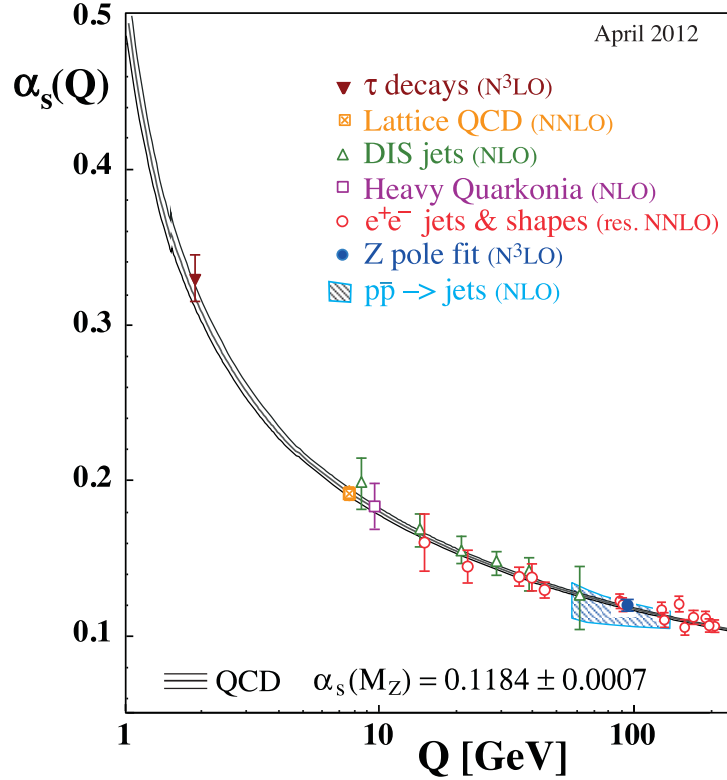


Figure 2.2. Compilation of measurements of the coupling constant, α_s , as a function of the energy scale, Q . The degree of QCD perturbation theory used in the extraction of α_s is indicated in parenthesis in the figure. (Figure taken from [45].)

constant increases with the scale of the process, gluon self-interactions result in negative values of $\beta(\alpha_s)$. The coupling constant therefore is sizeable at low values of Q^2 , leading to confined partons, and decreases as Q^2 increases, leading to asymptotic freedom [46].

The parton model, parton distribution functions and evolution

Asymptotic freedom allows QCD to be described using point-like constituents at sufficiently large energies. The first evidence of this behaviour was given by the SLAC experiments [47] and interpreted by Feynman using the *parton model* [34]. Later on, it was realised that the momentum scale

introduced by renormalisation needed to be accommodated, and the *improved parton model* was developed [48]. Starting from these ideas, the perturbative evolution of quarks and gluons can be predicted independently of the soft, non-perturbative physics, allowing for theoretical calculation of QCD processes.

The differential cross section for lepton-hadron (lh) inelastic scattering can be parameterised, starting from that of elastic scattering of fundamental particles,

$$\frac{d^2\sigma^{lh}}{dx dQ^2} = \frac{1}{q^4} (f(y)x F_1(x, Q^2) + g(y)F_2(x, Q^2)) , \quad (2.6)$$

where F_1 and F_2 are the *structure functions*, which reflect the structure of the nucleon. They are parametrized in terms of the momentum transfer, Q^2 , and of x , which represents (at leading order) the fraction of hadron momentum carried by the massless struck quark. Similarly, $f(y)$ and $g(y)$ are functions which depend on the kinematics of the scattering, where the parameter y measures the ratio of the energy transferred to the hadronic system, to the total leptonic energy available in the target rest frame.

The structure function F_2 can be written as

$$F_2 = \sum_i^{N_q} e_i^2 x f_i(x) , \quad (2.7)$$

where e_i^2 and $f_i(x)$ are respectively the squared charge and momentum distribution of the i^{th} quark, and the sum goes over all quarks in the hadron (in total N_q quarks). The $f_i(x)$ functions can be interpreted (at leading order of perturbation theory) as the probability densities of finding a quark with flavour i , carrying a fraction x of the hadron momentum. The momentum distribution for a given quark or gluon is also called the *parton distribution function* (PDF). The two structure functions are not independent, due to the fact that quarks have spin 1/2. This is expressed by the Callan-Gross relation [49],

$$F_2 = 2x F_1 . \quad (2.8)$$

Probability conservation requires that

$$\int_0^1 x \sum_i^{N_q} f_i(x) dx = 1 , \quad (2.9)$$

also called the *momentum sum rule*. However, calculation of the integral comes up to about 0.5. This calls for the presence of gluons. Conventionally, partons composing a hadron are divided between gluons, *valence quarks* and *sea quarks*. Valence quarks are responsible for the quantum numbers of the hadron, while sea quarks are quark/anti-quark pairs that are generated due to quantum fluctuations.

The independence of the structure function from momentum transfer, Q^2 , at fixed values of x , is known as *Bjorken scaling*. Interactions among the partons lead to deviation from the naive parton model in terms of *scaling violations*. The latter have been observed experimentally, as seen in [figure 2.3](#), where measurements at a given value of x are shown to depend on Q^2 . Intuitively, an increase in Q^2 can be seen as an increase in the resolving power of the probe; if the internal structure of the hadron can be probed at smaller distances, then the number of partons “seen” increases, as gluons can produce quark/anti-quark pairs and quarks or anti-quarks can radiate gluons. The

H1 and ZEUS

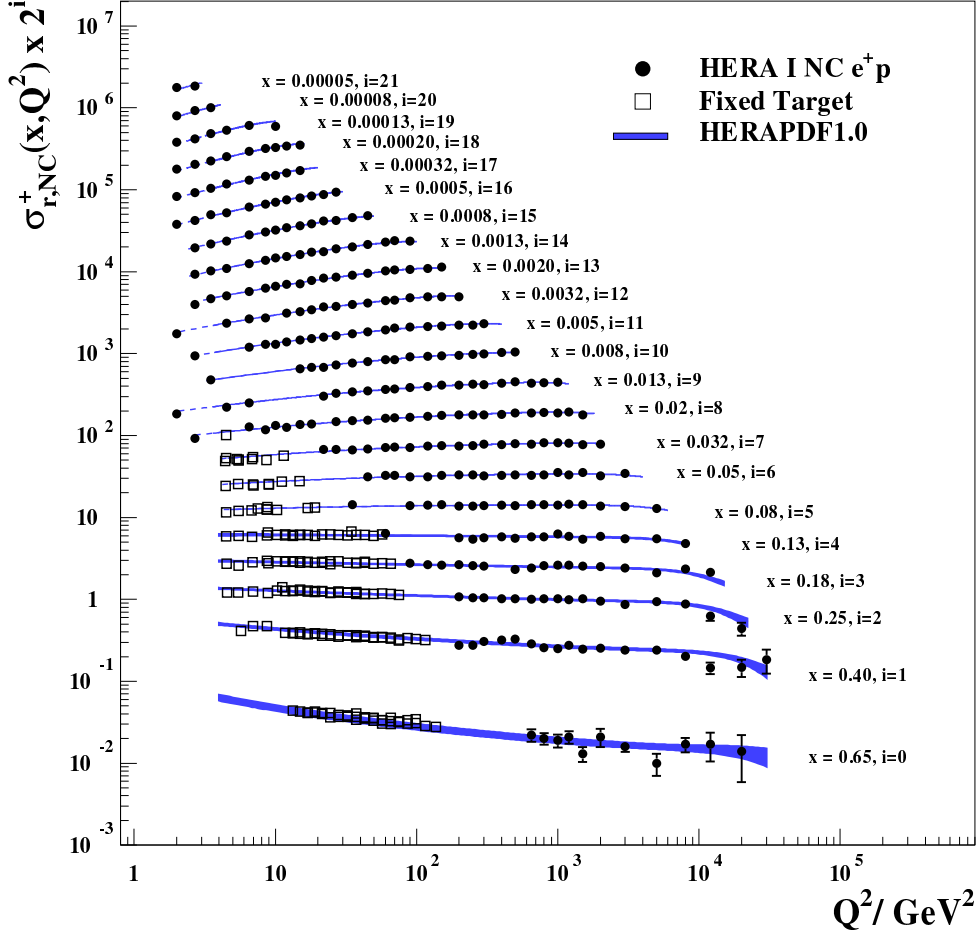


Figure 2.3. HERA combined neutral current (NC) e^+p reduced cross section and fixed-target measurements as a function of momentum transfer, Q^2 , at fixed values of Bjorken- x . The error bars indicate the total experimental uncertainty. A PDF set, called HERAPDF1.0 [50], is superimposed. The bands represent the total uncertainty of the PDF fit. Dashed lines are shown for Q^2 values not included in the QCD analysis. (See [50] for further details.)

DGLAP (Dokshitzer, Gribov, Lipatov, Altarelli and Parisi) formalism [51–53] models these interactions through splitting functions, and uses them to *evolve* perturbatively the renormalised parton densities that contain the Q^2 dependence. The implication of PDF evolution is that measuring parton distributions for one scale, μ_0 , allows their prediction for any other scale, μ_1 , as long as both μ_0 and μ_1 are large enough for both $\alpha_s(\mu_0)$ and $\alpha_s(\mu_1)$ to be small.

The DGLAP formalism gives information on the evolution of the PDFs, though not on their shape. The latter is derived using a combination of experimental data on the structure functions at a given scale, $Q^2 = Q_0^2$, and an initial analytical form. Seven functions should be determined, one for the gluon and the others for each one of the light quarks and anti-quarks. Typically, specific functional forms are postulated for the PDFs with a set of free parameters. The functional form assumed for several PDF sets (such as CTEQ [8]), motivated by counting rules [54] and Regge theory [55], is

$$f_i(x, Q_0^2) = x^{\alpha_i} (1-x)^{\beta_i} g_i(x), \quad (2.10)$$

where α_i and β_i are fit parameters and $g_i(x)$ is a function that asymptotically ($x \rightarrow 0$, $x \rightarrow 1$) tends to a constant.

QCD Factorisation

One of the reasons for the success of QCD as a predictive theory, is that the short-distance component of the scattering process described by pQCD can be separated from the non-perturbative long-distance component; this result is known as the *factorisation theorem* [48]. Factorisation implies that perturbation theory can be used to calculate the hard scattering cross section, while universal functions such as the PDFs¹ can be included a posteriori to obtain the full theoretical prediction. This takes the form,

$$d\sigma_{\text{full}}(p_A, p_B, Q^2) = \sum_{ab} \int dx_a dx_b f_{a/A}(x_a, \mu_F^2) f_{b/B}(x_b, \mu_F^2) \times d\sigma_{ab \rightarrow cd}(\alpha_s(\mu_R^2), Q^2/\mu_R^2), \quad (2.11)$$

where the full and hard scattering cross sections are denoted by σ_{full} and $\sigma_{ab \rightarrow cd}$ respectively. Two partons, a and b , respectively originating from hadrons A and B with momenta p_A and p_B , are the constituents of the hard process. The integral is performed over the respective parton momenta fractions x_a and x_b , weighted by $f_{a/A}$ and $f_{b/B}$, which denote the parton momentum densities for the two interacting partons. The sum is over parton flavours in the hadrons.

Factorisation is a byproduct of a procedure that absorbs singularities into physical quantities in the same fashion as renormalisation. A new scale, μ_F^2 , called the *factorisation scale*, is therefore introduced in addition to the renormalisation scale μ_R^2 and the momentum transfer, Q^2 . Both μ_R^2 and μ_F^2 are generally chosen to be of the order of Q^2 . When truncating calculations at a given order, the uncertainties due to the choice of scale need to be calculated in order to account for higher order terms. The primary sources of uncertainty on QCD calculations are discussed next.

Uncertainties on QCD calculations

There are three main sources of uncertainties in the calculation of pQCD observables, summarized in the following:

- **higher order terms and scale dependence** - the lack of knowledge of higher order terms, neglected in the calculation, is estimated by varying the renormalization scale, μ_R , usually by a factor of two with respect to the default choice. The factorization scale, μ_F , is independently varied in order to evaluate the sensitivity to the choice of scale, where the PDF evolution is separated from the partonic cross section. The envelope of the variation that these changes introduce in an observable is taken as a systematic uncertainty;
- **knowledge of the parameters of the theory** - uncertainties on parameters of QCD, such as the coupling constant, α_s , and the masses of heavy quarks, are propagated into a measured observable;
- **PDF uncertainties** - PDF uncertainties on an observable are evaluated differently for different PDF sets. They account for several factors; uncertainties on the data used to evaluate the PDFs; tension between input data sets; parametrisation uncertainties; and various theoretical uncertainties.

¹ It has been shown experimentally that due to factorisation, PDFs are universal [56]; that is, they can be derived from different physics processes and then used to provide full theoretical predictions independently from the calculation of the hard scattering cross section.

2. Theoretical background

For the LHC, a major source of uncertainty is linked to the fact that pp interactions at center-of-mass energies $\sqrt{s} = 7$ TeV, probe very low momenta of the partons in the proton, as illustrated in [figure 2.4](#). This low- x region is dominated by the gluon density [[57](#)], which is less well constrained by measurements than the quark densities.

Example are shown in [figure 2.5](#), where the PDFs being compared differ in the data samples from which they were derived, and in the assumed value of α_s . In [figures 2.5a - 2.5b](#) the fractional uncertainties of the luminosities of quarks and gluons may be compared for several PDF sets. The uncertainty on the gluon luminosities is larger than on those of the quarks, especially for low and high values of x . An alternative way to illustrate this point is presented in [figures 2.5c - 2.5d](#), where the effect of the uncertainties on observable cross section predictions may be deduced; the gg cross section for Higgs production is compared to that of Z production, the latter originating from $q\bar{q}$ interactions. The relative spread of cross section predictions depending on the gluonic PDFs is roughly twice that of the quarks’.

HERA measurements at low- x , and in particular forward jet production [[59, 60](#)], indicate that the DGLAP dynamic used in deriving the PDFs may not be sufficient to describe the interactions in this region [[61](#)]. This may indicate the need to include higher order pQCD corrections, or use of the formalism of Balitsky, Fadin, Kuraev and Lipatov (BFKL) [[62–64](#)].

2.3. Full description of a hard pp collision

A full description of the final state of a pp collision incorporates two elements. The first is the hard scattering, involving a large transfer of transverse momentum and calculable in pQCD. The second part pertains to non perturbative effects, taking into account low- p_t interactions and hadronization. The two aspects of the computation are discussed in the following sections.

2.3.1. The hard scattering

The hard scattering is computed at a fixed order (in the strong coupling constant) in perturbation theory. The dominant contributions to jet cross sections arise from Feynman diagrams that contribute to jet production at leading order (LO), known as $(2 \rightarrow 2)$ diagrams. Some examples of LO diagrams are shown for quark/quark t -channel scattering, quark/anti-quark s -channel annihilation, and gluon/gluon t -channel scattering in [figures 2.6a - 2.6c](#). A calculation at next-to-leading order (NLO) may include either a $(2 \rightarrow 2)$ process with one virtual loop, as shown in [figure 2.6d](#), or a $(2 \rightarrow 3)$ interaction, as in [figure 2.6e](#), where one of the incoming or outgoing partons radiates a third parton.

The results of a full NLO calculation of the differential dijet mass cross section, using the NLO-JET++ package [[65](#)], are compared to ATLAS data in [chapter 8](#).

2.3.2. Non-perturbative effects

As mentioned above, complete pQCD calculations are performed up to a fixed order in α_s . However, the enhanced soft-gluon radiation and collinear configurations at higher orders can not be neglected. These are taken into account in the parton shower (PS) approximation, that sums the leading contributions of such topologies to all orders. MC generator programs include the PS approximation,

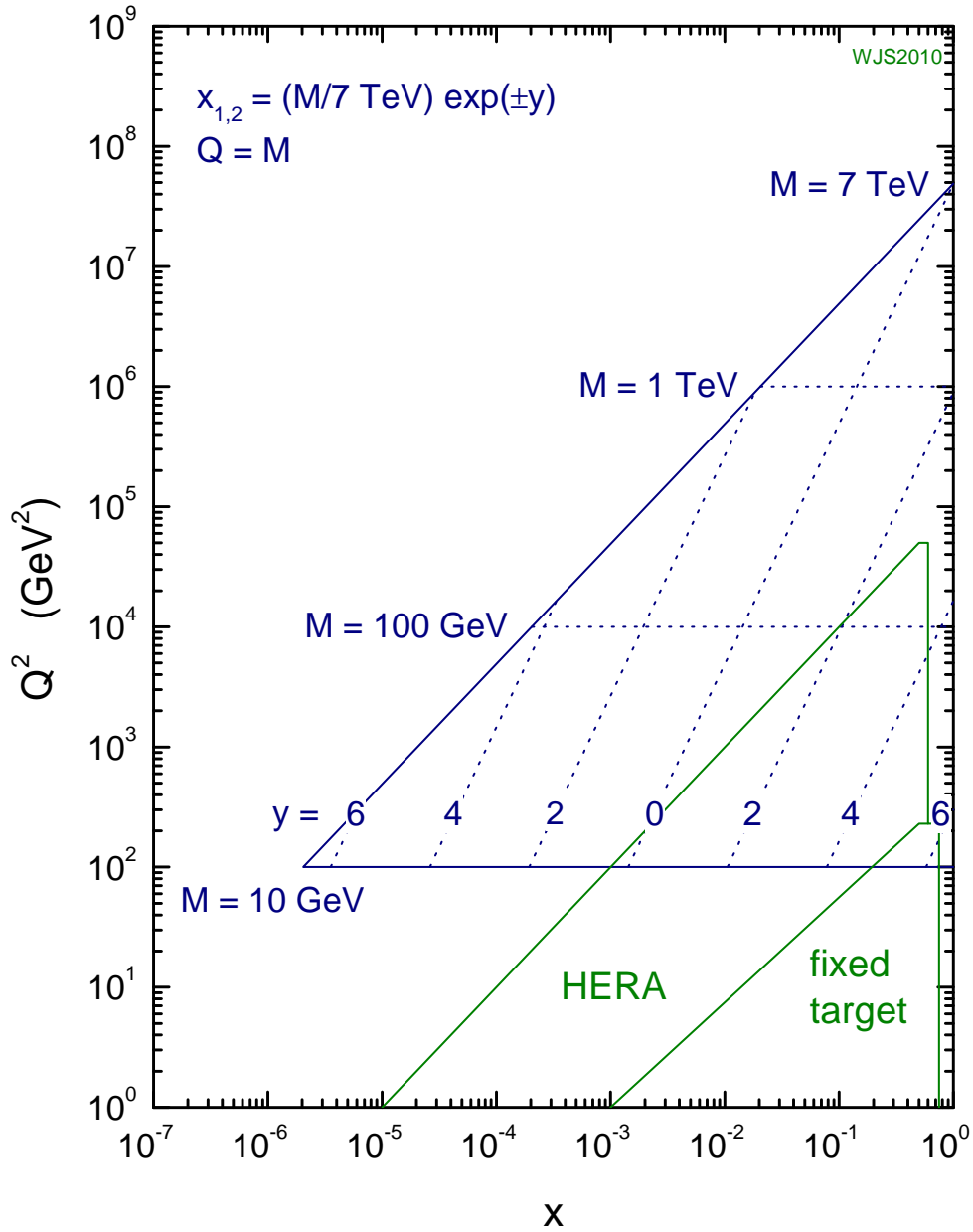


Figure 2.4. The (x, Q^2) kinematic plane for LHC at $\sqrt{s} = 7$ TeV, where x denotes the fraction of the momentum of the proton carried by an interacting parton, and Q^2 stands for the momentum transfer of the interaction. Shown also are the ranges covered by HERA and fixed-target experiments. The x and Q^2 ranges probed by the production of mass, M , or a hard final state at fixed rapidity, y , are indicated by the dashed lines. (Figure taken from <http://projects.hepforge.org/mstwpdf/>, courtesy of J. Stirling.)

2. Theoretical background

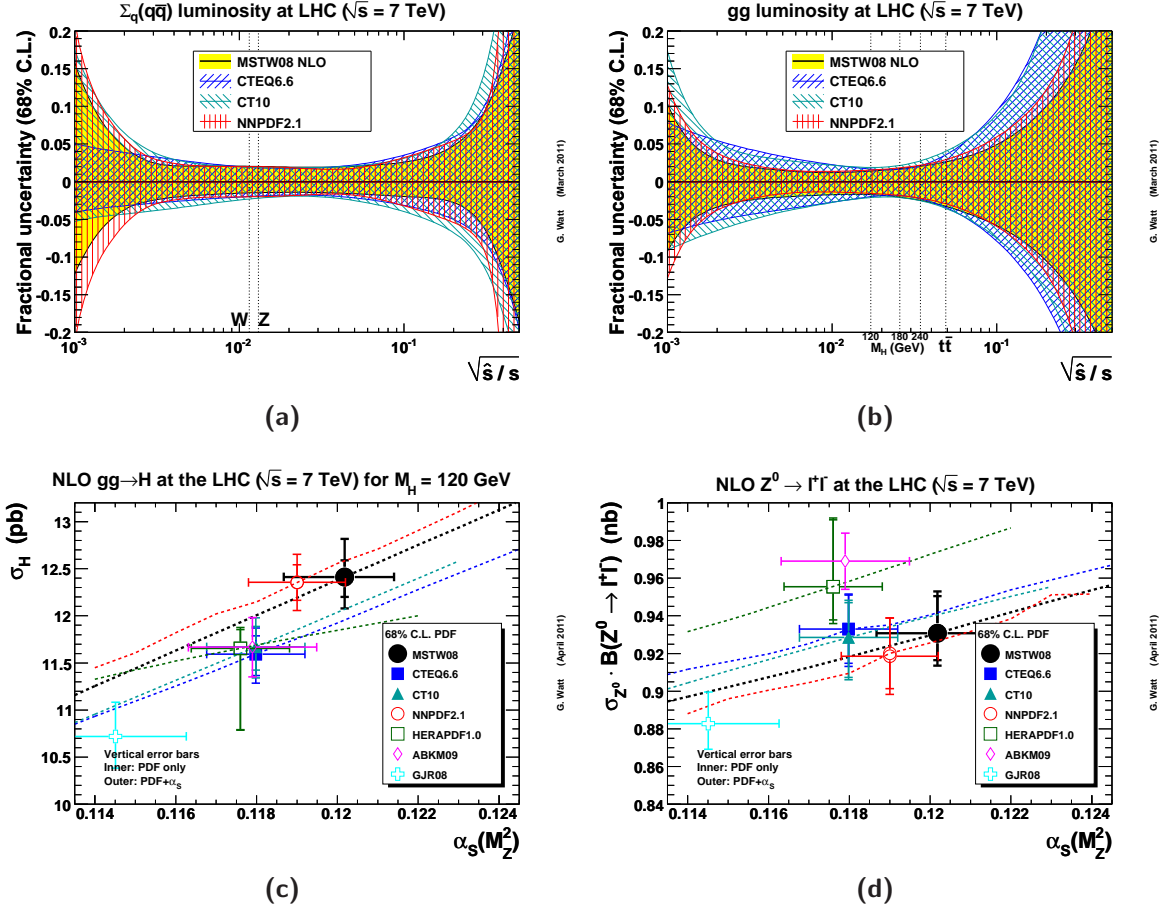


Figure 2.5. (a)-(b) Fractional uncertainties on the NLO parton-parton luminosities for quarks and for gluons, derived using different PDF sets, as indicated in the figures. The uncertainties are shown as a function of the fractional center-of-mass energy of the partonic system responsible for the scattering, denoted by $\sqrt{\hat{s}}/s$.

(c)-(d) Cross sections for Higgs and Z_0 production at $\sqrt{s} = 7$ TeV for different PDF sets, as indicated in the figures. The cross sections are shown as a function of the strong coupling constant (at the scale of the Z), $\alpha_s(M_Z^2)$, which is used in the derivation of the PDFs. The error bars represent the uncertainties on the respective PDFs excluding (inner) or including (outer) the uncertainty on $\alpha_s(M_Z^2)$. The dashed lines interpolate the cross section predictions calculated with each PDF set for different values of $\alpha_s(M_Z^2)$.

(Figures are taken from [58].)

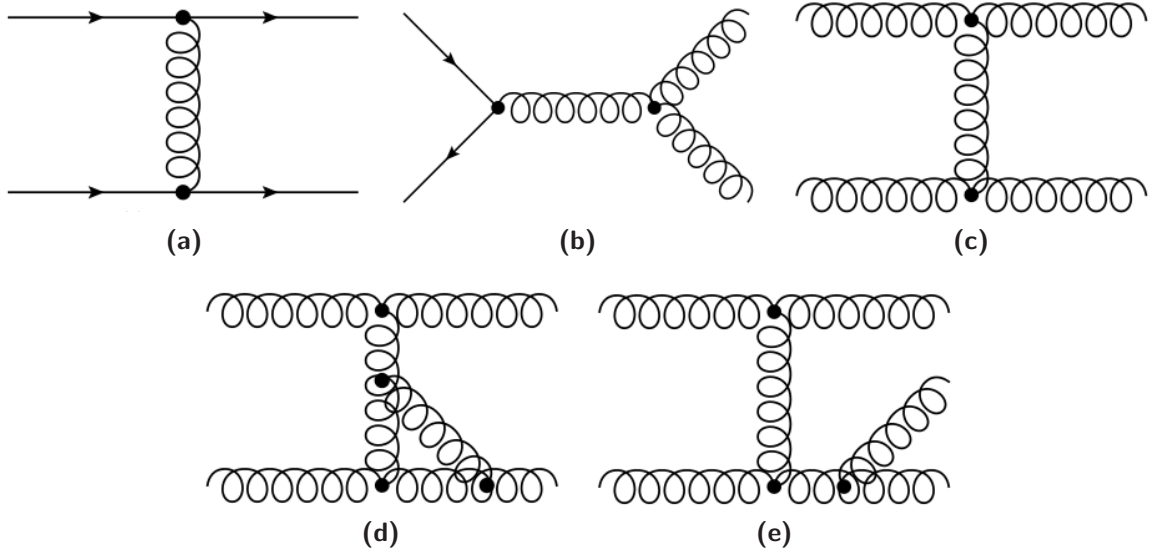


Figure 2.6. Examples for leading-order ((a)-(c)) and next-to-leading order ((d)-(e)) Feynman diagrams for jet production in proton-proton collisions at the LHC; t -channel scattering (a), quark/anti-quark s -channel annihilation (b), gluon/gluon t -channel scattering (c), a $(2 \rightarrow 2)$ diagram with a virtual loop (d), a $(2 \rightarrow 3)$ diagram where the third outgoing parton is produced via real emission from another parton (e).

as well as models to reproduce non-perturbative effects, such as hadronization and the underlying event.

Since non-perturbative physics models are by necessity deeply phenomenological, they usually account for the majority of parameters incorporated into event generators. For instance, typical hadronization models require parameters to describe e.g., the kinematic distribution of transverse momentum in hadron fragmentation, baryon-to-meson ratios, strangeness and suppression of η and η' mesons, and the assignment of orbital angular momentum to final state particles. Event generators are therefore tuned to data in specific regions of phase-space. At times it is not possible to match all features of the data, e.g., simultaneous description of both the transverse momentum and the multiplicity distributions of charged particles in hadron-hadron collisions [66]. Different tunes are usually compared in order to assess the theoretical uncertainty associated with non-perturbative processes.

The different elements of event generators, apart from the hard scattering itself, are discussed next.

Parton showers

The PS approximation describes successive parton emission from the partons taking part in the hard interaction. In principle, the showers represent higher-order corrections to the hard subprocess. However, it is not feasible to calculate these corrections exactly. Instead, an approximation scheme is used, in which the dominant contributions are included in each order. These dominant contributions are associated with collinear parton splitting or soft gluon emission, illustrated in figure 2.7.

The evolution of the shower is usually governed by the DGLAP equations, though at low- x , as mentioned above, BFKL dynamics may be required. Numerical implementation of the parton

2. Theoretical background

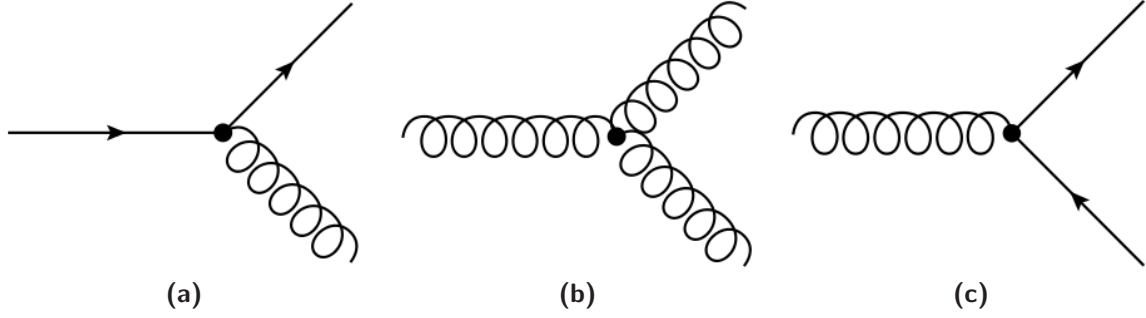


Figure 2.7. Examples of leading-order ($1 \rightarrow 2$) Feynman diagrams for the splitting of quarks and gluons; a quark emitting a gluon (a), a gluon emitting another gluon (b), a gluon splitting into a quark/anti-quark pair (c).

shower is achieved using the *Sudakov form factors* [67]; these represent the probability that a parton does not branch between some initial scale and another, lower scale. In each step, as a branching $a \rightarrow bc$ occurs from scale t_a , subsequent branchings are derived from the scales t_b and t_c of the products of the initial state. Branchings can be angle- or transverse momentum-ordered. For the former, the opening angles between each successive branchings become smaller; for the latter, emissions are produced in decreasing order of intrinsic p_t . Successive branching stops at a cutoff scale of the order of Λ_{QCD} , after producing a high-multiplicity partonic state.

Since quarks and gluons can not exist isolated, MC programs contain models for the hadronization of the partons into colorless hadrons, discussed in the following.

Hadronization

The hypothesis of local *parton-hadron duality* states that the momentum and quantum numbers of hadrons follow those of their constituent partons [68]. This makes up the general guideline of all hadronization models. There exist two main models of hadron production in the popular physics generators, the string model and the cluster model.

The string model [69] for hadronization, depicted schematically in figure 2.8a, is based on an observation from lattice simulations of QCD; at large distances, the potential energy of colour sources, such as heavy quark/anti-quark ($q\bar{q}$) pairs, increases linearly with their separation. This indicates a distance-independent force of attraction, thought to be due to the self-attraction of the gluonic field.

In the model, the field between each $q\bar{q}$ pair is represented by a string with uniform energy per unit length. As the q and the \bar{q} move apart from each other, the energy of the color field increases and the string connecting the two is tightened. Eventually the string breaks, and its two ends form a new quark/anti-quark pair. If the invariant mass of either of these string pieces is large enough, further breaks may occur in addition. The string break-up process is assumed to proceed until only on-mass-shell hadrons remain. In the simplest approach of baryon production, a diquark (D) is treated just like an ordinary anti-quark; a string can break either into a quark/anti-quark or into a diquark/anti-diquark pair, leading to three-quark states.

The cluster model [70] for hadronization is based on the so-called *preconfinement* property of QCD, discovered by Amati and Veneziano [71]. They showed that at evolution scales, q , much smaller than the scale of the hard subprocess, the partons in a shower are clustered in colourless groups. These groups have an invariant mass distribution that is independent of the nature and

scale of the hard subprocess, depending only on q and on Λ_{QCD} . It is then natural to identify these clusters at the hadronization scale, Q_0 , as *proto-hadrons* that later decay into the observed final-state hadrons.

In practical terms, at a scale around Q_0 , gluons from the PS are split into light quark/anti-quark or diquark/anti-diquark pairs, as illustrated in figure 2.8b. Color-singlet clusters are formed from the different pair combinations; mesonic ($q\bar{q}$ and $D\bar{D}$), barionic (qD) and anti-barionic ($\bar{q}\bar{D}$). The clusters thus formed are fragmented into two hadrons. If a cluster is too light to decay into two hadrons, it is taken to represent the lightest single hadron of its flavor; its mass is therefore shifted to the appropriate value by an exchange of momenta with a neighboring cluster. If the cluster is too heavy, it decays into two clusters, which are further fragmented into hadrons.

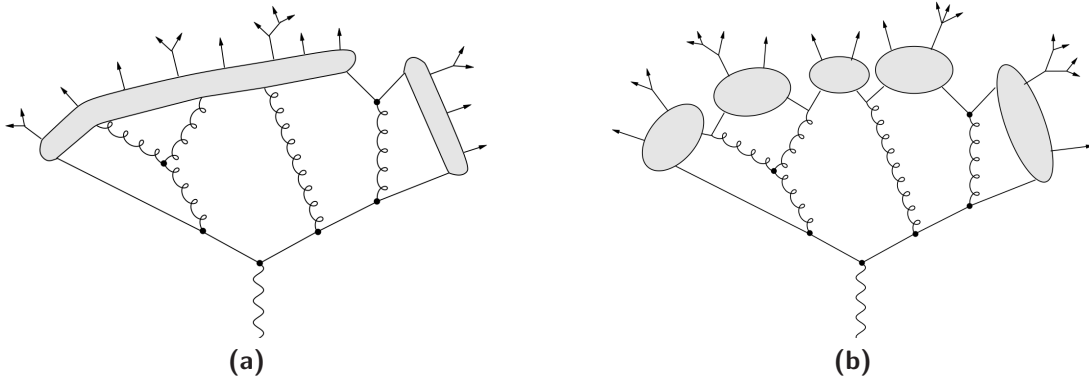


Figure 2.8. Schematic illustration of hadronization in the string (a) and in the cluster (b) models.

The underlying event

In events that contain a hard subprocess, there is extra hadron production that cannot be ascribed to showering from the coloured partons participating in the subprocess, known as the underlying event (UE). Furthermore, this extra activity is greater than that in so-called minimum-bias events (collisions that do not yield an identifiable hard subprocess). The UE is believed to arise from collisions between those partons in the incoming hadrons that do not directly participate in the hard subprocess.

The most common hard subprocess at the LHC is elastic gluon-gluon scattering, $gg \rightarrow gg$. The leading-order differential cross section for this subprocess diverges at zero momentum transfer, due to the exchange of a massless virtual gluon. This divergence is presumably regularized below some momentum transfer, t_{min} , by higher-order and non-perturbative effects. Nevertheless, for reasonable values of t_{min} , the integrated cross section for gluon-gluon scattering is very large, larger even than the total proton-proton (pp) scattering cross section. This result indicates that the average number of gluon-gluon collision per pp collisions is greater than one. Including the cross sections for elastic scattering of quarks, anti-quarks and gluons in all possible combinations (all of which diverge in leading order), multiple parton interactions (MPI) are found to be highly probable

This is the basis on which modern event generators model both minimum-bias collisions and the UE. To account for the extra hadron production when a hard subprocess is present, an event

2. Theoretical background

generator must model the impact parameter structure of hadron-hadron collisions. The partons in each incoming hadron are distributed over a transverse area of the order of 1 fm^2 . The impact parameter of a collision is the transverse distance between the centroids of these areas before the collision. When the impact parameter is large, the areas overlap little and the collision is peripheral; this configuration is associated with a low probability of a hard parton-parton interaction and few MPI. On the other hand, at small impact parameter values, the collision is central and has a large overlap of areas; several multiple interactions and a higher probability of a hard interaction are therefore expected.

To summarize, the presence of a hard subprocess is correlated with more MPI and a higher level of UE activity. Most of the multiple-interactions are soft, though hard MPI is also possible. As mentioned in [chapter 1](#), hard MPI are an important background for e.g., new physics signals involving multi-jet final states. As such, hard MPI are given special attention beyond the general discussion in the context of the UE. The most simple (and often most prominent) case, that of double parton scattering, is reviewed in the next section.

2.4. Double parton scattering

The formalism to deal with (semi-)hard double parton scattering in hadronic interactions at center-of-mass energy \sqrt{s} [[21](#), [22](#)] may be summarized by

$$\sigma_{(A,B)}^{\text{DPS}}(s) = \frac{m}{2} \sum_{i,j,k,l} \int \Gamma_{ij}(x_1, x_2, \mathbf{d}; Q_A, Q_B) \hat{\sigma}_{ik}^{(A)}(x_1, x'_1, s) \Gamma_{kl}(x'_1, x'_2, \mathbf{d}; Q_A, Q_B) \times \hat{\sigma}_{jl}^{(B)}(x_2, x'_2, s) dx_1 dx_2 dx'_1 dx'_2 d^2 \mathbf{d}, \quad (2.12)$$

where $\sigma_{(A,B)}^{\text{DPS}}$ is the differential double parton scattering cross section for the inclusive production of a combined system $A+B$ at a given \sqrt{s} ; the terms $\hat{\sigma}_{ik}^{(A)}$ denote the differential partonic cross sections for the production of a system A in the collision of partons i and k ; the terms $\Gamma_{ij}(x_1, x_2, \mathbf{d}; Q_A, Q_B)$ represent double parton distribution functions (DPDFs); and the parameter m is a symmetry factor such that $m = 1$ if $A = B$ and $m = 2$ otherwise. The integration over the momentum fractions x_1 and x_2 is constrained by energy conservation, such that $(x_1 + x_2 \leq 1)$. Summation over all possible parton combinations is performed. A sketch of double parton scattering is shown in [figure 2.9](#) for illustration.

The DPDFs, $\Gamma_{ij}(x_1, x_2, \mathbf{d}; Q_A, Q_B)$, may be loosely interpreted as the inclusive probability distribution to find a parton i (j) with longitudinal momentum fraction x_1 (x_2) at scale Q_A (Q_B) in the proton, with the two partons separated by a transverse distance \mathbf{d} . The scale Q_A (Q_B) is given by the characteristic scale of subprocess A (B). It is assumed that the DPDFs may be decomposed into longitudinal and transverse components,

$$\Gamma_{ij}(x_1, x_2, \mathbf{d}; Q_A, Q_B) \simeq D_{ij}(x_1, x_2; Q_A, Q_B) F(\mathbf{d}). \quad (2.13)$$

The longitudinal component, $D_{ij}(x_1, x_2; Q_A, Q_B)$, has a rigorous interpretation in leading order pQCD, as the inclusive probability of finding a parton i with momentum fraction x_1 at scale Q_A , as well as and a parton j with momentum fraction x_2 at scale Q_B in a proton. Accurate prediction of double parton scattering cross sections and of event signatures requires good modelling of $D_{ij}(x_1, x_2; Q_A, Q_B)$ and of the transverse component, $F(\mathbf{d})$. In particular, one must correctly take

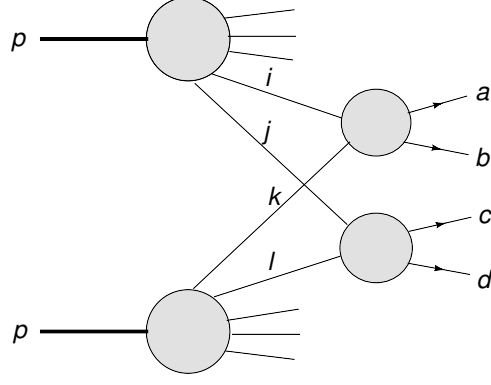


Figure 2.9. Sketch of a double parton scattering process, in which the active partons originating from one proton are i and j and from the other are k and l . The two hard scattering subprocess are $A(i k \rightarrow a b)$ and $B(j l \rightarrow c d)$.

account of the effects of correlations in both longitudinal momenta and transverse positions in these functions.

Correlations between the partons in transverse space are highly significant; at the very least, they must tie the two partons together within the same hadron. However, their precise calculation is not possible using perturbation theory. Existing models typically use Gaussian or exponential forms (or their combination) to describe $F(\mathbf{d})$ [36, 72]. The transverse component is usually expressed simply as

$$\sigma_{\text{eff}}(s) = \left[\int d^2\mathbf{d} (F(\mathbf{d}))^2 \right]^{-1}. \quad (2.14)$$

The quantity $\sigma_{\text{eff}}(s)$ is defined at the parton-level, and has the units of a cross section. In the formalism outlined here, it is independent of the process and of the phase-space under consideration. Naively, it may be related to the geometrical size of the proton. That is, given that one hard scattering occurs, the probability of the other hard scattering is proportional to the flux of accompanying partons; these are confined to the colliding protons, and therefore their flux should be inversely proportional to the area (cross section) of a proton. This leads to an estimate of $\sigma_{\text{eff}} \approx \pi R_p^2 \approx 50$ mb, where R_p is the proton radius. Alternatively, σ_{eff} may be connected to the inelastic cross section, which would lead to $\sigma_{\text{eff}} \approx \sigma_{\text{inel}} \approx 70$ mb at $\sqrt{s} = 7$ TeV [73, 74]. For hard interactions, assuming uncorrelated scatterings, σ_{eff} can be estimated from the gluon form factor of the proton [75] and comes out to be ~ 30 mb.

A number of measurements of σ_{eff} have been performed in pp or $p\bar{p}$ collisions at different center-of-mass energies, as specified in table 2.1. The energy dependence of the measured values of σ_{eff} yielded an increase from about 5 mb at the lowest energy (63 GeV) to about 15 mb at LHC energies (7 TeV). Attempts to explain the differences between these values have used the Constituent Quark Model [76, 77], such as in [78], or have introduced non-trivial correlations between the two scattering systems, as in [16–20]. A complete explanation, however, is still elusive. A recent argument, suggested in [79–81] may resolve the discrepancy; it goes as follows. In DPS, two partons from one proton collide with two partons from the other proton. The two partons from a given proton can originate from the non-perturbative hadron wave function or, alternatively, emerge from perturbative splitting of a single parton from the hadron. The former represents a double-(2→2) interaction, and the latter a (3→4) interaction. The (3→4) process could explain the difference

2. Theoretical background

Experiment	\sqrt{s} [GeV]	Final state	σ_{eff} [mb]
[23] AFS (pp), 1986	63	4 jets	~ 5
[24] UA2 ($p\bar{p}$), 1991	630	4 jets	> 8.3 (95% C.L.)
[25] CDF ($p\bar{p}$), 1993	1800	4 jets	$12.1^{+10.7}_{-5.4}$
[26] CDF ($p\bar{p}$), 1997	1800	$\gamma + 3\text{-jets}$	$14.5 \pm 1.7^{+1.7}_{-2.3}$
[27] DØ ($p\bar{p}$), 2010	1960	$\gamma + 3\text{-jets}$	$16.4 \pm 0.3 \pm 2.3$
[28] ATLAS (pp), 2012	7000	$W + 2\text{-jets}$	$15 \pm 3^{+5}_{-3}$

Table 2.1. Summary of published measurements of σ_{eff} .

between the experimental value of σ_{eff} of ~ 15 mb, and the expected value of ~ 30 mb.

In the absence of a rigorous formalism, measurements of σ_{eff} typically assume a simple factorization ansatz for the DPDFs,

$$D_{ij}(x_1, x_2; Q_A, Q_B) \simeq D_i(x_1; Q_A) D_j(x_2; Q_B) . \quad (2.15)$$

The differential double parton scattering cross section defined in [equation \(2.12\)](#) therefore reduces to

$$\sigma_{(A,B)}^{\text{DPS}} = \frac{m}{2} \frac{\sigma_A \sigma_B}{\sigma_{\text{eff}}} . \quad (2.16)$$

The assumption of factorization is problematic. For one, this naive representation does not obey the relevant momentum and number sum rules. In addition, while previous experiments suggest that approximate factorisation holds at moderately low x [26], this can not be true for all values of x . Namely, if $D_i(x_1; Q_A)$ and $D_j(x_2; Q_B)$ each satisfy DGLAP evolution, then the naive product, $D_i(x_1; Q_A) D_j(x_2; Q_B)$, can not be a solution of the *double-DGLAP equations* (dDGLAP), suggested e.g., in [17]. In order to use the factorization ansatz, the unknown correlations are absorbed into σ_{eff} , which then possibly becomes dependant on the process (and respective phase-space) under consideration.

A measurement of the rate of double parton scattering in four jet events in ATLAS is presented in this thesis, using the simplified form of the effective cross section given in [equation \(2.15\)](#). Only the double-($2 \rightarrow 2$) topology is considered in the analysis, as discussed in [chapter 9](#).

3. The ATLAS experiment at the LHC

3.1. The Large Hadron Collider

The Large Hadron Collider (LHC) is the world's largest and highest-energy particle accelerator. LHC is a proton-proton (pp) collider, located at the Franco-Swiss border near Geneva, Switzerland. It lies in a tunnel 27 km in circumference at an average depth of 100 meters. The tunnel houses 1232 superconducting bending dipole magnets, cooled using liquid helium to an operating temperature of 1.9 K, producing a magnetic field of about 8 T. The use of dipole magnets allows to keep protons traveling clockwise and counter-clockwise on orbit at the same time. In total, 392 quadrupole magnets are used to keep the beams focused and to collide them at the four interaction points (IPs) of the LHC experiments. The design center-of-mass energy of the LHC is $\sqrt{s} = 14$ TeV.

Protons are produced by ionizing hydrogen atoms in an electric field. They are injected into RF cavities and accelerated to 750 keV. The beam is then transmitted to the LINAC 2, a linear accelerator, which increases the energy to 50 MeV. The protons are accelerated to 1.4 GeV by the Proton Synchrotron Booster and then further to 26 GeV by the Proton Synchrotron. Next, the Super Proton Synchrotron accelerates the protons to 450 GeV, the minimum energy required to maintain a stable beam in the LHC. Finally, the LHC accelerates them to the operating energy.

During the first two years of operation (2010-2011), the LHC operated at a center-of-mass energy of $\sqrt{s} = 7$ TeV, with 3.5 TeV per proton. This center-of-mass energy has been chosen to ensure a safe operating margin for the magnets in the accelerator. So far, up to the end of the 2011 run, the LHC delivered 5.61 fb^{-1} total integrated luminosity with a peak luminosity of $3.65 \times 10^{33} \text{ cm}^{-2}\text{s}^{-1}$ [82]. The bunch separation was 50 ns for most of the running period. The full 2010 and most of the 2011 datasets are used in this analysis.

3.2. The ATLAS detector

ATLAS (A Toroidal Lhc ApparatuS) [83, 84] is a general-purpose detector surrounding IP 1 of the LHC. ATLAS consists of three main sub-systems, the inner detector (ID), the calorimeters and the muon spectrometer (MS). Figure 3.1a shows a schematic view of the ATLAS detector and its sub-systems.

Detector sub-systems

The ID is used to measure the tracks of charged particles. It covers the pseudo-rapidity range, $|\eta| < 2.5$ ¹, and has full coverage in azimuth. It is made of three main components, arranged in concentric layers, all of which are immersed in a 2 T field provided by the inner solenoid magnet. Three

¹ The coordinate system used by ATLAS is a right-handed Cartesian coordinate system. The positive z -direction is defined as the direction of the anti-clockwise beam. Pseudo-rapidity is defined as $\eta = \ln \tan(\theta/2)$, where θ is the angle with respect to the z -axis. The azimuthal angle in the transverse plane ϕ is defined to be zero along the x -axis, which points toward the center of the LHC ring.

3. The ATLAS experiment at the LHC

layers of silicon pixel detectors provide a two-dimensional hit position very close to the interaction point. Silicon microstrip detectors are then used in the next four layers, providing excellent position resolution for charged tracks. A transition-radiation detector is the final component of the tracker, with poorer position resolution with respect to the silicon, but providing many measurement points and a large lever-arm for track reconstruction in addition to particle identification capabilities.

The ATLAS calorimeter, shown schematically in [figure 3.1b](#), is the principal tool used in the analysis. The calorimeter is composed of several sub-detectors. The liquid argon (LAr) electromagnetic (EM) calorimeter is divided into one barrel ($|\eta| < 1.475$) and two end-cap components ($1.375 < |\eta| < 3.2$). It uses an accordion geometry to ensure fast and uniform response and fine segmentation for optimum reconstruction and identification of electrons and photons. The hadronic scintillator tile calorimeter consists of a barrel covering the region, $|\eta| < 1.0$, and two extended barrels in the range $0.8 < |\eta| < 1.7$. The LAr hadronic end-cap calorimeter ($1.5 < |\eta| < 3.2$) is located behind the end-cap electromagnetic calorimeter. The forward calorimeter covers the range $3.2 < |\eta| < 4.9$ and also uses LAr as the active material.

The MS forms the outer part of the ATLAS detector and is designed to detect muons exiting the barrel and end-cap calorimeters and to measure their momentum in the pseudo-rapidity range $|\eta| < 2.7$. It is also designed to trigger on muons in the region $|\eta| < 2.4$. The MS operates inside an air-core toroid magnet system with a peak field in the coil windings of 4 T. The precision momentum measurement is performed by the Monitored Drift Tube chambers covering the pseudo-rapidity range $|\eta| < 2.7$ (except in the innermost end-cap layer where their coverage is limited to $|\eta| < 2.0$). In the forward region ($2.0 < |\eta| < 2.7$), Cathode-Strip Chambers are used in the innermost tracking layer. The capability to trigger on muon tracks is achieved by a system of fast trigger chambers capable of delivering track information within a few tens of nanoseconds after the passage of the particle. In the barrel region ($|\eta| < 1.05$), Resistive Plate Chambers were selected for this purpose, while in the end-cap ($1.05 < |\eta| < 2.4$) Thin Gap Chambers were chosen.

The Trigger System

The ATLAS detector has a three-level trigger system consisting of Level 1 (L1), Level 2 (L2) and Event Filter (EF). The L1 trigger rate at design luminosity is approximately 75 kHz. The L2 and EF triggers reduce the event rate to approximately 200 Hz. Another trigger system used in ATLAS relies on the minimum-bias trigger scintillators (MBTS). The MBTS trigger requires one hit above threshold from either one of the sides of the detector. The different triggers used in the analysis are described in further detail in [chapter 6, section 6.2](#).

Luminosity Measurement

Accurate measurement of the delivered luminosity is a key component of the ATLAS physics program. For cross section measurements of SM processes, the uncertainty on the delivered luminosity is often one of the dominant systematic uncertainties.

The instantaneous luminosity of proton-proton collisions can be calculated as

$$\mathcal{L} = \frac{R_{\text{inel}}}{\sigma_{\text{inel}}}, \quad (3.1)$$

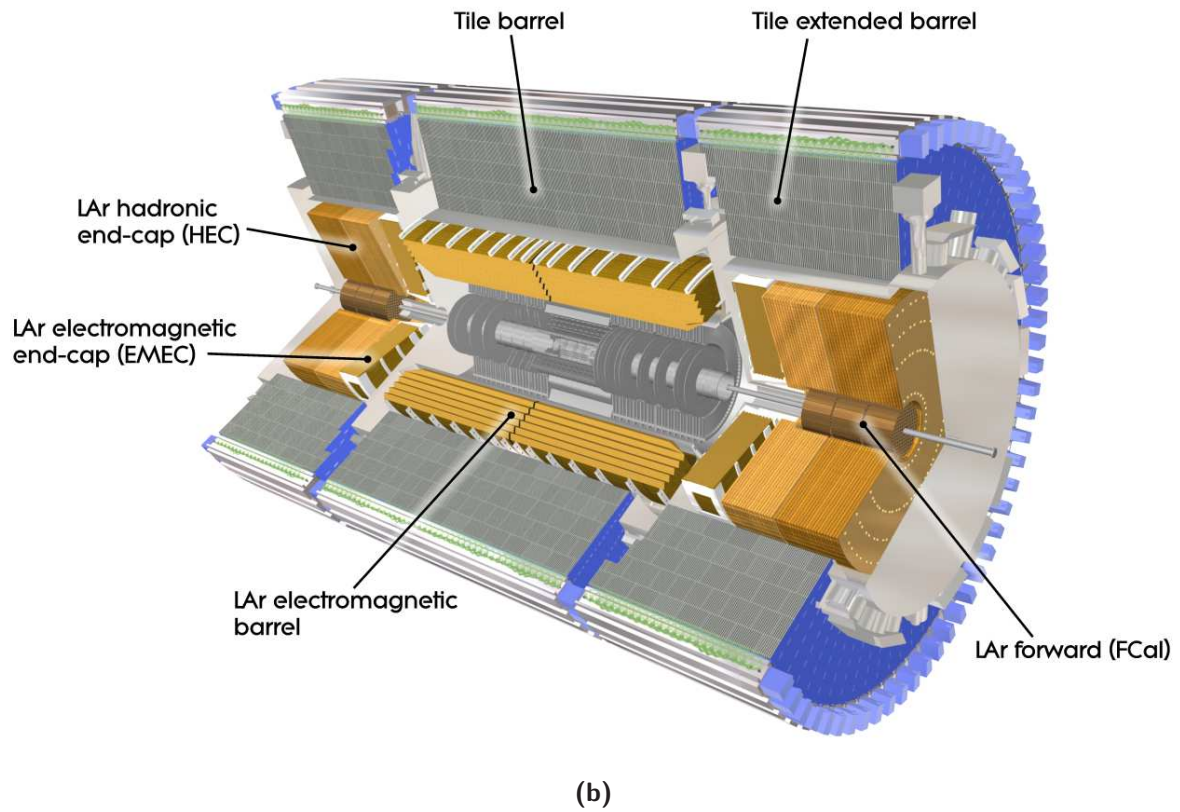
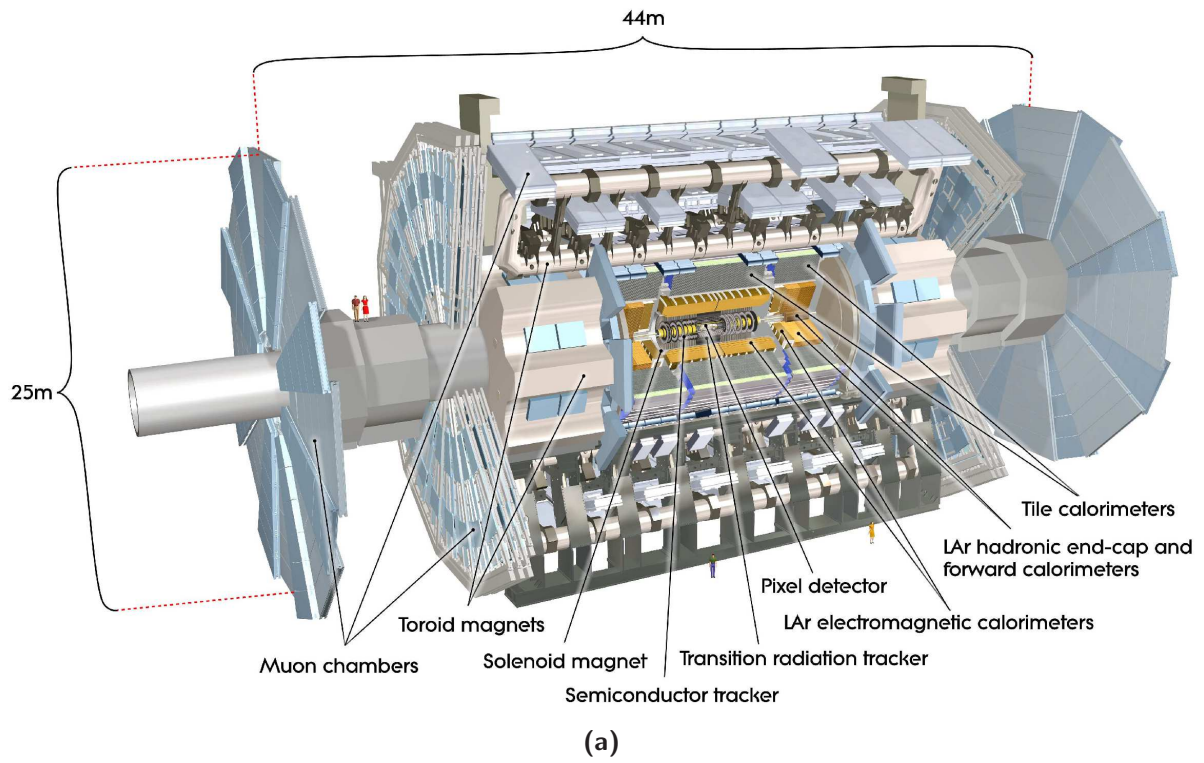


Figure 3.1. Schematic view of the ATLAS detector (a) and of the ATLAS calorimeter system (b).

3. The ATLAS experiment at the LHC

where R_{inel} is the rate of pp interactions and σ_{inel} is the inelastic cross section. Any detector sensitive to inelastic pp interactions can be used as a source for relative luminosity measurement. However, these detectors must be calibrated using an absolute measurement of the luminosity.

The recorded luminosity can be written as

$$\mathcal{L} = \frac{\mu_{\text{vis}} n_b f_{\text{rev}}}{\sigma_{\text{vis}}}, \quad (3.2)$$

where μ_{vis} is the visible number of interactions per bunch crossing in the detector, n_b is the number of bunch pairs colliding in ATLAS, $f_{\text{rev}} = 11245.5$ Hz is the LHC revolution frequency and σ_{vis} is the visible cross section, to be determined via calibration for each detector.

The calibration is done using dedicated beam separation scans, also known as *van der Meer* scans [85], where the two beams are stepped through each other in the horizontal and vertical planes to measure their overlap function. The delivered luminosity is measured using beam parameters,

$$\mathcal{L} = \frac{n_b f_{\text{rev}} n_1 n_2}{2\pi \Sigma_x \Sigma_y}, \quad (3.3)$$

where n_1 and n_2 are respectively the bunch populations (protons per bunch) in beam 1 and in beam 2 (together forming the bunch charge product), and Σ_x and Σ_y respectively characterize the horizontal and vertical profiles of the colliding beams.

By comparing the delivered luminosity to the peak interaction rate, $\mu_{\text{vis}}^{\text{Max}}$, observed by a given detector during the *van der Meer* scan, it is possible to determine the visible cross section,

$$\sigma_{\text{vis}} = \mu_{\text{vis}}^{\text{Max}} \frac{2\pi \Sigma_x \Sigma_y}{n_1 n_2}. \quad (3.4)$$

Two detectors are used to make bunch-by-bunch luminosity measurements in 2010 and in 2011, LUCID and BCM. LUCID is a Cerenkov detector specifically designed for measuring the luminosity in ATLAS. It is made up of sixteen mechanically polished aluminum tubes filled with C_4F_{10} gas surrounding the beampipe on each side of the IP at a distance of 17 m, covering the pseudo-rapidity range, $5.6 < |\eta| < 6.0$. The beam conditions monitor (BCM) consists of four small diamond sensors on each side of the ATLAS IP arranged around the beam-pipe in a cross pattern. The BCM is a fast device, primarily designed to monitor background levels. It is also capable of issuing a beam-abort request in cases of possible damage to ATLAS detectors, due to beam losses.

The relative uncertainty on the luminosity scale for pp collisions during 2010 [86] and 2011 [85] was found to be, respectively ± 3.4 and $\pm 3.9\%$ ².

² The uncertainty on the luminosity in 2011 quoted here is larger than the value given in [85]. The increased value is a consequence of recent studies by the Luminosity group in ATLAS, which show significant non-linear correlations between the *van der Meer* scans in the horizontal and vertical directions [87]. These correlations were not previously known and are not yet fully understood.

4. Monte Carlo simulation

Any analysis involving a complex detector such as ATLAS, requires a detailed detector Monte Carlo (MC) simulation. The MC is used in order to compare distributions of observables, as simulated by physics generators, with the data. In addition, it is used to study the performance of the detector by estimating reconstruction efficiencies, geometrical coverage, the performance of triggers etc.

A description of the MC generators and of the ATLAS detector simulation used in the analysis is presented in the following.

4.1. Event generators

The four-momenta of particles produced in pp collisions at the LHC are simulated using various event generators. An overview of MC event generators for LHC physics can be found in [88]. The different MC samples used for comparison with data taken during 2010 and during 2011 are denoted respectively as MC10 and MC11. The following event generators, using different theoretical models, are utilized in the analysis.

Pythia

PYTHIA [89] simulates non-diffractive pp collisions using a $2 \rightarrow 2$ matrix element at leading order in the strong coupling to model the hard subprocess. It uses p_t -ordered parton showers to model additional radiation in the leading-logarithmic approximation [90]. Multiple parton interactions [36, 91], as well as fragmentation and hadronization, based on the Lund string model [69], are also simulated.

Several PYTHIA 6 tunes utilizing different parton distribution function (PDF) sets are used. The nominal version used in this analysis employs the modified leading-order PDF set, MRST LO* [7]. The parameters used for tuning the underlying event include charged particle spectra measured by ATLAS in minimum bias collisions [92]. The samples used to compare with the 2010 and with the 2011 data respectively use the AMBT1 [93] and AMBT2B [94] tunes.

Several additional combinations of PYTHIA versions, PDF sets and underlying event tunes are used in chapter 8 in order to evaluate non-perturbative corrections to the dijet mass cross section. These include the following; PYTHIA 6.425 with the MRST LO* PDF set and the AUET2B [94] tune; PYTHIA 6.425 with the CTEQ6L1 [8] PDF set and the AMBT2B and AUET2B tunes; PYTHIA 8 (v150) [95] with the MRST LO** PDF set and 4C [96] tune.

Herwig, Herwig++

HERWIG uses a leading order ($2 \rightarrow 2$) matrix element supplemented with angular-ordered parton showers in the leading-logarithm approximation [97–99]. The so called cluster model [70] is used for the hadronization. Multiple parton interactions are modelled using JIMMY [100]. The model parameters of HERWIG+JIMMY have been tuned to ATLAS data (AUET1 tune) [101]. The MRST LO* PDF set is used.

4. Monte Carlo simulation

HERWIG++ [102] (v2.5.1) is based on HERWIG, but redesigned in the C++ programming language. The generator contains a few modelling improvements. It also uses angular-ordered parton showers, but with an updated evolution variable and a better phase-space treatment. Hadronization is performed using the cluster model, as in HERWIG. The underlying event and soft inclusive interactions are described using a hard and soft multiple partonic interactions model [72]. The MRST LO* and the CTEQ6L1 PDF sets are used with the UE7000-3 [94] underlying event tune, in order to evaluate non-perturbative corrections to the dijet mass cross section in chapter 8.

Alpgen

ALPGEN is a tree level matrix-element generator for hard multi-parton processes ($2 \rightarrow n$) in hadronic collisions [103]. It is interfaced to HERWIG to produce parton showers in the leading-logarithmic approximation. Parton showers are matched to the matrix element with the MLM matching scheme [104]. For the hadronization, HERWIG is interfaced to JIMMY in order to model soft multiple parton interactions. The PDF set used is CTEQ6L1. ALPGEN is used in chapter 8 in order to evaluate the systematic uncertainty associated with the unfolding procedure of the dijet mass cross section measurement.

Sherpa

SHERPA is a general-purpose tool for the simulation of particle collisions at high-energy colliders, using a tree-level matrix-element generator for the calculation of hard scattering processes [105]. The emission of additional QCD partons off the initial and final states is described through a parton-shower model. To consistently combine multi-parton matrix elements with the QCD parton cascades, the approach of Catani, Krauss, Kuhn and Webber [106] is employed. A simple model of multiple interactions is used to account for underlying events in hadron-hadron collisions. The fragmentation of partons into primary hadrons is described using a phenomenological cluster-hadronization model [107]. A comprehensive library for simulating tau-lepton and hadron decays is provided. Where available form-factor models and matrix elements are used, allowing for the inclusion of spin correlations; effects of virtual and real QED corrections are included using the approach of Yennie, Frautschi and Suura [108]. The CTEQ6L1 PDF sets together with the default underlying event tune are used. The CKKW matching scale is set at 15 GeV, where the latter refers to the energy scale in which matching of matrix elements to parton showers begins. The implication of this choice is that partons with transverse momentum above 15 GeV in the final state, necessarily originate from matrix elements, and not from the parton shower.

SHERPA is employed in the analysis as part of the double parton scattering measurement in chapter 9. Events are generated without multiple interactions, by setting the internal flag, `MI_HANDLER=None`. The generated events serve as input to a neural network.

4.2. Simulation of the ATLAS detector

Event samples produced using the different event generators described above are passed through the full ATLAS detector simulation and are reconstructed as the data. The GEANT software toolkit [109] within the ATLAS simulation framework [110] propagates the generated particles through the ATLAS detector and simulates their interactions with the detector material. The energy deposited by particles in the active detector material is converted into detector signals with the same format as the ATLAS detector read-out. The simulated detector signals are in turn reconstructed with the same reconstruction software as used for the data.

In GEANT the model for the interaction of hadrons with the detector material can be specified for various particle types and for various energy ranges. For the simulation of hadronic interactions in the detector, the GEANT set of processes called QGSP_BERT [111] is chosen. In this set of processes, the *Quark Gluon String model* [112–116] is used for the fragmentation of the nucleus, and the *Bertini cascade model* [117–120] for the description of the interactions of hadrons in the nuclear medium.

The GEANT simulation, and in particular the hadronic interaction model for pions and protons, has been validated with test-beam measurements for the barrel [121–125] and endcap [126–128] calorimeters. Agreement within a few percent is found between simulation and data for pion momenta between 2 and 350 GeV. Further tests have been carried out *in-situ* comparing the single hadron response, measured using isolated tracks and identified single particles [129, 130]. Good agreement between simulation and data is found for particle momenta from a few hundred MeV to 6 GeV.

Studies of the material of the inner detector in front of the calorimeters have been performed using secondary hadronic interactions [131]. Additional information is obtained from studying photon conversions [132] and the energy flow in minimum bias events [133]. The ATLAS detector geometry used in the 2010 and in the 2011 simulation campaigns reflects the best current knowledge of the detector at the time the simulations were made. Subsequently, compared to MC10, a more detailed description of the geometry of the LAr calorimeter was used for MC11. The improvement in understanding of the geometry introduced an increased calorimeter response to pions below 10 GeV of about 2%.

The MC11 simulation is made up of different *MC-periods*. Each MC-period represents different data-taking conditions, such as malfunctioning hardware or changes in the amount of *in-time pile-up*, additional *pp* collisions, coinciding with the hard interaction. Events in the different MC-periods are given relative weights according to the integrated luminosity of the respective data-taking periods they represent.

A note regarding the simulation in chapter 7; before the start of data-taking in 2011, a transitional MC simulation was created, denoted as MC10b. MC10b was generated as part of the MC10 campaign. It used the 2010 simulation settings as described above, with the exception of highly increased pile-up conditions matching the expected characteristics of the 2011 data. The study described in chapter 7 was originally performed using an MC10b PYTHIA sample. When MC11 became available, most of the results were reproduced; those which were not, are presented here using the previous version of the simulation. Unless otherwise indicated, MC11 is used in conjunction with the 2011 data.

4.3. Bunch train structure and overlapping events

The LHC bunch train structure of the 2010 and the 2011 data is modelled in MC. In MC10 the simulated collisions are organised in double trains with 225 ns separation. Each train contains eight filled proton bunches with a bunch separation of 150 ns. In MC11 the simulation features four trains with 36 bunches per train and 50 ns spacing between the bunches.

The MC samples are generated with additional minimum bias interactions, using PYTHIA 6 with the AMBT1 underlying event tune and the MRST LO* PDF set for MC10, and PYTHIA 6 with the AUET2B tune and the CTEQ6L1 PDF set for MC11. These minimum bias events are used to form pile-up events, which are overlaid onto the hard scattering events. The number of overlaid events

4. Monte Carlo simulation

follows a Poisson distribution around the average number of additional pp collisions per bunch crossing, as measured in the experiment. The average number of additional interactions depends on the instantaneous luminosity (see [equation \(7.1\)](#) in [section 7.1.1](#)); it is thus greater in MC11 compared to MC10, following the trend in the data.

The small separation between bunches in the 2011 data (and respectively in MC11) requires inclusion of the effect of *out-of-time pile-up*¹ in the simulation. The properties of this effect depend on the distance of the hard scatter events from the beginning of the bunch train. The first ten (approximately) bunch crossings are characterized by increasing out-of-time pile-up contributions from the previous collisions. For the remaining 26 bunch crossings in a train, the out-of-time pile-up is stable within the bunch-to-bunch fluctuations in proton intensity at the LHC.

¹ A feature of the 2011 data is that the signal in the calorimeter is sensitive to collisions from several consecutive bunch crossings; out-of-time pile-up refers to this fact. See [section 7.1](#) for a detailed discussion.

5. Jet reconstruction and calibration

5.1. Jet reconstruction algorithms

Jets originate from the fragmentation of partons. Due to color flow at the parton-level, there is no one-to-one correspondence between the hadrons inside a jet and the partons which initiated the jet. Because the measurements are performed at the hadron-level and the theoretical expectations at the parton-level, a precise definition of jets is required. The algorithm that relates a jet of hadrons to partons must satisfy,

- **infrared safety** - the presence or absence of additional soft particles between two particles belonging to the same jet should not affect the recombination of these two particles into a jet. Generally, any soft particles not coming from the fragmentation of a hard scattered parton should not affect the number of produced jets;
- **collinear safety** - a jet should be reconstructed independently whether the transverse momentum is carried by one particle, or if that particle is split into two collinear particles;
- **order independence** - the algorithm should be applicable at parton- hadron- or detector-level, and lead to the same origin of the jet.

An illustration of infrared and collinear sensitivity in jet-finding is given in [figure 5.1](#).

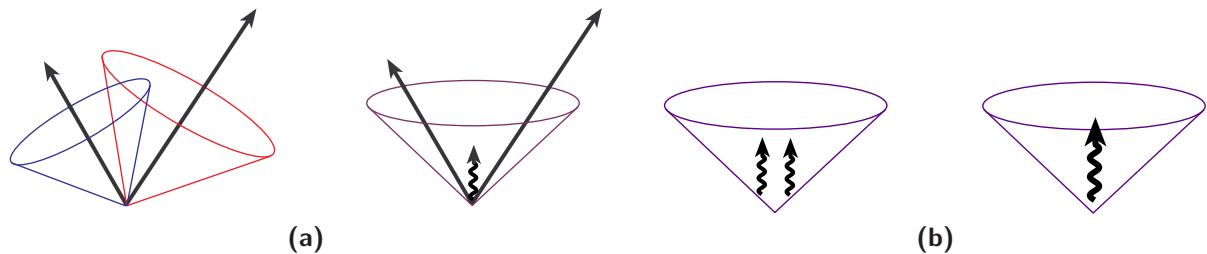


Figure 5.1. An illustration of infrared (a) and collinear (b) sensitivity in jet finding.

There are many jet algorithms which have been proposed over the years. These include fixed sized cone algorithms as well as sequential recombination algorithms (cluster algorithms), which are based on event shape analysis [134]. The term cone algorithm is applied to a wide range of jet algorithms which broadly aim at maximizing E_t inside a geometric circle in the η, ϕ coordinates space. The radius of the circle, R , is a key parameter of the algorithm. On the other hand, clustering algorithms are based upon pair-wise clustering of the input constituents. In general, an algorithm defines a distance measure between constituents, as well as some condition upon which clustering into a jet should be terminated.

5. Jet reconstruction and calibration

The anti- k_{\perp} [135], k_{\perp} [136] and Cambridge/Aachen [137, 138] clustering algorithms are used in this analysis. The clustering algorithms begin by computing for each jet constituent, the quantity d_{iB} and for each pair of constituents the quantity d_{ij} , defined as

$$d_{iB} = k_{Ti}^{2p}, \quad (5.1)$$

$$d_{ij} = \min(k_{Ti}^{2p}, k_{Tj}^{2p}) \frac{(\Delta R)_{ij}^2}{R^2}, \quad (5.2)$$

where

$$(\Delta R)_{ij}^2 = (y_i - y_j)^2 + (\phi_i - \phi_j)^2.$$

The variables R and p are constants of the algorithm, and k_{Ti} , y_i and ϕ_i are respectively the transverse momentum, the rapidity and the azimuth of the i^{th} constituent. The d_{ij} parameter, represents the distance between a pair of jet constituents, while d_{iB} is the distance between a given constituent and the beam.

The algorithm proceeds by comparing for each constituent the different d values. In the case that the smallest entry is a d_{ij} , constituents i and j are combined and the list is remade. If the smallest entry is d_{iB} , this constituent is considered a complete jet and is removed from the list.

The variable R sets the resolution at which jets are resolved from each other as compared to the beam. For large values of R , the d_{ij} are smaller, and thus more merging takes place before jets are complete. The variable p can also take different values; for the k_{\perp} algorithm $p = 1$, for the Cambridge/Aachen algorithm $p = 0$, and for the anti- k_{\perp} algorithm $p = -1$.

The nominal jet collection used for physics in the analysis uses the anti- k_{\perp} algorithm with size parameter, $R = 0.6$, reconstructed with the FASTJET package [139]. Jets built with the k_{\perp} algorithm are also used, but only as part of the jet energy calibration procedure, as discussed in chapter 7. The Cambridge/Aachen algorithm is used in order to evaluate the systematic uncertainty of said calibration.

5.2. Inputs to jet reconstruction

5.2.1. Calorimeter jets

The input to *calorimeter jets* are topological calorimeter clusters (*topo-clusters*) [126, 140]. Topo-clusters are groups of calorimeter cells that are designed to follow shower development in the calorimeter. A topo-cluster is defined as having an energy equal to the energy sum of all the included calorimeter cells, zero mass and a reconstructed direction calculated from the weighted averages of the pseudo-rapidities and azimuthal angles of its constituent cells. The weight used in the averaging is the absolute cell energy. The positions of the cells are relative to the nominal ATLAS coordinate system.

Clustering algorithm

The topo-cluster algorithm is designed to suppress calorimeter noise. The algorithm starts from a *seed* cell, whose signal-to-noise (S/N) ratio is above a threshold, $S/N = 4$. Cells neighbouring the seed (or the cluster being formed) that have a signal-to-noise ratio, $S/N \geq 2$, are included iteratively. Finally, all calorimeter cells neighbouring the formed topo-cluster are added.

The noise is estimated as the absolute value of the energy deposited in the cell, divided by the RMS of the energy distribution of the cell, measured in events triggered at random bunch crossings. For data taken during 2010, cell-noise was dominated by electronic noise. Due to the shortened bunch crossing interval and increased instantaneous luminosity during 2011 data-taking, the noise increased. An additional component was added, originating from energy deposited in a given cell from previous collisions, but inside the window of sensitivity of the calorimeters. This added energy is referred to as *pile-up* (see chapter 7 for a detailed discussion). Subsequently, different nominal noise thresholds, σ_{noise} , are used to reconstruct topo-clusters in 2010 and in 2011,

$$\sigma_{\text{noise}} = \begin{cases} \sigma_{\text{noise}}^{\text{elc}} & (2010) \\ \sqrt{(\sigma_{\text{noise}}^{\text{elc}})^2 + (\sigma_{\text{noise}}^{\text{pu}})^2} & (2011) \end{cases} \quad (5.3)$$

Here $\sigma_{\text{noise}}^{\text{elc}}$ is the electronic noise, and $\sigma_{\text{noise}}^{\text{pu}}$ is the noise from pile-up. On an event-by-event basis, the magnitude of the latter term may vary, as the pile-up is sensitive to the instantaneous luminosity, characterized by the average number of interactions per bunch crossing, μ , (see section 7.1.1). A constant baseline is chosen for cluster reconstruction throughout 2011. This baseline corresponds to the noise which results from eight additional pile-up interactions, $\mu = \mu^{\text{ref}} = 8$, and reflects the conditions under which the average effects of pile-up in the 2011 data are minimal.

The change in time of the total nominal noise and its dependence on calorimeter pseudo-rapidity is observed by comparing figures 5.2a and 5.2b. The former shows the energy-equivalent cell-noise

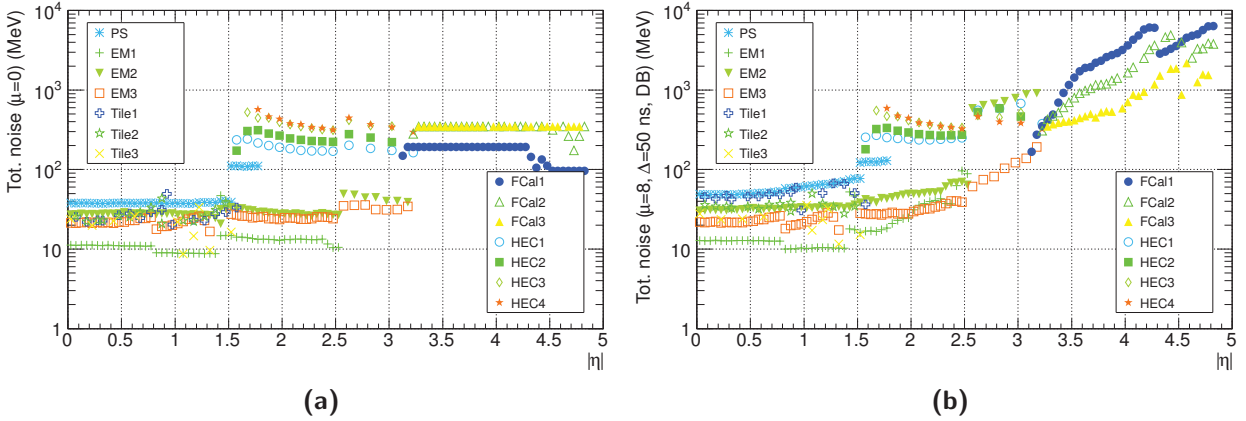


Figure 5.2. The energy-equivalent cell-noise in the ATLAS calorimeters at the electromagnetic (EM) scale, as a function of pseudo-rapidity, η . The magnitude of the noise represents the configurations used for cluster reconstruction in 2010 (a) and in 2011 (b). These respectively use $\mu = 0$ and $\mu = 8$ as baseline values for the average number of interactions. The various data points indicate the noise in different calorimeter elements; the pre-sampler (PS); the first three layers of the EM calorimeter (EM1, EM2 and EM3); the first three layers of the Tile calorimeter (Tile1, Tile2 and Tile3); the first three layers of the forward FCal calorimeter (FCal1, FCal2 and FCal3); the first four layers of the hadronic end-cap calorimeter (HEC1, HEC2 and HEC3). (Figures are taken from [141].)

5. Jet reconstruction and calibration

in different calorimeter regions in 2010, representing the baseline electronic noise; the latter shows the respective cell-noise in 2011, for which pile-up contributes as well. In most calorimeter regions, the pile-up induced noise is smaller or of the same magnitude as the electronic noise. The exception is the forward calorimeters, where $\sigma_{\text{noise}}^{\text{pu}} \gg \sigma_{\text{noise}}^{\text{elec}}$.

The topo-cluster algorithm also includes a splitting step in order to optimise the separation of showers from different close-by particles: All cells in a topo-cluster are searched for local maxima in terms of energy content with a threshold of 500 MeV. This means that the selected calorimeter cell has to be more energetic than any of its neighbours. The local maxima are then used as seeds for a new iteration of topological clustering, which splits the original cluster into more topo-clusters.

Energy scale of clusters

Topo-clusters are initially constructed from energy at the electromagnetic (EM) scale. The EM scale correctly reconstructs the energy deposited by particles in an electromagnetic shower in the calorimeter. This energy scale is established using test-beam measurements for electrons in the barrel [121, 142–145] and the endcap calorimeters [126, 127]. The absolute calorimeter response to energy deposited via electromagnetic processes was validated in the hadronic calorimeters using muons, both from test-beams [121, 146] and produced *in-situ* by cosmic rays [147]. The energy scale of the electromagnetic calorimeters is corrected using the invariant mass of Z bosons produced *in-situ* in proton-proton collisions ($Z \rightarrow e^+e^-$ events) [148].

An additional calibration step may also be used, where so called *Local Calibration Weights* (LCW) are applied to topo-clusters, bringing the clusters to the LCW calibration scale [149]. Starting at the EM scale, topo-clusters are classified as either *EM-like* or *hadron-like*, using cluster shape moments. Clusters classified as EM-like are kept at the original energy scale. On the other hand, hadron-like topo-clusters are subject to recalibration. In the first step this entails a cell weighting procedure, which aims to compensate for the lower response of the calorimeter to hadronic deposits. Next, out-of-cluster corrections are applied. These try to account for lost energy deposited in calorimeter cells outside of reconstructed clusters. Finally, dead material corrections are applied, accounting for energy deposits outside of active calorimeter volumes, e.g., in the cryostat, the magnetic coil and calorimeter inter-modular cracks.

Calorimeter jets are built using either EM or LCW scale topo-clusters. In either case, further corrections need to be applied to calibrate jets to the particle-level. This final step is referred to as the *jet energy scale* (JES) calibration.

5.2.2. Other types of jets

Track jets

Jets can also be built using inner detector tracks as inputs to the jet finding algorithm. Track-based jets, called *track jets*, are reconstructed using the anti- k_{\perp} algorithm with size parameter, $R = 0.6$. Track jets are required to be composed of at least two tracks; tracks are required to have transverse momentum above 500 MeV, at least one pixel detector hit, at least six hits in the silicon-strip detector, and impact parameters in the transverse plane and in the z -direction, both smaller than 1.5 mm. In order to be fully contained in the tracking region, track jets are required to have $|\eta| < 1.9$. Track jets are also required to have transverse momentum larger than 4 GeV.

Truth jets

Monte Carlo simulated particle jets are referred to as *truth jets*. They are defined as those built from stable interacting particles with a lifetime longer than 10 ps in the Monte Carlo event record (excluding muons and neutrinos) that have not been passed through the simulation of the ATLAS detector. Truth jets are built using the anti- k_{\perp} algorithm with size parameter $R = 0.6$, and are required to have transverse momentum larger than 10 GeV.

5.3. Jet energy calibration

The jet energy calibration relates the jet energy measured with the ATLAS calorimeter to the true energy of the corresponding jet of stable particles entering the detector. The jet calibration corrects for the following detector effects that affect the jet energy measurement;

- **calorimeter non-compensation** - partial measurement of the energy deposited by hadrons;
- **dead material** - energy losses in inactive regions of the detector;
- **leakage** - energy of particles reaching outside the calorimeters;
- **out of calorimeter jet cone** - energy deposits of particles which are not included in the reconstructed jet, but were part of the corresponding truth jet and entered the detector;
- **noise thresholds and particle reconstruction efficiency** - signal losses in calorimeter clustering and jet reconstruction.

Jets reconstructed in the calorimeter system are formed from calorimeter energy depositions reconstructed at either the EM or the LCW scale, as described above. The correction for the lower response to hadrons is solely based on the topology of the energy depositions observed in the calorimeter. The measured jet energy is corrected on average, using:

$$E^{\text{calib}} = E^{\text{det}} \times \mathcal{F}_S^{\text{calib}}(E_S^{\text{det}}, \eta), \quad \text{with } E_S^{\text{det}} = E_S - \mathcal{O}_{\text{fst}}^S, \quad \text{for } S = \text{EM}, \text{LCW}. \quad (5.4)$$

Here E_S is the calorimeter energy measured at the EM or LCW scales, denoted collectively by S . The variable E^{calib} is the hadron-level calibrated jet energy, and $\mathcal{F}_S^{\text{calib}}$ is a calibration function. The latter depends on the measured jet energy, and is evaluated in small jet-pseudo-rapidity, η , regions. The baseline PYTHIA MC samples described in [chapter 4](#) are used to derive $\mathcal{F}_S^{\text{calib}}$; the procedure is explained in the following.

The variable E_S^{det} denotes the EM- or LCW-level energy after the contribution of pile-up (additional multiple proton-proton interactions) has been subtracted. The pile-up energy is expressed through the function $\mathcal{O}_{\text{fst}}^S$, called the *jet offset correction*. The offset correction in 2010 and in 2011 depends on the number of pp collisions which occur within the same bunch crossing as the collision of interest. This is referred to as *in-time pile-up* and is estimated by the number of primary vertices, N_{PV} , in a given event. In addition, $\mathcal{O}_{\text{fst}}^S$ exhibits a strong rapidity dependence, due to the varying calorimeter response in η , and to the rapidity distribution of the pile-up interactions. The offset correction is parametrized separately for EM and for LCW jets, based in each case on jet constituents which are calibrated in the respective energy scale.

The offset correction performs well for data taken in 2010 [[150](#)]. For the case of the 2011 data, the nature of pile-up becomes more complicated, as interactions in bunch crossings proceeding

5. Jet reconstruction and calibration

and following the event of interest affect the signal in the calorimeter; this effect is called *out-of-time pile-up*. The offset correction is modified in 2011 in order to account for this effect, but the performance is nonetheless degraded with regard to 2010. A detailed discussion of out-of-time pile-up and the exact functional form of $\mathcal{O}_{\text{fst}}^{\text{S}}$ are given in [section 7.1](#). An alternative to the offset correction using a data-driven method, referred to as the *jet area/median method*, is introduced in [chapter 7](#). The offset correction is used for the calibration of jets in the 2010 data in this analysis; the jet median approach is used as the nominal pile-up correction for the 2011 data.

The two calibrations schemes, which respectively use jets constructed from either EM- or LCW-calibrated topo-clusters, are referred to as EM+JES and LCW+JES. For data taken during 2010, only the simpler EM+JES calibration is available for this analysis. For the 2011 data, the nominal jet collection is calibrated using LCW+JES. The calibration schemes include several steps, described in the following:

- jet origin correction;
- jet energy correction;
- jet pseudo-rapidity correction;
- residual *in-situ* calibration (2011 data only).

Jet origin correction

Calorimeter jets are reconstructed using the geometrical center of the ATLAS detector as reference to calculate the direction of jets and their constituents. The jet four-momentum is corrected for each event such that the direction of each topo-cluster points back to the primary (highest- p_t) reconstructed vertex. The kinematic observables of each topo-cluster are recalculated using the vector from the primary vertex to the topo-cluster centroid as its direction. The raw jet four-momentum is thereafter redefined as the vector sum of the topo-cluster four-momenta. This correction improves the angular resolution and results in a small improvement ($< 1\%$) in the jet p_t response. The jet energy is unaffected.

Jet energy correction

The principle step of the EM+JES and of the LCW+JES jet calibrations restores the reconstructed jet energy to the energy of the corresponding MC truth jet. Since pile-up effects have already been accounted for, the MC samples used to derive the calibration do not include multiple pp interactions.

The calibration is derived using isolated calorimeter jets that have a matching isolated truth jet within $\Delta R = 0.3$. Distance is defined in η, ϕ space as

$$\Delta R = \sqrt{(\phi^{\text{rec}} - \phi^{\text{truth}})^2 + (\eta^{\text{rec}} - \eta^{\text{truth}})^2}, \quad (5.5)$$

where ϕ^{truth} (η^{truth}) and ϕ^{rec} (η^{rec}) are respectively the azimuthal angles (pseudo-rapidities) of truth and reconstructed jets. An isolated jet is defined as one having no other jet with $p_t > 7$ GeV within $\Delta R = 2.5 \cdot R$, where R is the size parameter of the jet algorithm.

The final jet energy scale calibration is parametrised as a function of detector-level pseudo-rapidity, η_{det} ,¹ and of jet energy at the detector-level energy scales, E_{S} . In the following, as above, S stands for either the EM or the LCW energy scales. The detector-level jet energy-response,

$$\mathcal{R}_{\text{S}} = E_{\text{S}}/E_{\text{truth}}, \quad (5.6)$$

¹ Here, pseudo-rapidity refers to that of the original reconstructed jet before the origin correction.

is measured for each pair of calorimeter and truth jets in bins of truth jet energy, E_{truth} , and of η_{det} . For each $(E_{\text{truth}}, \eta_{\text{det}})$ -bin, the averaged jet-response, $\langle \mathcal{R}_S \rangle$, is defined as the peak position of a Gaussian fit to the E_S/E_{truth} distribution. In addition, in the same $(E_{\text{truth}}, \eta_{\text{det}})$ -bin, the average jet energy-response, $\langle E_S \rangle$, is derived from the mean of the distribution of E_S .

For a given η_{det} -bin, k , the jet energy-response calibration function, $\mathcal{F}_{\text{calib}}^{(k)}(E_S)$, is obtained using a fit of the $(\langle E_S \rangle_j, \langle \mathcal{R}_S \rangle_j)$ values for each E_{truth} -bin j . The fitting function is parameterised as

$$\mathcal{F}_{\text{calib}}^{(k)}(E_S) = \sum_{i=0}^{N_{\text{max}}} a_i (\ln E_S)^{(i)}, \quad (5.7)$$

where a_i are free parameters, and N_{max} is chosen between 1 and 6, depending on the goodness of the fit.

The final jet energy scale correction that relates the measured calorimeter jet energy to the true energy, is then defined as $\mathcal{F}_S^{\text{calib}}$ in the following:

$$E_{S+\text{JES}} = \frac{E_S}{\mathcal{F}_{\text{calib}}^S(E_S)|_{\eta_{\text{det}}^k}} = E_S \times \mathcal{F}_S^{\text{calib}}, \quad (5.8)$$

where $\mathcal{F}_{\text{calib}}(E_S)|_{\eta_{\text{det}}^k}$ is the jet-response calibration function for the relevant η_{det} -bin k .

As an example, the average jet energy scale correction for EM jets in 2010, $\langle \mathcal{F}_{\text{EM}}^{\text{calib}} \rangle$, is shown as a function of calibrated jet p_t for three η -intervals in figure 5.3a. The response of 2010 EM+JES jets, \mathcal{R}_{EM} , is shown for various energy and η_{det} -bins in figure 5.3b. As the transverse momentum of jets increases, the response and subsequent JES correction factor decrease. The corrections are also highly rapidity-dependant, due in part to the changing structure of calorimeter elements; in transition regions of the calorimeter (around $|\eta| = 1.5, 3.3$) the response is significantly higher, due to energy loss in dead material or through leakage. Larger correction factors are therefore required in these regions. Corresponding figures for 2011 LCW+JES jets may be found in [151].

Jet pseudo-rapidity correction

After the jet origin and energy corrections, the origin-corrected pseudo-rapidity of jets is further corrected for a bias due to poorly instrumented regions of the calorimeter. In these regions topo-clusters are reconstructed with a lower energy with respect to better instrumented regions (see figure 5.3b). This causes the jet direction to be biased towards the better instrumented calorimeter regions.

The η -correction is derived as the average difference between the pseudo-rapidity of reconstructed jets and their truth jet counterparts. It is parametrized according to the energy and detector-level pseudo-rapidity of reconstructed jets, $\Delta\eta = \eta_{\text{truth}} - \eta_{\text{origin}}$. The correction is very small (< 0.01) for most regions of the calorimeter, and up to five times larger in the transition regions.

Residual in-situ calibration (2011 data only)

Following the pseudo-rapidity correction, the transverse momentum of jets in the 2011 data is compared to that in MC using *in-situ* techniques. The latter exploit the balance between the transverse momentum of a jet, p_t , and that of a reference object, p_t^{ref} [151]. The ratio,

$$f_{\text{in-situ}} = \frac{\langle p_t/p_t^{\text{ref}} \rangle_{\text{data}}}{\langle p_t/p_t^{\text{ref}} \rangle_{\text{MC}}}, \quad (5.9)$$

5. Jet reconstruction and calibration

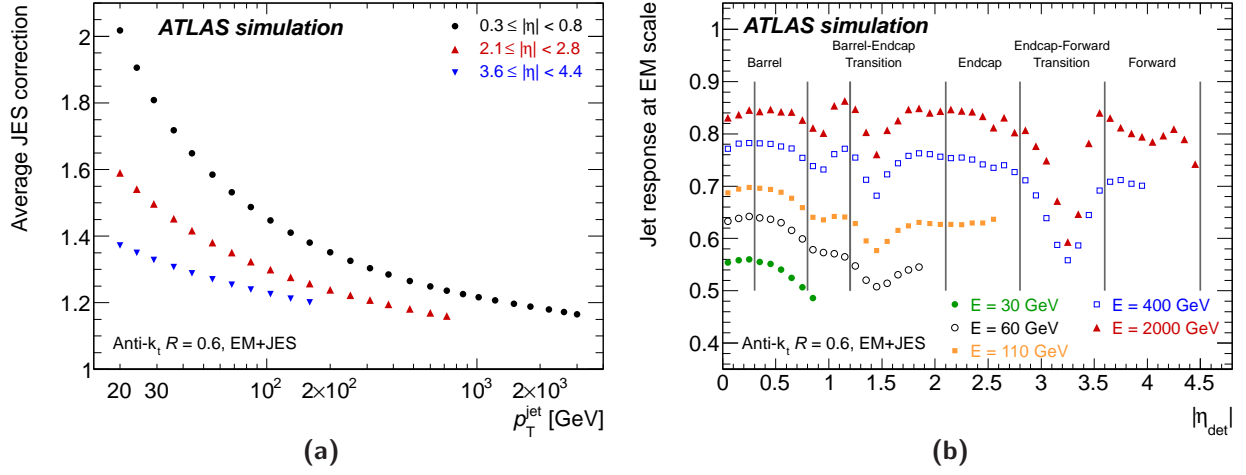


Figure 5.3. (a) Average jet energy scale correction for EM+JES jets as a function of the calibrated jet transverse momentum, p_T^{jet} , for three pseudo-rapidity, η , regions, as indicated in the figure. (b) Average simulated jet-response at the EM scale in bins of detector pseudo-rapidity, η_{det} . Different jet energies, E , are represented (using EM+JES jets) as indicated in the figure. The parallel lines mark the regions over which the JES correction is evaluated. The inverse of the response shown in each bin is equal to the average jet energy scale correction. (Figures are taken from [150].)

called the *residual in-situ JES correction*, is used on jets measured in data. It is derived using the following methods:

- the p_T of jets within $0.8 < |\eta| < 4.5$ is equalized to the p_T of jets within $|\eta| < 0.8$, exploiting the p_T balance between central and forward jets in events with only two high p_T jets;
- an *in-situ* JES correction for jets within $|\eta| < 1.2$ is derived using the p_T of a photon or a Z boson (decaying to e^+e^- or $\mu^+\mu^-$) as reference;
- events where a system of low- p_T jets recoils against a high- p_T jet are used to calibrate jets in the TeV regime. The low- and high- p_T jets are required to respectively be within $|\eta| < 2.8$ and $|\eta| < 1.2$.

5.4. Jet quality selection

Jets at high transverse momenta produced in pp collisions must be distinguished from background jets not originating from hard scattering events. The main sources of background are listed in the following:

- large calorimeter noise;
- beam-gas events, where one proton of the beam collided with the residual gas within the beam pipe;
- beam-halo events, e.g., caused by interactions in the tertiary collimators in the beam-line far away from the ATLAS detector;

- cosmic ray muons overlapping in-time with collision events.

These backgrounds are divided into two categories, calorimeter noise and non-collision interactions.

Calorimeter noise - two types of calorimeter noise are addressed, sporadic noise bursts and coherent noise. Sporadic noise bursts in the hadronic endcap calorimeter (HEC) commonly result in a single noisy calorimeter cell, which contributes almost all of the energy of a jet. Such jets are therefore rejected if they have high HEC energy fractions, denoted by f_{HEC} . The signal shape quality, \mathcal{S}_{HEC} , may also be used for rejection, the latter being a measure of the pulse shape of a calorimeter cell compared to nominal conditions. Due to the capacitive coupling between channels, neighbouring calorimeter cells around the noise burst have an apparent negative energy, denoted by E_{neg} . A high value of E_{neg} is therefore used to distinguish jets which originate in noise bursts. On rare occasions, coherent noise in the electromagnetic calorimeter develops. Fake jets arising from this background are characterised by a large EM energy fraction, f_{EM} , which is the ratio of the energy deposited in the EM calorimeter to the total energy. Similar to the case of noise bursts in the HEC, a large fraction of calorimeter cells exhibit poor signal shape quality, \mathcal{S}_{EM} , in such cases.

Non-collision backgrounds - cosmic rays or non-collision interactions are likely to induce events where jet candidates are not in-time with the beam collision. A cut on the jet-time, t_{jet} , may therefore be applied to reject such jets. Jet-time is reconstructed from the energy deposition in the calorimeter by weighting the reconstructed time of calorimeter cells forming the jet with the square of the cell energy. The calorimeter time is defined with respect to the event time (recorded by the trigger). A cut on f_{EM} is applied to make sure that jets have some energy deposited in the calorimeter layer closest to the interaction region, as expected for a jet originating from the nominal interaction point. Since real jets are expected to have tracks, the f_{EM} cut may be applied together with a cut on the jet charged fraction, f_{ch} , defined as the ratio of the scalar sum of the p_t of the tracks associated to the jet, divided by the jet p_t . The jet charged fraction cut is, naturally, only applicable for jets within the acceptance of the tracker. A cut on the maximum energy fraction in any single calorimeter layer, f_{max} , is applied to further reject non-collision background.

Two sets of quality criteria are defined, denoted as Loose and Medium selection. These incorporate requirements on the rejection variables defined above, and are specified in detail in [section A.1](#), [table A.1](#). For the 2010 data, the tighter, Medium selection, is required. Since these criteria are not fully efficient, an efficiency correction is applied to jets. The selection efficiency for jets in two pseudo-rapidity regions is shown in [figure 5.4](#) for illustration. In general, for transverse momenta larger than ~ 50 GeV, the efficiency is above 99% across all rapidities. For lower jet p_t , efficiencies range between 96-98% within $|\eta| < 2.1$, and are above 99% otherwise. Further details are available in [\[150\]](#). For the 2011 data, due to improved understanding of the calorimeter, a reduced version of the 2010 Loose selection is used. The efficiency is above 99.8% for jets with $p_t > 30$ GeV across all rapidities.

5.5. Systematic uncertainties on the kinematic properties of jets

5.5.1. Jet energy scale uncertainties

The systematic uncertainty associated with the jet energy scale (JES) is the primary source of uncertainty in the analysis. It has been determined for the 2010 and 2011 datasets in [\[152\]](#) and in [\[151\]](#),

5. Jet reconstruction and calibration

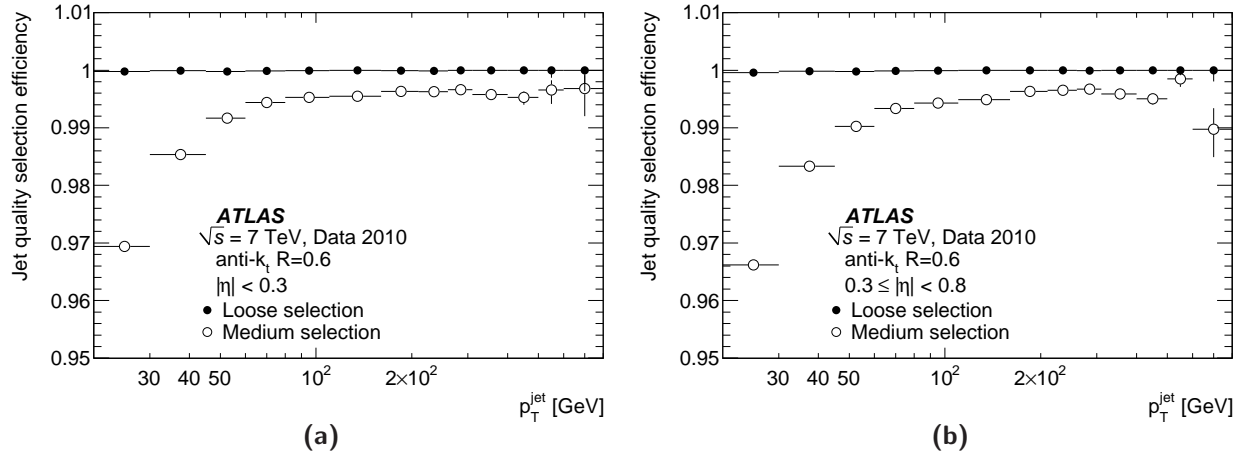


Figure 5.4. Jet quality selection efficiency for anti- k_T jets with size parameter, $R = 0.6$, measured as a function of the transverse momentum of jets, p_T^{jet} , in two pseudo-rapidity, η , regions. The Loose and Medium selection criteria used for data taken during 2010 are represented, as indicated in the figures. (Figures taken from [150].)

using integrated luminosities of 38 pb^{-1} and 4.7 fb^{-1} , respectively. In total seven sources of uncertainty on the jet energy scale are considered in 2010 and thirteen in 2011.

The sources of uncertainty on the 2010 measurement are the following:

- **single hadron response** - uncertainty associated with the response of a single particle entering the calorimeter. Discrepancies may arise due to the limited knowledge of the exact detector geometry; due to the presence of additional dead material; and due to the modelling of the exact way particles interact in the detector;
- **cluster thresholds** - uncertainty associated with the thresholds for reconstructing topo-clusters. The clustering algorithm is based on the signal-to-noise ratio of calorimeter cells. Discrepancies between the simulated noise and the real noise, or changes in time of the noise in data, can lead to differences in the cluster shapes and to the presence of fake topo-clusters;
- **Perugia 2010 and Alpgen+Herwig+Jimmy** - uncertainty associated with the modelling of fragmentation and the underlying event, or with other choices in the event modelling of the MC generator. The response predicted by the nominal PYTHIA generator are compared to the PYTHIA Perugia 2010 tune and to ALPGEN, coupled to HERWIG and JIMMY;
- **intercalibration** - uncertainty associated with the rapidity-intercalibration method, in which dijet events are used *in-situ* to measure the response in two η regions in the calorimeter. The measurement is done in different rapidity intervals simultaneously, by minimizing a response matrix. The uncertainty is estimated by comparing the response with that measured *in-situ* in events in which one of the jets is constrained to be central;
- **relative non-closure** - uncertainty associated with the non-closure of the energy of jets in MC following the JES calibration;
- **in-time pile-up** - uncertainty associated with the simulation and subtraction of in-time pile-up.

For the LCW+JES calibration scheme, which is used in this analysis for the 2011 dataset, the baseline JES uncertainty is estimated using a combination of *in-situ* techniques. In total, the different sources of uncertainty coming from the *in-situ* techniques in 2011 data amount to 60 components. These are combined, assuming they are fully correlated in p_t and η , into six *effective nuisance parameters* (ENP). The combination procedure involves diagonalizing the covariance matrix of the JES correction factors and selecting the five eigenvectors that have the largest corresponding eigenvalues. An additional sixth effective parameter represents all residual sources of uncertainty.

The sources of uncertainty on the 2011 measurement are the following:

- **ENP 1-6** - uncertainty associated with the six effective nuisance parameters, which combine the 60 components of the *in-situ* methods used to estimate the JES uncertainty in 2011;
- **intercalibration, single hadron response and relative non-closure** - same as for 2010;
- **close-by jets** - uncertainty associated with event topologies in which two jets are reconstructed in close proximity;
- **in-time PU, out-of-time PU and PU p_t** - uncertainty associated with the simulation and subtraction of in- and out-of-time pile-up.

The final fractional JES uncertainties for the 2010 and the 2011 data are compared in [figure 5.5](#) as a function of the p_t of jets in the central region. The uncertainty on the 2011 data is much improved

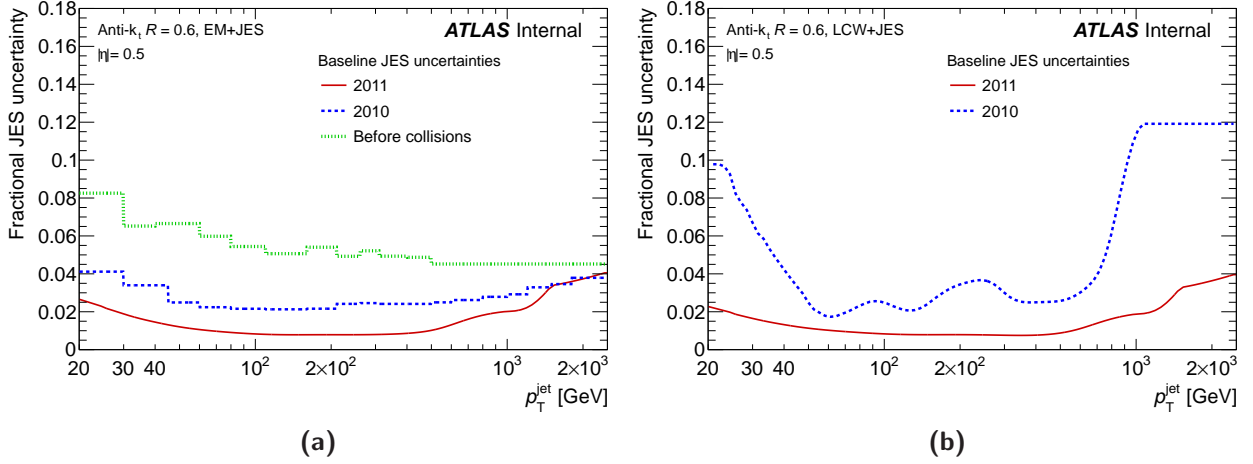


Figure 5.5. Fractional jet energy scale systematic uncertainty as a function of the transverse momentum of jets, p_T^{jet} , for jets with pseudo-rapidity, $|\eta| = 0.5$, calibrated under EM+JES (a) and LCW+JES (b). As indicated in the figures, estimates of the uncertainty before beginning of collisions in the LHC, for data taken during 2010 and for data taken during 2011, are compared. The 2011 uncertainty presented here includes only the *in-situ* components of the systematic uncertainty. (Figure are taken from [151].)

compared to 2010. This is due both to the increase in 2011 in the statistics which are used to derive uncertainty, and to the use of sophisticated *in-situ* techniques. For EM+JES jet in 2010 the total

5. Jet reconstruction and calibration

uncertainty is roughly 2% for jets with $40 < p_t < 2 \cdot 10^3$ GeV, increasing up to roughly twice that for lower or higher transverse momenta. For LCW+JES jets in 2011, the uncertainty is roughly 1% in the respective mid- p_t range, increasing up to 2% between 20 and 40 GeV and up to 4% between 0.5 and 2 TeV.

5.5.2. Jet energy and angular resolution

In addition to the jet energy scale, which is the primary source of uncertainty for most measurements involving jets, the jet energy and angular resolution must also be taken into account. These are addressed in the following.

Jet energy resolution

The baseline parameterization of the jet energy resolution in MC is derived using the nominal PYTHIA MC simulation for jets with transverse momentum, $30 < p_t < 500$ GeV [153]. *In-situ* measurements are also made for jets with rapidities, $|\eta| < 2.8$ and $p_t > 20$ GeV. In this kinematic range, the comparison of the resolution measured with the *in-situ* techniques between the data and the MC shows agreement better than 10%. The uncertainty on the jet energy resolution for each rapidity region is assigned from the weighted average of the systematic errors on the relative difference between the data and the MC, and is flat as a function of p_t . Outside the kinematic range of *in-situ* measurements, the MC parameterization is kept but the uncertainty is conservatively increased.

In order to illustrate the behaviour of the transverse momentum resolution in MC, the *relative transverse momentum offset* between the p_t of a truth jet, p_t^{truth} , and that of the corresponding matched reconstructed jet, p_t^{rec} , is defined as

$$O_{p_t} = \frac{p_t^{\text{rec}} - p_t^{\text{truth}}}{p_t^{\text{truth}}}. \quad (5.10)$$

Matching is performed by selecting a reconstructed jet within distance $\Delta R_{\text{match}} = 0.5 \cdot R$ of the truth jet, where $R = 0.6$ is the size parameter of the jet. In order to keep the sample pure, isolation of the matched truth jets from their counterparts within $\Delta R_{\text{iso}} = 2 \cdot R$ is also imposed.

The average relative transverse momentum offset represents the fractional bias in p_t of jets. The relative p_t resolution is parametrized by the width of the distribution of O_{p_t} , denoted by $\sigma(O_{p_t})$. The dependence of the average O_{p_t} and of $\sigma(O_{p_t})$ on truth jet p_t is shown in figure 5.6 for jets in different pseudo-rapidity regions in MC10 and in MC11. At $p_t < 20$ GeV in 2010 and at $p_t < 30$ GeV in 2011, O_{p_t} changes sign. These transverse momentum values mark the corresponding thresholds in either year for which the energy calibration of jets becomes valid. The relative bias in transverse momentum is lower in absolute value than 1% (6%) for jets with $p_t < 100$ GeV within $|\eta| < 2.1$ ($|\eta| < 4.5$) in 2010. In 2011, the bias is lower than 2% for central jets within $|\eta| < 2.8$. For higher values of transverse momentum the relative bias decreases, becoming negligible for non-central jets in 2010 above 200 GeV and for central jets in 2011 above 100 GeV. The relative resolution, $\sigma(O_{p_t})$, is also rapidity- and momentum-dependent. For the various η -regions the relative resolution decreases from 21% in 2010 (and 27% in 2011) for jets with $p_t = 20$ GeV, down to 4-6% for jets with $p_t > 300$ GeV. Both O_{p_t} and $\sigma(O_{p_t})$ are generally higher for low- p_t jets in MC11 compared to MC10, due to the increase in pile-up in 2011.

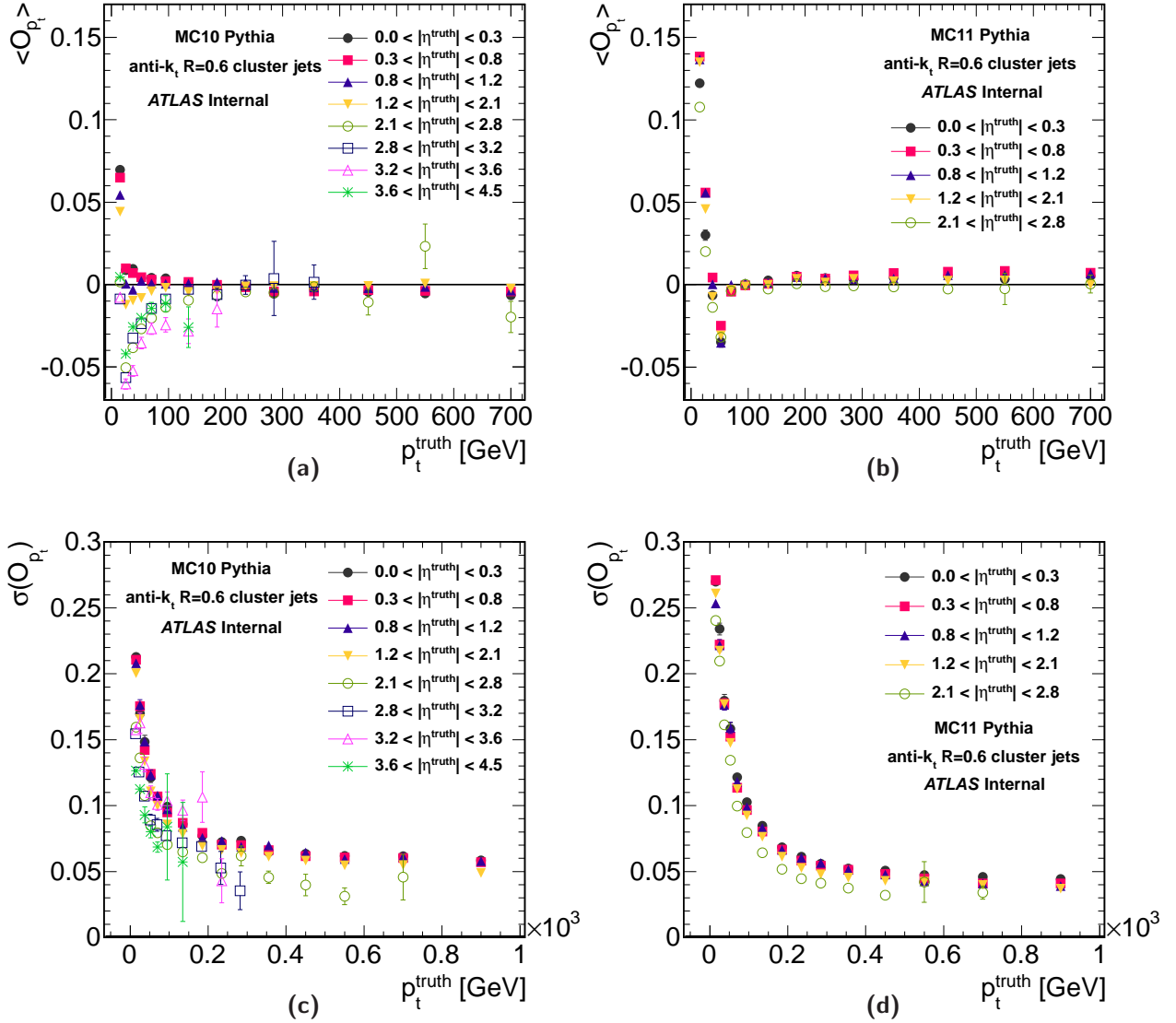


Figure 5.6. Dependence of the average relative transverse momentum offset, $\langle O_{p_t} \rangle$, ((a) and (b)) and of the width of the distribution of the relative offset, $\sigma(O_{p_t})$, ((c) and (d)) on the transverse momentum of truth jets, p_t^{truth} . Several regions of truth jet pseudo-rapidity, η^{truth} , are presented for jets in MC10 and in MC11, as indicated in the figures.

Jet angular resolution

In addition to the p_t resolution, the rapidity and azimuthal resolutions are used in [section 8.5](#) to estimate a component of the systematic uncertainty associated with the dijet mass measurement. A parametrization of the angular resolutions for different jet transverse momenta and rapidities is derived from the following.

The *pseudo-rapidity offset* and the *azimuthal offset* of jets are respectively defined in MC as

$$O_\eta = \eta^{\text{rec}} - \eta^{\text{truth}} \quad \text{and} \quad O_\phi = \phi^{\text{rec}} - \phi^{\text{truth}}, \quad (5.11)$$

by matching truth and reconstructed jets, as discussed with regard to [equation \(5.10\)](#). Here, as before, η^{truth} (ϕ^{truth}) and η^{rec} (ϕ^{rec}) are respectively the pseudo-rapidities (azimuthal angles) of truth and reconstructed jets. The parameters O_η and O_ϕ represent the angular bias of jets. The width of the distributions of O_η and O_ϕ represent the angular resolution of jets, denoted respectively as $\sigma(O_\eta)$ and $\sigma(O_\phi)$.

The dependence of the average angular offset parameters and of the angular resolution parameters on truth jet p_t is shown in [figures 5.7 - 5.8](#) for jets in different pseudo-rapidity regions in MC10 and in MC11. The pseudo-rapidity offset is smaller than $3 \cdot 10^{-3}$ in all η regions for jets with low p_t in 2010, becoming insignificant for transverse momentum values above 200 GeV. For jets in 2011 a small bias of roughly $2 \cdot 10^{-3}$ is observed for all η regions. The η resolution is roughly 0.04 for jets with $p_t = 20$ GeV in MC10 and for jets with $p_t = 30$ GeV in MC11. For jets with higher transverse momenta, the resolution decreases, reaching values smaller than $3 \cdot 10^{-3}$ above 200 GeV. The slightly degraded performance for jets in 2011 compared to 2010 is due to the increase in pile-up.

The azimuthal offset and resolution follow similar trends as do the pseudo-rapidity offset and resolution parameters. The magnitude of the offset is smaller than $3 \cdot 10^{-3}$ for low p_t jets, becoming insignificant (consistent with zero within errors) above ~ 100 GeV. The azimuthal resolution also improves with growing jet p_t , decreasing from 0.07 for jets with $p_t = 20$ GeV ($p_t = 30$ GeV) to roughly 0.02 above 200 GeV for jets in MC10 (MC11).

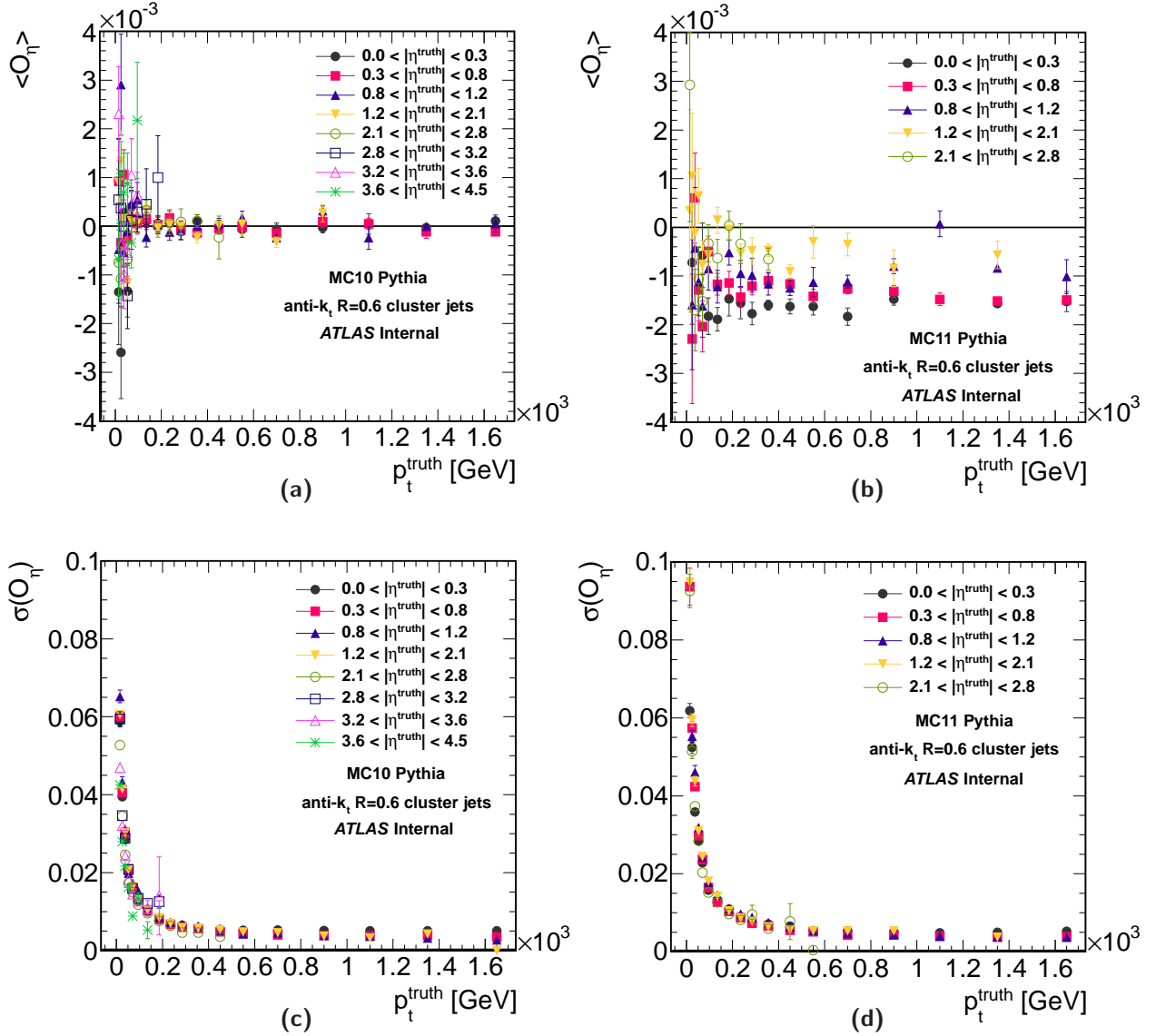


Figure 5.7. Dependence of the average pseudo-rapidity offset, $\langle O_\eta \rangle$, ((a) and (b)) and of the width of the distribution of the offset, $\sigma(O_\eta)$, ((c) and (d)) on the transverse momentum of truth jets, p_t^{truth} . Several regions of truth jet pseudo-rapidity, η^{truth} , are presented for jets in MC10 and in MC11, as indicated in the figures.

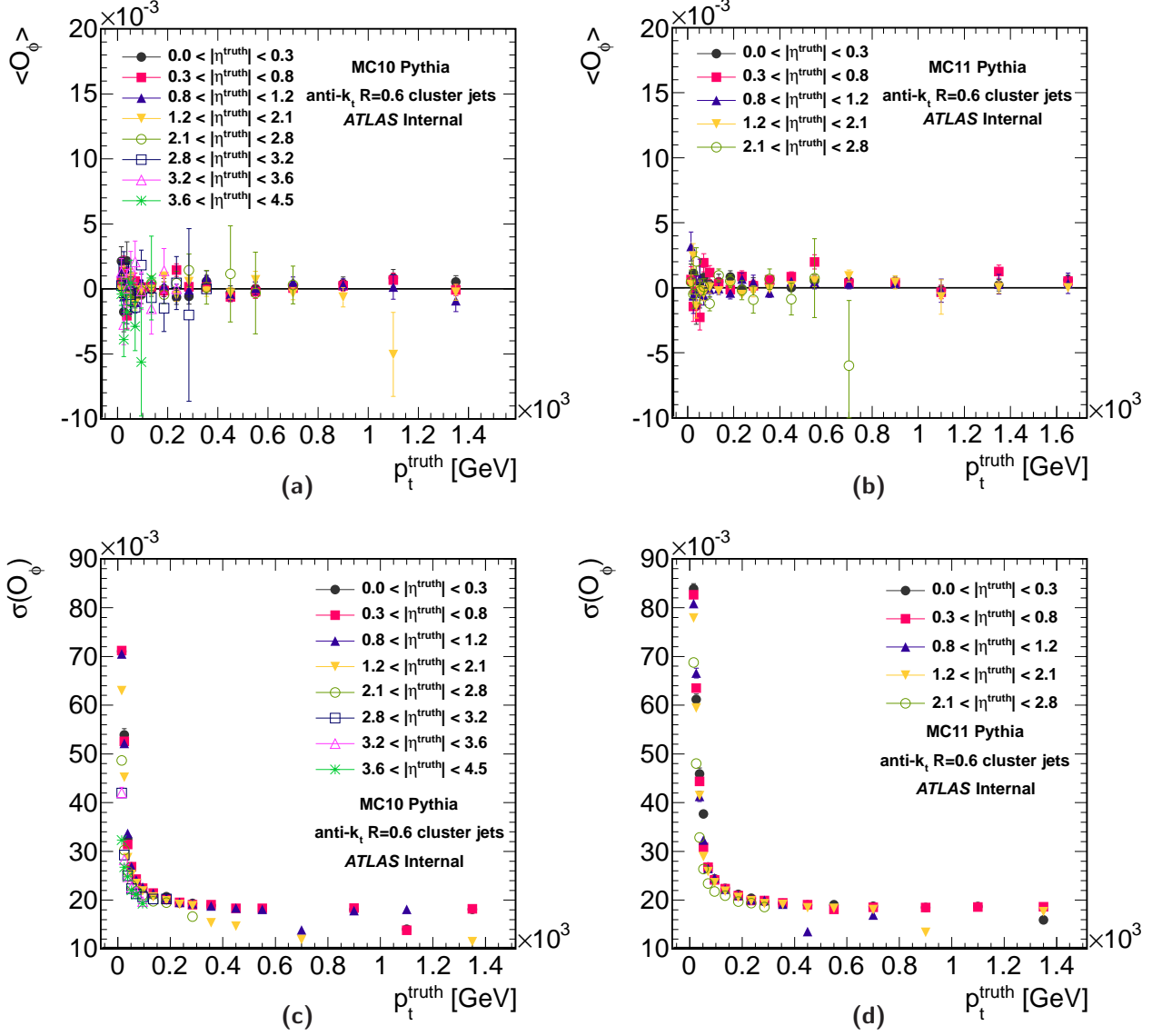


Figure 5.8. Dependence of the average azimuthal offset, $\langle O_\phi \rangle$, ((a) and (b)) and of the width of the distribution of the offset, $\sigma(O_\phi)$, ((c) and (d)) on the transverse momentum of truth jets, p_t^{truth} . Several regions of truth jet pseudo-rapidity, η^{truth} , are presented for jets in MC10 and in MC11, as indicated in the figures.

6. Data selection

6.1. Dataset

The measurements presented in this thesis are performed on data of pp collisions at $\sqrt{s} = 7$ TeV, collected by the ATLAS experiment during 2010 and during 2011. The former include all data taken during 2010 with two exceptions, for the low- p_t and the forward regions. For the low- p_t region (events where the highest- p_t jet has $20 < p_t < 60$ GeV), only data runs taken up to the beginning of June are considered. For these data the instantaneous luminosity of the accelerator was low enough that pile-up contributions were negligible, and the majority of the bandwidth was allocated to the minimum bias trigger. The forward jet trigger (covering rapidities $|y| > 2.8$) was not active in the first data-taking period.

The 2011 dataset includes data taken during April, and between July and October, corresponding respectively to 2011 periods D and I–M. Before period D, the LHC was not operating at the nominal data-taking conditions used in this analysis; the solenoid and/or toroid fields were off, the bunch train frequency was varied and the center-of-mass energy was changed. Data taken during these periods are therefore not included in this analysis. In data periods E–H, corresponding to 20% of the luminosity recorded in 2011, six LAr Front End Boards (FEBs) were lost. LAr FEBs contain the electronics for amplifying, shaping, sampling, pipelining, and digitizing the liquid argon calorimeter signals. As a result, a region, $-0.1 < \eta < 1.5$ in pseudo-rapidity and $-0.9 < \phi < -0.5$ in azimuth were affected. Jets which fell in this area of the calorimeter suffered a 30% loss in energy and a $\sim 50\%$ increase in energy resolution at high p_t . Data periods E–H are therefore excluded from the analysis.

All data events considered in the following require good detector status for the L1 central trigger processor, solenoid magnet, inner detectors (Pixel, SCT, and TRT), calorimeters (barrel, endcap, and forward), luminosity, as well as tracking, jet, and missing energy reconstruction performance. In addition, good data quality is required for the high-level trigger during the periods when this device is used for rejection. Events have at least one reconstructed vertex; vertices are reconstructed with constraints on their associated ID tracks, and are consistent with the beam-spot.

In total $37 \pm 3.4\%$ pb^{-1} of data taken during 2010, and $3776 \pm 3.9\%$ pb^{-1} of data taken during 2011, are used in the analysis.

6.2. Trigger and luminosity

6.2.1. Description of the trigger

Four different triggers are used in this analysis, a random trigger, the central jet trigger ($|\eta| < 3.2$), the forward jet trigger ($3.1 < |\eta| < 4.9$), and the minimum bias trigger (MBTS).

6. Data selection

The central and forward jet triggers are composed of three consecutive levels; Level 1 (L1), Level 2 (L2) and Event Filter (EF). The central and forward jet triggers independently select data using several jet transverse energy thresholds that each require the presence of a jet with sufficient transverse energy at the electromagnetic (EM) scale, E_t^{EM} . For each L1 threshold, there is a corresponding L2 threshold that is generally placed 15 GeV above the L1 value. The following convention is used for jet trigger names; names begin with the trigger-level and end with a number. The number stands for the trigger threshold, such that e.g., L1_J5 is a Level 1 trigger with a threshold, $E_t^{\text{EM}} > 5$ GeV. Jet trigger names also contain a “regional” identifier, the letter J for central triggers, and the combination FJ for forward triggers.

The MBTS trigger (denoted by L1_MBTS at Level 1 and by EF_MBTS for the Event Filter) requires at least one hit in the minimum bias scintillators located in front of the endcap cryostats, covering $2.09 < |\eta| < 3.84$, and is the primary trigger used to select minimum-bias events in ATLAS. It has been demonstrated to have negligible inefficiency for the events of interest for this analysis [154] and is generally used to select events with low- p_t jets. It is used in this study only for data taken during 2010. Events with low- p_t jets in 2011 data are selected using a random trigger.

The complete list of triggers used in the analysis in the different data-taking periods is given in Tables A.3 - A.5 in section A.2.

6.2.2. Trigger efficiency

The per-jet efficiency is determined from the probability that a single jet passes a given trigger threshold, regardless of what the other jets in the event do. In order to determine the efficiency, the off-line reconstructed jets are matched to central or forward trigger objects by the shortest distance,

$$\Delta R = \sqrt{(\phi_{\text{trig}} - \phi_{\text{jet}})^2 + (\eta_{\text{trig}} - \eta_{\text{jet}})^2},$$

using the pseudo-rapidity and azimuth of the trigger object, η_{trig} and ϕ_{trig} , and of the selected jet, η_{jet} and ϕ_{jet} .

There is an ambiguity whether to associate a jet in the transition region $2.8 < |\eta| < 3.6$ to a central or to a forward trigger object. The rapidity resolution between off-line jets and L1 trigger objects, which seed the higher trigger chain, can therefore lead to central trigger objects that are reconstructed as forward jets, and vice versa. The problem is aggravated by the fact that the forward L1 jet trigger has no η information in the FCal. In order to resolve the ambiguity, two candidate trigger objects are assigned to an off-line jet, one from the central and one from the forward trigger systems. This is done using all available information, that is, central trigger objects are matched by the smallest ΔR with respect to the selected jet, and forward trigger objects by the smallest $\Delta\phi$. In the next step, the candidate which is closest to the off-line jet between the two is chosen. A detailed description of the matching procedure may be found in [155].

The efficiencies for various central jet triggers are shown in figure 6.1 for the 2010 and for the 2011 data. Additional rapidity bins are presented in section A.2, figures A.1 - A.2. These include three regions: The first is the crack region between the calorimeter barrel and endcap, $1.3 < |y| < 1.6$; there, the per-jet L1 and L2 trigger efficiencies never become fully efficient due to calorimeter inhomogeneities. The second is the transition region between the central and the forward trigger systems, $2.8 < |y| < 3.6$; in this region, trigger selection is performed by matching jets to either the central or the forward triggers, as described above. The third is the forward region, $3.6 < |y| < 4.4$, where the forward jet trigger is used; due to a dead FCal trigger tower that spans a

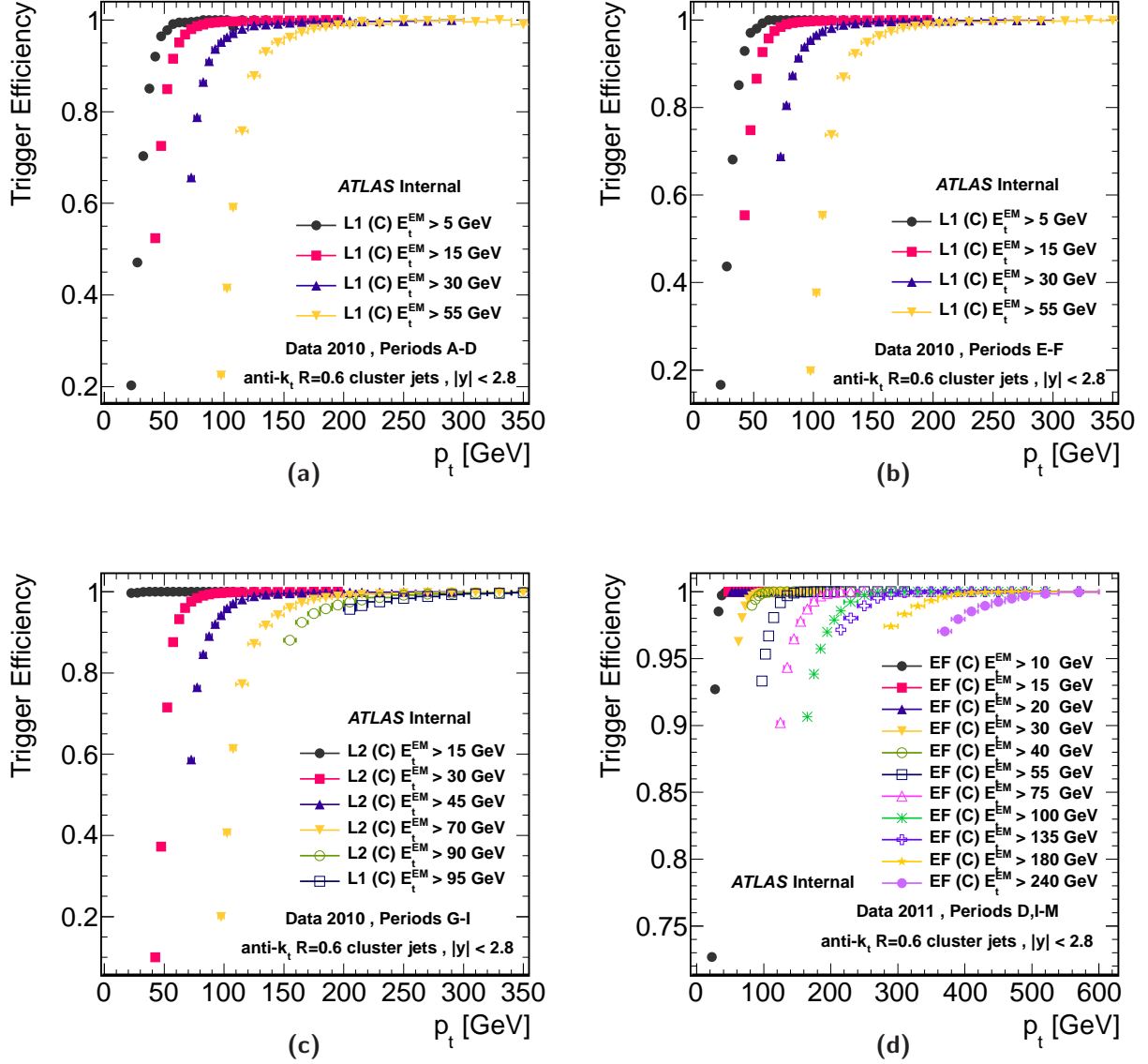


Figure 6.1. Trigger efficiency curves for various Level 1 (L1), Level 2 (L2) and Event Filter (EF) triggers. Different 2010 ((a), (b) and (c)) and 2011 (d) data taking periods are represented, as indicated in the figures. The triggers are associated with jets within rapidity $|y| < 2.8$, belonging to the central jet trigger system, denoted by (C). Trigger thresholds are denoted by E_t^{EM} , signifying the minimal transverse energy at the electromagnetic scale, of a jet which is required to fire the trigger. Additional rapidity bins are presented in [section A.2](#), [figures A.1 - A.2](#).

6. Data selection

width of $\Delta\phi = \pi/4$ in the rapidity region $|y| > 3.1$, the forward jet triggers are not fully efficient in this region.

As the instantaneous luminosity increased throughout data-taking, it was necessary to prescale triggers with lower E_t thresholds. For each bin of jet- p_t considered in this analysis, a dedicated trigger threshold is chosen such that the efficiency is as close as possible to 100% and the prescale is as small as possible. Table 6.1 presents the various triggers used in the analysis as a function of jet transverse momenta and rapidity, for data taken throughout 2010. The per-jet trigger efficiencies are shown in section A.2, table A.2. The triggers used for the 2011 data are listed in table 6.2. The EF triggers used in 2011 have efficiency $\gtrsim 99\%$ within the rapidity region of interest ($|y| < 2.8$).

6.2.3. Luminosity calculation using a two-trigger selection scheme

A *two-trigger* strategy is used in the analysis, following the prescription employed in [156]. An event may be accepted if at least one of the two leading (highest- p_t) jets passes a dedicated trigger, determined by the transverse momentum and pseudo-rapidity of the jet. The event is then assigned to one of two luminosity classes, $\mathcal{L}_{\text{single}}^{\text{jet}}$ or $\mathcal{L}_{\text{double}}^{\text{jet}}$. The former, a *single-trigger* luminosity class, is for events where the two jets are assigned to the same trigger. The latter, a *double-trigger* luminosity class, is for events in which each jet is assigned to a different trigger.

In order to account for different prescale combinations of the two jets, the *Inclusive method for fully efficient combinations* [157] is used. This method entails calculation of the integrated luminosity of each trigger over the entire event sample, and combination of the per-trigger luminosities on an event-by-event basis. Let \mathcal{L}_{LB} denote the integrated luminosity in a luminosity-block (LB), and let Ps_{LB} denote the prescale of a given jet trigger within this LB. The effective luminosity of a single trigger for the entire dataset can then be written as

$$\mathcal{L}_{\text{single}}^{\text{jet}} = \sum_{\text{LB}} \frac{\mathcal{L}_{\text{LB}}}{\text{Ps}_{\text{LB}}}, \quad (6.1)$$

where the summation is over all luminosity-blocks. The effective luminosity for a pair of triggers takes into account the probability that two triggers with prescales, Ps_{LB}^0 and Ps_{LB}^1 , fired simultaneously in a given event; it is defined by

$$\mathcal{L}_{\text{double}}^{\text{jet}} = \sum_{\text{LB}} \frac{\mathcal{L}_{\text{LB}}}{\text{Ps}_{\text{LB}}^0 \text{Ps}_{\text{LB}}^1 / (\text{Ps}_{\text{LB}}^0 + \text{Ps}_{\text{LB}}^1 - 1)}. \quad (6.2)$$

Tables A.3 - A.5 in section A.2 show the integrated single- and double-trigger luminosities for the different trigger-bins used in the analysis.

The combined trigger efficiency of the two leading jets is computed in a similar manner as in equation (6.2), using the corresponding per-jet trigger efficiencies (given in table A.2 for the 2010 data and taken as unity for the 2011 data) and the single-jet reconstruction efficiency (see section 5.4). Together these yield the probability for an event to have fired a given trigger (or trigger combination), and for a jet (or pair of jets) to have been reconstructed and matched to the trigger(s). The inverse of the combined trigger and reconstruction efficiency factor is multiplied by the luminosity of the selected luminosity class; this produces the final luminosity weight for each event.

p_t [GeV]	Trigger name			
	Period A Run < 152777	Periods A-D (Run \geq 152777)	Periods E-F (excl. E1-E4)	Periods G-I

$ y < 3.6$				
20 < p_t \leq 42.5	L1_MBTS	L1_MBTS	L1_MBTS	EF_MBTS
42.5 < p_t \leq 70	L1_MBTS	L1_J5	L1_J5	L2_J15
70 < p_t \leq 97.5	L1_MBTS	L1_J15	L1_J15	L2_J30
97.5 < p_t \leq 152.5	L1_MBTS	L1_J30	L1_J30	L2_J45
152.5 < p_t \leq 197.5	L1_MBTS	L1_J55	L1_J55	L2_J70
197.5 < p_t \leq 217.5	L1_MBTS	L1_J55	L1_J55	L2_J90
$p_t \geq$ 217.5	L1_MBTS	L1_J55	L1_J55	L1_j95

$2.8 < y < 3.6$				
20 < p_t \leq 42.5	L1_MBTS	L1_MBTS	L1_MBTS	EF_MBTS
42.5 < p_t \leq 62.5	L1_MBTS	L1_MBTS	L1_FJ10	EF_MBTS
62.5 < p_t \leq 72.5	L1_MBTS	L1_MBTS	L1_FJ10	L2_FJ25
72.5 < p_t \leq 95	L1_MBTS	L1_MBTS	L1_FJ30	L2_FJ25
95 < p_t \leq 160	L1_MBTS	L1_MBTS	L1_FJ30	L2_FJ45
$p_t \geq$ 160	L1_MBTS	L1_MBTS	L1_FJ30	L2_FJ70

$3.6 < y < 4.4$				
20 < p_t \leq 42.5	L1_MBTS	L1_MBTS	L1_FJ10	EF_MBTS
42.5 < p_t \leq 50	L1_MBTS	L1_MBTS	L1_FJ10	L2_FJ25
50 < p_t \leq 67.5	L1_MBTS	L1_MBTS	L1_FJ30	L2_FJ25
67.5 < p_t \leq 100	L1_MBTS	L1_MBTS	L1_FJ30	L2_FJ45
$p_t \geq$ 100	L1_MBTS	L1_MBTS	L1_FJ30	L2_FJ70

Table 6.1. The trigger chains used in the analysis for the 2010 data as a function of jet transverse momentum, p_t , in various data-taking periods and rapidity regions, y , as indicated in the table. Level 1 (L1) and Level 2 (L2) jet trigger names end with a number. This number stands for the trigger threshold in transverse energy at the EM scale, E_t^{EM} ; e.g., L1_J5 is a Level 1 trigger with a threshold, $E_t^{\text{EM}} > 5$ GeV. The L1 and Event Filter (EF) minimum bias triggers are respectively named L1_MBTS and EF_MBTS.

p_t [GeV]	Trigger name Periods D,I-M
20 $< p_t \leq$ 47	EF_rd0
47 $< p_t \leq$ 52	EF_J10
52 $< p_t \leq$ 60	EF_J15
60 $< p_t \leq$ 82	EF_J20
82 $< p_t \leq$ 97	EF_J30
97 $< p_t \leq$ 122	EF_J40
122 $< p_t \leq$ 160	EF_J55
160 $< p_t \leq$ 207	EF_J75
207 $< p_t \leq$ 275	EF_J100
275 $< p_t \leq$ 365	EF_J135
365 $< p_t \leq$ 472	EF_J180
$p_t \geq$ 472	EF_J240

Table 6.2. The trigger chains used in the analysis of the 2011 data as a function of jet transverse momentum, p_t , as indicated in the table. Event Filter (EF) jet trigger names end with a number. This number stands for the trigger threshold in transverse energy at the EM scale, E_t^{EM} ; e.g., EF_J10 is an Event Filter trigger with a threshold, $E_t^{\text{EM}} > 10$ GeV. The EF random trigger is named EF_rd0.

7. The jet area/median method for pile-up subtraction

As discussed in [section 5.3](#), an important component of the energy calibration of jets is the subtraction of pile-up, that is the extra energy which originates from additional pp interactions that occurred in the same bunch-crossing. The current strategy in ATLAS for dealing with pile-up involves the subtraction of an average correction derived from MC simulation, called the offset correction. The offset correction is parametrized in variables which reflect the magnitude of the different components of the pile-up in a given event. As the parametrization is derived from MC, it suffers from uncertainties due to miss-modelling of the pile-up and requires adjustments based on *in-situ* measurements.

In the following, an alternative data-driven method is introduced, called the jet area/median method. The median method combines parametrization of the average contributions of pile-up in data, as well as an event-by-event estimation of the local pile-up energy around the jets of interest. The median correction is used to calibrate the energy of jets in data taken during 2011, and the performance is compared to the default offset correction.

As mentioned in [section 4.2](#), a few of the results shown in the following use the transitional simulation, MC10b. Unless otherwise indicated, MC11 is used.

7.1. Pile-up in ATLAS

7.1.1. In- and out-of-time pile-up

Pile-up in ATLAS is usually separated into *in-time pile-up* and *out-of-time pile-up*. The former refers to the number of pp collisions which occur within the same bunch crossing as the collision of interest, and the latter to interactions in previous or subsequent bunch crossings. The exact nature of out-of-time pile-up depends on the bunch-structure of the LHC, and on the specifics of the reconstruction of calorimeter signals.

For the data used in this study, the spacing between adjacent bunches was 50 ns. This number should be compared with the typical signal shaping time of the liquid Argon calorimeters, which is roughly 400 ns [[158](#)], as illustrated in [figure 7.1](#). The figure shows the shaped signal in a typical calorimeter element (cell). The shaping integrates the electronic signal registered in the cell in two phases. In the first phase, which takes ~ 100 ns, the signal is integrated with a positive amplitude. In the second phase, which takes ~ 400 ns, the signal is integrated with a negative amplitude; the latter is smaller in magnitude compared to the positive amplitude in the first phase. The shaping is such that the total integral of the positive- and the negative-amplitude phases is zero, such that for the case of random noise, the integrated signal is minimal.

A consequence of the long integration time (compared to the short bunch crossing rate) is that the energy deposits from several bunch crossings are typically overlaid with any event of interest. The

7. The jet area/median method for pile-up subtraction

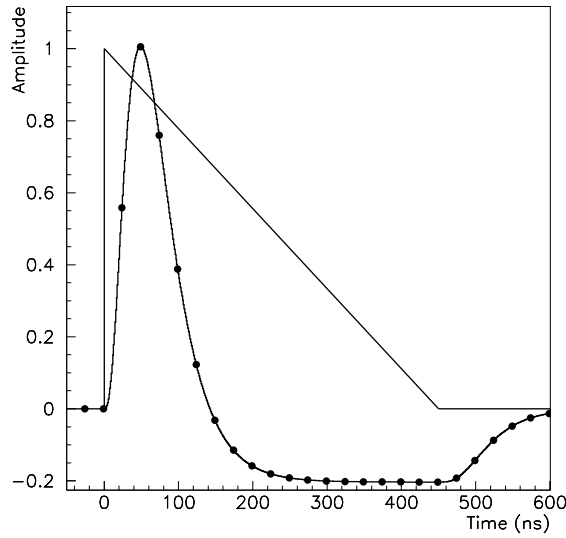


Figure 7.1. Signal shape as produced in the detector (triangle), and after shaping (curve with dots). The dots represent the position of the successive bunch crossings for a bunch spacing configuration of 25 ns. (Figure taken from [158].)

situation is further complicated by the mixture of positive and negative amplitudes of the shaping. The resulting pile-up signal can therefore be composed of both positive- and negative-energy components within a given 50 ns readout window. The shaping is designed such that out-of-time pile-up should have an overall negative effect that cancels the positive effect from in-time pile-up on average. However, this only works if the bunch intensity and subsequent occupancy of cells is constant over the integration time of the calorimeter. By design of the shaping amplifier, the most efficient suppression is achieved for 25 ns bunch spacing in the LHC beams. The 2011 beam conditions, with 50 ns bunch spacing, do not allow for full pile-up suppression by signal shaping. In addition, a given cell would not necessarily have contributions from pile-up from every bunch crossing, and so while there is approximate cancellation of positive and negative pile-up on average, there are large fluctuations on an even-by-event basis. Special attention must also be given to the position of the bunch crossing within the bunch train. For example, at the beginning of a bunch train there is insufficient out-of-time pile-up to cancel the in-time pile-up; the calorimeter response in such events is therefore systematically higher.

During reconstruction, calorimeter cells are combined into topo-clusters (see [section 5.2](#)). Due to the presence of the negative-energy signals, two effects come into play; the positive energy of positive topo-clusters is reduced, and purely negative-energy topo-clusters are formed. In the current jet reconstruction scheme of ATLAS, there is no calibration for negative-energy jet constituents, therefore these are discarded and not used in the reconstructing of jets. The energy of a jet which includes positive- and negative-energy cells is subsequently not a simple linear combination of cell energies. Rather, it is the sum of energies of those positive-energy clusters, which had enough positive-energy cells to pass the reconstruction threshold.

For the 2010 data, the relatively large spacing between adjacent bunches and the low instantaneous luminosity mean that the magnitude of the out-of-time pile-up is negligible. Consequently, out-of-time pile-up is only discussed here in the context of the 2011 data and MC.

On average, one can parametrize the amount of energy originating from pile-up by the number of interactions, which is measured by counting the number of reconstructed vertices in a given event, N_{PV} .

Vertices are reconstructed from ID tracks, with a requirement of at least five or three tracks per vertex for data taken respectively during 2010 or 2011. Tracks are selected in 2010 and in 2011 using the following criteria:

$$\begin{array}{l}
 \text{2010:} \quad p_t^{\text{trk}} > 150 \text{ MeV} , N_{\text{pixel}} + N_{\text{SCT}} \geq 7 \\
 \quad \quad \quad |d_0| < 1 \text{ mm} , |z_0| < 1.5 \text{ mm} \\
 \hline
 \text{2011:} \quad p_t^{\text{trk}} > 500 \text{ MeV} , N_{\text{pixel}} \geq 1 , N_{\text{SCT}} \geq 6 \\
 \quad \quad \quad |d_0| < 1 \text{ mm} , |z_0 \sin \theta| < 1 \text{ mm} , (\chi^2/\text{NDF})_{\text{trk}} < 3.5
 \end{array}$$

Here p_t^{trk} is the transverse momentum of a track and N_{pixel} and N_{SCT} are respectively the number of hits from the pixel and SCT detectors that are associated with the track. The parameters d_0 and z_0 are the transverse and longitudinal impact parameters measured with respect to the vertex to which the tracks are extrapolated. The ratio $(\chi^2/\text{NDF})_{\text{trk}}$ represents the quality of the fit of the track parameters divided by the number of degrees of freedom of the fit. Vertices are also required to be consistent with the beam-spot.

The constraints on vertex reconstruction used here for the 2011 data are tighter than what is usually used in analyses in ATLAS, in that the common 2011 selection criteria do not impose the track selection requirements described above. Vertices selected with these looser constraints will be referred to as N_{PV}^{loose} in the following. The relation between the average of N_{PV} and N_{PV}^{loose} is shown in [figure 7.2a](#) for reference. The relation between the two definitions is linear, suggesting that on average the two factors provide equivalent characterization of the amount of in-time pile-up in an event. The MC describes the data well.

The number of in-time interactions, N_{PV} , contributes purely-positive pile-up energy to a given event. Depending on the position of a given collision within the bunch train, out-of-time pile-up has on average different negative and positive energy components. In order to estimate the amount of out-of-time pile-up, one would in principle need to measure N_{PV} during collisions before and after the event of interest, within a time window of ~ 400 ns. Due to the trigger strategy of ATLAS, these events may have been discarded. Subsequently, the only handle on out-of-time pile-up is the average number of pp collisions in a given time-frame, which depends on the instantaneous luminosity. The number of collisions is described by a Poissonian distribution with some mean value, μ . The mean is computed over a rather large window in time, Δt , which safely encompasses the time interval during which the ATLAS calorimeter signal is sensitive to the activity in the collision history ($\Delta t \gg 400$ ns for the liquid argon calorimeters). The average number of interactions can be reconstructed from the average luminosity over this time window, \mathcal{L}_{avg} , the total inelastic pp cross section, $\sigma_{\text{inel}} = 71.5$ mb [[159](#)], the number of colliding bunches in LHC, N_{bunch} , and the LHC revolution frequency, f_{rev} , [[86](#)]

$$\mu = \frac{\mathcal{L}_{\text{avg}} \times \sigma_{\text{inel}}}{N_{\text{bunch}} \times f_{\text{rev}}} . \quad (7.1)$$

The correlation between μ and the average N_{PV} is shown in [figure 7.2b](#) for data taken during 2011 and for the nominal MC11 PYTHIA simulation. There is strong correlation between the two factors, as expected. Good agreement is observed between the data and the MC.

7. The jet area/median method for pile-up subtraction

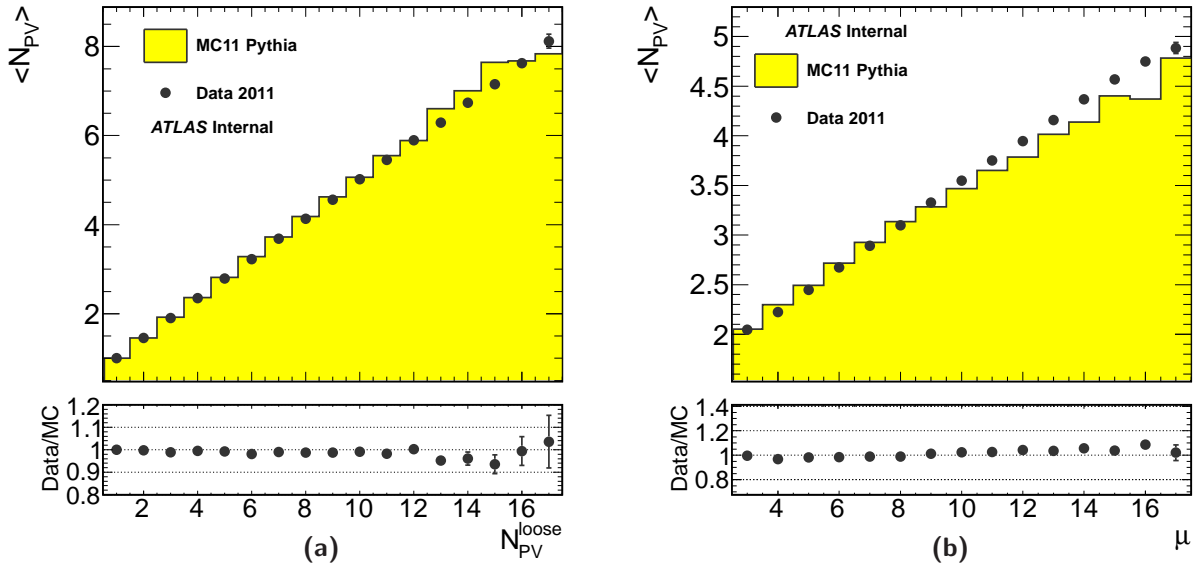


Figure 7.2. (a) Dependence of the average number of reconstructed vertices, $\langle N_{PV} \rangle$, on the number of vertices which are reconstructed with the loose quality criteria, N_{PV}^{loose} . (b) The average, $\langle N_{PV} \rangle$, as a function of the average number of interactions, μ . As indicated in the figures, data taken during 2011 are compared to MC11 in the top panels, and the ratio of data to MC is shown in the bottom panels.

In order to properly describe pile-up in data, MC samples are weighted such that the distributions of the number of reconstructed vertices in MC10 and MC11 match the respective distributions in the 2010 and in the 2011 data. The reweighted MC N_{PV} distributions are compared to the ones in the data in figure 7.3. Full agreement is achieved.

Comparison of the N_{PV} distributions between 2010 and 2011 also helps to emphasize the increase in pile-up in 2011 compared to the previous year. In 2010, the percentage of single- double- and triple-vertex events out of the full event-sample are 81.8%, 11.2% and 4.6%. In 2011, the corresponding values are 20.7%, 20.5% and 18.1%. Thus, more than 79% of events in 2011 are multi-vertex events, and require dedicated calibration. The standard method to remove pile-up from jets in ATLAS is called the jet offset correction, and is the subject of the following section.

7.1.2. The jet offset pile-up correction

As mentioned in section 5.3, pile-up changes the energy of jets. An example is shown in figure 7.4. The figure shows the transverse energy of calorimeter jets which are matched with track jets. Track jets are insensitive to pile-up effects, and therefore represent the unbiased energy scale of the respective calorimeter jets. This scale is represented by the transverse momentum of the track jets, $p_{T}^{\text{track jet}}$. Within a given bin of $p_{T}^{\text{track jet}}$, one would expect to measure a stable (within energy resolution) value of calorimeter jet $p_{T,i}$. However, as pile-up increases (N_{PV} grows), so does the energy of calorimeter jets in each $p_{T}^{\text{track jet}}$ bin.

Pile-up must therefore be subtracted as part of the calibration procedure of jets. The current strategy in ATLAS analyses involves linear parametrization of the energy content of jets due to pile-

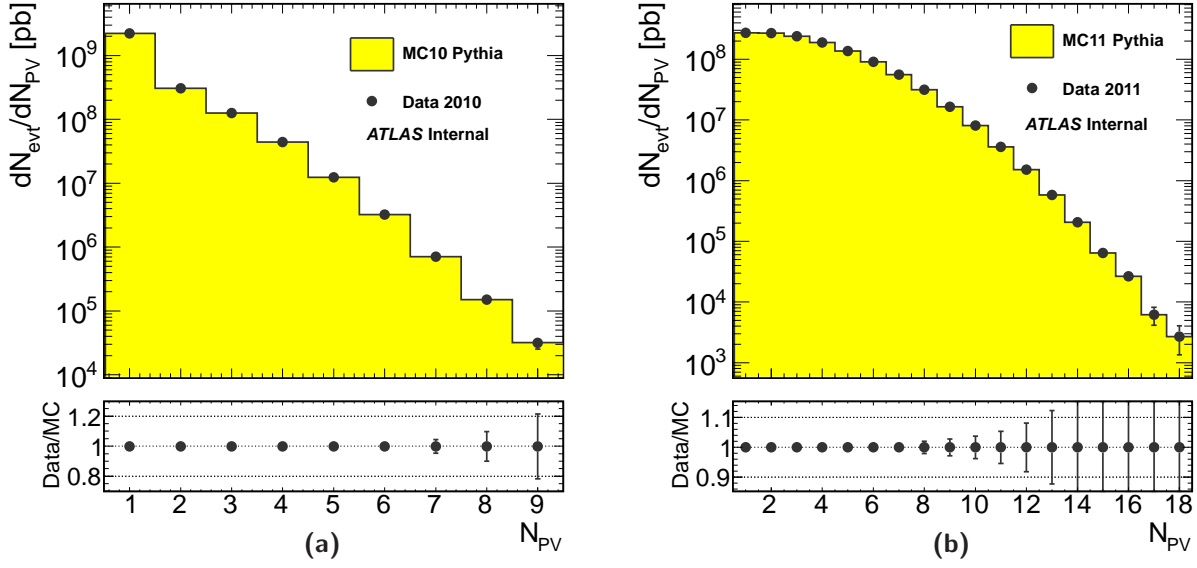


Figure 7.3. Distribution of the reconstructed number of vertices, N_{PV} , for data taken in 2010 (a) and in 2011 (b), and the respective distributions in MC10 and MC11. The top panels show the N_{PV} distributions and the bottom panels show the respective ratio of data to MC.

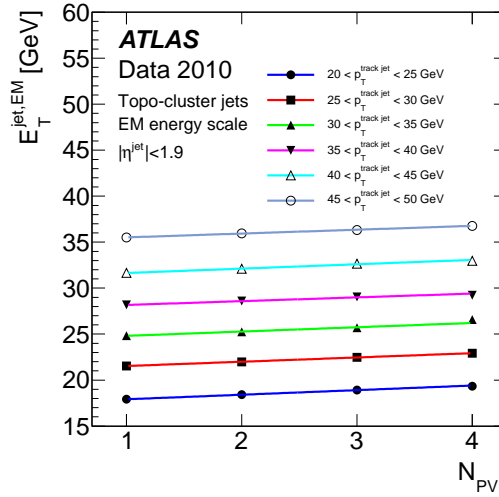


Figure 7.4. The most probable value of the transverse jet energy, $E_T^{jet,EM}$, of calorimeter jets with pseudo-rapidity, $|\eta^{jet}| < 1.9$, measured in 2010 at the EM scale, as a function of the number of reconstructed vertices, N_{PV} . The different symbols represent calorimeter jets which are associated to track jets with different transverse momenta, $p_T^{track jet}$, as indicated. (Figure taken from [150].)

7. The jet area/median method for pile-up subtraction

up, called the *offset* of a jet. Different methods are used to estimate to offset in 2010 and in 2011, due to the variant nature of pile-up discussed above. The parametrizations are rapidity dependent due to the differences in calorimeter granularity and occupancy after topo-cluster reconstruction; the differences in the signal shaping in the calorimeter; and the differences in the energy flow of the pile-up across the detector.

The offset correction in 2010

The pile-up correction devised for 2010 is derived from MC. The correction is a function of in-time pile-up, estimated by the number of reconstructed vertices, N_{PV} . It is based on calorimeter towers, which are static, $\Delta\eta \times \Delta\phi = 0.1 \times 0.1$, grid elements built directly from calorimeter cells. Calorimeter towers are calibrated at the EM scale. As such they are appropriate for use in correcting the energy of EM+JES calibrated jets.

The calorimeter *tower offset*, $\mathcal{O}_{fst(tow)}^{EM}$, is determined by measuring the average transverse energy of towers, E_t^{tower} , in events with different values of N_{PV} . This average is then compared to the one for events with $N_{PV} = N_{PV}^{ref} = 1$,

$$\mathcal{O}_{fst(tow)}^{EM}(\eta, N_{PV}) = \langle E_t^{tower}(\eta, N_{PV}) \rangle - \langle E_t^{tower}(\eta, N_{PV}^{ref}) \rangle. \quad (7.2)$$

The tower offset is an estimation of the local average pile-up density. The EM jet offset, \mathcal{O}_{fst}^{EM} , may therefore be approximated as this density, multiplied by the *effective tower area* of a jet, $\mathcal{A}_{jet}^{tower}$,

$$\mathcal{O}_{fst}^{EM} = \mathcal{O}_{fst(tow)}^{EM} \times \mathcal{A}_{jet}^{tower}. \quad (7.3)$$

The effective tower area stands for the number of towers contained within the jet. In order to derive $\mathcal{A}_{jet}^{tower}$ for a given jet, calorimeter cells belonging to the constituent topo-clusters are used.

The offset correction in 2011

With the increased instantaneous luminosity and the shorter bunch spacing, the LCW offset correction in 2011, \mathcal{O}_{fst}^{LCW} , depends on out-of-time pile-up as well as on in-time pile-up. These two components are respectively parametrized as proportional to the number of reconstructed vertices, N_{PV} , and to the average number of interactions, μ . The offset is derived from MC simulation,

$$\begin{aligned} \mathcal{O}_{fst}^{LCW}(N_{PV}, \mu, \eta) &= p_t^{LCW}(N_{PV}, \mu, \eta) - p_t^{truth(LCW)} \\ &= \frac{\partial p_t^{LCW}}{\partial N_{PV}}(\eta) \times (N_{PV} - N_{PV}^{ref}) + \frac{\partial p_t^{LCW}}{\partial \mu}(\eta) \times (\mu - \mu^{ref}) \\ &= \alpha(\eta) \times (N_{PV} - N_{PV}^{ref}) + \beta(\eta) \times (\mu - \mu^{ref}). \end{aligned} \quad (7.4)$$

The offset is defined for a jet with transverse momentum at the LCW scale, p_t^{LCW} , which is associated with a truth jet with transverse momentum (at the LCW scale), $p_t^{truth(LCW)}$. The reference values for N_{PV} and μ , $N_{PV}^{ref} = 1$ and $\mu^{ref} = 8$, are set such that $\mathcal{O}_{fst}^{LCW}(N_{PV}^{ref}, \mu^{ref}, \eta) = 0$.

Using the offset to correct the energy scale of jets

The offset is determined in MC by matching calorimeter jets to truth jets. In this way, the average tower transverse energy (for 2010) and the coefficients $\alpha(\eta)$ and $\beta(\eta)$ (for 2011), are derived.

It is assumed that the pile-up contamination affects the momentum and the energy of jets in a similar manner¹. Jets in the data and in the MC are corrected for pile-up by estimating the percentage of the jet transverse energy or transverse momentum originating from pile-up,

$$\wp_t^{\mathcal{O}_{\text{fst}}^{\text{S}}} = \begin{cases} \frac{\mathcal{O}_{\text{fst}}^{\text{EM}}(N_{\text{PV}}, \eta)}{E_t^{\text{EM}}} & (2010) \\ \frac{\mathcal{O}_{\text{fst}}^{\text{LCW}}(N_{\text{PV}}, \mu, \eta)}{p_t^{\text{LCW}}} & (2011) \end{cases} . \quad (7.5)$$

The four-momentum of a jet is modified for pile-up by the transformation,

$$E^{\text{det}} \rightarrow E^{\text{S}} \times \left(1 - \wp_t^{\mathcal{O}_{\text{fst}}^{\text{S}}}\right) , \quad \eta \rightarrow \eta , \quad \phi \rightarrow \phi , \quad p_t^{\text{det}} \rightarrow p_t^{\text{S}} \times \left(1 - \wp_t^{\mathcal{O}_{\text{fst}}^{\text{S}}}\right) , \quad (7.6)$$

where E^{S} (p_t^{S}) and E^{det} (p_t^{det}) are the S-scale energy (transverse momentum) of a jet, respectively before and after pile-up subtraction, and η and ϕ are respectively its pseudo-rapidity and azimuthal angle. Here, as defined previously, S stands for the EM scale or the LCW scale for jets in 2010 or 2011 respectively. Following the pile-up subtraction, the JES correction, $\mathcal{F}_S^{\text{calib}}$, is applied, taking the jet from the EM or LCW scale to the hadronic energy-scale (see [equation \(5.4\)](#)). The fully calibrated jet has transverse momentum,

$$p_t^{\text{calib}} = p_t^{\text{det}} \times \mathcal{F}_S^{\text{calib}}(p_t^{\text{det}}, \eta) . \quad (7.7)$$

7.2. A pile-up correction using the jet area/median method

A novel approach to estimate the pile-up energy content of jets, the *jet area/median method*, has been proposed by Cacciari, Salam and Soyez [161, 162]. Therein, under the assumption that pile-up is distributed uniformly in a given event, the pile-up transverse momentum density, ρ , may be calculated, and then subtracted from the jets which originate from the hard scatter. In order to do this, one must first define the *jet area*, \mathcal{A}_{jet} . One possible definition of the area, used in the following, is the so-called *active area*. The area is calculated by adding to the event a dense coverage of infinitely soft (zero momentum) *ghost particles* and counting how many are clustered inside a given jet. It can be understood as a measure of the susceptibility of a jet to contamination from an underlying distribution of particles with uniform, diffuse structure. A possible way to calculate the p_t -density in a given event, is by taking the median of the distribution of the p_t -density of all jets in the event,

$$\rho_{\text{evt}} = \text{median}_{j \in \text{jets}} \left[\left\{ \frac{p_{t,j}}{\mathcal{A}_{\text{jet},j}} \right\} \right] . \quad (7.8)$$

The logic behind the use of the median is that it is much less susceptible to contamination from outliers (i.e. hard perturbative jets) than the mean. A pile-up correction to the transverse momentum of a jet could then take the form

$$p_t^{\text{det}} = p_t^{\text{LCW}} - \mathcal{A}_{\text{jet}} \cdot \rho_{\text{evt}} , \quad (7.9)$$

¹ This is not necessarily true for the effect of pile-up on the mass of jets. For the mass, sophisticated methods may be needed, such as jet grooming techniques aiming at removing jet constituents associated with pile-up [160]. Such procedures are, however, beyond the scope of this analysis.

7. The jet area/median method for pile-up subtraction

where p_t^{LCW} and p_t^{det} are the LCW scale transverse momenta of a jet with area A_{jet} , respectively before and after pile-up subtraction.

It is important to note that according to this definition, ρ_{evt} encompasses contributions from the underlying event (UE) as well as from pile-up. An alternative approach, which only subtracts pile-up energy, is to parametrize the dependence of ρ_{evt} on the amount of pile-up by determining an average response as a function of the number of interactions. The drawback of this approach as opposed to using ρ_{evt} directly, is that one has to determine beforehand the average p_t -density, a quantity which depends on specific trigger and selection cuts. A combination of the average and the event-by-event approaches is used in this analysis.

Two important choices which have to be considered are those of the jet algorithm and the jet radius, R , which are used to calculate ρ_{evt} . Both the k_{\perp} [136, 163] and the Cambridge/Aachen [137, 138] algorithms are suitable options, because they produce jets whose area distribution is representative of the jet particle content. In contrast, algorithms that give mostly conical jets (like anti- k_{\perp} [135] and, to a lesser extent, SISCone [164]) tend not to be suitable, because they fill in the holes between the cones with jets with very small areas, which can have unrepresentative p_t -density values. The question of what R value to use is one of the freedoms of the method. The effect on the performance of changing the baseline parameters of the median calculation are studied in section 7.3.1.

In the following, unless otherwise stated, the median is calculated using k_{\perp} jets with $R = 0.4$. The constituents which compose these jets are topo-clusters, which are calibrated at the LCW energy scale.

7.2.1. Parametrization of the average pile-up energy

In order to take into account the rapidity-dependence of the calorimeter-response and of the rate of scattering due to multiple pp collisions, the p_t -density of jets is calculated in bins of η . Equation (7.8) is therefore modified, such that the median, ρ , is calculated using jets within a limited η -window of size $2\delta\eta = 0.2$,

$$\rho \equiv \rho(|\eta|) = \underset{j \in \text{jets}, |\eta_j - \eta| < \delta\eta}{\text{median}} \left[\left\{ \frac{p_t^j}{A_{\text{jet}}^j} \right\} \right]. \quad (7.10)$$

The median is calculated on an event-by-event basis from distributions of the p_t -density of jets, calibrated at the LCW scale. Figure 7.5a shows distributions in data² and in MC of the density, p_t/A_{jet} . The corresponding distributions of ρ are presented in figure 7.5b. The agreement between the data and the MC is very good. The observed trend is for the p_t -density to increase with N_{PV} . The median of the distribution of the density also grows in magnitude as pile-up increases. The distribution of the median has long tails at high values of ρ . Despite this fact, it will be shown in the following that the average value of ρ is a good estimator for the contribution of pile-up in an event.

The average median for events with $N_{\text{PV}} = 1$ and different μ ranges is shown in figure 7.6 for data and for MC. The dips in the value of $\langle \rho \rangle$ around $|\eta| = 0.8, 1.8$ and 2.8 correspond to transition regions between elements of the calorimeter, where the jet response is in general lower (see also section 5.3, figure 5.3b). For $|\eta| > 3.2$, $\langle \rho \rangle$ is very small, which has to do with the increase in out-of-time pile-up in forward rapidities. The high rate of pile-up in this region results in a uniform flux

² Here and in the following, events in data are selected after having passed one of the jet triggers. The random trigger will be addressed in section 7.3.

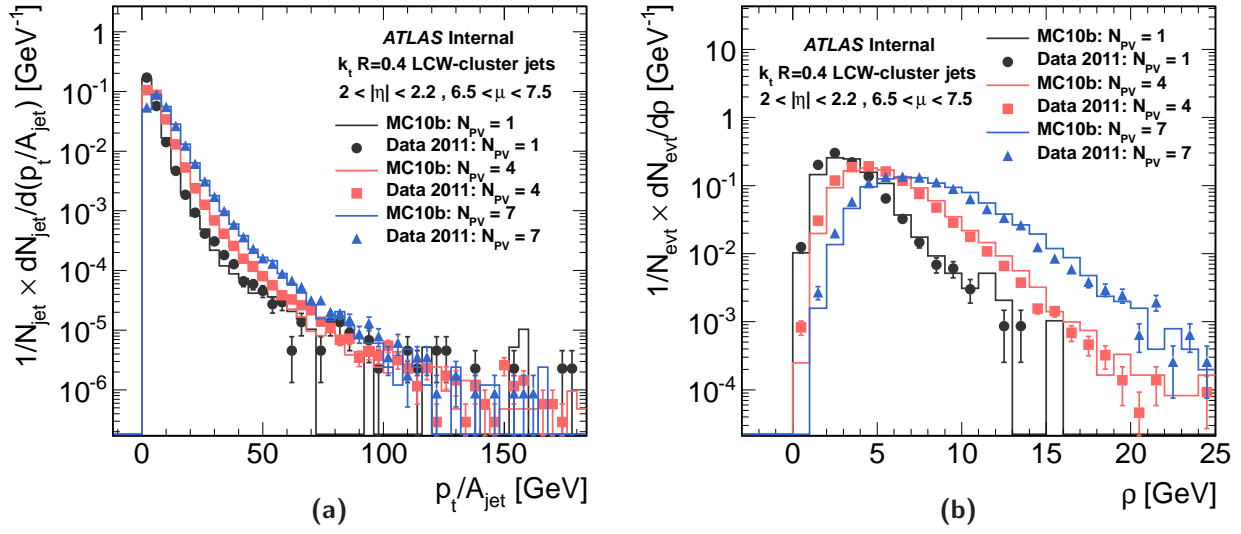


Figure 7.5. Distributions of the p_t -density of jets, p_t/A_{jet} (a) and of the corresponding median, ρ , (b), in data and in MC10b, as indicated in the figures. Jets are constructed with the k_\perp algorithm with a size parameter, $R = 0.4$, and have pseudo-rapidity, $2 < |\eta| < 2.2$. Events with an average number of interactions, $6.5 < \mu < 7.5$, and several values of reconstructed vertices, N_{PV} , are used.

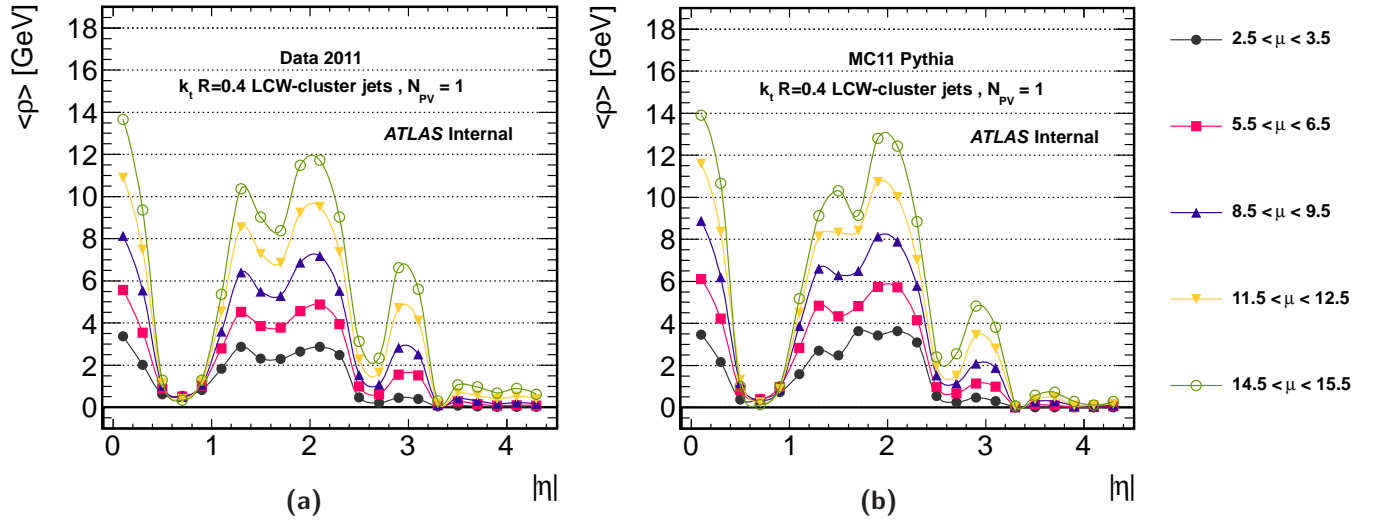


Figure 7.6. Dependence of the average median, $\langle \rho \rangle$, on pseudo-rapidity, η , for events with a single reconstructed vertex, N_{PV} , and different ranges of the average number of interactions, μ , as indicated in the figures, for data (a) and for MC (b). The connecting lines are intended to guide the eye.

7. The jet area/median method for pile-up subtraction

of particles which flood the calorimeter. The integrated positive- and negative-energy signals cancel each other out. The subsequent occupancy of positive-energy clusters in the forward calorimeter is thus very low.

As μ increases in the data, so does the average median. While the MC describes this general feature of the data, the magnitude of $\langle \rho \rangle$ in a given μ bin in the MC is slightly different. In addition, compared to the data, the dependence on η in MC is different in the transition region between the barrel and the endcap ($1.2 < \eta < 1.8$). These differences stem from two sources. The first is miss-modelling of the distribution of dead material around the crack areas. The second is the difference in the energy flow of the pile-up; the MC does not describe well the low- p_t region of the pile-up particle spectrum.

The dependence of the average median on N_{PV} for a limited range of μ values, and its dependence on μ for a fixed $N_{PV} = 1$ is shown in [figure 7.7](#). The median is calculated using jets within limited regions in $|\eta|$ in a given event. Additional rapidity bins are shown in [section A.3, figures A.3 - A.4](#). A strong dependence on N_{PV} and on μ is observed. The magnitude of $\langle \rho \rangle$ generally increases with N_{PV} . The dependence is moderate below $N_{PV} \sim 4$, above which a sharp rise is observed in most η regions. The dependence on μ is linear in the range of μ values considered. A strong dependence on rapidity is also observed, as expected. The rapidity regions in which the dependence of $\langle \rho \rangle$ on N_{PV} and on μ is weak, correspond to the transition regions between the different elements of the calorimeter, as discussed above.

The dependence on N_{PV} and on μ is parametrized using second-degree polynomials. These parametrizations are used in the following in order to estimate the pile-up p_t -density as a function of N_{PV} , μ and η in a given event.

7.2.2. Pile-up subtraction with the median

As discussed above, it is possible to estimate the amount of pile-up in an event using the p_t -density. The four-momentum of a jet can then be corrected by rescaling it according to the density in its region. Given a measured density, ρ , around a jet with area \mathcal{A}_{jet} , the percentage of the momentum of the jet originating from pile-up can be estimated as the ratio

$$\wp_t^\rho = \frac{\rho \times \mathcal{A}_{\text{jet}}}{p_t^{\text{LCW}}}, \quad (7.11)$$

where p_t^{LCW} is the transverse momentum of the jet before any pile-up correction. The four momentum is then rescaled as in [equation \(7.6\)](#) with the substitution $\wp_t^{\text{O}_{\text{1st}}^{\text{LCW}}} \rightarrow \wp_t^\rho$. Since the JES correction is derived for jets which have been recalibrated using the offset correction, a different correction using the median can cause a bias. An additional scaling function, $f(p_t^{\text{calib}}, \eta)$ may therefore be required after the calibration step from LCW- to hadronic-scale,

$$p_t^{\text{calib}} = p_t^{\text{det}} \times \mathcal{F}_{\text{LCW}}^{\text{calib}}(p_t^{\text{det}}, \eta), \quad p_t^{\text{calib}} \rightarrow p_t^{\text{calib}} \times \left(1 + f(p_t^{\text{calib}}, \eta)\right). \quad (7.12)$$

The appropriate value of the median can be calculated in several ways. One has the option of either using the parametrization of $\langle \rho \rangle$ derived in [section 7.2.1](#), or of calculating the p_t -density from event-level observables. For the latter, there is freedom in choosing the area over which the median is calculated. One may choose e.g., to include in the median only jets from the vicinity of the jet which is to be calibrated. Another option would be to estimate the pile-up contamination in the

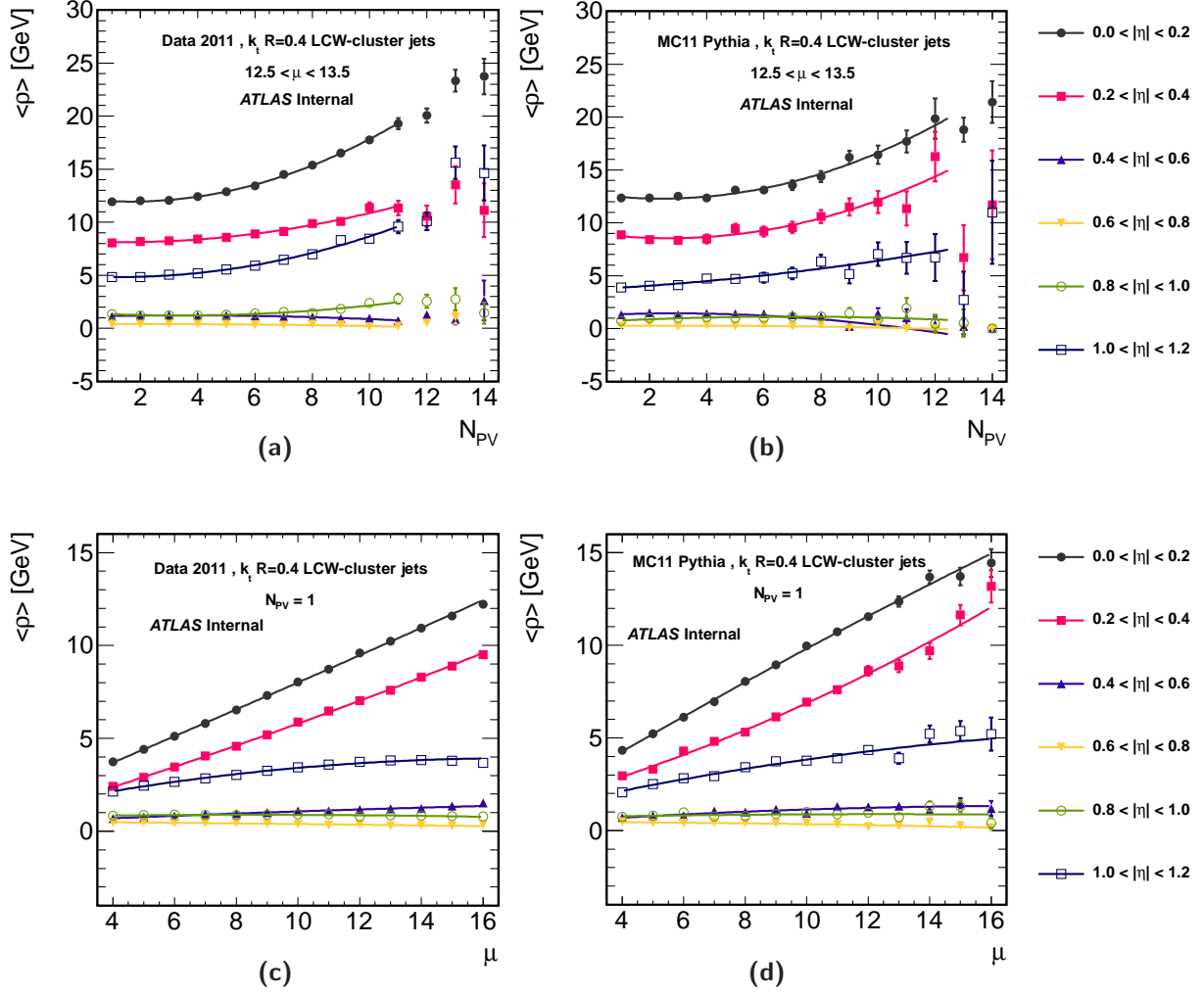


Figure 7.7. (a)-(b) Dependence of the average median, $\langle \rho \rangle$, on the number of reconstructed vertices, N_{PV} , for events with an average number of interactions, $12.5 < \mu < 13.5$. (c)-(d) Dependence of $\langle \rho \rangle$ on μ for events with $N_{PV} = 1$. Several pseudo-rapidity, η , bins are shown for data and for MC, as indicated in the figures. The lines represent polynomial fits to the points.

7. The jet area/median method for pile-up subtraction

event, in a region of the calorimeter where the pile-up is stable over time. Several such schemes have been explored. The notation ε_i is used to define the different correction procedures,

- ε_0 - **no correction**;
- ε_1 - **default offset correction** - the current correction method used in ATLAS. (See [section 7.1.2](#));
- ε_2 - **central rapidity correction** - the median is calculated on an even-by-event basis, as an average within the central rapidity region, $|\eta| < 1.8$. The average is calculated using the value of ρ in 18 pseudo-rapidity bins of 0.2 units width;
- ε_3 - **local correction** - the median is calculated on an even-by-event basis, as an average within a range of ± 1 pseudo-rapidity units around the jet for which the correction is made. The average is calculated using the value of ρ in six pseudo-rapidity bins of 0.2 units width;
- ε_4 - **average correction** - the average pile-up p_t -density is parametrized as a function of N_{PV} , μ and η . The correction is applied with regard to a reference value, $N_{PV} = 1$;
- $\varepsilon_5 = \varepsilon_3 \oplus \varepsilon_4$ - **local/average combination** - a combination of the local (ε_3) and of the average (ε_4) median calculations. The relative weights between the two elements depend on rapidity (at central rapidity, higher significance is given to the local median correction).

For all of the above (ε_0 - ε_5), jets undergo pile-up subtraction using the respective calculation of ρ , followed by the original JES calibration ([equation \(7.7\)](#)). A special configuration, incorporating the correction introduced in [equation \(7.12\)](#), is

- $\varepsilon_6 = \varepsilon_5 \otimes f(p_t, \eta)$ - **local/average combination with JES factor** - the combination of the local and of the average median calculations, ε_5 , is modified by introducing a p_t dependant JES scaling function, $f(p_t, \eta)$, in addition to the baseline JES calibration.

As will be shown in the following, the best performance is achieved using ε_6 . This is therefore defined as the nominal correction.

It should be emphasized that unlike the offset correction ([equation \(7.4\)](#)), the average correction defined in ε_4 and used in ε_5 and ε_6 uses a reference value for N_{PV} , but does not use one for μ . Instead, the dependence on N_{PV} is binned in μ .

Due to the discrepancy between data and MC (observed e.g., in [figure 7.6](#)), the MC is not used for calculation of the average pile-up correction for data. Instead, the median ([equation \(7.6\)](#)) is taken directly from the data. The MC is used in order to derive $f(p_t, \eta)$, used in ε_6 . An associated uncertainty for the $f(p_t, \eta)$ correction is introduced, as discussed below.

7.2.3. Performance of the median correction in MC

Using truth jets, it is possible to test the performance of different pile-up subtraction methods in MC. This may be done using the *relative transverse momentum offset*, O_{p_t} , which is the relative difference between the transverse momentum of truth and reconstructed calorimeter jets, respectively denoted by p_t^{truth} and p_t^{rec} . It has previously been defined in [equation \(5.10\)](#) as,

$$O_{p_t} = \frac{p_t^{\text{rec}} - p_t^{\text{truth}}}{p_t^{\text{truth}}}.$$

Truth and calorimeter jets are matched within $\Delta R_{\text{match}} = 0.5 \cdot R$ of the truth jet, where $R = 0.6$ is the size parameter of the jets. In addition, truth jets are isolated from their counterparts within $\Delta R_{\text{iso}} = 2 \cdot R$. No such isolation condition is required of reconstructed jets.

A distribution of the relative p_t offset is shown in figure 7.8 for jets within $0.2 < |\eta| < 0.4$, calibrated using ϵ_6 . A tail towards high values of O_{p_t} is observed in the first p_t bin, indicating that

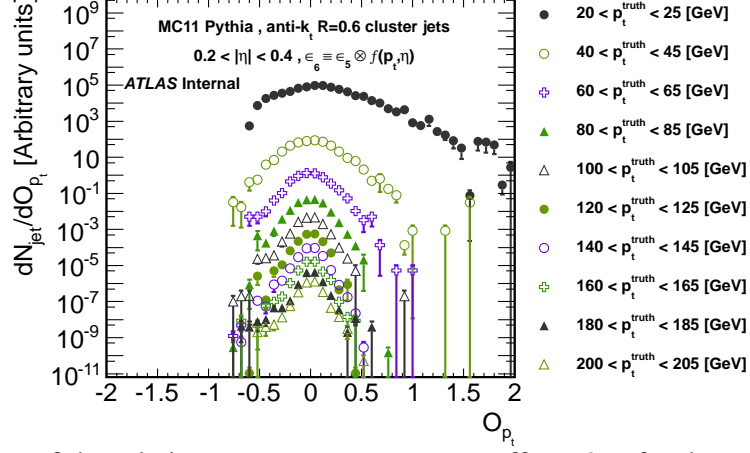


Figure 7.8. Distributions of the relative transverse momentum offset, O_{p_t} , for detector jets, calibrated using ϵ_6 , within pseudo-rapidity, $0.2 < |\eta| < 0.4$, and in several ranges of truth jet transverse momentum, p_t^{truth} , as indicated in the figure.

the low- p_t jets tend to be over-calibrated. As p_t increases, the intrinsic energy resolution improves. In addition, the fractional magnitude of the pile-up decreases as the p_t of the jet increases. As a result, the distribution of O_{p_t} becomes narrower.

The relative p_t offset is used to assess the quality of the different pile-up subtraction methods. Figure 7.9 shows the dependence of the average O_{p_t} on N_{PV} and on μ for jets within $|\eta| < 1.8$ and different p_t ranges. Two correction schemes are compared, ϵ_0 (no pile-up subtraction) and ϵ_6 (nominal correction). Jets which are not corrected for pile-up (figures 7.9a and 7.9c) show a strong N_{PV} and μ dependence. The dependence is especially strong for low- p_t jets, as the pile-up constitutes a significant percentage of the reconstructed jet p_t . Following the nominal pile-up subtraction procedure (figures 7.9b and 7.9d), most of the dependence is removed. The residual dependence on μ is stronger compared to the respective dependence on N_{PV} . Jets with $20 < p_t^{\text{truth}} < 30$ GeV exhibit a bias of ~ 150 MeV compared to higher p_t values.

In order to quantify the residual dependence following the pile-up correction, O_{p_t} is parametrized as

$$O_{p_t}(N_{PV}) = \alpha_{p_t}^{N_{PV}} + \beta_{p_t}^{N_{PV}} \cdot N_{PV} \quad \text{and} \quad O_{p_t}(\mu) = \alpha_{p_t}^{\mu} + \beta_{p_t}^{\mu} \cdot \mu. \quad (7.13)$$

The slope parameters, $\beta_{p_t}^{N_{PV}}$ and $\beta_{p_t}^{\mu}$, represent respectively the per- N_{PV} and per- μ dependence of the offset. In the case of complete pile-up subtraction, both would be zero. It is also helpful to inspect the ratio of slope parameters between that of a given correction, $\beta_{p_t}^{N_{PV}}(\epsilon_i)$, (with $i \in 1-6$) and the case where no pile-up correction is applied, $\beta_{p_t}^{N_{PV}}(\epsilon_0)$. Accordingly, the *slope ratio parameters* are defined as

$$\mathcal{R}_{\beta}^{N_{PV}} = \frac{\beta_{p_t}^{N_{PV}}(\epsilon_0) - \beta_{p_t}^{N_{PV}}(\epsilon_i)}{\beta_{p_t}^{N_{PV}}(\epsilon_0)} \quad \text{and} \quad \mathcal{R}_{\beta}^{\mu} = \frac{\beta_{p_t}^{\mu}(\epsilon_0) - \beta_{p_t}^{\mu}(\epsilon_i)}{\beta_{p_t}^{\mu}(\epsilon_0)}, \quad (7.14)$$

7. The jet area/median method for pile-up subtraction

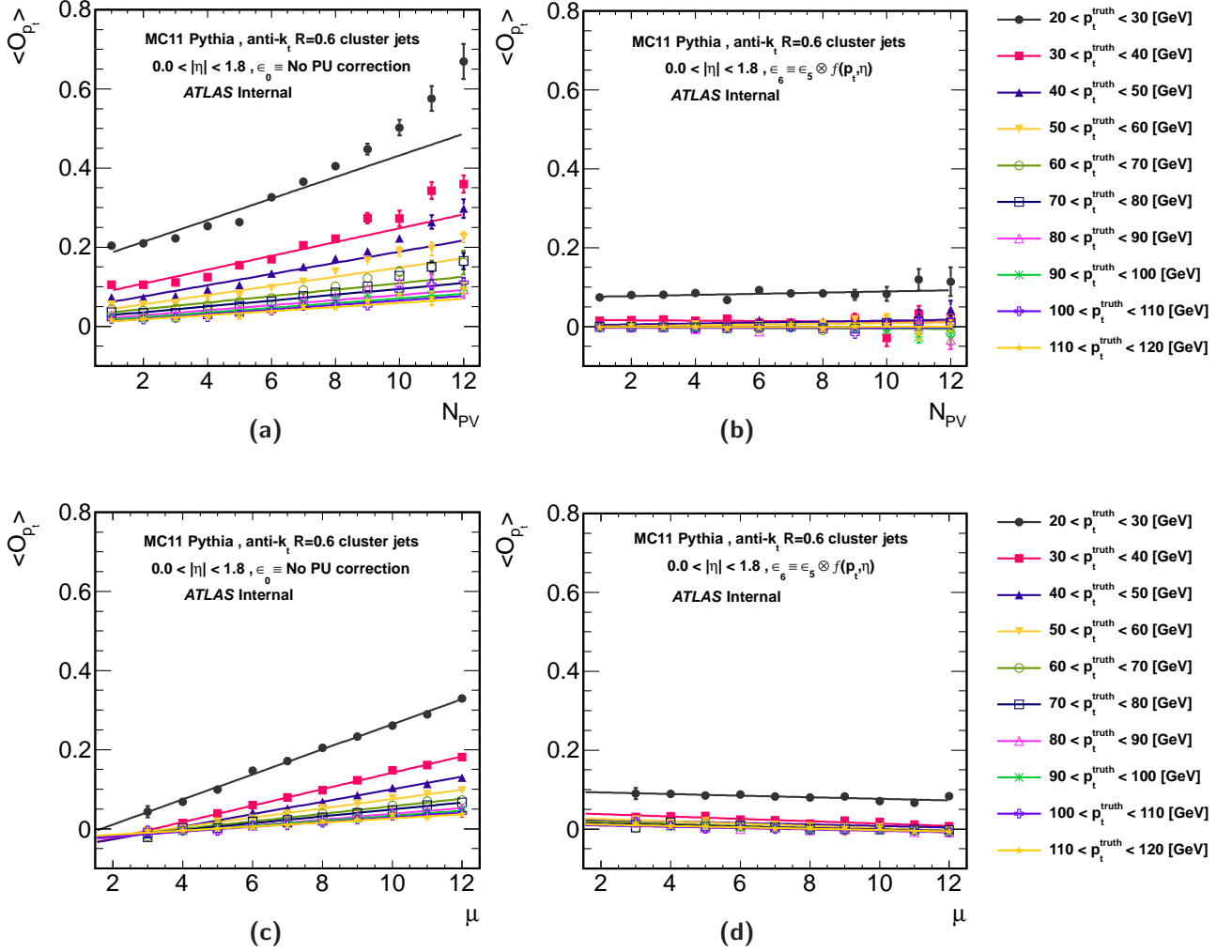


Figure 7.9. Dependence of the average relative transverse momentum offset, $\langle O_{p_t} \rangle$, on the number of reconstructed vertices, N_{PV} , ((a), (b)) and on the average number of interactions, μ , ((c), (d)), using jets with pseudo-rapidity, $|\eta| < 1.8$, corrected for pile-up with ϵ_0 or ϵ_6 , for several ranges of truth jet transverse momentum, p_t^{truth} , as indicated. The lines represent linear fits to the points.

where in the case of a perfect correction, $\mathcal{R}_\beta^{N_{PV}} = \mathcal{R}_\beta^\mu = 1$. The slope ratio parameters represent the residual fractional dependence, of the mean relative p_t offset on N_{PV} and on μ .

A linear fit is performed on the mean of O_{p_t} for the different correction methods, ϵ_0 - ϵ_6 . The values of the slope parameters from the fits are presented in figure 7.10 as a function of jet p_t for jets³ within $|\eta| < 1.8$. Additional rapidity bins are shown in section A.3, figure A.5. The fit results for $\mathcal{R}_\beta^{N_{PV}}$ and for \mathcal{R}_β^μ are presented in figure 7.11 as a function of jet p_t for jets within $|\eta| < 1.8$.

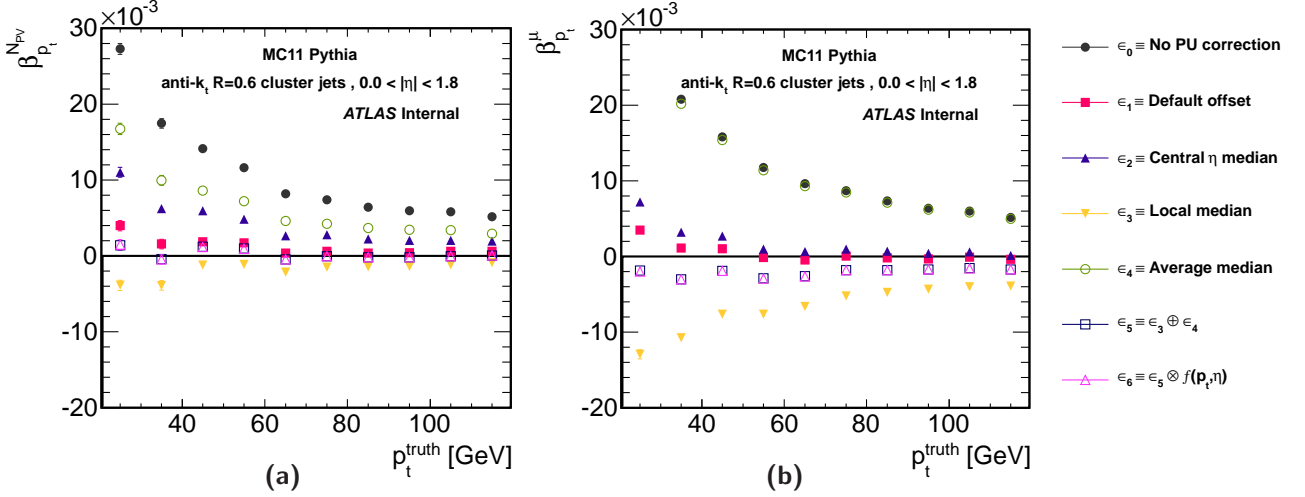


Figure 7.10. Dependence on truth jet transverse momentum, p_t^{truth} , of the parameters defined in equation (7.13), $\beta_{p_t}^{N_{PV}}$ (a) and $\beta_{p_t}^\mu$ (b), using jets with pseudo-rapidity, $|\eta| < 1.8$, corrected for pile-up with ϵ_0 - ϵ_6 , as indicated in the figures.

All correction methods tend to decrease the dependence on N_{PV} and on μ . The average correction (ϵ_4) tends to underestimate the amount of p_t . Among the event-by-event corrections, the central rapidity correction (ϵ_2) underestimates the pile-up contamination, while the local correction (ϵ_3) overestimates it. The corrections ϵ_5 and ϵ_6 , which combine the average and the local methods, achieve the best closure. The residual dependence of the latter two on N_{PV} fluctuates around zero. The respective residual dependence on μ is of the order of $2 \cdot 10^{-3}$. For reference, in absolute scale the bias in μ is of the order of $40 \text{ MeV}/\mu$ for jets with $p_t = 20 \text{ GeV}$.

As mentioned previously, the average correction does not use a reference value for μ , therefore there is no improvement between ϵ_0 and ϵ_4 in figure 7.10b. Several alternative correction methods were tested. These included a reference value in μ instead of, or in addition to, the reference value in N_{PV} . The combined residual dependence on N_{PV} and on μ was found to be greater for such configurations. The μ dependence is thus not addressed directly within the scope of the average correction. However, taking into account the combined local and average calculation of ρ , the remaining dependence on μ is negligible.

³ The first three p_t bins in figure 7.9a exhibit a strong dependence on N_{PV} , not captured by the linear fit. The respective slopes are therefore slightly underestimated. This feature is unique to ϵ_0 , and so does not affect the interpretation of the result.

7. The jet area/median method for pile-up subtraction

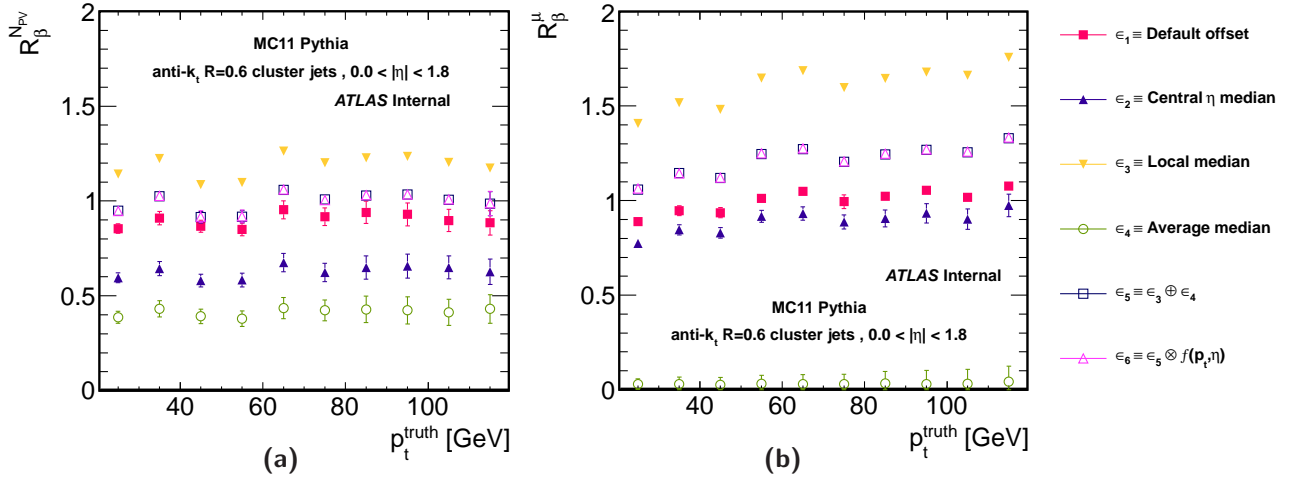


Figure 7.11. Dependence on truth jet transverse momentum, p_t^{truth} , of the parameters defined in equation (7.14), $\mathcal{R}_\beta^{N_{\text{pv}}}$ (a) and \mathcal{R}_β^μ (b), for jets with pseudo-rapidity, $|\eta| < 1.8$, corrected for pile-up with ϵ_1 - ϵ_6 , as indicated in the figures.

The dependencies of the mean of the distributions of $(O_{p_t} \times p_t^{\text{truth}})$ and of O_{p_t} on p_t are presented in figure 7.12. The former (figures 7.12a - 7.12b) are used to illustrate in absolute units the bias in p_t for the different pile-up subtraction schemes. The latter (figures 7.12c - 7.12d) illustrate the significance of the bias with regard to the p_t -scale of jets. Corrections ϵ_0 - ϵ_6 are applied for jets in two η regions. For the case of ϵ_5 , a linear fit is performed within $50 < p_t^{\text{truth}} < 250$ GeV. The results are extrapolated to higher p_t values and used to derive the JES scaling function, $f(p_t, \eta)$, (see equation (7.12)) which is used for ϵ_6 . From figure 7.13, one may compare the performance of the default offset correction, ϵ_1 , with that of the nominal median-based correction, ϵ_6 , in different η bins.

The closure using ϵ_6 is comparable to that which is achieved using ϵ_1 above 100 GeV. At low- p_t , the reach of jet reconstruction using ϵ_6 is extended down to 30 GeV and the overall performance is improved.

Another important figure of merit is the jet p_t -resolution. The resolution is estimated by the standard deviation of the distribution of the p_t offset, O_{p_t} . The standard deviation for jets which are calibrated with ϵ_0 - ϵ_6 within a limited η range is compared in figure 7.14a. Different η bins are shown in figure 7.14b, where jets are calibrated by ϵ_6 . The resolution using ϵ_6 is comparable to that which is achieved using the default offset correction (ϵ_1) across η .

7.3. Systematic checks of the median correction

7.3.1. Stability in MC for different parameters of the jet algorithm

A basic assumption of the jet area/median method to correct for pile-up the jets of the hard interaction, is that the p_t -density of accompanying jets provides a good handle on the pile-up in that event. Implicit in this assumption, is that ρ is independent of the type of jets used to calculate it. Another

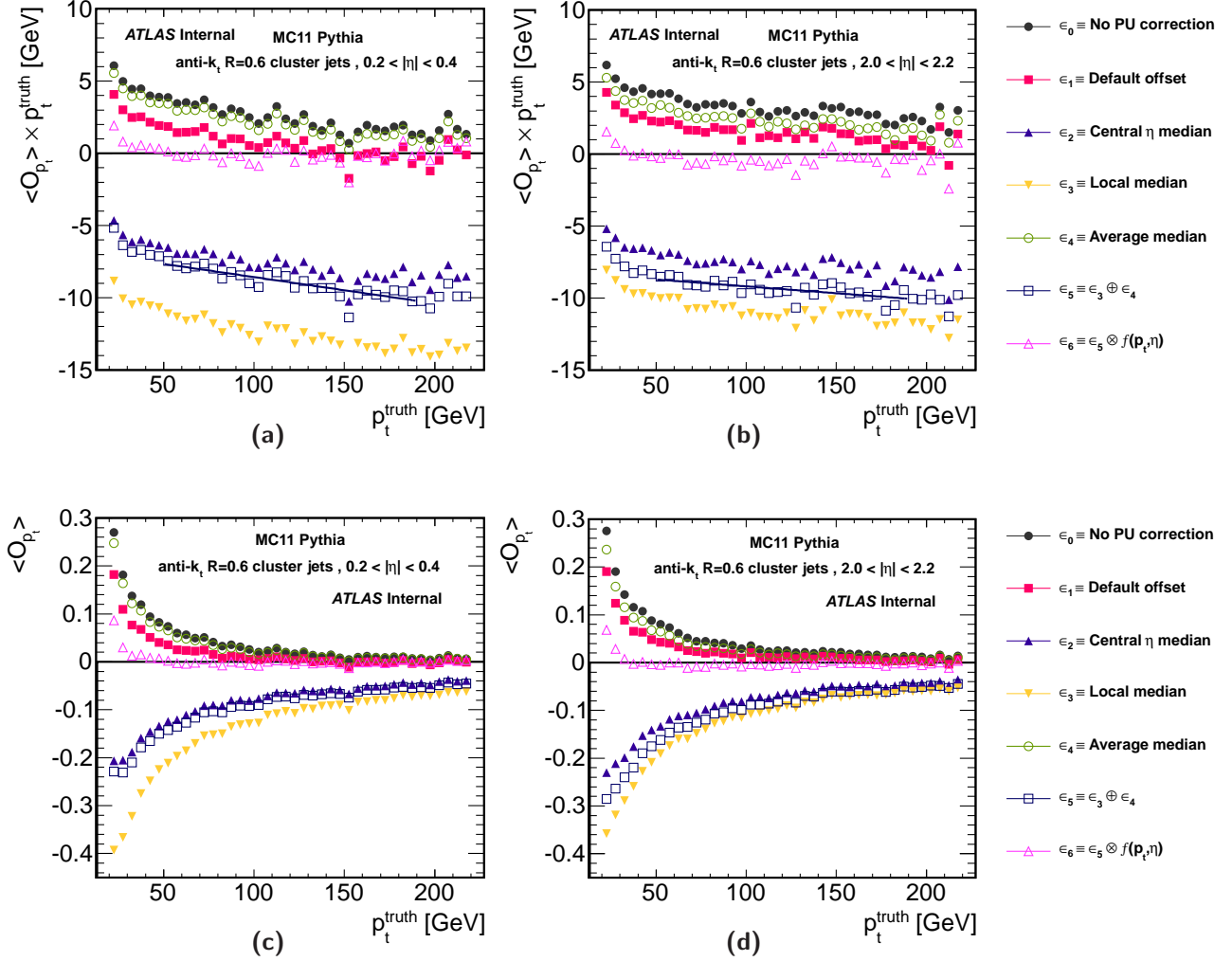


Figure 7.12. Dependence on truth jet transverse momentum, p_t^{truth} , of $\langle O_{p_t} \times p_t^{\text{truth}} \rangle$ ((a), (b)) and of $\langle O_{p_t} \rangle$ ((c), (d)), where O_{p_t} is the relative transverse momentum offset, using jets within two pseudo-rapidity, η , regions, corrected for pile-up with ϵ_0 - ϵ_6 , as indicated in the figures. The lines in (a) and (b) represent linear fits to points in ϵ_5 .

7. The jet area/median method for pile-up subtraction

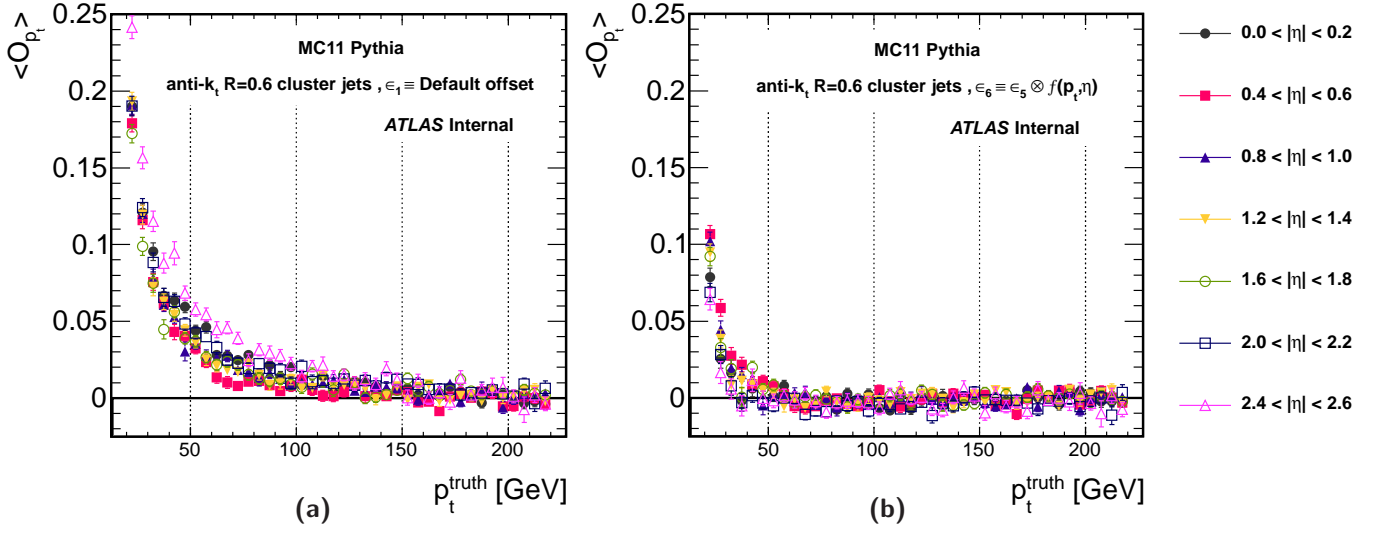


Figure 7.13. Dependence on truth jet transverse momentum, p_t^{truth} , of the mean transverse momentum offset, $\langle O_{p_t} \rangle$, for two correction methods, ϵ_1 (a) and ϵ_6 (b), for jets within several pseudo-rapidity, η , regions, as indicated in the figures.

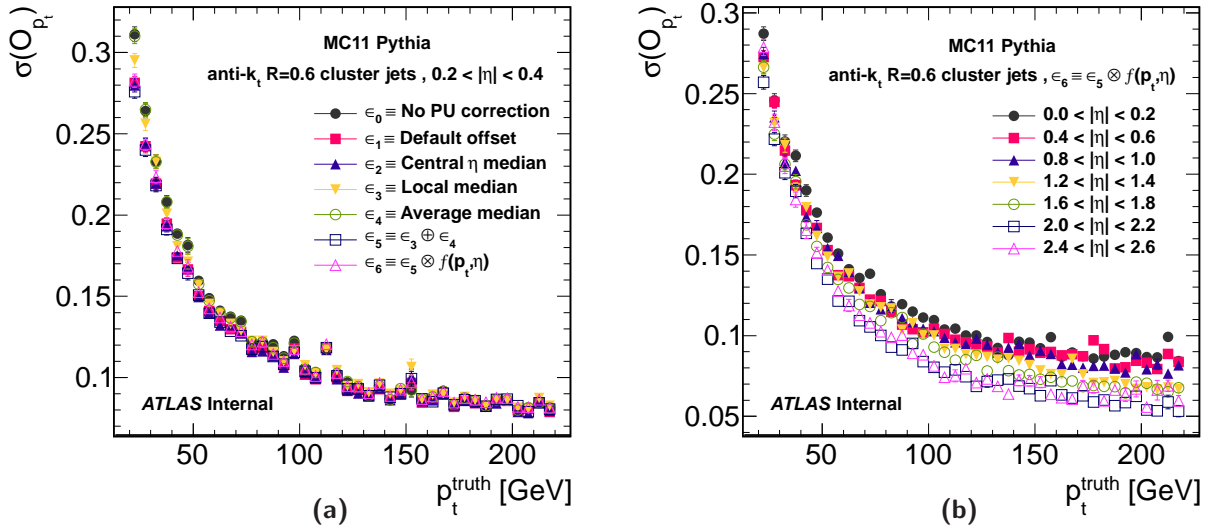


Figure 7.14. Dependence on truth jet transverse momentum, p_t^{truth} , of the standard deviation of the transverse momentum offset, $\sigma(O_{p_t})$, for jets with pseudo-rapidity, $0.2 < |\eta| < 0.4$, corrected for pile-up with ϵ_0 - ϵ_6 (a), and for jets within different η regions, corrected for pile-up with ϵ_6 (b), as indicated in the figures.

requirement of the method, is that the correction is independent of the type of hard jets. The validity of these two properties is investigated in the following.

Figures 7.15a and 7.15b respectively show the dependence of the slope parameter, $\beta_{p_t}^\mu$, (see equation (7.13)) and of the slope ratio parameter, $\mathcal{R}_\beta^{N_{PV}}$, (see equation (7.14)) on truth jet transverse momentum⁴. The median used for the pile-up correction is calculated from k_\perp jets with size parameters, $0.3 < R < 0.6$. Here, the average correction method, ε_4 , is used to subtract pile-up from anti- k_\perp jets with $R = 0.6$. A stable result, independent of R , is achieved in the range, $R > 0.2$.

Figure 7.16a illustrates the change in performance, according to the choice of algorithm used for reconstructing the jets from which ρ is calculated. The best results are achieved for the k_\perp algorithm, with slightly worse performance of the Cambridge/Aachen algorithm. A drop of roughly 10% on average is exhibited by anti- k_\perp jets in comparison, as expected. In Figure 7.16b the nominal definition of ρ (calculated from k_\perp jets with $R = 0.4$) is used. Here the local (ε_3) and the average (ε_4) pile-up correction methods are applied to correct anti- k_\perp jets with two different size parameters. The difference in performance for the different jet sizes is small.

7.3.2. Stability in data

Stability of the average median in the data is validated by comparing sub-samples of events. The following possible sources of bias are investigated:

- **dependence on the data-taking period** - the median may depend on changing conditions in the calorimeter over time (due to e.g., radiation damage and faulty electronics);
- **dependence on the trigger** - the median may depend on the p_t scale of the hard interaction in an event, which is correlated with the trigger selection;
- **dependence on the position of the bunch-crossing in the bunch train** - out-of-time pile-up depends on the history of collisions within any ~ 400 ns window; accordingly, so may the median.

Dependence on the data-taking period

In figure 7.17 the dependence of the average median, $\langle \rho \rangle$, on N_{PV} is compared between data taken in different periods, and with the average over all periods (inclusive sample). The response is very stable; no dependence on the date-taking period is observed.

Dependence on the trigger

Figure 7.18 shows the dependence of $\langle \rho \rangle$ on N_{PV} using data taken with different triggers⁵. The random trigger, EF_rd0, and the first five (ordered by trigger threshold) jet triggers, EF_J10 - EF_J40, are compared in figure 7.18a; the random trigger and an inclusive sample, consisting of all eleven jet triggers, EF_J10 - EF_J240, (see table 6.2), are compared in figure 7.18b. Data taken using the different jet triggers present a consistent response within errors; data taken with the random trigger is characterized by smaller values of $\langle \rho \rangle$ in comparison.

⁴ The following study was performed using MC10b. The values of the fit results presented, are therefore slightly different than those shown in previous sections. However, the conclusions regarding jet parameters and the subsequent performance are a feature of the correction method and hold true.

⁵ Using the two-trigger selection scheme, these refer to the triggers which are associated with the highest- p_t jet in the event.

7. The jet area/median method for pile-up subtraction

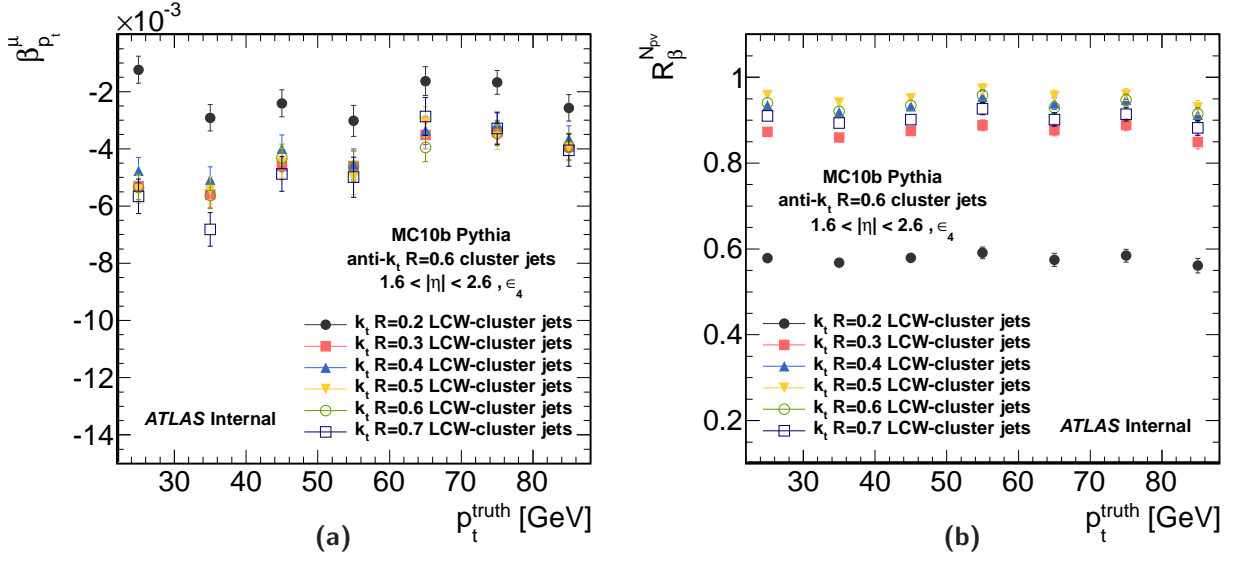


Figure 7.15. Dependence on truth jet transverse momentum, p_t^{truth} , of the parameters $\beta_{p_t}^{\mu}$ (a) and $R_{\beta}^{N_{\text{pv}}}$ (b), defined in equations (7.13) and (7.14), for jets in MC10b with size parameter, $R = 0.6$, and pseudo-rapidity, $1.6 < |\eta| < 2.6$. Jets are corrected for pile-up with ϵ_4 , which is calculated using k_{\perp} jets with different size parameters, as indicated in the figures.

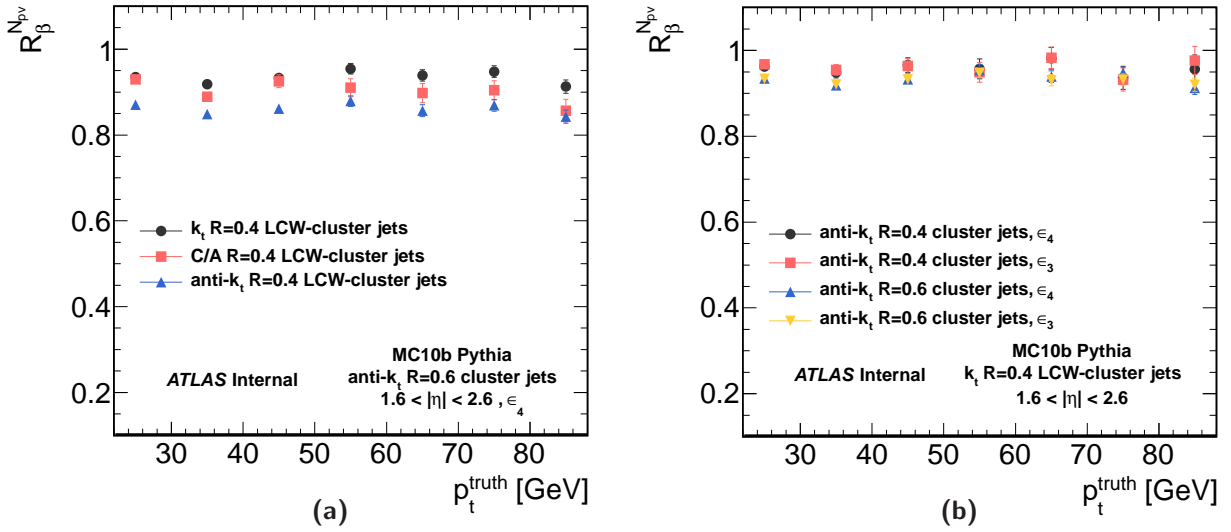


Figure 7.16. Dependence in MC10b on truth jet transverse momentum, p_t^{truth} , of the parameter $R_{\beta}^{N_{\text{pv}}}$ defined in equation (7.13).

(a) Jets of type anti- k_{\perp} with size parameter, $R = 0.6$, and pseudo-rapidity, $1.6 < |\eta| < 2.6$, are corrected for pile-up with ϵ_4 . The correction is calculated from jets which are reconstructed using different algorithms, as indicated.

(b) Jets of type anti- k_{\perp} with size parameters, $R = 0.4$ and $R = 0.6$, and pseudo-rapidity, $1.6 < |\eta| < 2.6$, are corrected for pile-up with ϵ_3 and ϵ_4 , calculated using $R = 0.4$ k_{\perp} jets (the nominal configuration of the correction), as indicated in the figure.

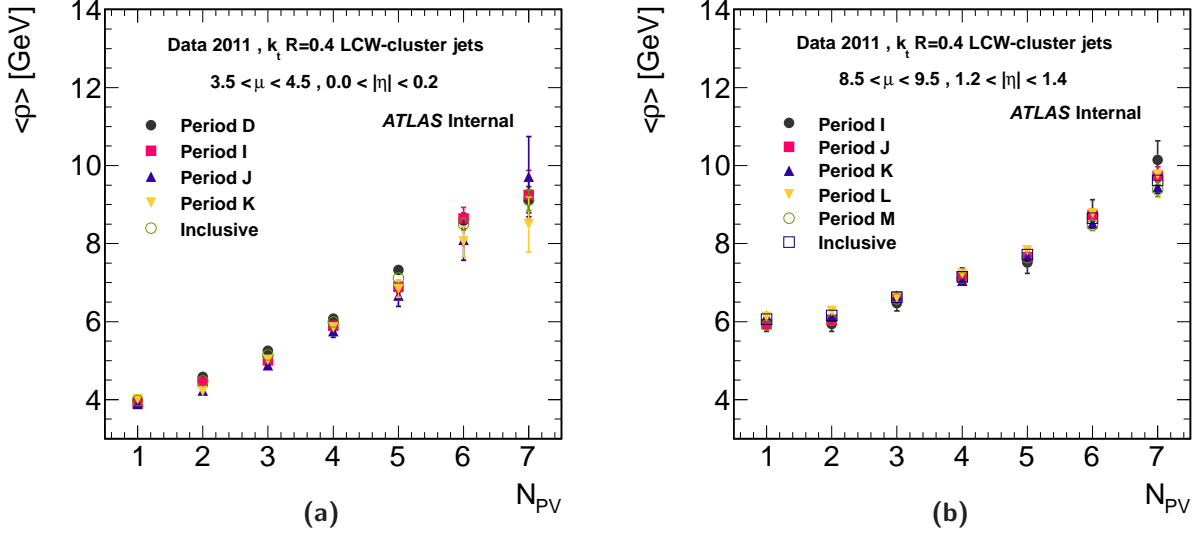


Figure 7.17. Dependence of the average median, $\langle \rho \rangle$, on the number of reconstructed vertices, N_{PV} , for jets with pseudo-rapidity, $|\eta| < 0.2$, in events with an average number of interactions, $3.5 < \mu < 4.5$ (a), and for jets with $1.2 < |\eta| < 1.4$ in events with $8.5 < \mu < 9.5$ (b). Different data-taking periods and an average over all periods (inclusive) are compared, as indicated in the figures.

The difference can be explained by the fact that events taken with the random trigger generally have lower jet multiplicity in comparison with those taken using jet triggers. This is due to the increase in underlying event activity with p_t for the low- p_t events, which are accessible by EF_r0. Beyond a certain threshold in the scale of the hard interaction (roughly 30 GeV), the energy density of the underlying event does not significantly increase [165]. The median is therefore constant on average for events picked up by the jet triggers. The averaging of ρ in a given region in η also takes into account events where no jets are reconstructed within that region ($\rho = 0$). Consequently, for the random trigger, more events with a low or a null value of the median are included in the calculation of $\langle \rho \rangle$.

In order to account for the different response between trigger streams, the average median is parametrized in data which are taken exclusively with jet triggers. A correction factor (generally between 0.6 and 1) is applied, when using this parametrization for correcting jets in random-triggered data.

Dependence on the position of the bunch-crossing in the bunch train

As discussed in section 7.1.1, the positive- and negative-energy components of out-of-time pile-up depend on the number of overlapping bunch-crossings, which are integrated in the span of calorimeter signal shaping. As a result, events at the beginning of a bunch train have different out-of-time pile-up composition compared with later events. Roughly 400 ns after the beginning of a bunch train, the typical shaping time of calorimeter elements, this dependence is expected to lessen.

In order to assess this effect, the average median is studied in events with different values of Δ_{bc} , which is defined as the amount of time separating an event from the beginning of its respective

7. The jet area/median method for pile-up subtraction

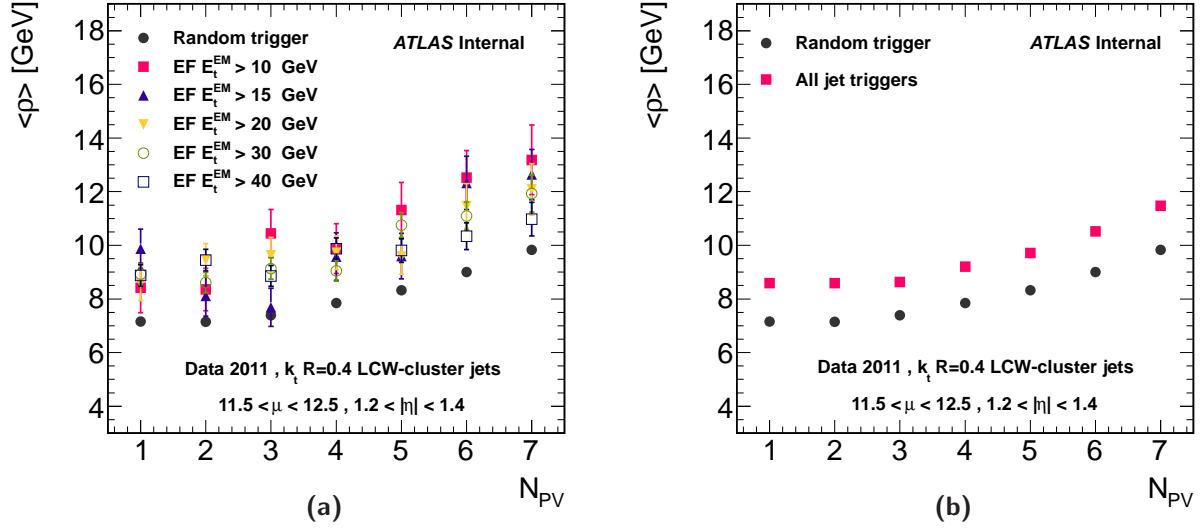


Figure 7.18. Dependence of the average median, $\langle p \rangle$, on the number of reconstructed vertices, N_{PV} , for jets with pseudo-rapidity, $1.2 < |\eta| < 1.4$, in events with an average number of interactions, $11.5 < \mu < 12.5$. Data taken with different triggers are compared, as indicated in the figures. The random trigger, EF_rd0, and the several jet triggers, EF_J10 - EF_J40, are compared in (a). The random trigger and an inclusive sample, consisting of all eleven jet triggers, EF_J10 - EF_J240, are compared in (b).

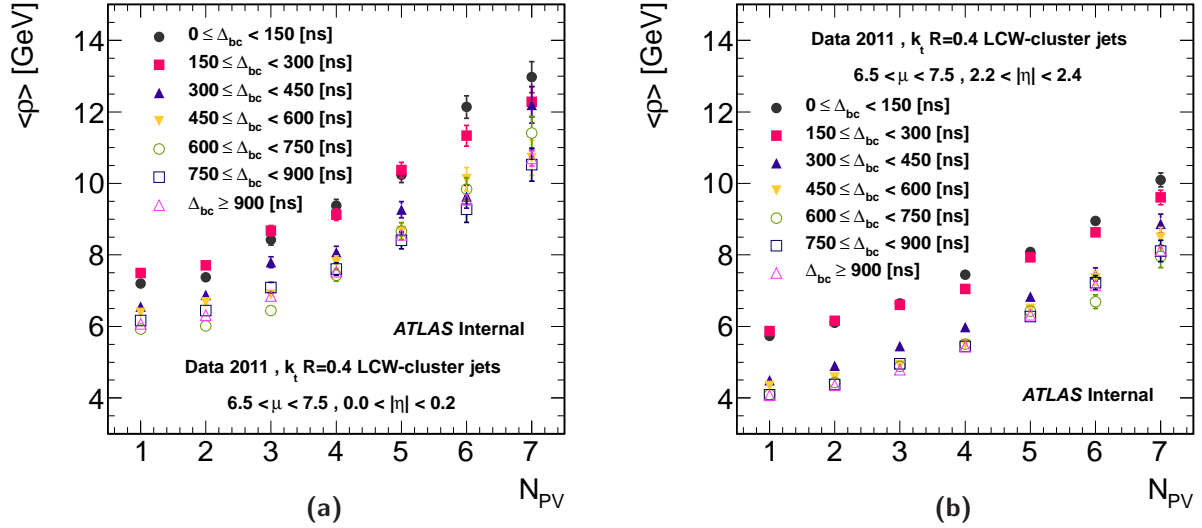


Figure 7.19. Dependence of the average median, $\langle p \rangle$, on the number of reconstructed vertices, N_{PV} , for jets with pseudo-rapidity, $|\eta| < 0.2$, (a) or with $2.2 < |\eta| < 2.4$ (b), in events with an average number of interactions, $6.5 < \mu < 7.5$, and different values of Δ_{bc} , the distance of an event from the beginning of the bunch train, as indicated in the figures.

bunch train. Several examples are shown in [figure 7.19](#). The values of ρ measured in events at the beginning of the bunch train ($\Delta_{bc} < 300$ ns) are on average higher than those which follow in time, as the negative component of the out-of-time pile-up is absent. For $\Delta_{bc} > 300$ ns the differences between Δ_{bc} classes are mostly within statistical errors. In order to account for this dependence, the average ρ is parametrized separately for events with $\Delta_{bc} < 150$, $150 < \Delta_{bc} < 300$ and $\Delta_{bc} > 300$ ns.

7.3.3. Associated systematic uncertainty of the jet energy scale

The effects of the different components of the JES uncertainties (see [section 5.5.1](#)) on the transverse momentum of jets, are estimated by introducing positive or negative variations to the energy scale of jets in the data. The variations are randomly distributed according to a Gaussian function, with the respective source of uncertainty as its width. After the energy of jets is shifted, they are re-sorted according to p_t , and the leading jet is redefined as the jet with the highest (shifted) p_t in the event. The p_t spectrum of the leading jet is remeasured. The relative changes per-bin of the p_t distribution are taken as a measure of the uncertainty. The different sources of uncertainty are individually varied, and are considered uncorrelated. The total uncertainty is thus the quadratic sum of the uncertainties derived from the different sources.

All of the components of the JES uncertainty are used in this analysis, with the exception of the in- and out-of-time pile-up components, which were derived for the default offset correction. The residual N_{PV} and μ dependencies of the median correction, expressed respectively through $\beta_{p_t}^{N_{PV}}$ and $\beta_{p_t}^\mu$ in [equation \(7.13\)](#), are used to estimate the pile-up uncertainty on the final energy scale of jets. A variation on the fully calibrated transverse momentum of jets is also performed, using the relative non-closure in MC. The latter is estimated by the average transverse momentum offset, $\langle O_{p_t} \rangle$. Any difference of $\langle O_{p_t} \rangle$ from zero indicates a bias in the final energy scale correction, $f(p_t, \eta)$, introduced in [equation \(7.12\)](#). The relative non-closure ranges between $0.2 \cdot 10^{-3}$ and $5 \cdot 10^{-3}$ for jets with $|\eta| < 2.8$. The three sources of uncertainty (variations in N_{PV} , μ and jet p_t) together make up the total systematic JES uncertainty associated with pile-up.

A breakdown of the different relative pile-up uncertainties is shown in [figure 7.20a](#) for jets with rapidity, $|\eta| < 0.3$, calibrated under ϵ_6 . The corresponding comparison of the complete set of systematic uncertainties originating from all *in-situ* sources as well as that of pile-up, is presented in [figure 7.20b](#). The relative pile-up uncertainty for jets calibrated with the nominal correction method, ϵ_6 , is compared with the respective uncertainty for jets calibrated with the default offset correction, ϵ_1 , in [figure 7.21](#).

To summarize, the total relative JES uncertainty on the p_t spectrum of the leading jet in an event is roughly 7% at $p_t < 50$ GeV. As p_t increases the uncertainty decreases down to 2%; the low uncertainty is kept up to 600 GeV, beyond which it rises up to $\sim 5\%$ in the p_t range considered. In absolute terms the uncertainty on pile-up following the median correction is roughly 1% at low transverse momenta, dropping to 0.1% for $p_t > 80$ GeV. The corresponding relative contribution of the pile-up uncertainties to the total JES uncertainty is roughly 15% at low p_t and 0.5% otherwise. The uncertainties associated with the median correction are much smaller in magnitude compared to those of the offset correction. This has to do with the fact that the median pile-up correction is completely data-driven; the offset correction on the other hand is based on MC, and has a relatively large uncertainty due to mis-modeling of the effects of pile-up on simulated jets [[141](#)].

7. The jet area/median method for pile-up subtraction

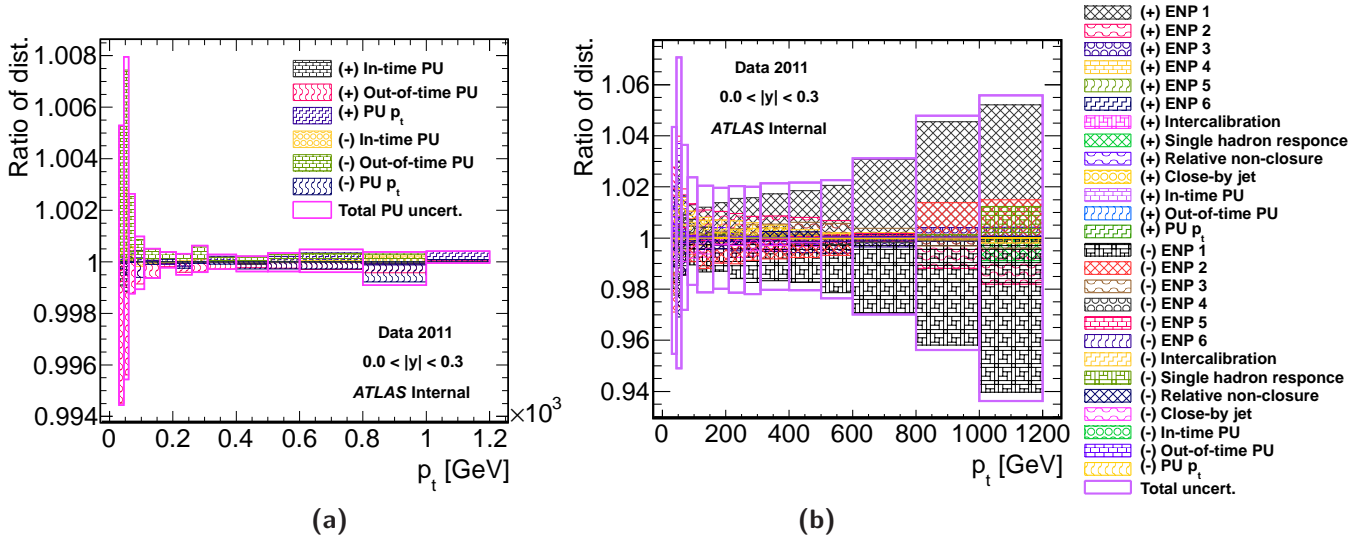


Figure 7.20. Dependence on the transverse momentum, p_t , of jets, of the ratio between the p_t distributions of jets with and without shifts of the jet energy scale (JES), for jets with rapidity, $|y| < 0.3$, corrected for pile-up with ϵ_6 in the 2011 data. Positive (+) and negative (-) shifts of the energy scale are made, as indicated in the figures.

(a) Breakdown of the systematic sources of uncertainty associated with pile-up; in-time pile-up (variations in N_{PV}), out-of-time pile-up (variations in μ) and PU p_t (variations in jet p_t due to non-closure in MC), as well as the total uncertainty from these three sources (total PU uncert.).

(b) Breakdown of all sources of uncertainty associated with the energy scale of jets, including those listed in section 5.5.1, those associated with pile-up, and the total JES systematic uncertainty (total uncert.).

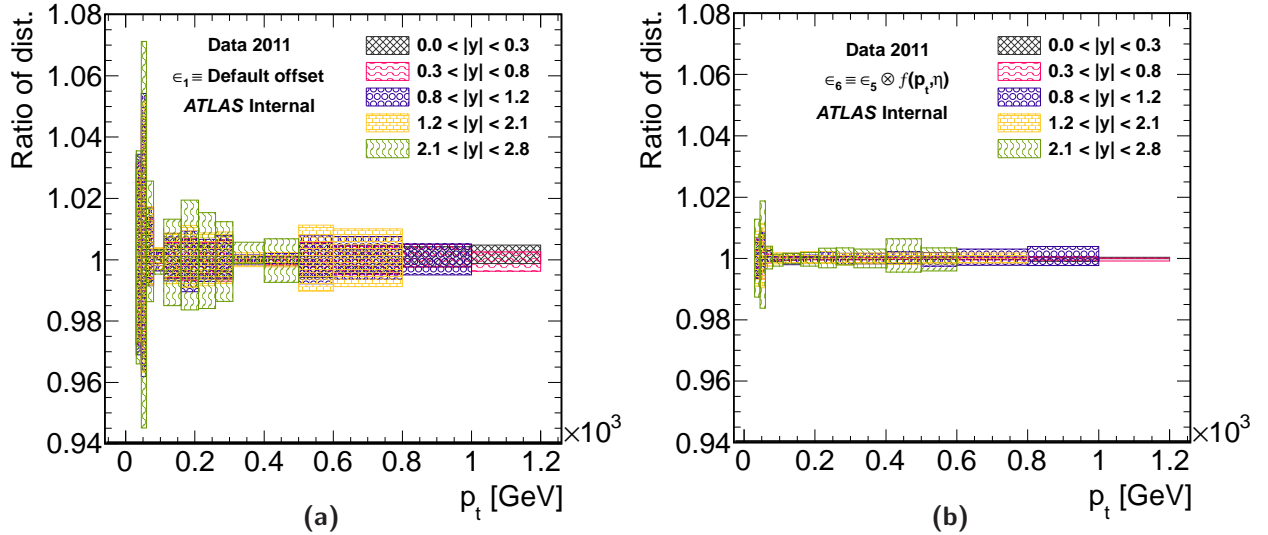


Figure 7.21. Dependence on the transverse momentum, p_t , of jets, of the ratio between the p_t distributions of jets with and without shifts of the jet energy scale associated with pile-up, for jets within different rapidity, y , regions, as indicated in the figures. Jets in the 2011 data are corrected for pile-up using the default offset correction, ϵ_1 , (a) or the nominal pile-up correction method, ϵ_6 , (b).

7.4. In-situ measurements

In order to test the performance of the median correction in data, several *in-situ* measurements are presented in the following.

7.4.1. Dijet balance

A common method to measure *in-situ* the p_t resolution of jets is the *dijet balance method*. The method is based on momentum conservation in the transverse plane. It works properly in the ideal case, in which there are two particle-level jets in an event, which are reconstructed as exactly two calorimeter-jets. Due to radiation from the hard interaction and to pile-up, one is unlikely to observe an event with exactly two jets, balanced in p_t . A p_t cut is therefore made on a possible third jet; events with exactly two jets above threshold, regardless of the number of reconstructed jets below threshold, are then defined as dijet events. The two selected jets are referred to as the leading jets in the event. In order to further enhance the signal, a restriction is also placed on the difference in azimuth between the two selected jets, $\Delta\phi_{1,2}$, such that the pair of jets is *back-to-back*,

$$\Delta\phi_{1,2} > 2.8. \quad (7.15)$$

The asymmetry between the transverse momenta of the two leading jets in a given event is defined as

$$B_{1,2} = \frac{p_{t,1} - p_{t,2}}{p_{t,1} + p_{t,2}}, \quad (7.16)$$

where $p_{t,1}$ and $p_{t,2}$ are the transverse momenta of the two jets. [Figure 7.22a](#) shows distributions of $B_{1,2}$ for jet pairs with different average transverse momenta, $\bar{p}_t = \frac{1}{2}(p_{t,1} + p_{t,2})$, where the nominal pile-up correction method, ϵ_6 , is used. As the average p_t of jet pairs increases, the asymmetry distributions become more narrow, due to the improvement in resolution.

The fitted Gaussian width of the asymmetry distribution, $\sigma(B_{1,2})$, is used to quantify the resolution. Assuming transverse momentum balance and requiring the jets to be in the same η region, the relation between $\sigma(B_{1,2})$ and the relative jet resolution is

$$\sigma(B_{1,2}) = \frac{\sqrt{(\sigma_{p_{t,1}})^2 + (\sigma_{p_{t,2}})^2}}{\langle p_{t,1} + p_{t,2} \rangle} \approx \frac{\sigma_{p_t}}{\sqrt{2}p_t}, \quad (7.17)$$

where the balance in transverse momentum implies that $\langle p_{t,1} \rangle \approx \langle p_{t,2} \rangle \equiv p_t$.

The fit results for the width of the asymmetry distribution as a function of the average momenta of the jet pairs are presented in [figure 7.22b](#). Different pile-up subtraction methods are compared, including dijet events where a third possible jet has transverse momentum, $p_t^{3\text{rd jet}} < 10$ GeV. In each case, \bar{p}_t is computed with jets which are corrected for pile-up with the same method as used for $B_{1,2}$.

Above 60 GeV in p_t , $\sigma(B_{1,2})$ is independent on the correction method. Below, $\sigma(B_{1,2})$ is smaller in magnitude for jets which are not corrected for pile-up, compared to those which are. This can be explained by the following. The pile-up subtraction decreases the energy of jets, but does not change their resolution. Accordingly, following the correction, the balance in p_t of the dijet system (the nominator in [equation \(7.17\)](#)) is unchanged, while the average (the denominator in [equation \(7.17\)](#))

7. The jet area/median method for pile-up subtraction

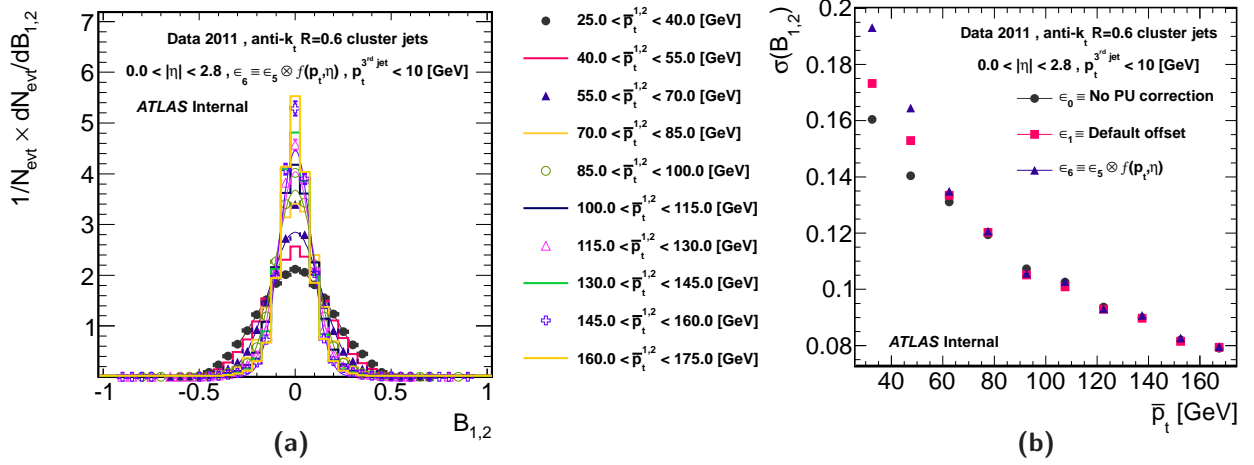


Figure 7.22. (a) Normalized distributions of the dijet asymmetry, $B_{1,2}$, for jet pairs with different average transverse momenta, \bar{p}_t , as indicated, using jets with pseudo-rapidity, $|\eta| < 2.8$, corrected for pile-up with ϵ_6 .

(b) Dependence on \bar{p}_t of the width of the $B_{1,2}$ distribution, $\sigma(B_{1,2})$, using jets with pseudo-rapidity, $|\eta| < 2.8$, corrected for pile-up with ϵ_0 , ϵ_1 or ϵ_6 , as indicated in the figure.

In both figures, a third possible jet in the event has transverse momentum, $p_t^{3\text{rd jet}} < 10$ GeV.

decreases. The value of $\sigma(B_{1,2})$ therefore increases following the pile-up correction. For larger values of \bar{p}_t , this effect becomes smaller, as the relative magnitude of the pile-up energy compared to the jet energy decreases.

In figure 7.23a the dependence of $\sigma(B_{1,2})$ on \bar{p}_t is compared for different pile-up correction schemes in data and in MC. Good agreement is observed above 60 GeV. Below, however, some differences are observed. These may be attributed to the miss-match of the p_t distributions of jets in MC compared to those in data, as observed in figure 7.23b. At low p_t , the data to MC ratio of the p_t spectrum of the leading jet is different than that of the sub-leading jets by up to 50%. The MC should reflect the physics of jet production, the performance of the detector and the pile-up conditions in the data. Correct description of the p_t distributions of the three leading jets in MC is essential, in order to reproduce both the balance in p_t between the two leading jets, and the dependence on $p_t^{3\text{rd jet}}$, observed in data. The differences in the p_t distributions, may therefore serve to explain the variance in $\sigma(B_{1,2})$ at low values of \bar{p}_t .

7.4.2. Jet p_t and dijet invariant mass spectra

In order to validate the performance of the pile-up correction, differential spectra of the transverse momentum of the leading jet, and of the invariant mass of the two leading jets, are measured for events with different numbers of reconstructed vertices.

The transverse momentum of the leading jet in an event is measured in bins of the absolute value of the rapidity of the jet, $|y|$, extending up to 2.8. The mass of the two leading jets, m_{12} , also includes jets with rapidity $|y| < 2.8$. The transverse momenta of the leading and of the sub-leading

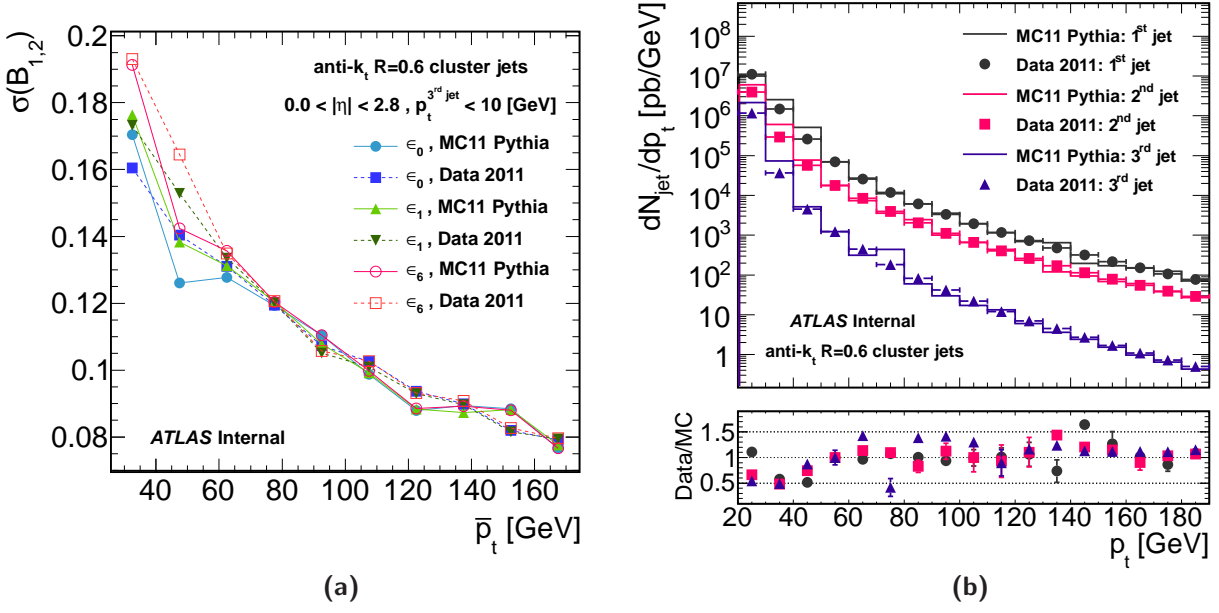


Figure 7.23. (a) Dependence on the average momenta of jet pairs, \bar{p}_t , of the width of the p_t asymmetry distribution in dijet events, $\sigma(B_{1,2})$, using jets with pseudo-rapidity, $|\eta| < 2.8$, corrected for pile-up with ϵ_0 (no pile-up subtraction), ϵ_1 (default offset correction) or ϵ_6 (the nominal pile-up correction), in data and in MC, as indicated in the figure. A third possible jet in the event has transverse momentum, $p_t^{3^{\text{rd}} \text{ jet}} < 10$ GeV. The connecting lines are intended to guide the eye.

(b) Distributions of the transverse momentum, p_t , of the three jets with the highest- p_t in an event, in data and in MC, as indicated in the figure, where the distributions in MC are rescaled such that they agree in normalization with the data at $p_t = 50$ GeV. The bottom panel shows the ratio of data to MC.

(second highest- p_t) jets in an event are respectively constrained to be, $p_{t,1} > 40$ and $p_{t,2} > 30$ GeV. Expressing the rapidities of the leading and sub-leading jets as y_1 and y_2 respectively, the rapidity of one of the outgoing partons associated with one of the jets in the two-parton center-of-mass frame is $y^* = |y_1 - y_2|/2$.

Luminosity in this study is calculated, as described in section 6.2.3, using a two-trigger selection procedure. Accordingly, luminosity classes are defined by the p_t and rapidity of the two leading jets in an event. The vertex distribution and trigger prescales are correlated, as prescale factors were modified with the increase in luminosity during data taking. Accordingly, the baseline luminosity classes are modified to account for event samples with any given value of N_{PV} ⁶.

The p_t spectrum of the leading jet within $|y| < 0.3$ and the dijet mass spectrum for $y^* < 0.5$ are shown in figure 7.24 for events with fixed values of N_{PV} . In order to quantify the performance of the pile-up correction, the standard deviation with regard to single-vertex events, $\sigma(N_{\text{PV}})$, is calculated. This is done by using the distributions with $N_{\text{PV}} = 1$ as reference, and calculating bin-by-bin the

⁶ This is done by extracting the probability for an event to have a given number of reconstructed vertices for each trigger bin; a trigger bin refers to the classification of an event according to the triggers associated with the two leading jets.

7. The jet area/median method for pile-up subtraction

differences with regard to respective multi-vertex ($N_{PV} > 1$) events,

$$\sigma(N_{PV}) = \sqrt{\frac{1}{n_{N_{PV}} - 1} \sum_{i=2}^{n_{N_{PV}}} (b_1 - b_i)^2}. \quad (7.18)$$

Here $n_{N_{PV}}$ represents the maximal number of reconstructed vertices, and b_i stands for the bin content of a given distribution, which has $N_{PV} = i$ reconstructed vertices.

Results for $\sigma(N_{PV})$ are given in [figure 7.25](#) for the first y and y^* bins of the respective p_t and mass spectra. Additional rapidity and y^* bins are shown in [section A.3, figures A.6 - A.7](#). As expected, both the offset correction (ϵ_1) and the median pile-up correction (ϵ_6) decrease the dependence on N_{PV} , expressed through smaller values of $\sigma(N_{PV})$. As p_t and m_{12} increase, the relative effect of pile-up decreases and so the N_{PV} dependence lessens. Some residual statistical fluctuations remain, generally of the order of 2% for $p_t > 300$ GeV and $m_{12} > 600$ GeV. The median correction (ϵ_6) generally performs better than the default offset correction (ϵ_1) at low p_t and mass. At respective higher values the performance is comparable between the two methods. Similar behaviour is observed for higher rapidities, though the magnitude of the fluctuations at high transverse momenta and masses are larger due to insufficient statistics.

7.5. Summary of the performance of the median pile-up correction

The jet area/median method is used to devise a data-driven pile-up subtraction scheme. The method combines parametrization of the average pile-up contribution to jets, as well as event-by-event estimates of the local pile-up p_t -density around a given jet. The correction is used to subtract pile-up from jets with $p_t > 30$ GeV and $|\eta| < 2.8$ in data taken during 2011.

Several performance tests are conducted using simulated events. The residual N_{PV} dependence of the p_t of jets following the correction is shown to be insignificant. The corresponding μ dependence is of the order of $0.2\%/\mu$ for low- p_t jets. The p_t dependence is likewise insignificant within this kinematic range, achieving p_t -closer better than 0.1% on average at 30 GeV. This extends the reach of the standard pile-up correction in ATLAS, the offset correction, for which the relative bias in p_t becomes negligible (roughly 0.2%) at 60 GeV. The p_t resolution is unchanged with regard to that achieved using the offset correction. The median method is shown to be robust under changes of jet algorithm and size parameter.

In data, the median correction is parametrized separately under different restrictions. These account for different p_t scales of jets which undergo the calibration, as well as for different restrictions on the history of previous collisions. The pile-up uncertainty on the jet energy scale following the median correction is estimated in data, and found to be smaller than the corresponding uncertainty for the offset correction.

In-situ measurements are performed of the p_t balance of dijets, where good agreement is observed between data and MC. Measurements are also made of the p_t spectra of jets in different rapidity regions and of the differential dijet mass spectra in different y^* bins. Following the median correction, the dependence on N_{PV} is shown to be alleviated with regard to events which are not corrected for pile-up; the achieved performance is on a par with or better than that of the offset correction.

The median method is used for pile-up subtraction in the dijet differential cross section measurement, which is the subject of the next chapter.

7.5. Summary of the performance of the median pile-up correction

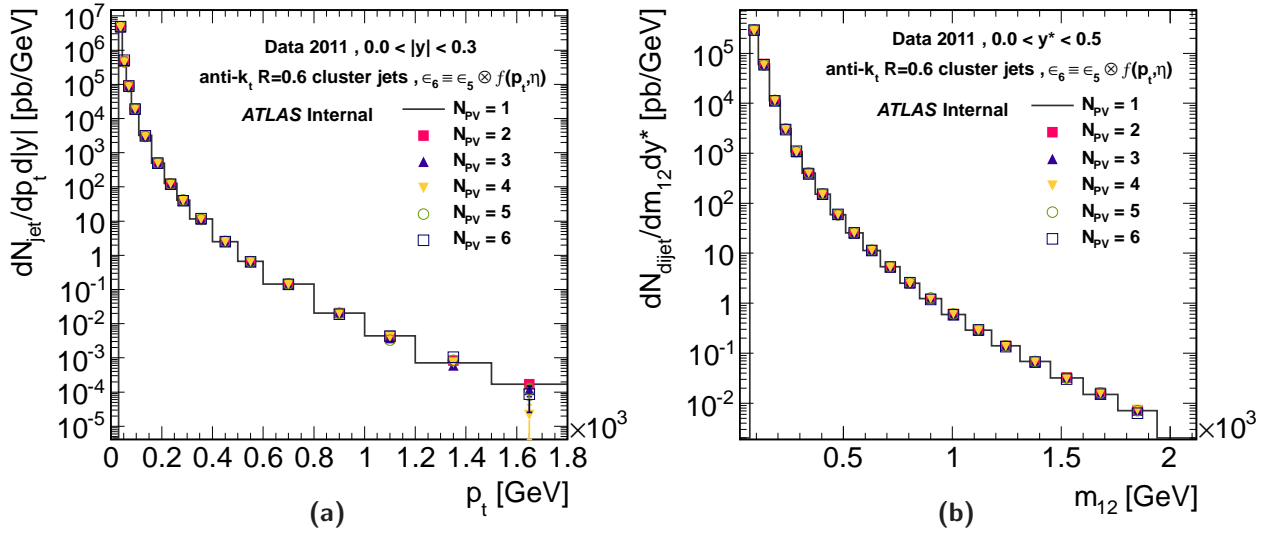


Figure 7.24. (a) Differential transverse momentum, p_t , spectra of the highest- p_t jet in an event, using jets with rapidity, $|y| < 0.3$.

(b) Differential spectra of the invariant mass distribution, m_{12} , of the two highest- p_t jets in an event, for center-of-mass jet rapidity, $y^* < 0.5$.

In both figures jets are calibrated using the nominal pile-up subtraction method, ϵ_6 , and events have a fixed number of reconstructed vertices, N_{PV} , as indicated.

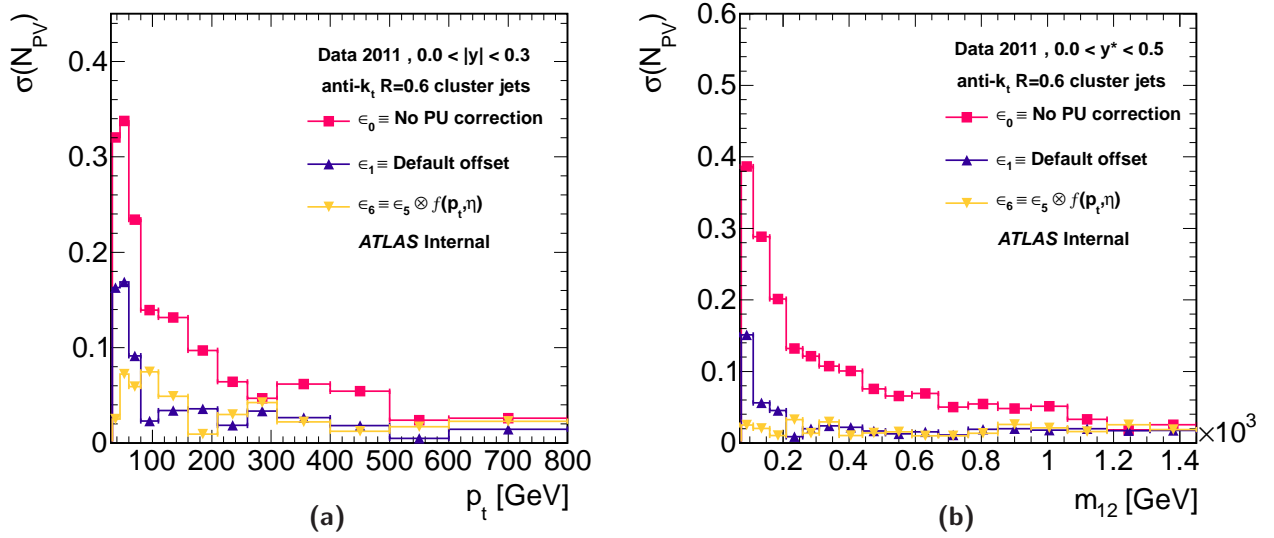


Figure 7.25. The standard deviation with regard to single-vertex events, $\sigma(N_{PV})$, (see [equation \(7.18\)](#)) for two observables, the differential transverse momentum, p_t , spectrum of the highest- p_t jet in an event, using jets with rapidity, $|y| < 0.3$, (a) and the differential mass, m_{12} , spectrum of the two highest- p_t jets in an event, for center-of-mass jet rapidity, $y^* < 0.5$ (b). Distributions for jets reconstructed with several pile-up correction schemes (ϵ_0 , ϵ_1 and ϵ_6) are compared, as indicated in the figures.

8. Dijet mass distribution

8.1. Cross section definition

The dijet cross section is defined using anti- k_{\perp} jets with size parameter, $R = 0.6$. The measurement is corrected for all experimental effects, and thus is defined for the particle-level final state of a pp collision [134]. The cross section is measured as a function of the invariant mass of the leading (highest p_t) and sub-leading (second highest- p_t) jets; the mass is defined as $m_{12} = \sqrt{(E_1 + E_2)^2 - (\vec{p}_1 + \vec{p}_2)^2}$, where E_1 and E_2 (\vec{p}_1 and \vec{p}_2) are the energies (momenta) of the leading and sub-leading jets respectively. The rapidities of the two leading jets are similarly defined as y_1 and y_2 . The cross section is binned in the variable, $y^* = |y_1 - y_2|/2$. For massless partons, y^* is determined by the polar scattering angle, θ^* , in the center-of-mass moving along the beamline,

$$y^* = \frac{1}{2} \ln \left(\frac{1 + |\cos \theta^*|}{1 - |\cos \theta^*|} \right). \quad (8.1)$$

It stands for the rapidity of one of the outgoing partons in the two-parton center-of-mass frame.

The following phase-space regions are used to define the cross section measurement for data taken during 2010 and during 2011:

$$\begin{aligned} (2010) \quad & p_{t,1} > 30 \text{ GeV}, \quad p_{t,2} > 20 \text{ GeV}, \quad |y_{1,2}| < 4.4, \\ (2011) \quad & p_{t,1} > 40 \text{ GeV}, \quad p_{t,2} > 30 \text{ GeV}, \quad |y_{1,2}| < 2.8, \end{aligned} \quad (8.2)$$

where $p_{t,1}$ and $p_{t,2}$ are the transverse momenta of the leading and sub-leading jets respectively. Requiring the leading jet to have p_t higher than that of the sub-leading jet improves the stability of the NLO calculation [166]. Due to the increase in pile-up in 2011 compared to 2010, both the rapidity coverage and the p_t coverage are more restricted in 2011.

In leading order (LO) approximation, the fractions of the proton momenta carried by the interacting partons, x , can be reconstructed from the two outgoing jets. The momentum fraction of the two interacting partons, denoted by (+) or (−), can be estimated as

$$x_{\pm} = \frac{1}{\sqrt{s}} (E_{t,1} e^{\pm \eta_1} + E_{t,2} e^{\pm \eta_2}), \quad (8.3)$$

where the center-of-mass energy of the collision is $\sqrt{s} = 7 \text{ TeV}$, and $E_{t,i}$ and η_i respectively stand for the transverse energy and pseudo-rapidity of jet i . The momentum transfer of the interaction, Q , is usually taken as the mass of the dijet system.

The (x, Q^2) kinematic plane for the 2010 and 2011 datasets is presented in figure 8.1. The results are equivalent for the momentum fractions of the two partons, and so only x_+ is shown. The data included in the figure are not corrected for detector effects, other than the JES calibration of jets.

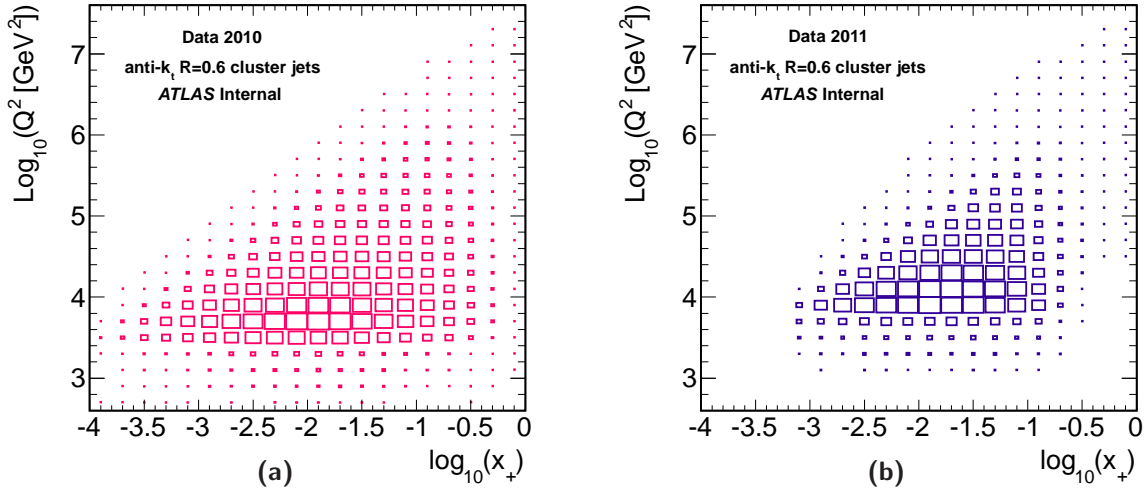


Figure 8.1. The (x, Q^2) kinematic plane for the dijet mass measurement, where x denotes (to leading order) the fraction of the momentum of the proton carried by an interacting parton, and Q^2 stands for the momentum transfer of the interaction. Shown are data collected during 2010 (a) and during 2011 (b) within the corresponding phase-space regions, as detailed in equation (9.14). Box sizes in the figures indicate the relative number of entries in a given bin, compared to other bins in the same figure.

The measurements cover masses from 70 GeV up to several TeV, and probe proton momentum fractions from 10^{-4} up to about 1. The 2010 dataset reaches lower values of x due to the extended range in rapidity and p_t .

8.2. Theoretical Predictions

The measured jet cross section is compared to fixed-order NLO pQCD predictions, which are corrected for non-perturbative effects. Theory calculations are performed in the same kinematic range as the measurement in data.

8.2.1. NLO calculation

The NLOJET++ (version 4.1.2) package [65] is used with the CT10 NLO parton distribution functions [167]. The same value, which corresponds to the transverse momentum of the leading jet, $p_{t,1}$, is used for the normalisation and factorisation scales, respectively denoted by μ_R and μ_F . The forward dijet cross section in NLOJET++ is numerically stable if instead of a scale fixed entirely by p_t , a scale that depends on the rapidity separation between the two jets is used¹. The values chosen for each bin in y^* follow the formula,

$$\mu = \mu_R = \mu_F = p_t e^{0.3y^*}, \quad (8.4)$$

¹If a scale fixed with jet p_t is used, NLOJET++ predicts an unstable or even negative cross section for large ($\gtrsim 3$) rapidity separations between the two jets.

8. Dijet mass distribution

which is illustrated in [figure 8.2](#). This choice is motivated by the formula,

$$\mu = \mu_R = \mu_F = \frac{m_{12}}{2 \cosh(0.7y^*)}, \quad (8.5)$$

that is suggested in [\[168\]](#).

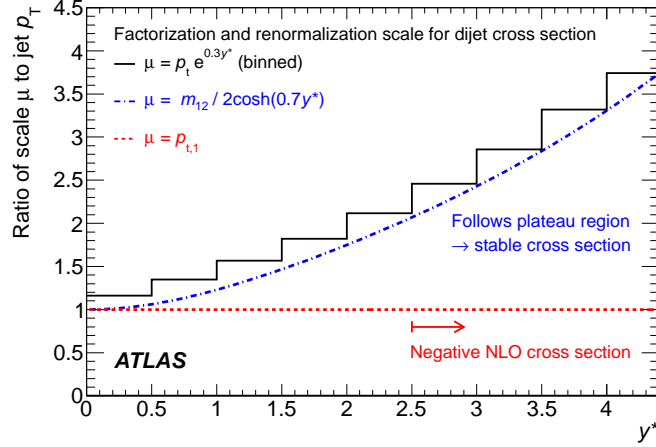


Figure 8.2. Ratio of the renormalisation and factorisation scale, μ , to the jet transverse momentum, p_T , used for the dijet predictions obtained with NLOJET++, as a function of center-of-mass jet rapidity, y^* , using several scale parametrizations; the chosen parametrization, given in [equation \(8.4\)](#) (full black line); the formula ([equation \(8.5\)](#)) suggested in [\[168\]](#) (dashed blue line); and a fixed scale proportional to the transverse momentum of the leading jet, $p_{t,1}$ (dashed red line). (Figure taken from [\[156\]](#).)

8.2.2. Non-perturbative corrections

The fixed-order NLO calculations predict parton-level cross sections, which must be corrected for non-perturbative effects in order to be compared with data. This is done by using leading-logarithmic parton shower generators. Several combinations of generators, PDF sets, and underlying event tunes are used (see [section 4.1](#)). The corrections are derived with

- PYTHIA 6.425 [\[89\]](#) with the MRST LO* [\[7\]](#) PDF set and the AUET2B [\[94\]](#) tune,

referred to as the nominal simulation setup in the following. Additional configurations are,

- PYTHIA 6.425 with the CTEQ6L1 [\[8\]](#) PDF set and the AUET2B and AMBT2B [\[94\]](#) tunes;
- PYTHIA 8 (v150) [\[95\]](#) with the MRST LO** PDF set and 4C [\[96\]](#) tune; and
- HERWIG++ [\[102\]](#) (v2.5.1) with the MRST LO* and the CTEQ6L1 PDF sets and the UE7000-3 [\[94\]](#) tune.

The hadron-level cross section is computed in simulation samples where hadronization and the underlying event are switched on, $\sigma_{(+\text{HU})}$, or off, $\sigma_{(-\text{HU})}$. The bin-wise ratio of cross sections,

$$\mathcal{R}_{\text{HU}}(m_{12}, y^*) = \frac{\sigma_{(+\text{HU})}(m_{12}, y^*)}{\sigma_{(-\text{HU})}(m_{12}, y^*)}, \quad (8.6)$$

is computed for each such configuration as a function of m_{12} and y^* . The non-perturbative correction factors are taken as the values of a functional fit to the ratio of cross sections in the nominal setup. The correction factors take the parton-level cross section, σ_{part} , to the hadron-level cross section, σ_{had} ,

$$\sigma_{\text{had}}(m_{12}, y^*) = \mathcal{R}_{\text{HU}}(m_{12}, y^*) \times \sigma_{\text{part}}(m_{12}, y^*). \quad (8.7)$$

Figure 8.3 shows the correction factors, \mathcal{R}_{HU} , for a single y^* bin for the 2010 and the 2011 phase-space definitions of the cross section. The lines represent fits to the different MC samples.

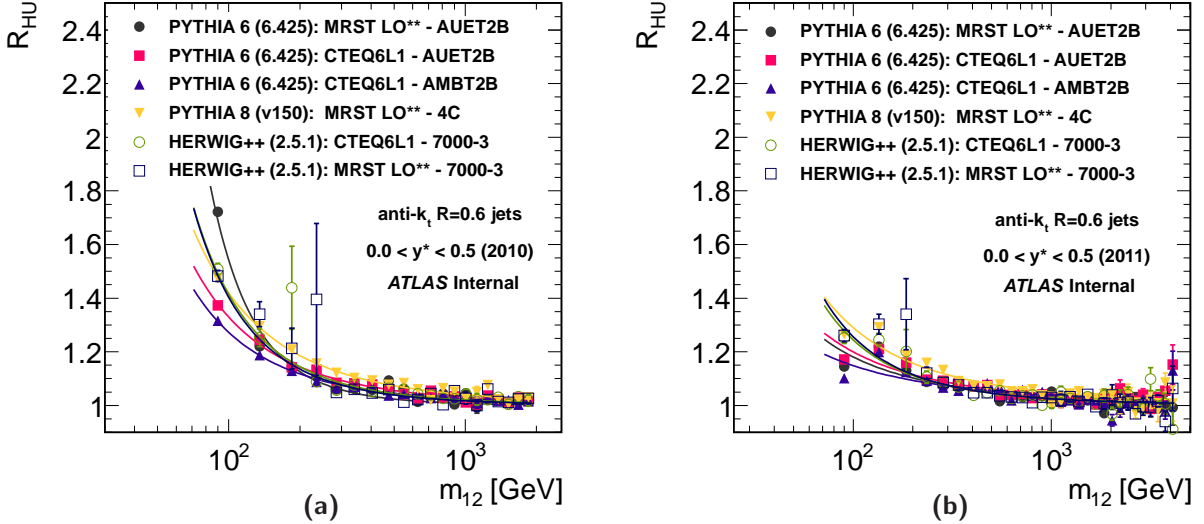


Figure 8.3. Non-perturbative correction factors, \mathcal{R}_{HU} , as a function of the invariant mass, m_{12} , of the two jets with the highest transverse momentum in an event, for center-of-mass jet rapidity, $y^* < 0.5$, for several combinations of generators, PDF sets, and underlying event tunes, as indicated in the figure and explained in the text. The lines represent fits to the various MC samples, using the 2010 (a) and the 2011 (b) phase-space definitions of the measurement.

Additional y^* bins using the 2011 phase-space definition are shown in [section A.4](#), [figure A.8](#). Similar values of \mathcal{R}_{HU} (not shown) were found for the 2010 measurement. The correction factors have a significant influence (up to 80%) at low dijet mass.

The uncertainty on the non-perturbative correction is taken as the spread of the fit results for the various MCs, compared to the nominal setup. Additional sources of uncertainty on the theoretical prediction are discussed in the following.

8.2.3. Uncertainties on the NLO prediction

In addition to the uncertainty associated with the hadronization and UE corrections, the main uncertainties on the NLO prediction come from several sources; the uncertainties on the PDFs; the choice of factorisation and renormalization scales; and the uncertainty on the value of the strong coupling constant, α_s . To allow for fast and flexible evaluation of PDF and scale uncertainties, the APPLGR [169] software was interfaced with NLOJET++ in order to calculate the perturbative coefficients once and store them in a look-up table. The PDF uncertainties are defined at 68% CL and evaluated following the prescriptions given for each PDF set. These account for the experimental uncertainties, tension between input data sets, parametrisation uncertainties, and various theoretical uncertainties related to PDF determination.

To estimate the uncertainty on the NLO prediction due to neglected higher-order terms, each observable was recalculated while varying the renormalization scale by a factor of two with respect to the default choice. Similarly, to estimate the sensitivity to the choice of scale where the PDF evolution is separated from the matrix element, the factorisation scale was separately varied by a factor of two. Cases where the two scales are simultaneously varied by a factor 2 in opposite directions were not considered due to the presence of logarithmic factors in the theory calculation that become large in these configurations. The envelope of the variation of the observables was taken as a systematic uncertainty.

The effect of the uncertainty on the value of the strong coupling constant, α_s , is evaluated following the recommendation of the CTEQ group [170], in particular by using different PDF sets that were derived using the positive and negative variations of the coupling from its best estimate. Electroweak corrections were not included in the theory predictions [171].

The total relative uncertainty on the NLO prediction and the breakdown to its components is shown in figure 8.4 for a single y^* bin, using the 2010 and the 2011 phase-space definitions of the cross section. Additional y^* bins of the measurement are shown in section A.4, figures A.9 - A.11. The uncertainty on the hadronization and UE corrections dominates at low values of m_{12} , while at high masses the uncertainty associated with the PDFs is most prominent. For intermediate mass values (roughly between 0.5 and 1 TeV) the total uncertainty is smaller than 10% in all y^* bins.

8.3. Bias and resolution in the invariant mass

The offset in y^* , O_{y^*} , and in m_{12} , $O_{m_{12}}$, of the dijet system are defined as

$$O_{y^*} = y^{*\text{rec}} - y^{*\text{truth}} \quad \text{and} \quad O_{m_{12}} = \frac{m_{12}^{\text{rec}} - m_{12}^{\text{truth}}}{m_{12}^{\text{truth}}}, \quad (8.8)$$

where $y^{*\text{truth}}$ (m_{12}^{truth}) and $y^{*\text{rec}}$ (m_{12}^{rec}) are the y^* (invariant mass) of the dijet system, determined at the hadron-level and at the detector-level, respectively. The two parameters respectively represent the bias in the rapidity and the fractional bias in the mass of the dijet system. The width of the distributions of O_{y^*} and $O_{m_{12}}$ represent the corresponding resolution of the two parameters, denoted as $\sigma(O_{y^*})$ and $\sigma(O_{m_{12}})$. The parameters are determined in MC by selecting the two leading jets at the hadron and at the detector levels in a given event, without requiring exact matching between the jets.

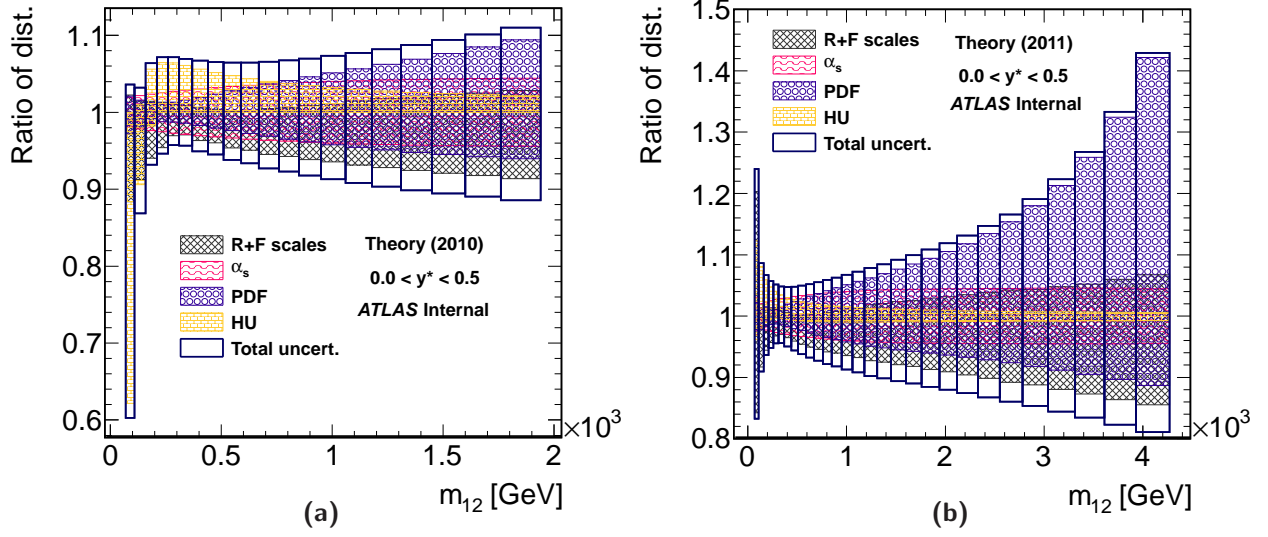


Figure 8.4. The ratio of NLOJET++ expectations obtained under different assumptions relative to the nominal calculation, as a function of the invariant mass, m_{12} , of the two highest- p_t hadron-level jets with center-of-mass rapidity, $y^* < 0.5$, for the 2010 (a) and for the 2011 (b) measurements. The variations on the nominal expectation include the uncertainty on the renormalization and factorisation scales (R+F scales), the uncertainty on the value of the strong coupling constant (α_s), use of different parton density functions (PDF), the uncertainty on the hadronization and UE corrections (HU) and the total uncertainty on all the latter (total uncert.).

The average O_{y^*} , the average $O_{m_{12}}$ and the corresponding resolution parameters are calculated in MC10 and in MC11 for dijet systems with different y^* values. Figures 8.5 - 8.6 show the dependence of the parameters on m_{12}^{truth} . The y^* offset is generally smaller in magnitude than 2%, decreasing as m_{12} increases. For mass values above ~ 200 GeV, O_{y^*} is mostly consistent with zero. Similar behaviour is exhibited in MC10 and in MC11. The resolution, $\sigma(O_{y^*})$, decreases with m_{12} from about 3% at low masses to below 1.5% above 600 GeV.

For dijet systems with $y^* < 2.5$, the mass offset, $O_{m_{12}}$, is typically smaller than 30% in 2010 and 10% in 2011. The exception is the low mass region (up to 100 GeV) in 2011, for which a bias of up to 40% is observed. For the last two bins in y^* in 2010, a slightly larger offset of up to 50% in absolute value is observed, decreasing with increasing m_{12} . The degraded performance at high y^* in 2010 and at low mass in 2011 is due to pile-up; the latter is dominant for jets in the forward region (which populate the high y^* bins in 2010), as well as for low energy jets (which comprise low dijet masses in 2011).

The relative dijet mass resolution, $\sigma(O_{m_{12}})$, decreases as m_{12} increases. This trend extends up to roughly 500 GeV for low values of y^* or to 1 – 1.5 TeV for high values of y^* . At high mass values the resolution is typically constant, consistent with the expected behaviour of the energy resolution of jets, also seen in chapter 5, figure 5.6. In general, $\sigma(O_{m_{12}})$ decreases from 10% to 4% in 2010 and from 13% to 3% in 2011. Comparable resolution is observed for low y^* and low mass as for dijets with higher y^* and higher mass. The reason for this is that for a given average p_t of the two jets, higher values of y^* are associated with higher dijet masses.

8. Dijet mass distribution

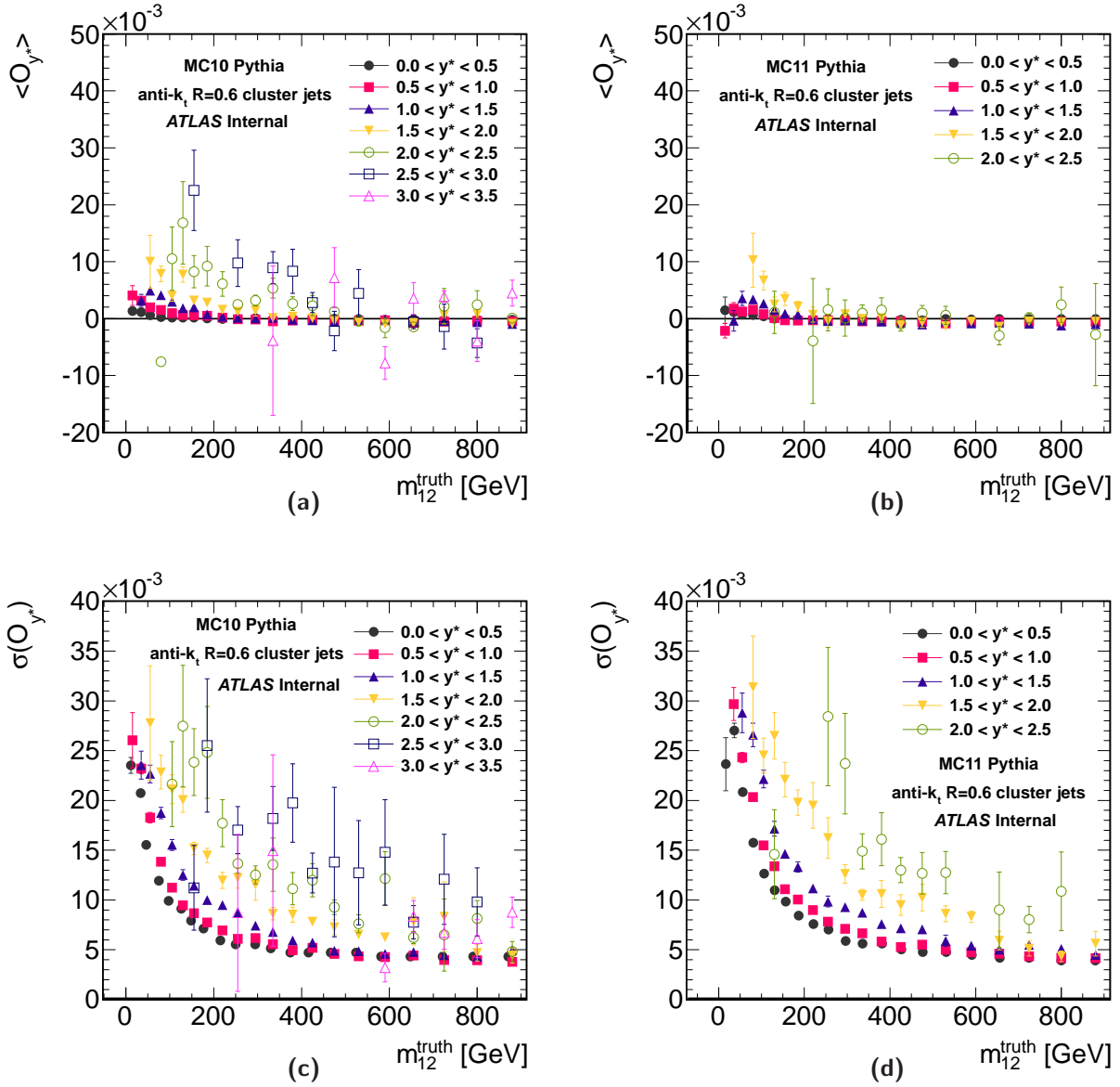


Figure 8.5. Dependence of the average rapidity offset, $\langle O_{y^*} \rangle$, ((a) and (b)) and of the width of the distribution of the offset, $\sigma(O_{y^*})$, ((c) and (d)) on the invariant mass, m_{12} , of the two jets with the highest transverse momentum in an event, for different center-of-mass jet rapidities, y^* , in MC10 and in MC11, as indicated in the figures.

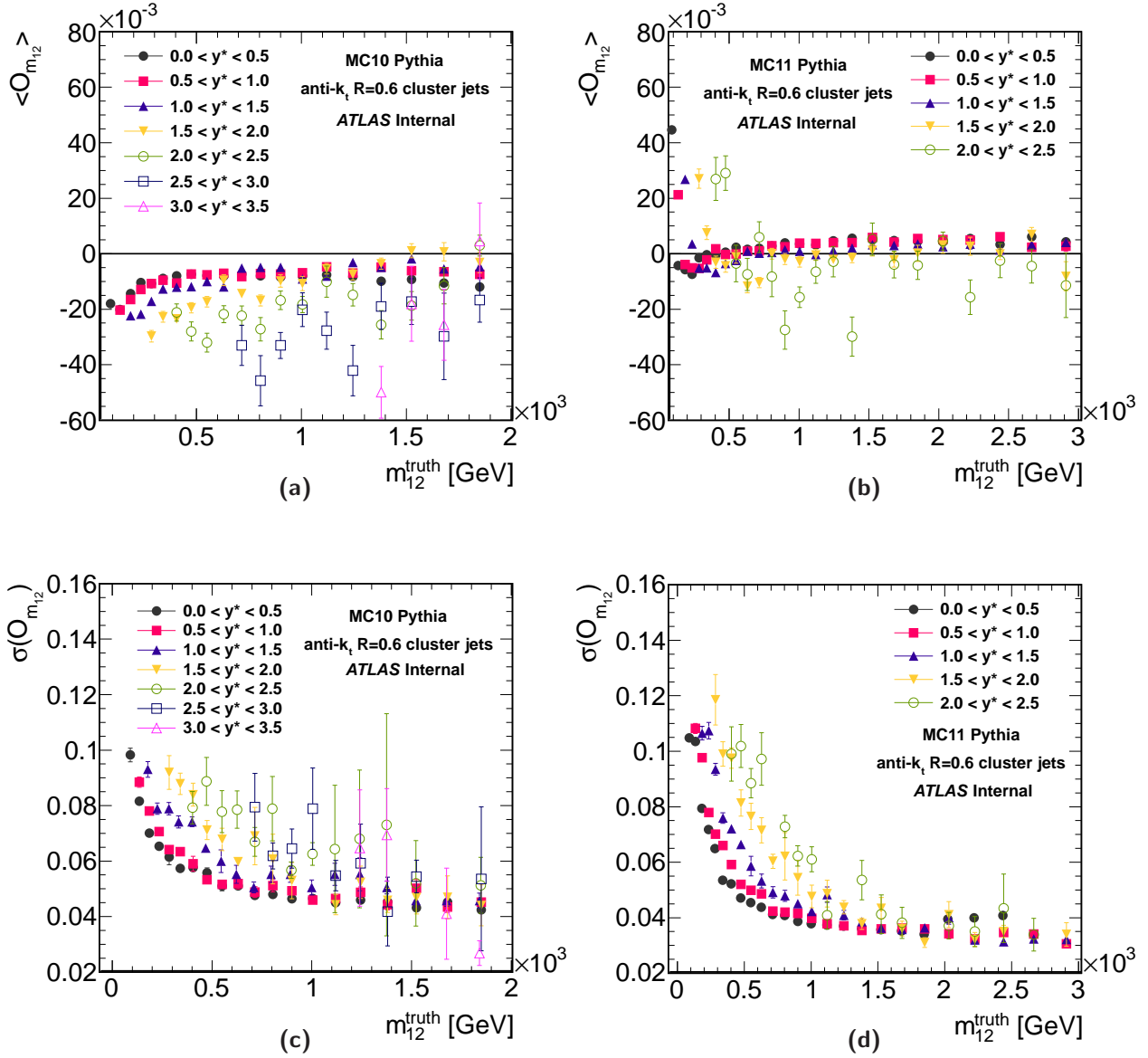


Figure 8.6. Dependence of the average mass offset, $\langle O_{m_{12}} \rangle$, ((a) and (b)) and of the width of the distribution of the offset, $\sigma(O_{m_{12}})$, ((c) and (d)) on the invariant mass, m_{12} , of the two jets with the highest transverse momentum in an event, for different center-of-mass jet rapidities, y^* , in MC10 and in MC11, as indicated in the figures.

In order to extract the invariant mass distribution at the particle-level, all the detector effects, such as efficiency and resolution, have to be corrected for. Aside from the JES correction, all other corrections are performed using an iterative unfolding procedure, discussed in the following.

8.4. Unfolding

Unfolding of the dijet mass differential distributions is performed using the *Iterative Bayes* algorithm provided by the RooUnfold software package [172]. The unfolding algorithm uses the method described by D'Agostini [173], and previously used in [174]. This procedure takes as input two elements, a measured distribution and a response matrix obtained from MC. For the case of the dijet mass measurement, the former is the detector-level two-dimensional distribution of the differential dijet mass cross section, binned in m_{12} and in y^* . The second element, the response matrix, provides a mapping between the kinematic variations of the reconstructed objects, and those obtained directly from the event generator.

Adjusting the kinematic distributions of jets in the MC

Due to the finite binning of the unfolding procedure and the very steep kinematic distributions that need to be unfolded, the response matrix depends on the shape of the input distribution in the MC. It is therefore advantageous to start the unfolding procedure with input distributions which are as close as possible to the corresponding distributions in the data.

For the case of MC10, the p_t spectrum of the two leading jets without any correction is presented in figure 8.7a. The distributions in MC are rescaled such that they agree in normalization with the data at $p_t = 50$ GeV. At low p_t , the MC underestimates the data by a factor of 2.3. As p_t increases, the difference between MC and data increases up to 50% at $p_t = 600$ GeV. The main origin of the weights in MC10 has been identified as the result of mismatch between the trigger in the data and in the MC.

To reach a better agreement, the p_t distribution in the MC is reweighted. Transverse momentum reweighting is performed in bins of rapidity. The weights are estimated from the ratio of the data distribution to the MC distribution at detector-level, which is then parametrized by a smooth function. This function is applied as a weight in the MC at the particle-level, based on truth jet p_t . The p_t distributions of the two leading jets in reweighted events are shown in figure 8.7b. The difference between MC and data is reduced compared to that before reweighting; this approximate procedure therefore seems adequate. The residual differences, at the level of 10 – 20%, are taken care of by the unfolding. Following the p_t reweighting, the multiplicity distribution of the reconstructed vertices, N_{PV} , in the MC is matched to that in the data (the reweighted vertex distribution is shown in chapter 7, figure 7.3a.) The vertex reweighting does not bias the p_t spectrum, as there is no correlation between N_{PV} and jet p_t in MC10.

Due to improvements in the simulation, no p_t reweighting based on truth jets is required for MC11. To achieve adequate agreement between the 2011 data and MC11, it is enough to constrain the spectrum of jets in MC, by matching the trigger conditions with those in the data. Trigger assignment is made according to the p_t of the two leading jets in an event (see section 6.2.3). Accordingly, events in MC11 are given weights such that the number of weighted events in each trigger bin² matches the corresponding number in data. As mentioned in section 4.2, MC11 is divided into

² The expression trigger bin refers here to the classification of an event according to the triggers associated with the two leading jets. Associations are made according to jet p_t and η , as specified in chapter 6, tables 6.1 - 6.2.

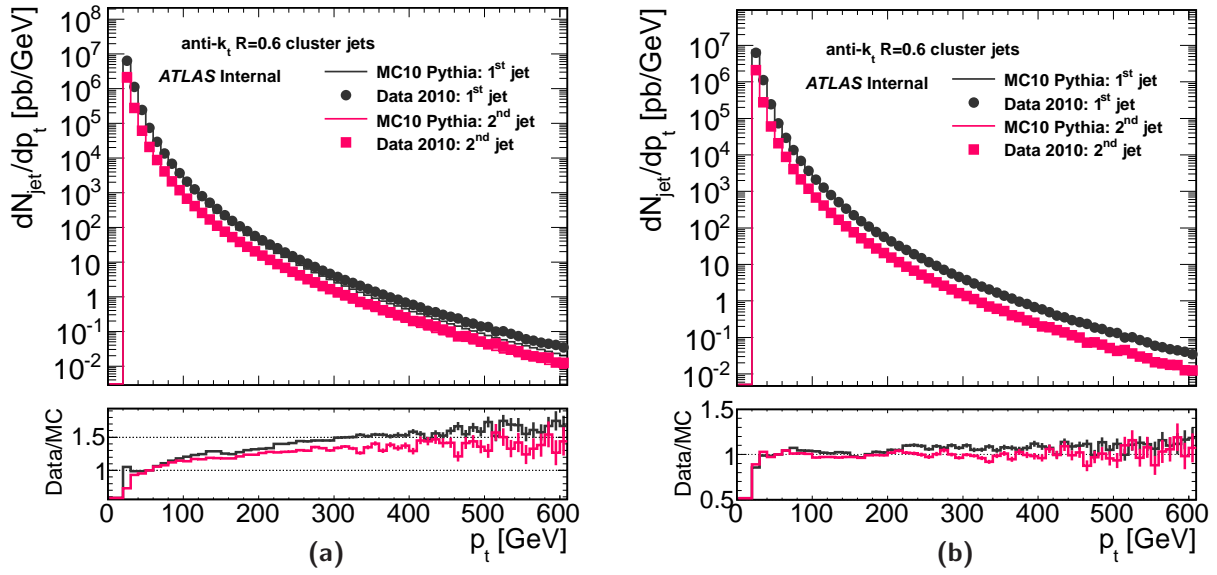


Figure 8.7. Transverse momentum, p_t , spectra of the two highest- p_t jets in an event, denoted as 1st and 2nd jet in the figures, for events before (a) and after (b) the reweighting procedure described in the text, using MC10 and the 2010 data, where the distributions in MC are rescaled such that they agree in normalization with the data at $p_t = 50$ GeV. The bottom panels show the ratio of data to MC of the various distributions.

several “periods”, which correspond to different pile-up conditions and trigger prescales. In order to avoid biasing the vertex distribution, trigger matching is performed separately for events with any given value of N_{PV} . Distributions of the number of reconstructed vertices in events assigned to several different trigger bins are shown in figure 8.8a. The p_t spectra of the two leading jets from the same events are shown in figure 8.8b. The distributions in MC are rescaled such that they agree in normalization with the data at $p_t = 50$ GeV. The p_t spectrum in MC11 differs from data by up to 20% for $p_t < 50$ GeV, by up to 10% within $50 < p_t < 500$ GeV and by up to 20% within $0.5 < p_t < 1$ TeV.

As already mentioned, the steeply falling distribution of jet p_t has a significant effect on migrations between mass bins in the unfolding response matrix. To a lesser degree, discrepancies in the relatively flat rapidity distribution of jets may also affect the unfolding. A comparison between the pseudo-rapidity of the two leading jets in MC10 and in MC11 with the corresponding data is shown in figure 8.9. The simulation samples are p_t -reweighted (MC10) or trigger-corrected (MC11), as discussed above. The differences between data and MC are smaller than 25% within $|\eta| < 2.5$ and within roughly 50% for $2.5 < |\eta| < 4.4$. In principle, it is possible to further improve the agreement in the η distributions of the MC with data. However, this comes at the cost of degrading the agreement in the p_t distributions, as the momentum and rapidity distributions of jets are correlated. No further correction for the rapidity of jets is therefore made.

The number of unfolding iterations

In order to unfold the data, the response matrix has to be inverted. In this case, the inversion of the matrix is notoriously difficult, as it is an ill-posed problem. The usual approach is to apply an iterative procedure with a smoothing function [173]. The latter prevents oscillations in the solution,

8. Dijet mass distribution

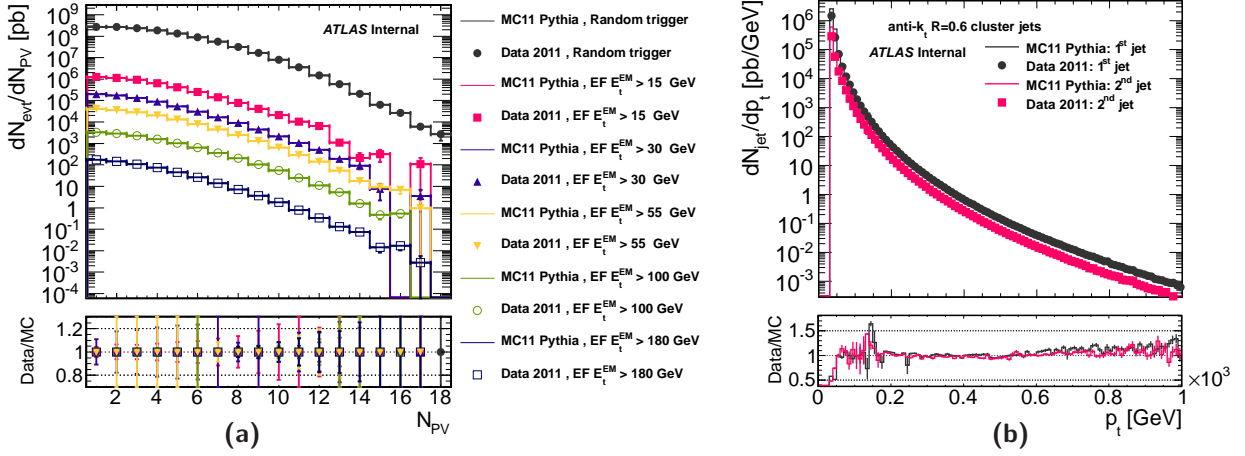


Figure 8.8. (a) Distributions of the number of reconstructed vertices, N_{PV} , in the 2011 data and in MC11, for events in which the jet with the highest transverse momentum is associated with different triggers, including a random trigger and jet triggers, where the latter are ordered by trigger thresholds at the EM scale, E_t^{EM} , as indicated in the figure.

(b) Transverse momentum, p_t , spectra of the two highest- p_t jets in an event, denoted as 1st and 2nd jet in the figure, in the 2011 data and in MC11, where the distributions in MC are rescaled such that they agree in normalization with the data at $p_t = 50$ GeV.

The bottom panels in both figures show the ratio of data to MC.

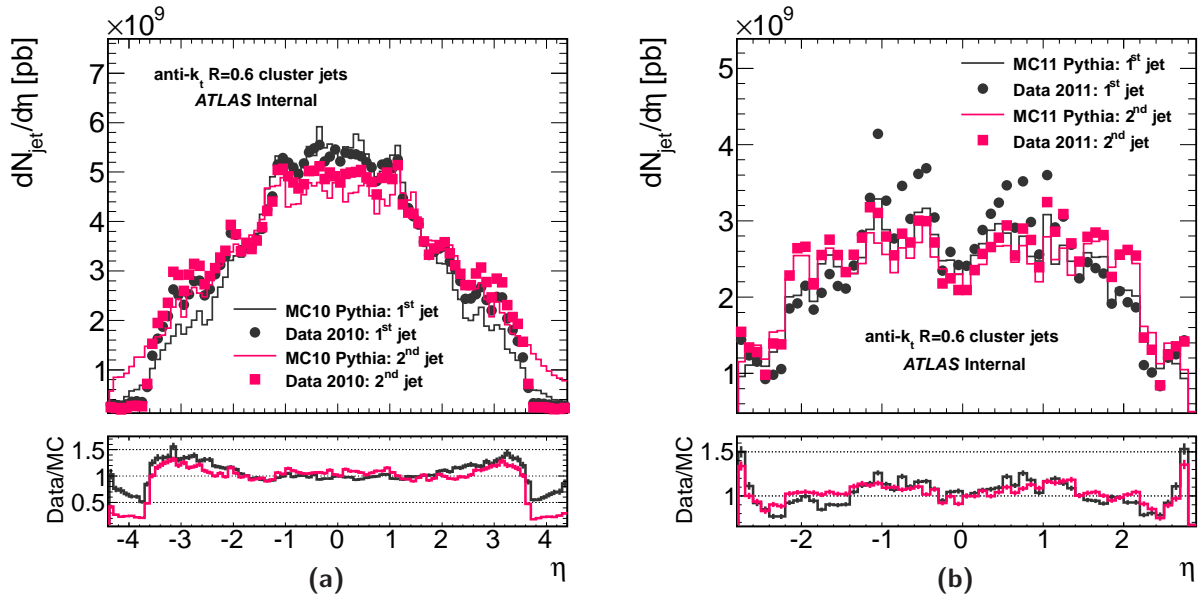


Figure 8.9. Pseudo-rapidity, η , distributions of the two jets with the highest transverse momentum in an event, denoted as 1st and 2nd jet in the figure, using the 2010 data with MC10 (a) or the 2011 data with MC11 (b), as indicated. The bottom panels show the ratio of data to MC.

which are generated by inherent correlations in the data. Such an approach is implemented as part of the unfolding algorithm in this analysis. The number of iterations used in the procedure, denoted by κ_{unf} , can not be determined beforehand, and must be optimized for a given measurement.

The value of κ_{unf} used in the analysis is determined from simulation. Half of the available MC statistics are used to reconstruct a response matrix; the other half, a statistically independent sample, is “unfolded” using this matrix, as would the data. One can then compare the “unfolded” MC distribution of the differential cross section with the respective truth-level distribution from the same events. The optimal value of κ_{unf} is one which minimizes the differences between these two distributions.

Figure 8.10a shows the first step in the optimization procedure of κ_{unf} . The dijet mass is constructed from truth jets in a single y^* bin in MC11, drawn as a function of m_{12} (the histogram is the figure.) The same variable is then constructed from calorimeter jets and drawn before (red squares) and after (blue triangles) unfolding. The agreement of the calorimeter-jet distribution with the truth-jet distribution is improved after unfolding.

The unfolding offset is defined as

$$O_{\text{unf}}^{m_{12}} = \frac{b_{\text{calo}}^{m_{12}, y^*} - b_{\text{truth}}^{m_{12}, y^*}}{b_{\text{truth}}^{m_{12}, y^*}}, \quad (8.9)$$

where $b_{\text{calo}}^{m_{12}, y^*}$ ($b_{\text{truth}}^{m_{12}, y^*}$) stands for the number of entries in a bin of the double-differential dijet mass distribution, constructed from calorimeter (truth) jets. The unfolding offset, derived from MC10 and from MC11, is presented in figures 8.10b and 8.10c. Several distributions are shown, corresponding to $O_{\text{unf}}^{m_{12}}$ without unfolding, and to $O_{\text{unf}}^{m_{12}}$ with unfolding and using several values of κ_{unf} . In MC11, the mean value of $O_{\text{unf}}^{m_{12}}$ is non-zero before unfolding, suggesting that the unfolding correction is significant. Otherwise, it is difficult to tell by eye which value of κ_{unf} gives the best result, either for MC10 or for MC11. The width of the distributions of the unfolding offset, denoted by $\sigma(O_{\text{unf}}^{m_{12}})$, is therefore used in order to quantify the performance.

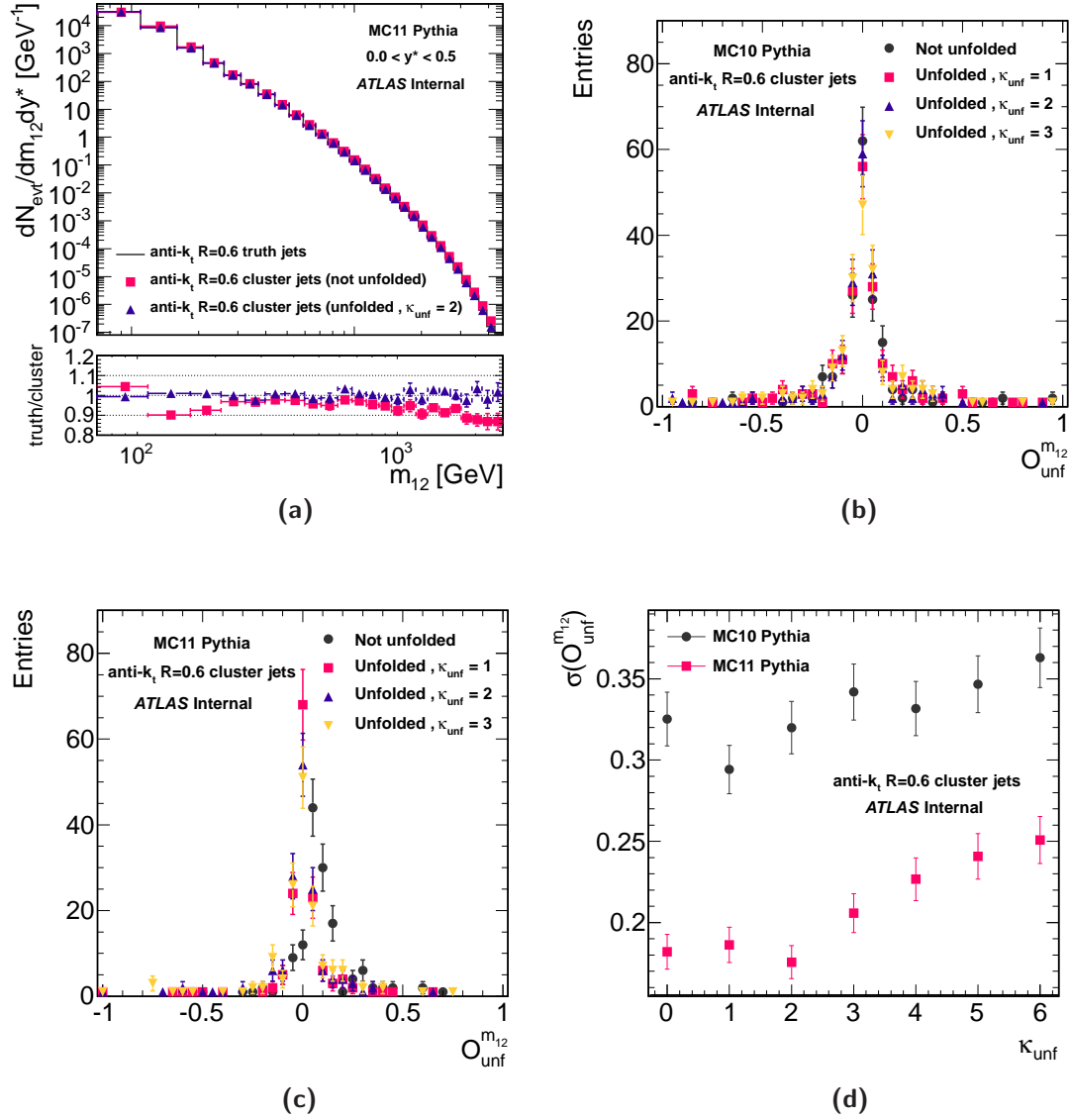
The dependence of $\sigma(O_{\text{unf}}^{m_{12}})$ on the number of unfolding iterations is shown in figure 8.10d. In MC10, the value of $\sigma(O_{\text{unf}}^{m_{12}})$ decreases between $\kappa_{\text{unf}} = 0$ (no unfolding) and $\kappa_{\text{unf}} = 1$. As κ_{unf} is increased above unity, the width of the unfolding offset grows. For MC11, $\sigma(O_{\text{unf}}^{m_{12}})$ of $\kappa_{\text{unf}} = 1$ is larger compared to the case of no unfolding. However, as mentioned with regard to figure 8.10c, the mean of $O_{\text{unf}}^{m_{12}}$ is smaller after unfolding, indicating an improved performance nonetheless. As κ_{unf} is increased above unity, the magnitude of $\sigma(O_{\text{unf}}^{m_{12}})$ reaches a minimum at $\kappa_{\text{unf}} = 2$. The values of the width of the offset in MC11 are generally smaller compared to the corresponding values in MC10.

The minimal values of $\sigma(O_{\text{unf}}^{m_{12}})$ represent the best agreement between the unfolded and corresponding truth-level distributions. The optimal values for MC10 and for MC11 are therefore chosen as $\kappa_{\text{unf}}^{2010} = 1$ and $\kappa_{\text{unf}}^{2011} = 2$ respectively.

8.5. Systematic uncertainties

Several sources of systematic uncertainty are considered for the measurement, discussed in the following sections. The uncertainty in each case is studied by changing the properties of jets, calculating the dijet mass cross section, and comparing the result to the nominal measurement.

8. Dijet mass distribution



The difference in the distributions is taken as an estimate of the uncertainty. The variations in the properties of jets are performed either in the data or in the MC. For the latter, the effect of the variations on the measurement is expressed through the changes induced in the unfolding response matrix, or in the way that it is used to unfold the data.

8.5.1. Systematic uncertainty on the jet energy scale

The JES is the dominant source of uncertainty in the measurement in most m_{12}, y^* regions. The following components, in total seven for the 2010 measurement and thirteen for 2011, are considered in the analysis:

- **2010** - single hadron response; cluster thresholds; Perugia 2010 and Alpgen+Herwig+Jimmy; intercalibration; relative non-closure; in-time pile-up;
- **2011** - ENP 1-6; intercalibration; single hadron response; relative non-closure; close-by jet; in-time PU, out-of-time PU and PU p_t .

The different components of the uncertainty are discussed in detail in [section 5.5](#), with the exception of the pile-up uncertainty for 2011, which is discussed in [section 7.3.3](#).

The effects of the different components of the JES uncertainties on the dijet mass measurement are estimated by introducing positive or negative variations to the energy scale of jets in data. After the energy of jets is varied, they are re-sorted according to p_t , and the two leading jets are chosen as the dijet pair. The dijet mass is reconstructed using the modified jets, and the differential cross section, $\partial^2\sigma/\partial m_{12}\partial y^*$, is unfolded. The mass spectra are finally compared to the nominal sample, which consists of an unfolded measurement of the differential cross section, performed without any JES shifts. The ratio between the shifted and the nominal distributions is taken as the relative JES uncertainty on the measurement. The total uncertainty is the quadratic sum of the uncertainties derived from the different sources.

The effect on the measurement due to the different sources of JES uncertainty, derived from positive or negative shifts of the energy scale of jets, may be inferred from [figure 8.11](#) for dijet systems with $y^* < 0.5$. The total JES uncertainty for $y^* < 0.5$ in 2010 is roughly 10% at low mass values, decreasing to between 5-6% for $m_{12} > 200$ GeV. In 2011 the total uncertainty for $y^* < 0.5$ is smaller in the mid mass range ($0.5 < m_{12} < 1.5$ TeV) compared to 2010; this is due to improvement in the understanding of the detector and in the techniques used to estimate the uncertainty. At low masses the uncertainty in 2011 is comparable to 2010, at around 5%; this is due to the increase in pile-up in 2011, the effect of which is relatively strong at low- p_t . For $m_{12} > 1.5$ TeV, the uncertainty increases up to 7%, and is kept fixed at this value for lack of statistics.

8.5.2. Other sources of uncertainty

In addition to the JES, the following sources of uncertainty on the measurement are studied:

- **jet energy and angular resolutions** - the properties of jets in the MC are varied according to the uncertainty on the jet energy and angular resolutions (see [section 5.5.2](#)), leading to a change in the unfolding response matrix;
- **physics model used for the unfolding** - the unfolding response matrix is computed using ALPGEN, coupled to HERWIG and JIMMY (AHJ) (see [section 4.1](#)), where the p_t and N_{PV} distributions in the MC are reweighted to match those in the data, following the procedure discussed in [chapter 7](#), [figure 7.3a](#);

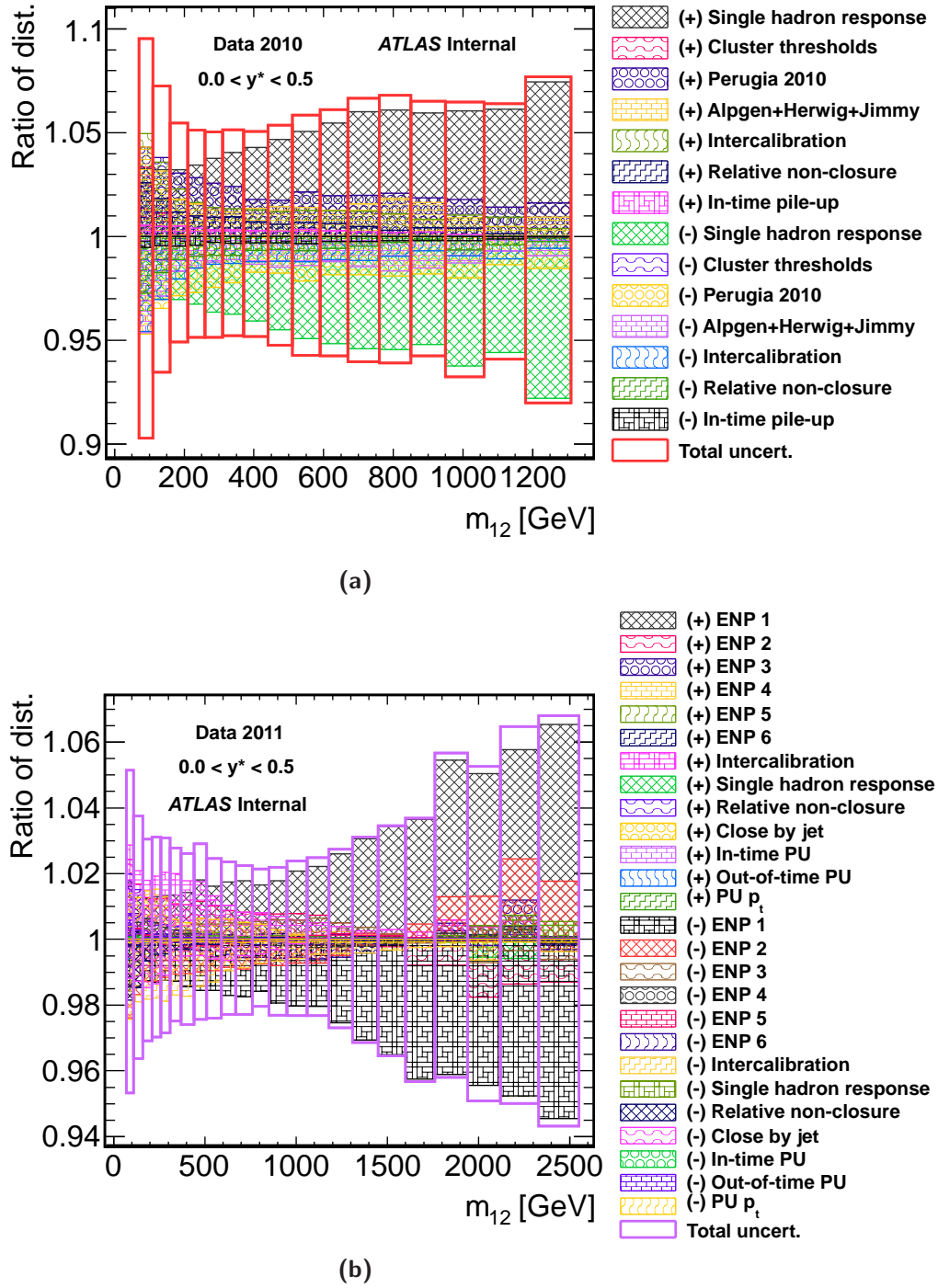


Figure 8.11. Dependence on the invariant mass, m_{12} , of the two jets with the highest transverse momentum in an event, of the ratio between the m_{12} distributions with and without systematic variations, for center-of-mass jet rapidity, $y^* < 0.5$, for the 2010 (a) and for the 2011 (b) measurements, where positive (+) and negative (−) variations are performed according to the different components (described in the text) of the uncertainty on the energy scale of jets (JES), and the total JES uncertainty is denoted by “total uncert.”

- **shape of the dijet mass spectrum in the unfolding** - the unfolding response matrix is constructed using a MC in which the shape of the dijet invariant mass distribution is distorted;
- **the number of unfolding iterations** - the unfolding procedure is performed using different values of κ_{unf} .

The uncertainty derived from the various sources is summarized in the next section.

8.5.3. Total systematic uncertainty

The total relative systematic uncertainty on the dijet mass cross section measurement for $y^* < 0.5$, as well as the different sources which comprise it, are depicted in [figure 8.12](#). The uncertainties are expressed through changes in the invariant mass distribution, induced by variation of the different sources of uncertainty. The various components of the uncertainty, described in the previous

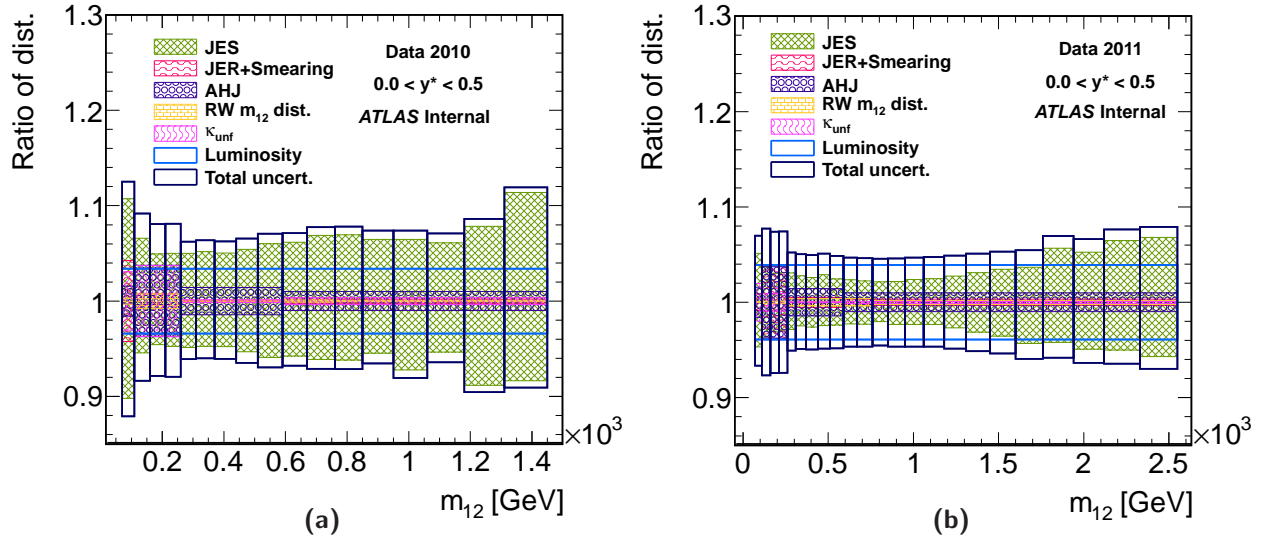


Figure 8.12. Dependence on the invariant mass, m_{12} , of the two jets with the highest transverse momentum in an event, of the ratio between the m_{12} distributions with and without systematic variations (described in the text), for center-of-mass jet rapidity, $y^* < 0.5$, in the 2010 (a) and in the 2011 (b) measurements, including the uncertainty on the jet energy scale (JES); the uncertainty on the jet energy and angular resolutions (JES + smearing); the uncertainty associated with the choice of physics generator (AHJ); the uncertainty associated with variation in the simulated shape of the m_{12} spectrum (RW m_{12} dist.); the choice of the number of iterations used in the unfolding procedure (κ_{unf}); the uncertainty on the luminosity (luminosity); and the total uncertainty on all the latter (total uncert.).

sections, are the jet energy scale; the jet energy and angular resolution; the uncertainty associated with the choice of physics generator; the uncertainty associated with the simulated shape of the

8. Dijet mass distribution

dijet mass differential spectrum; and the choice of the number of iterations used in the unfolding procedure. In addition, the uncertainty on the luminosity (3.4% for 2010 and 3.9% for 2011) is also taken into account.

The total relative uncertainty for $y^* < 0.5$ is between 6 – 12% in 2010 and between 5 – 8% in 2011. Additional y^* bins are presented in [section A.4](#), [figures A.12 - A.14](#).

8.6. Results

The dijet double-differential cross section, for anti- k_{\perp} $R = 0.6$ jets, is measured as a function of the dijet invariant mass for various values of y^* . The 2010 measurements include dijet masses between 70 GeV and 3.04 TeV, with values of y^* up to 3.5, using jets within pseudo-rapidity, $|\eta| < 4.4$. The 2011 measurements extend the mass range to 4.27 TeV, but for a smaller y^* range, $y^* < 2.5$, and for jets with $|\eta| < 2.8$. In the 2010 measurements, the jets are required to have $p_t > 30$ GeV for the leading jet, and $p_t > 20$ GeV for the sub-leading jet. In 2011, these limits are higher by 10 GeV.

The measured cross sections have been corrected for all detector effects. The systematic uncertainties include variations of the jet energy scale and the jet energy and angular resolutions, several checks of the unfolding procedure, and the uncertainty on the luminosity. The measurements are compared to fixed-order NLO pQCD predictions from NLOJET++, using the CT10 PDF set, and corrected for non-perturbative effects. The theoretical uncertainties take into account scale variations, change in the parton distribution functions, and stability of the non-perturbative corrections.

The cross section results are presented in [figures 8.13 and 8.14](#). Within the uncertainties (statistical, systematic and theoretical), the fixed-order NLO pQCD predictions give a good description of the measurements over 12 orders of magnitude. The good agreement between the measurements performed in 2010 and in 2011, under very different beam conditions, indicate that in-time pile-up and out-of-time pile-up are experimentally well under control.

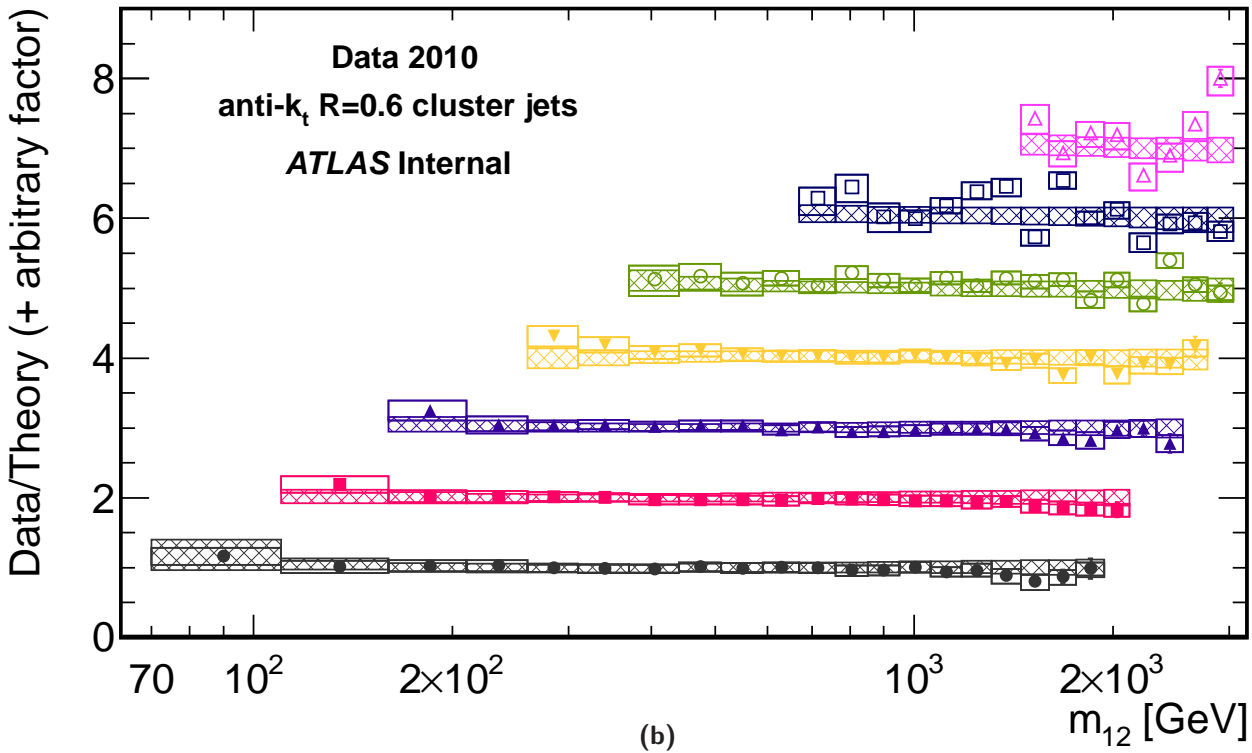
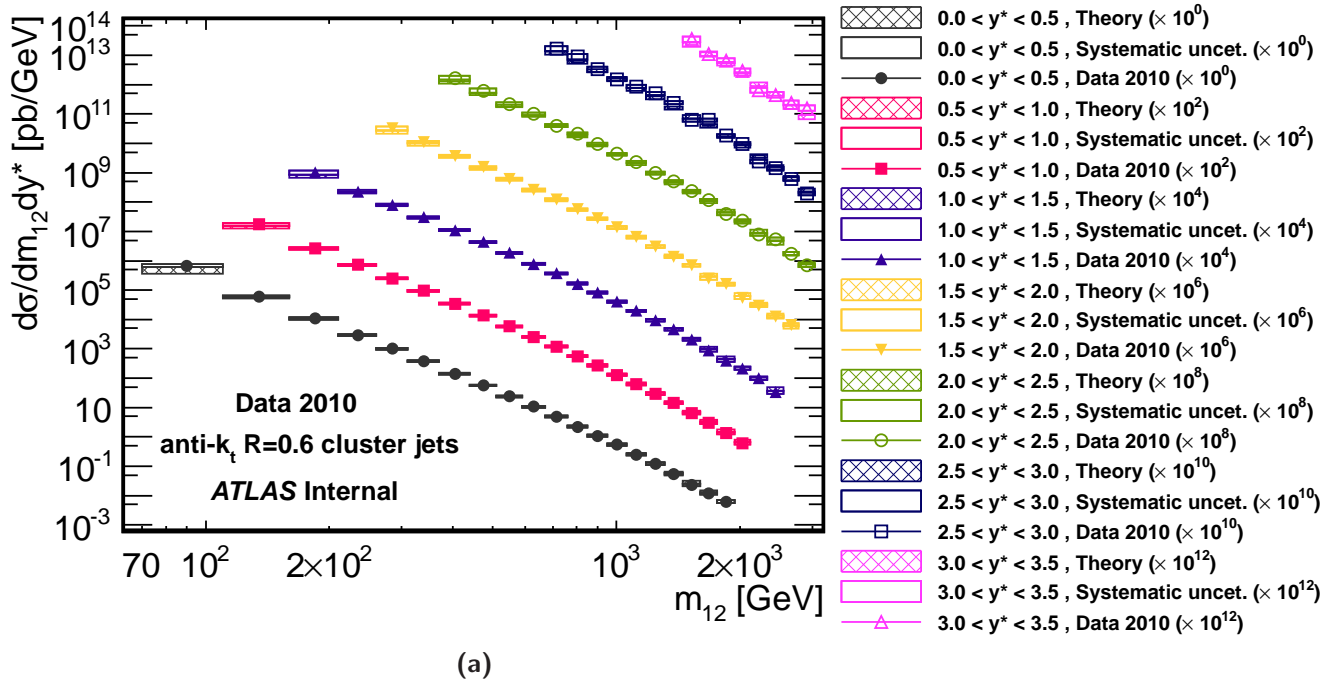
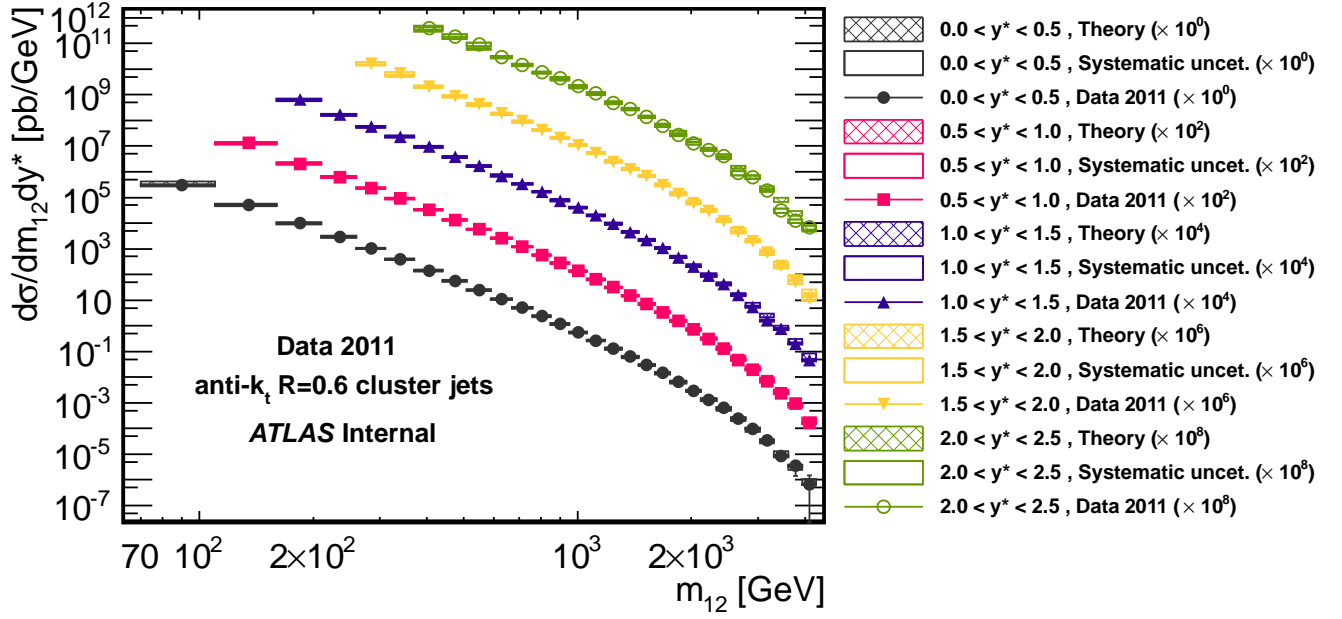


Figure 8.13. Double-differential dijet cross section as a function of the invariant mass, m_{12} , binned in center-of-mass jet rapidity, y^* , in the 2010 data, compared to NLOJET++ pQCD calculations using the CT10 PDF set, which are corrected for non-perturbative effects. The uncertainty on the theoretical calculations, the systematic uncertainty on the data and the statistical uncertainty on the data (generally too small to discern) are shown as well.

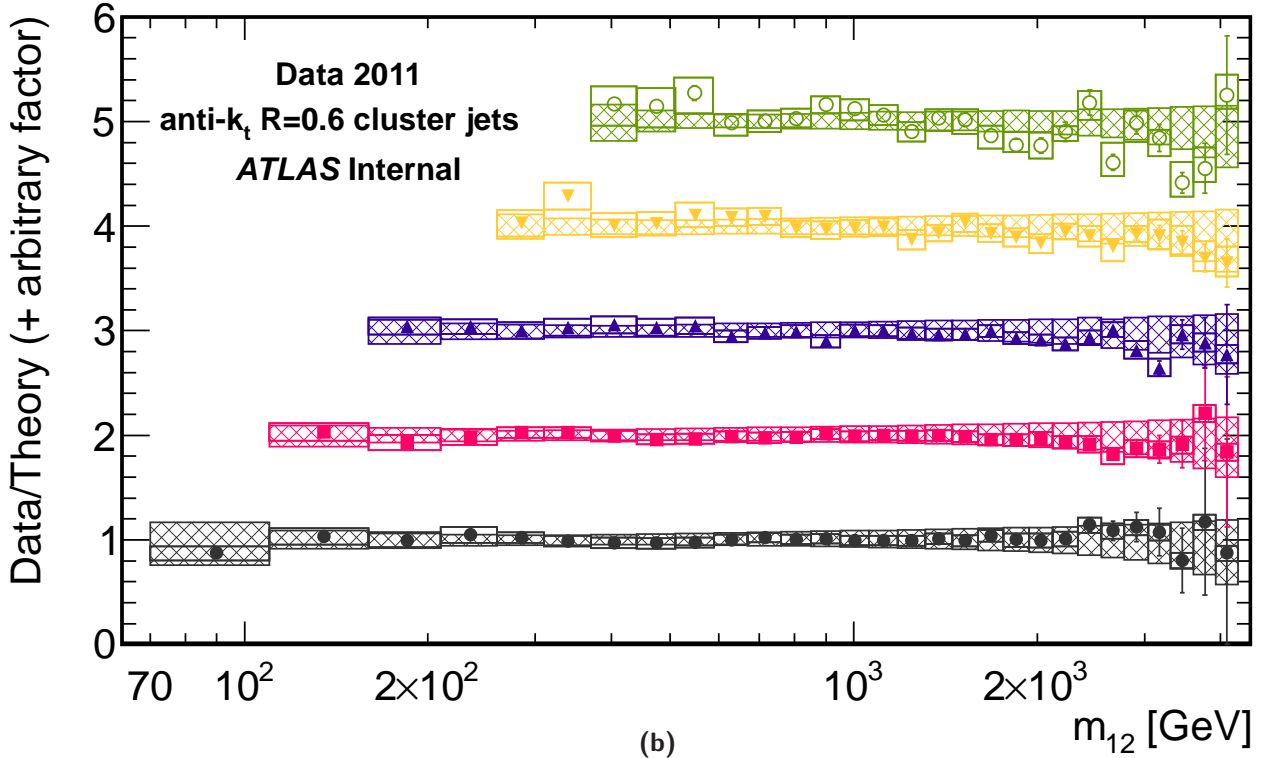
(a) Invariant mass distributions, multiplied by the factors specified in the legend.

(b) Ratio of the data to the theoretical predictions, where the results for different y^* bins are separated by arbitrary constants for convenience.

8. Dijet mass distribution



(a)



(b)

Figure 8.14. Double-differential dijet cross section as a function of the invariant mass, m_{12} , binned in center-of-mass jet rapidity, y^* , in the 2011 data, compared to NLOJET++ pQCD calculations using the CT10 PDF set, which are corrected for non-perturbative effects. The uncertainty on the theoretical calculations, the systematic uncertainty on the data and the statistical uncertainty on the data (generally too small to discern) are shown as well.

(a) Invariant mass distributions, multiplied by the factors specified in the legend.

(b) Ratio of the data to the theoretical predictions, where the results for different y^* bins are separated by arbitrary constants for convenience.

9. Hard double parton scattering in four-jet events

The dominant mechanism for the production of events containing four high- p_t jets at the LHC is double gluon bremsstrahlung. This process is described quantitatively (up to LO) by pQCD. A few Feynman diagrams depicting such events are shown in [figure 9.1](#). This topology is characterized by

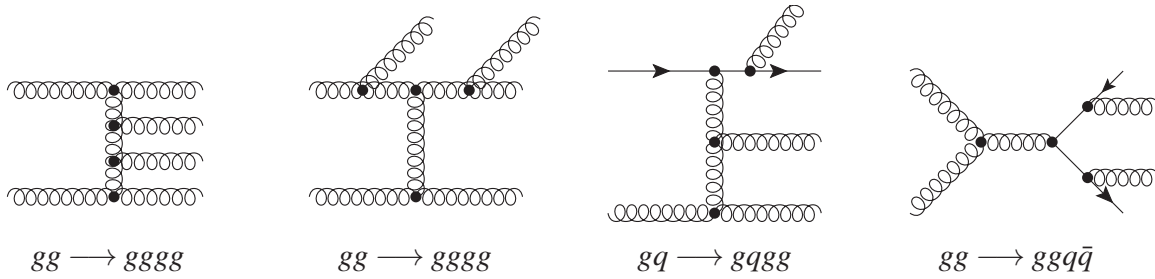


Figure 9.1. Four of the Feynman diagrams which contribute to the leading-order matrix element expression for the double gluon bremsstrahlung process.

two partons in the initial state and four in the final state, denoted as $(2 \rightarrow 4)$. Alternatively, four-jet final states can also be produced through the double parton scattering (DPS) mechanism, which is discussed in [section 2.4](#). In the case of DPS, two pairs of dijet events occur simultaneously in a single pp collision. The process of DPS is denoted in the following as $(2 \rightarrow 2)^{\times 2}$.

Recently it has been advocated that in addition to the two processes discussed above, a third process should contribute, in which a parton from one of the protons, splits perturbatively into two partons, which then interact with two partons from the other proton. This configuration, denoted as $(3 \rightarrow 4)$, leads to slightly different topologies of the four jets than expected in the $(2 \rightarrow 2)^{\times 2}$ and $(2 \rightarrow 4)$ processes, although its contribution may be substantial [\[81\]](#). In this analysis, no attempt is made to differentiate between the $(2 \rightarrow 2)^{\times 2}$ and the $(3 \rightarrow 4)$ topologies, as the differences may be too small for the typical jet energy resolution, for jets with $p_t \sim 20$ GeV.

On an event-by-event basis, it is impossible to determine whether a $(2 \rightarrow 4)$ or a $(2 \rightarrow 2)^{\times 2}$ interaction describes an event. However, several kinematic features distinguish the two processes on average. The natural approach would have been to devise a strategy of extracting the DPS signal, based on a sample of MC generated events, which contained multi-parton interactions and full detector simulation. Unfortunately, a MC simulating four-jet final states through matrix-elements, such as ALPGEN, coupled to HERWIG and JIMMY (AHJ), or SHERPA, turned out not to be adequate. The available AHJ sample, in which the user can identify jets which originate from extra

parton scatterings in the event-record, did not have enough hard double-scattering events passing the experimental selection cuts. On the other hand, in SHERPA, the information on the extra scatters in the event is not available to the user. A different strategy was therefore devised, that of using a neural network.

In the following analysis, the rate of DPS in four jet events in the 2010 ATLAS data is extracted using the neural network approach. The respective value of σ_{eff} (defined in [section 2.4](#), [equation \(2.14\)](#)) is subsequently measured.

9.1. Strategy of the analysis

Phase-space and data sample of the measurement

The rate of hard double parton scattering is measured in events which have exactly four jets in the final state. Events are selected using the two-trigger selection scheme described in [section 6.2.3](#). The measurement also uses exclusive dijet events as part of the calculation of σ_{eff} . Dijet events are defined in a similar manner as four-jet events, in that they have exactly two jets in the final state. Jets are reconstructed using the anti- k_{\perp} algorithm with size parameter, $R = 0.6$. They are defined as having transverse momentum, $p_t > 20$ GeV, and pseudo-rapidity, $|\eta| < 4.4$. Additional requirements on jet- p_t may be imposed for four-jet or dijet event selection, as discussed in the following. Jets in dijet and in four-jet events are ordered in descending order of their transverse-momenta. That is, denoting by $p_{t,i}$ the transverse momentum of the i^{th} jet in an event, the p_t of jets in e.g., a four-jet event, fulfil the condition,

$$p_{t,1} > p_{t,2} > p_{t,3} > p_{t,4} .$$

Pile-up constitutes a major source of background to the measurement. It introduces fake four-jet or dijet events and removes legitimate events. There are two main sources of miss-counting of four-jet events (with similar considerations for dijet events). The first are three-jet events in which the p_t of a fourth jet should be smaller than 20 GeV, but is increased above threshold due to pile-up. The second are five-jet events, in which one of the jets is split due to pile-up, and the two split jets are both below threshold. It is also possible for additional hard jets, which originate from a different pp collision, to be counted as part of the main interaction. Thus an event may move in to or out of the accepted phase-space. In order to avoid such uncertainty, only single-vertex events taken during 2010 are used in the analysis.

In addition to the requirements specified above, the leading jet in a four-jet event is required to have $p_t > 42.5$ GeV. Restricting the p_t of the leading jet to be higher than the minimal threshold for reconstruction, creates a scale separation between the jets. This helps to combine the four jets in DPS events into two pairs, each originating from a different scattering, as discussed in the next sections. The restriction on the leading jet is also motivated by the trigger strategy of the analysis. It amounts to the requirement that at least one jet in the event fires a jet trigger (see [table 6.1](#)). Four-jet events in which the two leading jets are associated with the MBTS trigger are not included. Such events constitute a very small fraction of the overall statistics, but dominate completely the phase-space region in which both leading jets have $20 < p_t < 42.5$ GeV. Since they are associated with very high luminosity weights, they tend to introduce large statistical fluctuations into the measurement.

To summarize, the measurement is performed for exclusive four-jet events which have

$$N_{\text{PV}} = 1, \quad N_{\text{jet}} = 4, \quad p_{t,1} > 42.5 \text{ GeV}, \quad p_{t,2-4} > 20 \text{ GeV}, \quad |\eta_{1-4}| < 4.4, \quad (9.1)$$

where N_{PV} is the number of reconstructed vertices in the event, N_{jet} is the number of reconstructed anti- k_{\perp} , $R = 0.6$ jets; and η_{1-4} stands for the pseudo-rapidity of the four leading jets.

The added restriction on jet- p_t may also be imposed on dijet events. Two classes of exclusive dijet events are defined, denoted by a and b . These are,

$$\begin{aligned} (a) \quad & N_{\text{PV}} = 1, \quad N_{\text{jet}} = 2, \quad p_{t,1-2} > 20 \text{ GeV}, \quad |\eta_{1,2}| < 4.4, \\ (b) \quad & N_{\text{PV}} = 1, \quad N_{\text{jet}} = 2, \quad p_{t,1} > 42.5 \text{ GeV}, \quad p_{t,2} > 20 \text{ GeV}, \quad |\eta_{1,2}| < 4.4. \end{aligned} \quad (9.2)$$

Here $p_{t,2}$ stands for the transverse momentum of the sub-leading jet in the event, and $\eta_{1,2}$ stands for the pseudo-rapidity of the two jets.

For completeness, the cross section for the four-jet final state is denoted by σ_{4j}^b , and those of the two classes of dijet final states are denoted by σ_{2j}^a and σ_{2j}^b . The superscripts a and b indicate the phase-space restrictions on the respective cross sections. The former (a) represents a cross section which includes the restriction that all jets have $p_t > 20 \text{ GeV}$. The latter (b) stands for cross sections which include events where the leading jet has $p_t > 42.5 \text{ GeV}$ and all other jets have $p_t > 20 \text{ GeV}$.

Definition of the observable

The cornerstone of the analysis is the extraction of f_{DPS} , the fraction of four-jet events in which the jets originate from a hard DPS, and the measurement of the ratio of dijet and four-jet cross sections. These are subsequently used to determine the value of σ_{eff} (see [section 2.4](#)) in the four-jet final state.

The simplified form,

$$\sigma_{\text{eff}} = \frac{m}{2} \frac{\sigma_{2j}^a \sigma_{2j}^b}{\sigma_{\text{DPS}}^b} = \frac{m}{2 f_{\text{DPS}}} \frac{\sigma_{2j}^a \sigma_{2j}^b}{\sigma_{4j}^b}, \quad (9.3)$$

is used, where the double parton scattering cross section,

$$\sigma_{\text{DPS}}^b = f_{\text{DPS}} \cdot \sigma_{4j}^b,$$

is extracted using the measured cross section for four-jet events, σ_{4j}^b . The latter includes all events with four-jet final states, that is both $(2 \rightarrow 4)$ and $(2 \rightarrow 2)^{\times 2}$ topologies. Four-jet final states of type b in DPS originate from two interactions, of which only one is restricted to have at least one jet with $p_t > 42.5 \text{ GeV}$. The expression for σ_{eff} therefore includes one instance of the dijet cross section of type a and one of type b .

In principle, the two cross sections, σ_{2j}^a and σ_{2j}^b , overlap in the region where the leading jet has $p_t > 42.5 \text{ GeV}$. However, due to the steep fall of the dijet cross section with p_t , the overlapping events constitute roughly 3.5% of σ_{2j}^a . The two dijet final states are, therefore, considered to a good approximation as different, such that the symmetry factor in [equation \(9.3\)](#) is

$$m = 2.$$

The small overlap also helps to correctly combine the four jets in DPS events into two pairs. The probability for a jet from a scattering of type a to have $p_t \sim 40 \text{ GeV}$ (or higher) is small. The two

9. Hard double parton scattering in four-jet events

leading jets are therefore likely to have originated from one scattering and the next two from the other scattering. This distinction helps to construct kinematic variables which differentiate between DPS and non-DPS events, as discussed in [section 9.3](#).

It is important to emphasise that the present determination of σ_{eff} is based on exclusive dijet and four-jet cross sections, while [equation \(2.16\)](#) is defined for inclusive cross sections. This choice greatly facilitates the separation between DPS and direct four-jet production, though it may not be theoretically sound. However, due to the 20 GeV cut on jet- p_t , the difference between the inclusive and the exclusive cross sections was found to have a negligible effect on the analysis.

In general, the cross sections for dijet and four-jet production take the form

$$\sigma_{nj} = \frac{N_{nj}}{\mathcal{A}_{nj}\varepsilon_{nj}\mathcal{L}_{nj}} = \frac{\hat{\sigma}_{nj}}{\mathcal{A}_{nj}}, \quad (9.4)$$

where the subscript, nj , denotes either dijet ($2j$) or four-jet ($4j$) topologies. For each n channel, N_{nj} is the number of measured events, \mathcal{A}_{nj} is the geometrical acceptance of the measurement, ε_{nj} is the efficiency for reconstructing the event¹, and \mathcal{L}_{nj} is the luminosity. Finally, $\hat{\sigma}_{nj} = N_{nj}/(\varepsilon_{nj}\mathcal{L}_{nj})$ is the *observed cross section* at the detector-level. Using this identity, [equation \(9.3\)](#) may be written as

$$\sigma_{\text{eff}} = \frac{1}{f_{\text{DPS}}} \frac{\hat{\sigma}_{2j}^a \hat{\sigma}_{2j}^b}{\hat{\sigma}_{4j}^b} \frac{\mathcal{A}_{4j}^b}{\mathcal{A}_{2j}^a \mathcal{A}_{2j}^b}. \quad (9.5)$$

The expression for σ_{eff} is simplified by defining the *acceptance ratio*,

$$\alpha_{2j}^{4j} = \frac{\mathcal{A}_{4j}^b}{\mathcal{A}_{2j}^a \mathcal{A}_{2j}^b}. \quad (9.6)$$

This factor is used to absorb the difference in the acceptance of the final states into a single quantity. Naively, one may expect that the acceptance factor for each jet in an event should be the same, which would result in $\mathcal{A}_{4j}^b = \mathcal{A}_{2j}^a \mathcal{A}_{2j}^b$ and $\alpha_{2j}^{4j} = 1$. In reality, the cancellation of efficiencies is not complete, as one has to take into account the effects of close-by-jets. Any departure of α_{2j}^{4j} from unity, is mainly due to configurations where a pair of jets overlap. Such topologies reduce the classification efficiency of an event as a $2j$ - or a $4j$ -event, and affect each channel in different proportions.

Following these considerations, [equation \(9.5\)](#) reduces to

$$\sigma_{\text{eff}} = \frac{\mathcal{S}_{4j}^{2j} \alpha_{2j}^{4j}}{f_{\text{DPS}}}, \quad (9.7)$$

with

$$\mathcal{S}_{4j}^{2j} = \frac{\hat{\sigma}_{2j}^a \hat{\sigma}_{2j}^b}{\hat{\sigma}_{4j}^b}, \quad (9.8)$$

where one may identify that $\mathcal{S}_{4j}^{2j} \alpha_{2j}^{4j} = \sigma_{2j}^a \sigma_{2j}^b / \sigma_{4j}^b$.

¹ In the 2010 data there is need to differentiate between the acceptance and the efficiency, as the non-geometrical inefficiencies of the detector (e.g., faulty electronic channels) were not properly simulated as part of the MC10 campaign.

To summarize, three elements, \mathcal{S}_{4j}^{2j} , α_{2j}^{4j} and f_{DPS} , enter the determination of σ_{eff} . These are discussed in turn in the following sections.

Uncertainty on the measurement

The systematic uncertainty on the measurement originates from uncertainties on the measured properties of jets in data, and on the simulated properties in the MC. The uncertainty in the data is mainly due to that on the jet energy scale (JES). In the MC, the uncertainty on the energy and angular resolutions and the dependence on the shape of the input distributions, all contribute to the total uncertainty.

The fraction of DPS events is extracted from the data using a neural network, which is based on the MC. The statistical as well as the JES uncertainties on the data, therefore, affect the fit-result for f_{DPS} . Similarly, the uncertainties on α_{2j}^{4j} and on f_{DPS} are correlated as well, since both elements depend on the simulated properties of jets in the MC. The different correlations between the elements of the measurement are taken into account when propagating the combined uncertainty to σ_{eff} , as discussed in [section 9.4](#).

9.2. Measurement of the ratio of dijet and four-jet cross sections

The ratio of observed cross sections

The ratio, \mathcal{S}_{4j}^{2j} , is estimated in data by counting the number of dijet and four-jet events, as defined in [equations \(9.1\) and \(9.2\)](#). Events are weighted by the appropriate luminosity factors and are corrected for trigger efficiency. In addition, jet reconstruction efficiency corrections are applied for each jet, depending on its transverse momentum and pseudo-rapidity. That is, a dijet (four-jet) event is given a weight according to the efficiency for reconstructing the two (four) jets.

The numbers of events used for the calculations of the cross sections are

$$N_{2j}^a = 1087776, \quad N_{2j}^b = 871830 \quad \text{and} \quad N_{4j}^b = 307236. \quad (9.9)$$

The combination of these numbers with the corresponding luminosity and efficiency factors, leads to determination of the observed cross sections,

$$\begin{aligned} \hat{\sigma}_{2j}^a &= 2.103 \cdot 10^8 \pm 5.3 \cdot 10^5 \text{ (stat.) pb} , \\ \hat{\sigma}_{2j}^b &= 1.562 \cdot 10^7 \pm 2.7 \cdot 10^4 \text{ (stat.) pb} , \\ \hat{\sigma}_{4j}^b &= 2.221 \cdot 10^6 \pm 9.7 \cdot 10^3 \text{ (stat.) pb} . \end{aligned} \quad (9.10)$$

Finally, the respective value of the ratio of observed cross sections comes out to be

$$\mathcal{S}_{4j}^{2j} = 1.48 \pm 0.04 \text{ (stat.) mb} . \quad (9.11)$$

The quoted errors on the observed cross sections and on \mathcal{S}_{4j}^{2j} are derived from the statistical uncertainties on the respective data samples. These are propagated to σ_{eff} , along with additional systematic uncertainties, as discussed in [section 9.4](#).

The acceptance ratio

The second component of the measurement is the acceptance ratio, α_{2j}^{4j} , which is determined in MC. In order to calculate α_{2j}^{4j} , the acceptance for each class of events (\mathcal{A}_{2j}^a , \mathcal{A}_{2j}^b or \mathcal{A}_{4j}^b) is individually estimated. Counting the number of events which pass the selection cuts for class n using truth (particle) jets, $N_{nj}^{a,b \text{ truth}}$, or using detector jets, $N_{nj}^{a,b \text{ calo}}$, the acceptance is defined as

$$\mathcal{A}_{nj}^{a,b} = \frac{N_{nj}^{a,b \text{ calo}}}{N_{nj}^{a,b \text{ truth}} + N_{nj}^{a,b \text{ calo}}}, \quad (9.12)$$

where the same restrictions on the phase-space of jets (equations (9.1) and (9.2)) are used for truth jets, as for detector jets.

The acceptance is sensitive to the migration of events in to and out of the phase-space of the measurement. The MC is therefore reweighted such that the p_t spectra of the four leading jets match the corresponding distributions in data. The weights are derived according to the p_t of the leading jet (as discussed in section 8.4), which also serves to correct the distributions of the other three jets. The reweighted MC may be compared to data in figure 9.2. The distributions in MC

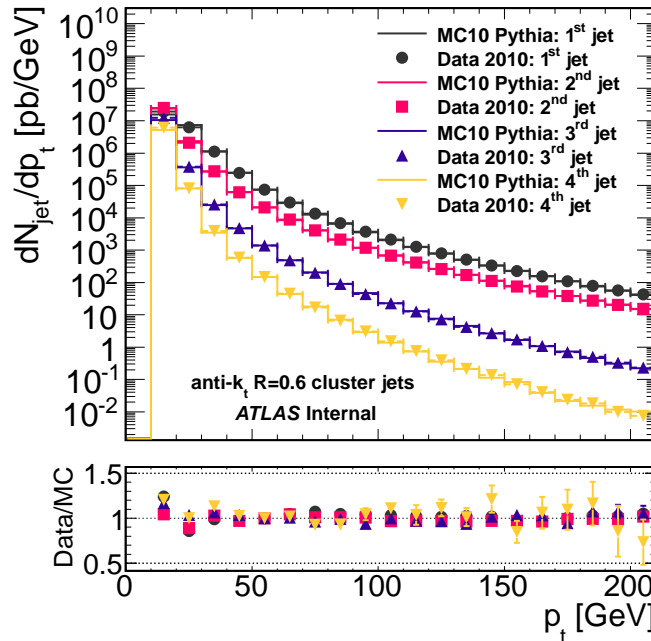


Figure 9.2. Transverse momentum, p_t , spectra of the four highest- p_t jets in an event, denoted as 1st, 2nd, 3rd and 4th jet in the figure, in the 2010 data and in MC, where the distributions in MC are rescaled such that they agree in normalization with the data at $p_t = 50$ GeV. The bottom panel shows the ratio of data to MC.

are rescaled such that they agree in normalization with the data at $p_t = 50$ GeV. The event samples in data and in MC are inclusive; the only requirement imposed is that in each event, at least two jets with $p_t > 20$ GeV are reconstructed. The differences between data and MC are at most of

the order of 20% for each of the four leading jets, for $p_t < 50$ GeV. For higher values of transverse momentum, the deviations of the MC with respect to data are generally below 10%. The dependence of the acceptance ratio on the shape of the p_t spectra in MC is estimated in the next section.

The values of the acceptance factors which are derived using the reweighted MC are

$$\mathcal{A}_{2j}^a = 1.11 \pm 0.01, \quad \mathcal{A}_{2j}^b = 1.13 \pm 0.01 \quad \text{and} \quad \mathcal{A}_{4j}^b = 1.10 \pm 0.03,$$

where the errors are due to the limited MC statistics. The corresponding value of the acceptance ratio is

$$\alpha_{2j}^{4j} = 0.88 \pm 0.03. \quad (9.13)$$

The statistical uncertainty on α_{2j}^{4j} is propagated to σ_{eff} in the following as a systematic uncertainty. Additional uncertainties are derived for α_{2j}^{4j} , and subsequently propagated to σ_{eff} , in [section 9.4](#).

9.3. Extraction of the fraction of DPS events using a neural network

An artificial neural network (NN) is a powerful method of solving complex problems, such as pattern recognition [175]. Neural networks use *supervised learning*, a machine-learning task of inferring a function from a set of training examples. Each example consists of an input object and a desired output value. Neural networks are organized into at least three layers; the input layer, the hidden layer, and the output layer. The three layers consist of various numbers of neurons. There can be more than one hidden layer; this does not necessarily coincide with an increase in performance, but instead raises the complexity of the network.

The analysis uses a Multi-Layer Perceptron, one of the better known artificial NN models. Learning occurs in the perceptron by changing connection weights after each piece of data is processed, based on the amount of error in the output compared to the predicted result. The learning process is carried out through backpropagation [176], a generalization of the least mean squares algorithm in the linear perceptron.

9.3.1. Input samples to the neural network

Two input sets are used in order to train the NN, referred to as the *NN background sample* and the *NN signal sample*. The background sample represents four-jet events in which no DPS occurs, and all four jets originate from a single interaction. This sample is constructed using MC events, where the option of turning MPI off is available. The signal sample represents DPS four-jet events, in which the two sets of jets originate from two separate interactions. Since the available MCs for the analysis do not describe well the features of hard DPS in four-jet events, this sample is constructed by an overlay of dijet events. These represent events in which two completely uncorrelated hard interactions take place in a given event.

The background and signal samples for the analysis are described in the following.

Background sample for the NN

The background input to the NN, standing for $(2 \rightarrow 4)$ pQCD events, is generated with SHERPA. The generator is run with multiple interactions turned off, using the `MI_HANDLER=None` setting.

9. Hard double parton scattering in four-jet events

The CKKW matching scale of SHERPA is set at 15 GeV. This implies that partons with transverse momentum above 15 GeV in the final state, necessarily originate from matrix elements, and not from the parton shower. All jets passing selection (having $p_t > 20$ GeV), are therefore associated with the hard interaction.

The SHERPA sample consists of truth (particle) jets, which are not passed through the full detector simulation. In order to stand on equal footing with data, the energy and momentum of truth jets are smeared according to the parametrized energy resolution of corresponding detector jets (see [section 5.5.2](#)). The energy smearing is performed as for the systematic study discussed in [section 8.5.2](#).

The p_t -spectra of the four leading jets in an event in the SHERPA sample, before and after the smearing procedure, are presented in [figure 9.3a](#). Following the smearing, the peak at low values of transverse momentum is enhanced. Due to the shape of the p_t distribution, more jets are pushed into the phase-space of the measurement than out of it. Overall, following the smearing procedure, an additional 4% of events are included in the phase-space of the measurement.

The relative p_t resolution of jets in the smeared SHERPA MC may be compared to that of detector jets in the nominal PYTHIA MC in [figure 9.3b](#). The relative p_t resolution is derived in PYTHIA by matching truth jets with detector jets. The width of the distribution of the variable,

$$O_{p_t} = \frac{p_t^{\text{rec}} - p_t^{\text{truth}}}{p_t^{\text{truth}}},$$

is taken as the relative resolution. For the PYTHIA sample, p_t^{truth} and p_t^{rec} represent the transverse momenta of truth and detector jets, respectively. For the SHERPA sample, smeared truth jets take the role of detector jets, and are matched to truth jets which are not smeared. The first bin ($10 < p_t^{\text{truth}} < 20$ GeV) in [figure 9.3b](#) shows that the resolution is over-estimated for smeared jets in SHERPA by 20%, relative to that of detector jets in PYTHIA. The discrepancy is due to the fact that the parametrized resolution is derived from *in-situ* techniques using jets with $p_t > 20$ GeV, and extrapolated to lower transverse momenta [153]. Above 20 GeV, good agreement is observed between the two MC samples. The dependence of the results of the DPS measurement on the p_t resolution of jets in SHERPA is estimated in the following. A corresponding systematic uncertainty is assigned to the measurement.

To summarize, the NN background sample consists of exclusive four-jet events. Events are selected by requiring the existence of exactly four smeared truth jets with transverse momentum, $p_t > 20$ GeV, where the leading jet is further required to have $p_t > 42.5$ GeV. This is consistent with the corresponding phase-space of the measurement, as defined in [equation \(9.1\)](#).

Signal sample for the neural network

The NN sample which describes DPS events is composed of overlaid dijet events. The natural choice would have been to use dijets from data in order to construct this sample. However, the number of events with two low- p_t jets in the data is too small in order to construct a statistically robust overlay sample. The dijets are therefore taken from the nominal PYTHIA simulation. In order to illustrate that PYTHIA describes well the characteristics of dijet events in data, distributions of the dijet invariant mass, m_{12} , are used. The measurement of the invariant mass spectra is discussed in detail in [chapter 8](#). Using the 2010 dataset, data unfolded to the hadron-level are compared to PYTHIA events in [figure 9.4](#), where truth (particle) jets are used to calculate m_{12} in PYTHIA. The PYTHIA MC is consistent with the data within the uncertainties.

The first step in constructing the overlaid sample is selection of exclusive dijet events in the MC. The latter refer to events in which exactly two detector jets are reconstructed, each with transverse

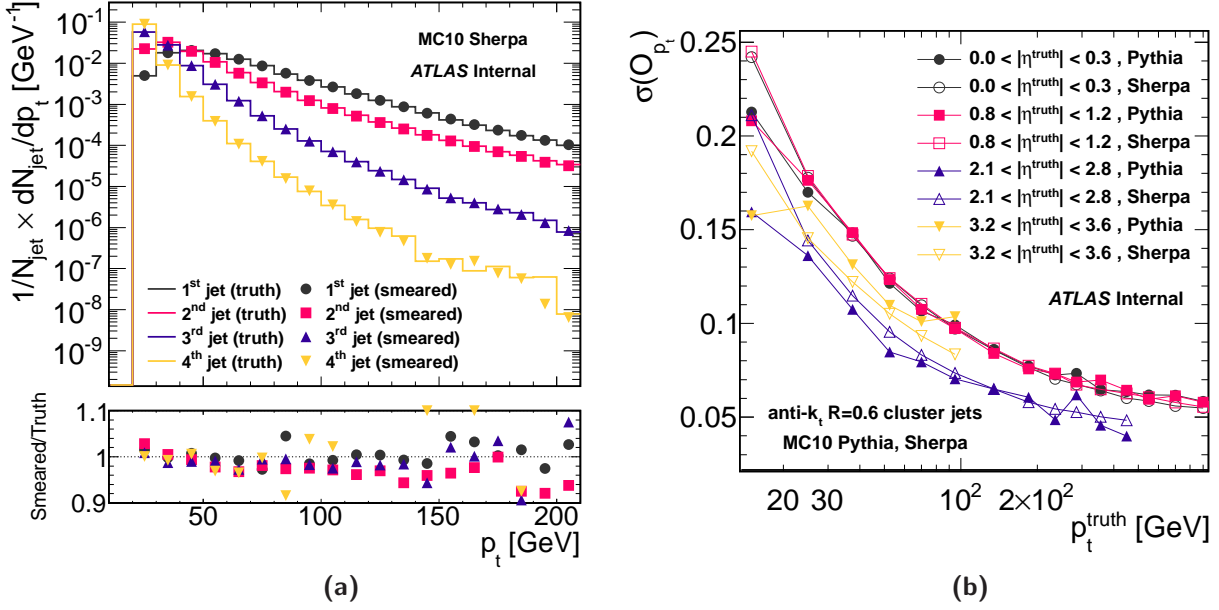


Figure 9.3. (a) Transverse momentum, p_t , spectra of truth jets and smeared truth jets in SHERPA, for the four highest- p_t jets in an event, denoted as 1st, 2nd, 3rd and 4th jet. The bottom panel shows the ratio between the spectra for each jet separately, as indicated.

(b) Relative transverse momentum resolution, $\sigma(O_{p_t})$, of jets in the smeared SHERPA MC and in the nominal PYTHIA MC, as a function of the transverse momentum of truth jets, p_t^{truth} , for jets within different ranges of pseudo-rapidity, η^{truth} , as indicated in the figure.

momentum, $p_t > 20$ GeV. Once a list of dijet events is assembled, pairs of events are overlaid into four-jet events. The conditions which must be fulfilled in order for a given pair of events to be overlaid are the following:

- none of the four jets overlaps in η, ϕ by a distance of less than 0.6 units;
- the vertex- z coordinates of the vertices in the two overlaid events are no more than 10 mm apart;
- at least one of the four jets has $p_t > 42.5$ GeV;
- only single-vertex PYTHIA events are used.

The first condition allows for the four-jet event to be reconstructed in the calorimeter to begin with; the second condition avoids possible bias, due to events where two jet pairs originate from separate vertices; the third condition is set in order to match the corresponding phase-space of the measurement; finally, the fourth condition is imposed in order to match the conditions in the data.

Once a pair of dijet events are overlaid into a four-jet event, the jets are re-ordered in p_t . As a result, the sub-leading jet in the four-jet overlay may have originally been either the sub-leading jet in the first dijet pair, or the leading jet in the second dijet pair. This reflects the signature of a four-jet DPS event in data; the ordering in p_t of the four reconstructed jets does not necessarily correspond to the two highest- p_t jets originating from one interaction and the second pair from the other interaction. The significance of the ordering in p_t of the four jets comes into play in the

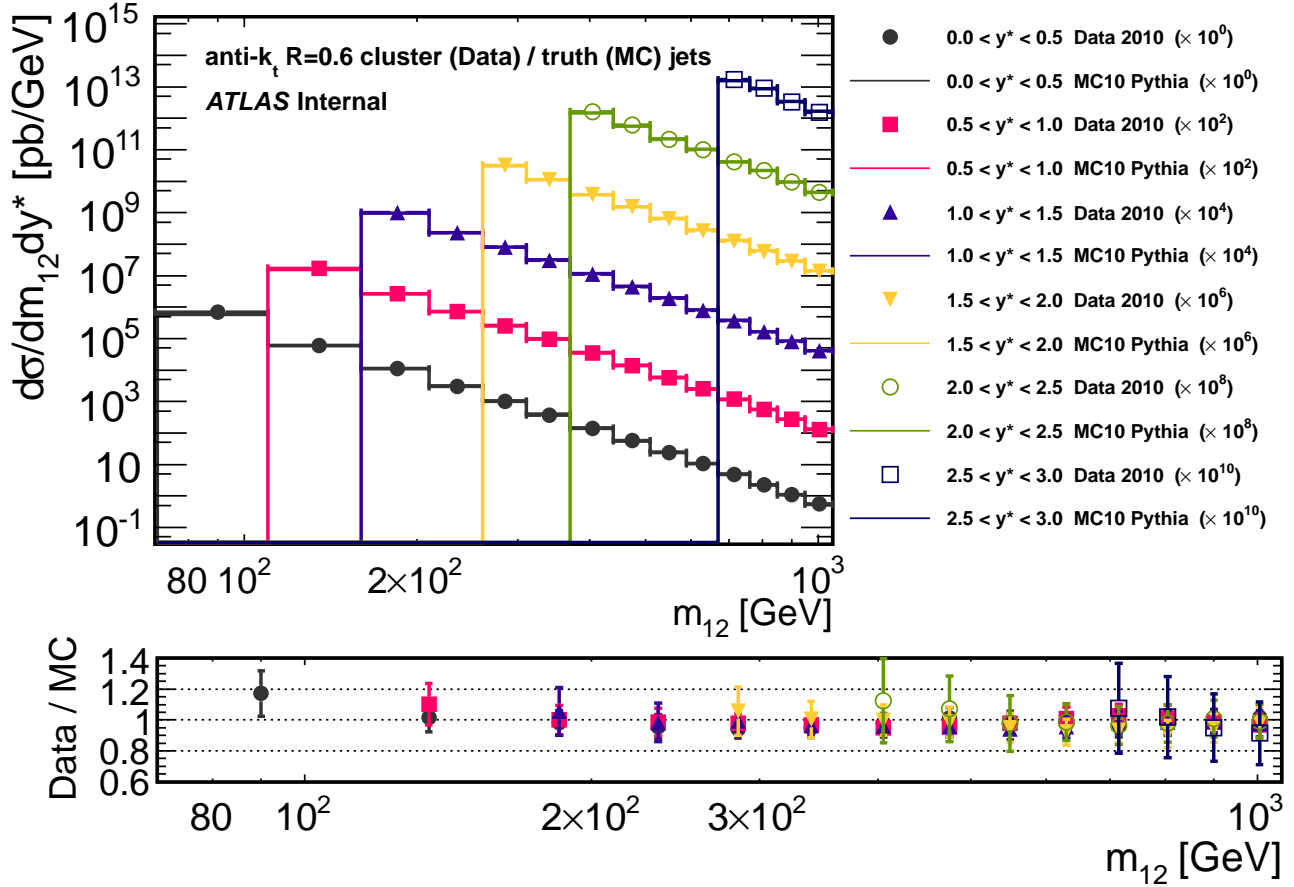


Figure 9.4. Double-differential dijet cross section as a function of the invariant mass, m_{12} , binned in center-of-mass jet rapidity, y^* , in the 2010 data, compared to the m_{12} distributions of particle (truth) jets in the nominal PYTHIA MC, where distributions are multiplied by the factors specified in the legend, the error bars represent the statistical and systematic uncertainties, added in quadrature, and the bottom panel shows the ratio of distributions between the data and the MC.

variables which constitute the input parameters to the NN. The latter are the subject of the following section.

9.3.2. Input variables to the neural network

The underlying assumption driving the analysis involving the NN is that for the case of DPS, two dijet interactions occur simultaneously and independently. On the other hand, in a $(2 \rightarrow 4)$ QCD four-jet interaction, there is correlation between all four jets in the final state.

The correlations in a $(2 \rightarrow 4)$ interaction have several characteristics; one would e.g., observe many events in which the third and fourth jets by order of p_t (assumed here to be higher-order radiative corrections to the hard scattering) are collinear in azimuth with either of the leading pair. Additionally, radiative jets are more likely to span the area in rapidity between the two hard scatterers, or between one of the latter and the beamline (the proton remnants). Up to detector effects (calibration and resolution) and additional energy flow (e.g., jets with $p_t < 20$ GeV), the four jets in

the final state are expected to all balance together in p_t . Finally, no pair-wise balance in p_t and no pair-wise back-to-back symmetry in azimuth are expected.

In a DPS event, under the assumption of uncorrelated $(2 \rightarrow 2)^{\times 2}$ QCD interactions, different topologies should be prominent. For instance, one would expect that there would be pair-wise balance in p_t between the two pairs corresponding to the two interactions. Each pair should be back-to-back in the transverse plane, and the azimuthal angle between the axes of interaction should have a random distribution. In addition, the rapidity differences between the two pairs of jets is expected to have a random distribution as well.

These potentially discriminating features motivate the choice of variables which are selected as input for the NN. Several combinations of different parameter sets have been explored. The best performance in discriminating between signal and background is achieved using the following variables:

$$\begin{aligned} \Delta_{12}^{p_t} &= \frac{|\vec{p}_{t,1} + \vec{p}_{t,2}|}{p_{t,1} + p_{t,2}} \quad , \quad \Delta_{34}^{p_t} = \frac{|\vec{p}_{t,3} + \vec{p}_{t,4}|}{p_{t,3} + p_{t,4}} \quad , \\ \Delta_{12}^{\phi} &= \phi_1 - \phi_2 \quad , \quad \Delta_{13}^{\phi} = \phi_1 - \phi_3 \quad , \quad \Delta_{23}^{\phi} = \phi_2 - \phi_3 \quad , \quad \Delta_{34}^{\phi} = \phi_3 - \phi_4 \quad , \\ \Delta_{13}^{\eta} &= \eta_1 - \eta_3 \quad , \quad \Delta_{14}^{\eta} = \eta_1 - \eta_4 \quad , \quad \Delta_{23}^{\eta} = \eta_2 - \eta_3 \quad , \quad \Delta_{24}^{\eta} = \eta_2 - \eta_4 \quad , \end{aligned} \quad (9.14)$$

where $p_{t,i}$, η_i and ϕ_i stand for the transverse momentum, pseudo-rapidity and azimuthal angle of jet i , respectively, with $i = 1, 2, 3, 4$.

The first two variables, $\Delta_{12}^{p_t}$ and $\Delta_{34}^{p_t}$, represent the normalized p_t balance between the two jets of the leading jet-pair and between the two jets of the sub-leading jet-pair, respectively. The p_t balance is normalized to the respective scalar sum of transverse momenta in order to avoid two types of bias. The first type has to do with the shape of the p_t spectrum of jets; one would like the NN to be insensitive to the shape in the MC, as it does not perfectly describe the data. A second possible source of bias is the uncertainty on the JES; dealing with normalized variables reduces the uncertainty, as the absolute energy scale does not play a direct role.

In the NN signal sample, there is no way of knowing which combination of two jet-pairs corresponds to the original configuration of the event. For instance, for a given event it is possible that jets 1 and 2 originated from one $(2 \rightarrow 2)$ interaction and jets 3 and 4 from the other; alternatively, it is also possible that jets 1 and 3 and jets 2 and 4 form the respective pairs. In order to resolve the ambiguity of jet pairing and be consistent with data, the information about which jet originated from which interaction is not used with the NN signal sample. The variables $\Delta_{12}^{p_t}$ and $\Delta_{34}^{p_t}$ are therefore constructed from the p_t -ordered jets.

Normalized distributions of $\Delta_{12}^{p_t}$ and of $\Delta_{34}^{p_t}$ in the NN signal and background samples are shown in [figure 9.5](#). For the NN signal sample, both distributions peak at low values, indicating that both the leading and the sub-leading jet pairs are balanced in p_t . The small peak around unity likely indicates events in which the re-ordering of jet- p_t switches the positions of jets 2 and 3. For the NN background sample, the leading jet-pair exhibits a wider peak at low values of $\Delta_{12}^{p_t}$ compared to that in the signal sample. This is due to the fact that the two leading jets can not balance well in p_t , as the second pair of jets carries some of the momentum of the same hard scatter. The distribution of $\Delta_{34}^{p_t}$ in the background sample peaks around unity, indicating that in most events jets 3 and 4 are both collinear with a single one of the two leading jets. The tail toward lower values of $\Delta_{34}^{p_t}$ corresponds to events in which each of the leading jets is collinear with one of the two sub-leading jets. In such events, a partial balance in p_t is possible, as the two leading jets are in most cases approximately back-to-back.

9. Hard double parton scattering in four-jet events

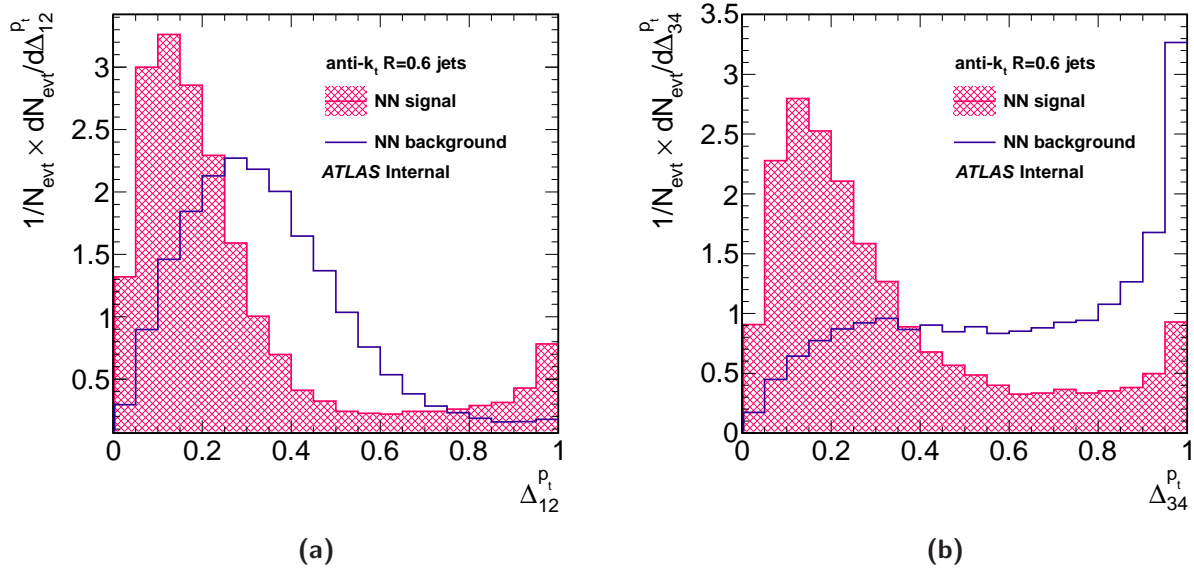


Figure 9.5. Normalized differential distributions of the variables, $\Delta_{12}^{p_t}$ (a) and $\Delta_{34}^{p_t}$ (b), which are defined in equation (9.14), for the signal and background input samples of the NN, as indicated.

The second set of input variables, Δ_{ij}^ϕ ($ij = 12, 13, 23$ and 34), represents the “back-to-back”-ness of the different jet-pair combinations, and the relative angles between the two axes of interaction for each combination of jet-pairs. Here information regarding all possible combinations is preserved (either explicitly, or through the difference between a pair of Δ_{ij}^ϕ variables); pairing ambiguity is thus avoided. Similarly, the variables Δ_{ij}^η ($ij = 13, 14, 23$ and 24) represent the full information of the relative pseudo-rapidity between any pair of jets of the four-jet system.

Normalized distributions of the different Δ_{ij}^ϕ and Δ_{ij}^η variables in the NN signal and background samples are shown in figures 9.6 and 9.7. As expected, the Δ_{ij}^ϕ variables show that in the NN signal sample the two pairs of jets are in most cases back-to-back. The corresponding distributions for the azimuthal differences between jets 1 and 3 and between jets 2 and 3 are relatively flat, as these differences are random by construction. The small enhancements around $\pm\pi$ represent events in which the re-ordering of jets in p_t had switched the order between jets 2 and 3. In the NN background sample, the two leading jets are only approximately back-to-back, resulting in wider peaks around $\pm\pi$ in Δ_{12}^ϕ , compared to the signal sample. The peaks around $\pm\pi$ in Δ_{13}^ϕ correspond to events in which jet 2 emits collinear radiation, and thus the leading jet approximately remains back-to-back with both jets 2 and 3. As expected, the distribution of Δ_{23}^ϕ features peaks close to zero. The angle between jets 3 and 4 in the background sample is mostly random, though small enhancements around $\pm\pi$ indicate events in which each of the leading jets is collinear with a jet of the sub-leading pair.

Inspection of the distributions of the Δ_{ij}^η variables shows significant differences between the signal and background samples, only for Δ_{23}^η and for Δ_{24}^η . The differences are characterized by peaks around small Δ_{23}^η and Δ_{24}^η values in the background sample, which are not present in the NN signal. As expected, these indicate that QCD radiation tends to fill-in the rapidity region between the hardest

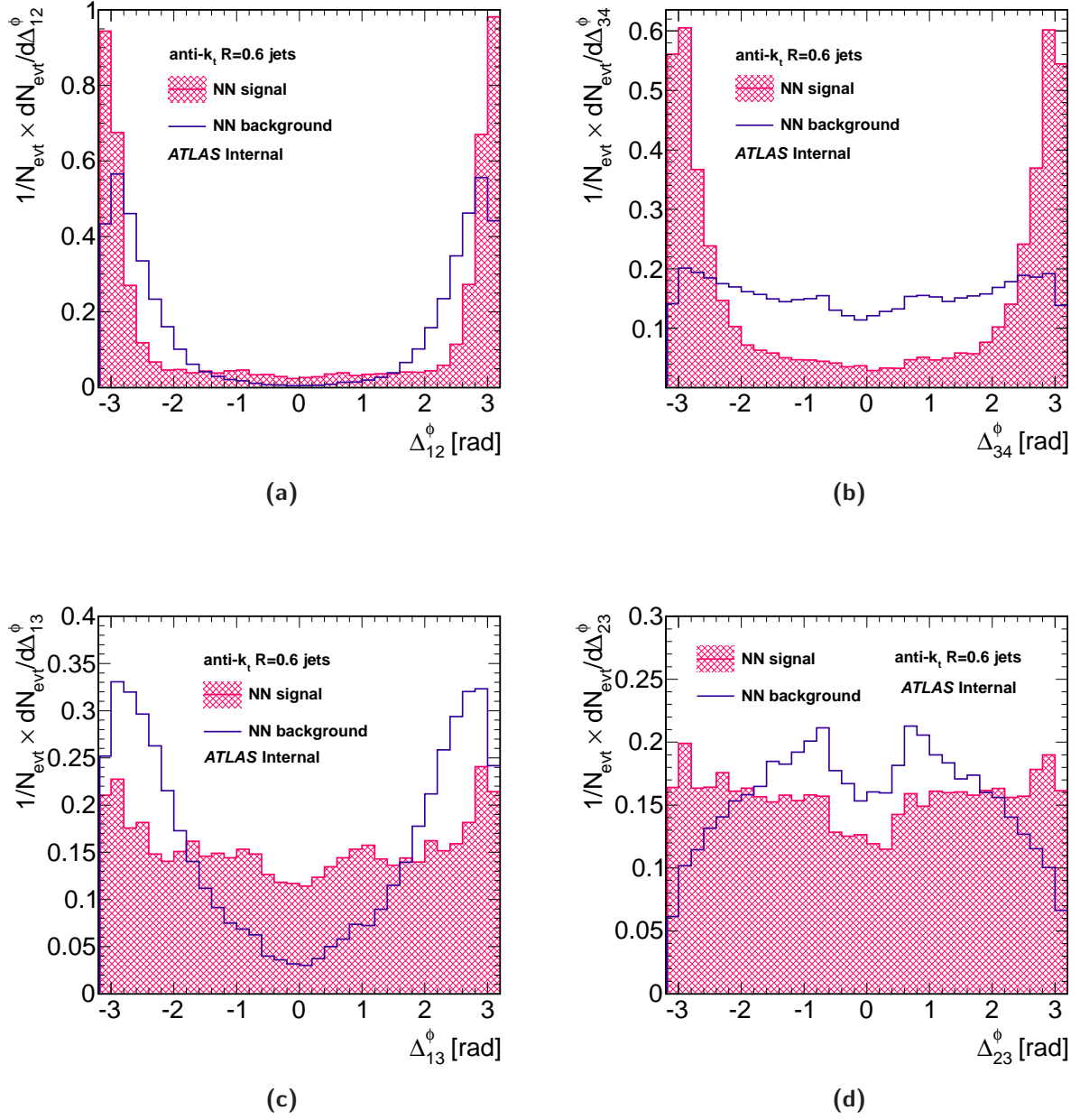


Figure 9.6. Normalized differential distributions of the variables, Δ_{12}^ϕ (a), Δ_{34}^ϕ (b), Δ_{13}^ϕ (c) and Δ_{23}^ϕ (d), which are defined in equation (9.14), for the signal and background input samples of the NN, as indicated.

9. Hard double parton scattering in four-jet events

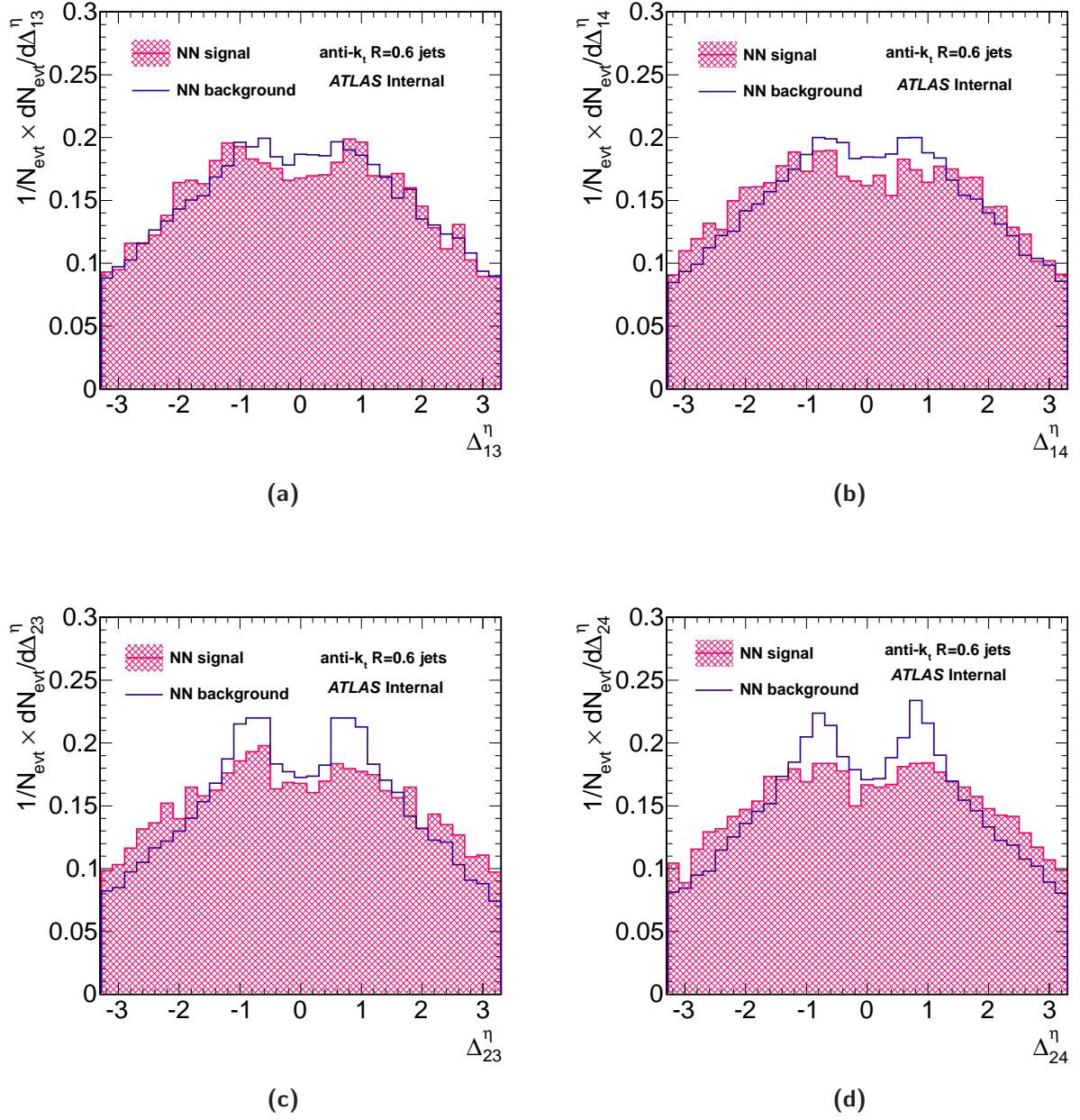


Figure 9.7. Normalized differential distributions of the variables, Δ_{13}^η (a), Δ_{14}^η (b), Δ_{23}^η (c) and Δ_{24}^η (d), which are defined in equation (9.14), for the signal and background input samples of the NN, as indicated.

scattering objects (or between the latter and the proton remnants).

9.3.3. Training and output of the neural network

Once the signal and background samples for the NN are prepared, events from each are divided into two (statistically independent) sub-samples, the *training sample* and the *test sample*. As the names imply, the former is used to train the NN, and the latter to test the robustness of the result. The same number of events from the signal and background samples is used for the training of the NN. In all subsequent figures, only the test signal and background samples are shown.

The final structure of the NN consists of two hidden layers. The input layer has ten neurons, the first and second hidden layers have eight and four neurons, respectively, and the output of the network is a single neuron (a single number). These choices represent the product of an optimization study on the performance of the NN, and balance the complexity of the network with the computation time of the training.

During the training phase of the NN, weights between the various input-layer neurons are modified, changing the output of the network. The result is quantified by an error function, E_{NN} , which measures the agreement of the response of the network with the desired result. Figure 9.8a shows the value of E_{NN} as a function of the number of training cycles of the network. The training should be stopped when E_{NN} deteriorates for the test sample relative to the training sample. Here, training is stopped after 2000 epochs, as E_{NN} converges to a stable value for the training sample, and there is an ever so slight indication of deterioration for the test sample. Attempts to use a higher number of training cycles did not achieve improved performance in E_{NN} . The chosen structure of the NN and the final set of weights after completion of the training are illustrated in figure 9.8b. The circles represent neurons, where each column stands for a layer of the network, and the width of a connecting line between neurons is proportional to the magnitude of the respective weight. The larger the weight of a given neuron, the more significant the contribution of the corresponding variable.

The output of the NN is quantified by the parameter, ξ_{NN} , which typically takes values in the range $[0, 1]$. An output close to zero is classified by the NN as more likely to belong to the background sample, while values close to unity are associated with signal events. Normalized distributions of the output of the NN for the signal and background training samples are shown in figure 9.9a. There is good separation between the two inputs, with prominent peaks of the background around zero and of the signal around unity, as required.

The NN is used in order to determine the fraction of DPS events in four-jet events in data. A distribution of ξ_{NN} in data, normalized to one (\mathcal{D}), is fitted to a combination of the distributions of the signal (\mathcal{S}) and background (\mathcal{B}) samples, each normalized to one. The result of the fit in the form,

$$\mathcal{D} = (1 - f_{\text{DPS}}) \cdot \mathcal{B} + f_{\text{DPS}} \cdot \mathcal{S} , \quad (9.15)$$

is shown in figure 9.9b. The fitted value is

$$f_{\text{DPS}} = 0.081 \pm 0.004 , \quad (9.16)$$

where the goodness-of-fit, χ^2 , divided by the number of degrees of freedom of the fit (NDF) yields

$$\chi^2/\text{NDF} = 1.2 .$$

9. Hard double parton scattering in four-jet events

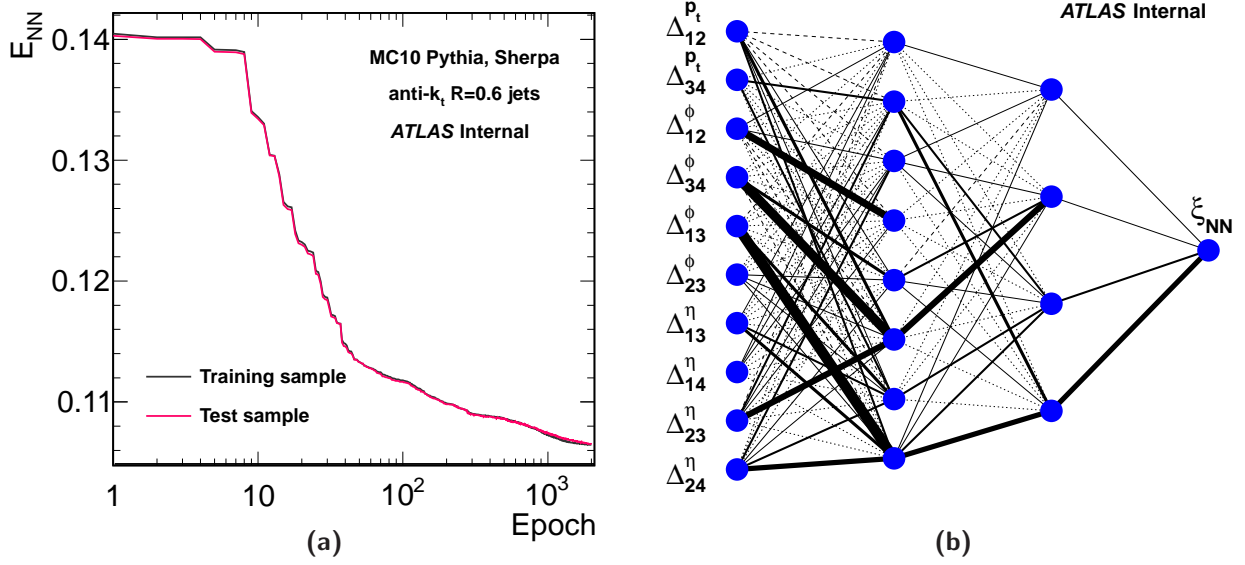


Figure 9.8. (a) Dependence of the value of the error function of the NN, E_{NN} , on the number of training cycles (epoch) of the network, for the NN training and test samples, as indicated in the figure.

(b) Schematic depiction of the structure of the NN, where neurons are denoted by blue circles, layers are denoted by columns of circles, and lines represent the weights which connect neuron pairs, where the thickness of a line is proportional to the relative magnitude of the corresponding weight. Each input variable, depicted by the various Δ symbols (see equation (9.14)), corresponds to a neuron in the first layer of the network. The output of the NN is denoted by ξ_{NN} .

In order to get a qualitative assessment of the fitted value of f_{DPS} , normalized distributions of the input variables to the NN are used. The data are compared to the expectation, based on a combination of the signal and background samples, in proportion according to $f_{DPS} = 8.1\%$. The results are shown in section A.5, figures A.15 - A.17. A good description of the data in most regions of phase-space is achieved. The difficulty in extracting the signal from an individual distribution can be inferred from this comparison. It is only the correlations between the variables, captured by the NN, that allow to improve the sensitivity to the presence of the signal.

Using the output of the NN, it is possible to construct samples of depleted ($\xi_{NN} \sim 0$) and enriched ($\xi_{NN} \sim 1$) DPS events. The momentum fraction of the two interacting partons, x , is computed, as in equation (8.3), for the leading and sub-leading jet pairs in four-jet events in the data. The distributions of x for depleted and enriched DPS events are compared in figure 9.10. The four-jet events in the data reach down to momentum fractions, $x \sim 10^{-4}$. The sub-leading pair of jets is on average associated with partons with lower values of x compared to the leading pair, due to the difference in jet p_t . The sample of enriched DPS events is characterised by slightly lower values of x compared to the depleted sample, as expected.

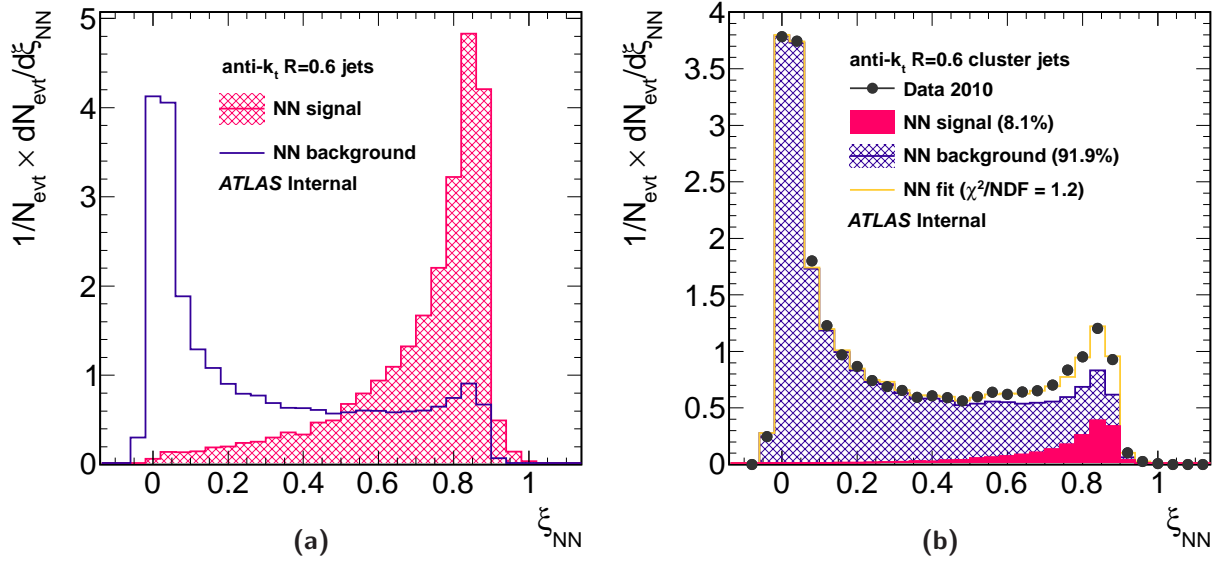


Figure 9.9. (a) Differential distributions, normalized to unity, of the output parameter of the NN, ξ_{NN} , for the signal and background input samples, as indicated in the figure. (b) Differential distributions of ξ_{NN} for four-jet events from the 2010 data, for the signal and background input samples of the NN and for the sum of the two input samples (denoted by “NN fit”), where the signal and background samples are each normalized according to the fit of the fraction of DPS events, as explained in the text. The goodness-of-fit and the number of degrees of freedom of the fit are respectively denoted by χ^2 and NDF.

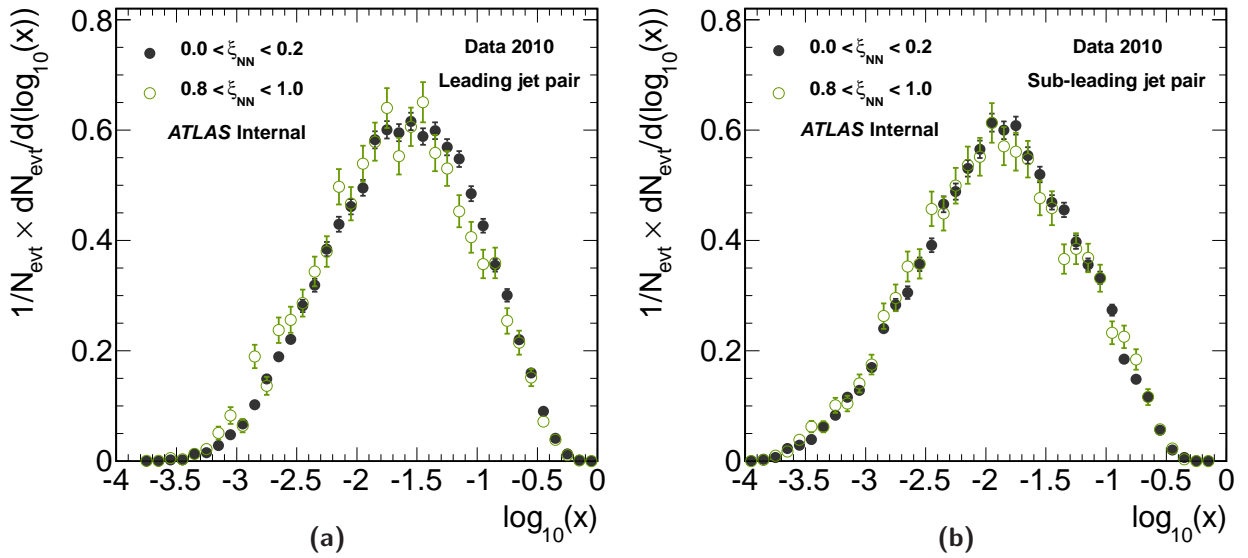


Figure 9.10. Normalized differential distributions of the momentum fraction of the two interacting partons, x , associated with the leading (a) and with the sub-leading (b) jet pairs in four-jet events in the 2010 data, for events with different values of the output parameter of the NN, ξ_{NN} , as indicated in the figures.

9.4. Systematic and statistical uncertainties

The measurement of σ_{eff} is sensitive to several sources of uncertainty, which are correlated in ways which are hard to evaluate. The primary uncertainty on σ_{eff} originates from that on the jet energy scale (JES), which influences distributions in the data. The JES uncertainty affects both the value of \mathcal{S}_{4j}^{2j} , which is directly measured in data, as well as that of f_{DPS} , since the fit on the value of the latter is performed using four-jet events from the data.

Additional sources of systematics have to do with the uncertainty in the simulation of the resolution of jets in energy, in azimuth and in rapidity. These types of uncertainties affect the value of α_{2j}^{4j} , which is directly evaluated in MC, as well as that of f_{DPS} , as the MC is used to construct the input samples of the NN. Estimation of the uncertainties in this case requires for the NN to be re-trained several times. The subsequent fit for the value of f_{DPS} on a re-trained network is subject not only to the uncertainty associated with the MC, but also to fluctuations in the data. Since the correlations are difficult to disentangle, a conservative approach is taken, in which they are considered uncorrelated.

Uncertainty on the jet energy scale

The procedure for evaluating the uncertainty on the JES follows that which is described in [section 8.5](#) for the measurement of the dijet mass cross section. Six sources of uncertainty (see [section 5.5](#)) are considered; single hadron response, cluster thresholds, Perugia 2010, Alpgen+Herwig+Jimmy, intercalibration and relative non-closure.

The effects of the different components of the JES uncertainties on the observed cross sections and on the fitted value of f_{DPS} are estimated by introducing positive and negative variations to the energy scale of jets. The variations are randomly distributed according to a Gaussian function, with the respective source of uncertainty as its width. After the energy of jets is varied, they are re-sorted according to p_t , and the event is either rejected, or accepted. Accepted events fall under one of the classifications of observed cross sections, a dijet event of type a or b , or a four-jet event of type b . The systematic uncertainty on the cross sections is estimated as the difference between the integrated observed cross sections with and without the JES variations.

For each source of uncertainty, the value of f_{DPS} is estimated. This is done by fitting a combination of the nominal signal and background samples of the NN to four-jet data, where the data had been subjected to JES variations. The uncertainty on f_{DPS} is taken as the difference between the result of this fit and the nominal value.

The value of σ_{eff} is recalculated for every change of the ratio $\mathcal{S}_{4j}^{2j}/f_{\text{DPS}}$, that is for every component of the JES uncertainty. The contributions to the uncertainty on σ_{eff} from the different sources are considered uncorrelated, and so the total uncertainty is computed as the quadratic sum of all components.

The uncertainties are listed in [table 9.1](#), where those on \mathcal{S}_{4j}^{2j} and on f_{DPS} are given separately, for completeness. The JES uncertainties on σ_{eff} come out asymmetric, and amount to $^{+5.1}_{-18.4}\%$. Most of the downward uncertainties on σ_{eff} originate from the increase of the energy scale in the data, relative to the MC. The increase in the energy scale results in increasing the number of low- p_t topologies in the data. This leads to an increase of f_{DPS} , which turns out to be stronger than the increase in the value of \mathcal{S}_{4j}^{2j} .

Uncertainty on the properties of jets in the MC

The main source of uncertainty on jets in the MC is that on the jet energy resolution. The uncertainty on the resolution directly affects α_{2j}^{4j} , as it influences the migration of events in and out of the

accepted phase-space of the measurement. The response of the NN is less sensitive to the energy resolution in comparison, since $\Delta_{12}^{p_t}$ and $\Delta_{34}^{p_t}$ do not have high NN-significance. On the other hand, the various Δ^ϕ variables, which carry high weights in the NN, cause the network to be sensitive to the uncertainty on the azimuthal angle of jets in the input samples.

In order to assess the effect of the MC uncertainties on the measurement, the properties of jets in the simulation are distorted. This is done, either according to the uncertainty on the various resolution parameters, or by re-weighting the p_t distribution. The distorted MC samples are used to estimate the acceptance for each class of events, \mathcal{A}_{2j}^a , \mathcal{A}_{2j}^b and \mathcal{A}_{4j}^b . The combination of these leads to a value of α_{2j}^{4j} which is different than the nominal value. The difference between the two is taken as the associated uncertainty.

In addition, the distorted MCs serve as input for training of the NN. Using the re-trained network, f_{DPS} is extracted by fitting a combination of the distorted signal and background samples to the nominal sample of four-jet data events. This value of f_{DPS} is compared to the nominal one in order to estimate the associated uncertainty.

The difference in the ratio $\alpha_{2j}^{4j}/f_{\text{DPS}}$ compared to the nominal value is computed for each source of uncertainty and translated into a change in σ_{eff} . The different sources are considered as uncorrelated, and so the quadratic sum of all such elements is taken as the combined uncertainty on σ_{eff} .

As mentioned above, the result of the fit for f_{DPS} is sensitive to fluctuations in the four-jet data sample. These fluctuations are not addressed each time the network is retrained, as the same data are compared to different combinations of MC samples (also used to train the network). The assumption that the different elements of the uncertainty are uncorrelated is, therefore, a conservative estimation of the uncertainty. The uncertainties are listed in [table 9.1](#), where those on α_{2j}^{4j} and on f_{DPS} are given separately, for completeness. The MC uncertainties on σ_{eff} amount to $^{+9.6}_{-11.5}\%$.

Statistical uncertainty on the data

The statistical uncertainty on the four-jet data sample and on the signal and background input samples to the NN, all affect the result of the fit for f_{DPS} . However, the statistical uncertainty on the data also affects the value of the observed four-jet cross section, and accordingly also the value of \mathcal{S}_{4j}^{2j} . Instead of calculating the correlation analytically, the combined uncertainty on σ_{eff} is estimated numerically. This is done by smearing the values of each data point in the distributions of ξ_{NN} of the NN inputs, and of the four-jet data sample. The shifts in value are performed within one standard deviation of the nominal values, where the magnitude of the deviations is derived from the respective statistical uncertainty. The smeared samples are then used to perform the fit for the fraction of DPS events, denoted as \tilde{f}_{DPS} . The ratio of observed cross sections is similarly treated (varying σ_{2j}^a and σ_{2j}^b in addition to σ_{4j}^b), resulting in the “smeared” ratio of cross sections, $\tilde{\mathcal{S}}_{4j}^{2j}$.

Using [equation \(9.7\)](#) together with the nominal value of the acceptance ratio, one may define the quantity,

$$\tilde{\sigma}_{\text{eff}} = \frac{\tilde{\mathcal{S}}_{4j}^{2j} \alpha_{2j}^{4j}}{\tilde{f}_{\text{DPS}}}, \quad (9.17)$$

which represents the value of σ_{eff} , following the smearing procedure. The fractional bias in the value of σ_{eff} due to the smearing is then defined as

$$O_{\tilde{\sigma}_{\text{eff}}} = \frac{\tilde{\sigma}_{\text{eff}} - \sigma_{\text{eff}}}{\sigma_{\text{eff}}}. \quad (9.18)$$

9. Hard double parton scattering in four-jet events

The smearing and fitting steps are performed many times, resulting in a distribution of values of $O_{\tilde{\sigma}_{\text{eff}}}$, shown in [figure 9.11](#). The distribution is asymmetric. The final relative uncertainty on σ_{eff} of $+2.9\%$, is thus obtained by finding the $\pm 35\%$ confidence region around zero.

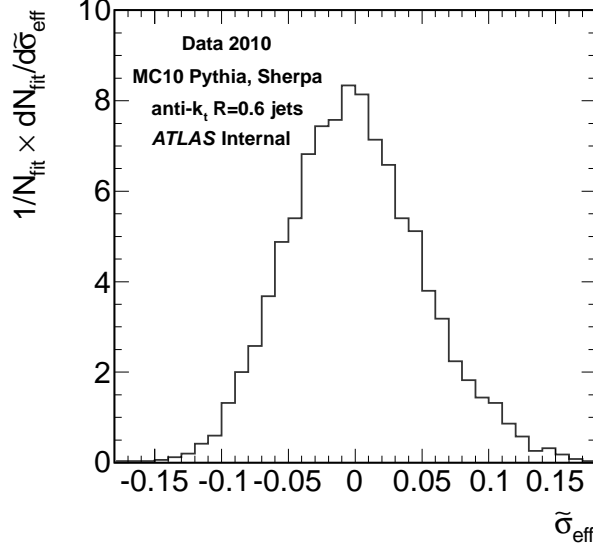


Figure 9.11. Normalized differential distribution of $O_{\tilde{\sigma}_{\text{eff}}}$, the relative bias in the effective cross section for DPS, due to the statistical uncertainty on the latter.

Summary of the uncertainties

A summary of the systematic and statistical uncertainties on the various elements of the measurement is shown in [table 9.1](#). The uncertainties on S_{4j}^{2j} , α_{2j}^{4j} and f_{DPS} are individually derived for completeness. The uncertainty on α_{2j}^{4j} due to limited MC statistics is propagated to σ_{eff} as a systematic uncertainty. In addition to the uncertainties discussed above, the uncertainty on the luminosity is considered as well.

The uncertainties on σ_{eff} are calculated by taking into account the respective combination of elements for each source, as previously discussed. The largest uncertainty on σ_{eff} is due to that on the JES. The final relative uncertainty on σ_{eff} comes out as $+3_{-5}^{\text{stat.}}$ $+12_{-22}^{\text{syst.}}$ %.

Source of uncert. in [%]	\mathcal{S}_{4j}^{2j}	α_{2j}^{4j}	f_{DPS}	σ_{eff}
Jet energy scale	+10.2 / -8.2	–	+28.9 / -12.8	+5.1 / -18.4
Luminosity	+3.5 / -3.3	–	–	+3.5 / -3.3
Jet properties in MC	–	± 7	± 11	+9.6 / -11.5
Limited MC statistics	–	± 3	–	± 3
Total relative syst. uncert.	+11 / -9	± 7.5	+31 / -17	+12 / -22
Relative stat. uncert.	± 3	–	± 5	+3 / -5

Table 9.1. Summary of the relative systematic and statistical uncertainties on the various elements of the DPS measurement; the ratio of observed cross sections, \mathcal{S}_{4j}^{2j} , the acceptance ratio, α_{2j}^{4j} , the fraction of DPS events, f_{DPS} , and the effective cross section for DPS, σ_{eff} . The individual components of the uncertainty are described in the text.

9.5. Results and summary of the measurement

A measurement of hard double parton scattering in four-jet events is performed. The measurement utilizes a sub-sample of the 2010 ATLAS dataset, consisting of single-vertex events of proton-proton collisions at center-of-mass energy, $\sqrt{s} = 7$ TeV. Four-jet events are defined as those in which exactly four jets with transverse momentum, $p_t > 20$ GeV, and pseudo-rapidity, $|\eta| < 4.4$, are reconstructed. Events are further constrained such that the highest- p_t jet has $p_t > 42.5$ GeV. The rate of DPS events is extracted from data using a neural network, assuming that the topology of the DPS events is the same as for a random combination of exclusive dijet production. Complemented by measurements of the dijet and four-jet cross sections in the appropriate phase-space regions, the effective cross section for DPS, σ_{eff} , is calculated.

The ratio of observed cross sections, the acceptance ratio, and the fraction of DPS events, are respectively found to be

$$\begin{aligned}
 \mathcal{S}_{4j}^{2j} &= 1.48 \pm 0.04 \quad (\text{stat.}) \quad {}^{+0.16}_{-0.13} \quad (\text{syst.}) \text{ mb} , \\
 \alpha_{2j}^{4j} &= 0.88 \quad \pm 0.07 \quad (\text{syst.}) , \\
 f_{\text{DPS}} &= 0.081 \pm 0.004 \quad (\text{stat.}) \quad {}^{+0.025}_{-0.014} \quad (\text{syst.}) .
 \end{aligned}$$

The combination of these yields

$$\sigma_{\text{eff}} = 16.0 {}^{+0.5}_{-0.8} \text{ (stat.) } {}^{+1.9}_{-3.5} \text{ (syst.) mb} . \quad (9.19)$$

This result is consistent with previous measurements, performed in ATLAS and in other experiments [23–28], all of which are summarized in [figure 9.12](#).

The measured value of σ_{eff} is smaller than would have been expected from the gluon form factor

of the proton. Following the suggestion in [81], an attempt in the signal-enhanced region of the NN ($\xi_{\text{NN}} > 0.8$), was made to look for the $(3 \rightarrow 4)$ topology discussed in section 2.4, in which the balance in p_t should be correlated between the two pairs of jets. No correlation was observed between $\Delta_{12}^{p_t}$ and $\Delta_{34}^{p_t}$ in this region, which does not preclude the existence of the $(3 \rightarrow 4)$ process, as it might be obscured by the resolution in the Δ^{p_t} variables.

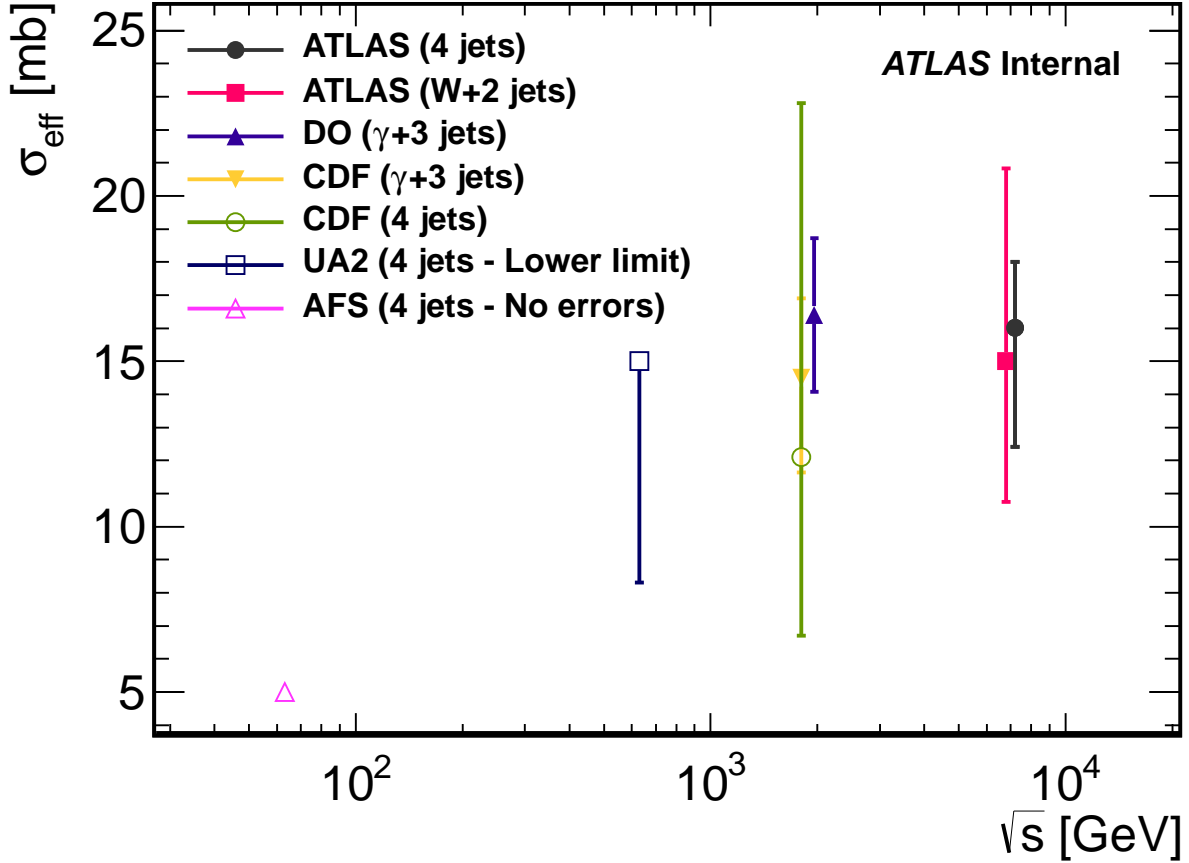


Figure 9.12. Dependence of the effective cross section for DPS, σ_{eff} , on center-of-mass energy, \sqrt{s} , in different processes and different experiments, including the current measurement (ATLAS (4 jets)), as well as those described in section 2.4, table 2.1 [23–28]. The error bars on the data points represent the statistical and systematic uncertainties, added in quadrature. The two ATLAS measurements at $\sqrt{s} = 7$ TeV are slightly shifted in center-of-mass energy, in order to improve the visual distinction between the two data points.

10. Summary

Jet production is the dominant hard scattering process in the Standard Model. As such, final states which involve high- p_t jets are an important background for many searches for new physics, e.g., those which involve the decay products of heavy objects. The study of jets also provides an ideal avenue to probe QCD and parton distribution functions, which describe the distribution of the momenta of quarks and gluons within a proton. The two measurements presented in this thesis, of the dijet double-differential cross section and of double parton scattering in four-jet events, provide insight into the high-energy regime of jet production.

The dijet double-differential cross section is measured as a function of the dijet invariant mass, for various center-of-mass jet rapidities, y^* . It uses anti- k_\perp , $R = 0.6$ jets in data taken during 2010 and during 2011 with the ATLAS experiment at a center-of-mass energy, $\sqrt{s} = 7$ TeV. Jets in the 2011 dataset are characterized by severe background of additional proton-proton collisions (pile-up). A new technique for pile-up subtraction, the jet area/median method, is developed and used in the analysis. The measurements are sensitive to dijet masses between 70 and 4.27 TeV, including y^* values up to 3.5. The data are compared to fixed-order NLO pQCD predictions, using NLOJET++ with the CT10 PDF set, and corrected for non-perturbative effects. The results, which span 12 orders of magnitude, agree well with the predictions within the theoretical and experimental uncertainties. These represent stringent tests of pQCD in an energy regime previously unexplored.

A measurement of hard double parton scattering in four-jet events is also performed, using a sub-sample of the 2010 ATLAS dataset. Here four-jet events are defined as those in which exactly four jets with transverse momentum, $p_t > 20$ GeV, and pseudo-rapidity, $|\eta| < 4.4$, are reconstructed, where the highest- p_t jet is further constrained to have $p_t > 42.5$ GeV. The rate of double parton scattering events is estimated using a neural network. A clear signal is observed, under the assumption that the DPS signal can be represented by a random combination of exclusive dijet production. The fraction of DPS candidate events is determined to be $f_{\text{DPS}} = 0.081 \pm 0.004$ (stat.) $^{+0.025}_{-0.014}$ (syst.) in the analyzed phase-space of four-jet topologies. Combined with measurements of the dijet and four-jet cross sections in the appropriate phase-space regions, the effective cross section is found to be, $\sigma_{\text{eff}} = 16.0^{+0.5}_{-0.8}$ (stat.) $^{+1.9}_{-3.5}$ (syst.) mb. This result is consistent within the quoted uncertainties with previous measurements of σ_{eff} at center-of-mass energies between 63 GeV and 7 TeV, using several final states.

A. Additional figures and tables

Auxiliary figures and tables, pertaining to different chapters in the thesis, are presented in the following.

A.1. Jet reconstruction and calibration

The quality criteria for jet selection, discussed in [chapter 5](#), [section 5.4](#), are summarized in [table A.1](#).

2010		
	Loose	Medium
HEC spikes	$(f_{\text{HEC}} > 0.5, \mathcal{S}_{\text{HEC}} > 0.5)$ OR $ E_{\text{neg}} > 60 \text{ GeV}$	Loose OR $f_{\text{HEC}} > 1 - \mathcal{S}_{\text{HEC}} $
Coherent EM noise	$(f_{\text{EM}} > 0.95, f_{\text{qlt}} > 0.8, \eta_{\text{jet}} < 2.8)$	Loose OR $(f_{\text{EM}} > 0.9, \mathcal{S}_{\text{EM}} > 0.8, \eta_{\text{jet}} < 2.8)$
Non-collision background	$ t_{\text{jet}} > 25 \text{ ns}$ OR $(f_{\text{EM}} < 0.05, f_{\text{ch}} < 0.05, \eta_{\text{jet}} < 2)$ OR $(f_{\text{EM}} < 0.05, \eta_{\text{jet}} \geq 2)$ OR $(f_{\text{max}} > 0.99, \eta_{\text{jet}} < 2)$	Loose OR $ t_{\text{jet}} > 10 \text{ ns}$ OR $(f_{\text{EM}} < 0.05, f_{\text{ch}} < 0.1, \eta_{\text{jet}} < 2)$ OR $(f_{\text{EM}} > 0.95, f_{\text{ch}} < 0.05, \eta_{\text{jet}} < 2)$

2011	
	Loose
HEC spikes	$(f_{\text{HEC}} > 0.5, \mathcal{S}_{\text{HEC}} > 0.5)$ OR $ E_{\text{neg}} > 60 \text{ GeV}$
Coherent EM noise	$(f_{\text{EM}} > 0.95, f_{\text{qlt}} > 0.8, \eta_{\text{jet}} < 2.8)$
Non-collision background	$ t_{\text{jet}} > 25 \text{ ns}$

Table A.1. Loose and Medium selection criteria, used to reject fake jets and non-collision background in data taken during 2010 and during 2011, as indicated. The pseudo-rapidity of jets is denoted as $|\eta_{\text{jet}}|$. (See also [section 5.4](#), [figure 5.4](#) and accompanying text for definition of the various variables.)

A.2. Data selection

Additional figures and tables pertaining to [chapter 6](#) are presented in the following; the efficiencies for various jet triggers are shown in [figures A.1 - A.2](#); the plateau per-jet trigger efficiency for various data taking periods in 2010 is shown in [table A.2](#); the integrated luminosity for different trigger combinations used in the analysis is shown in [tables A.3 - A.5](#).

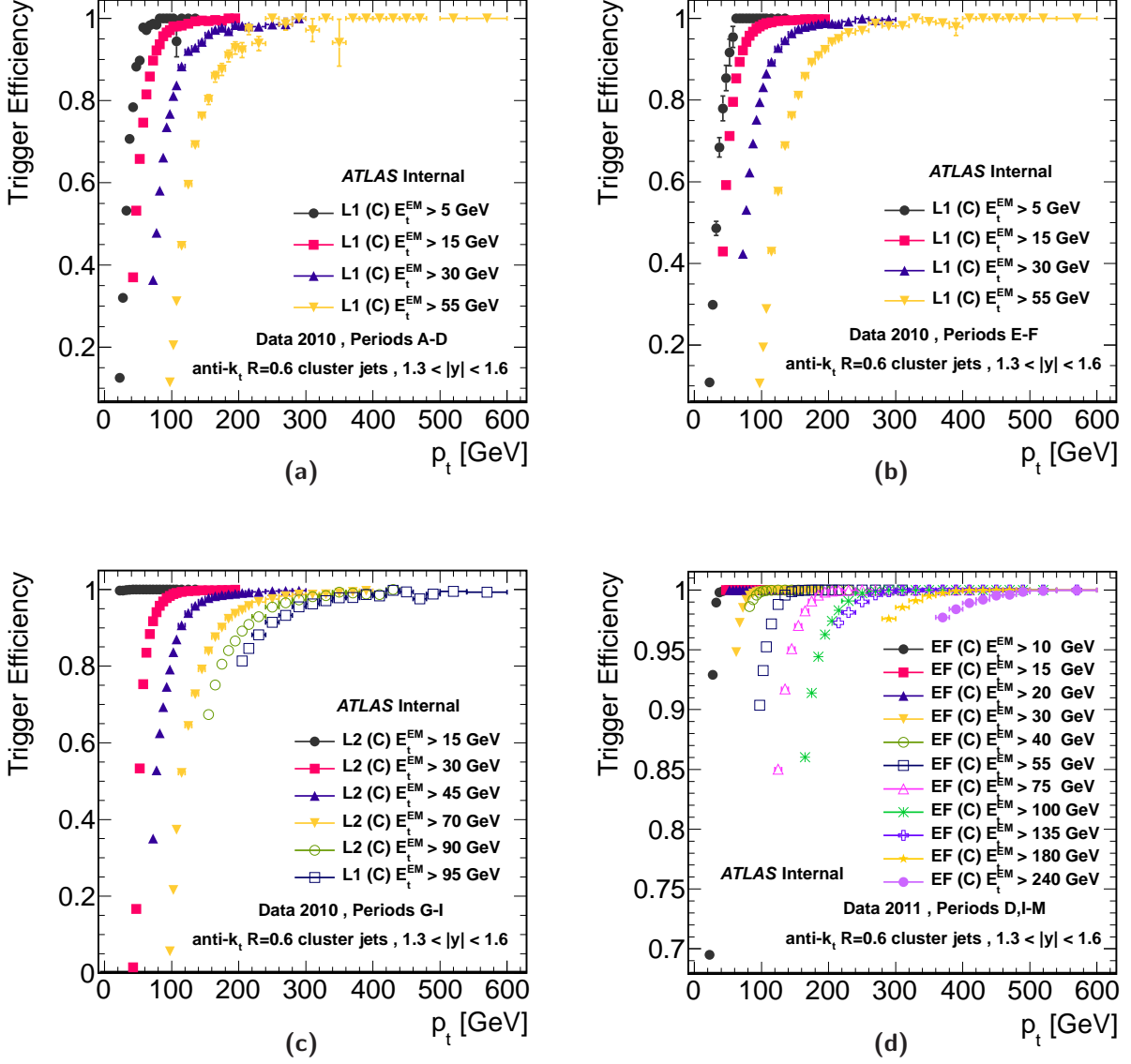


Figure A.1. Trigger efficiency curves for various Level 1 (L1), Level 2 (L2) and Event Filter (EF) triggers. Several 2010 ((a), (b) and (c)) and 2011 (d) data taking periods are represented, as indicated in the figures. The triggers are associated with jets within rapidity $1.3 < |y| < 1.6$, belonging to the central jet trigger system, denoted by (C). Trigger thresholds are denoted by E_t^{EM} , signifying the minimal transverse energy at the electromagnetic scale, of a jet which is required to fire the trigger. (See also [chapter 6](#), [figure 6.1](#) and accompanying text.)

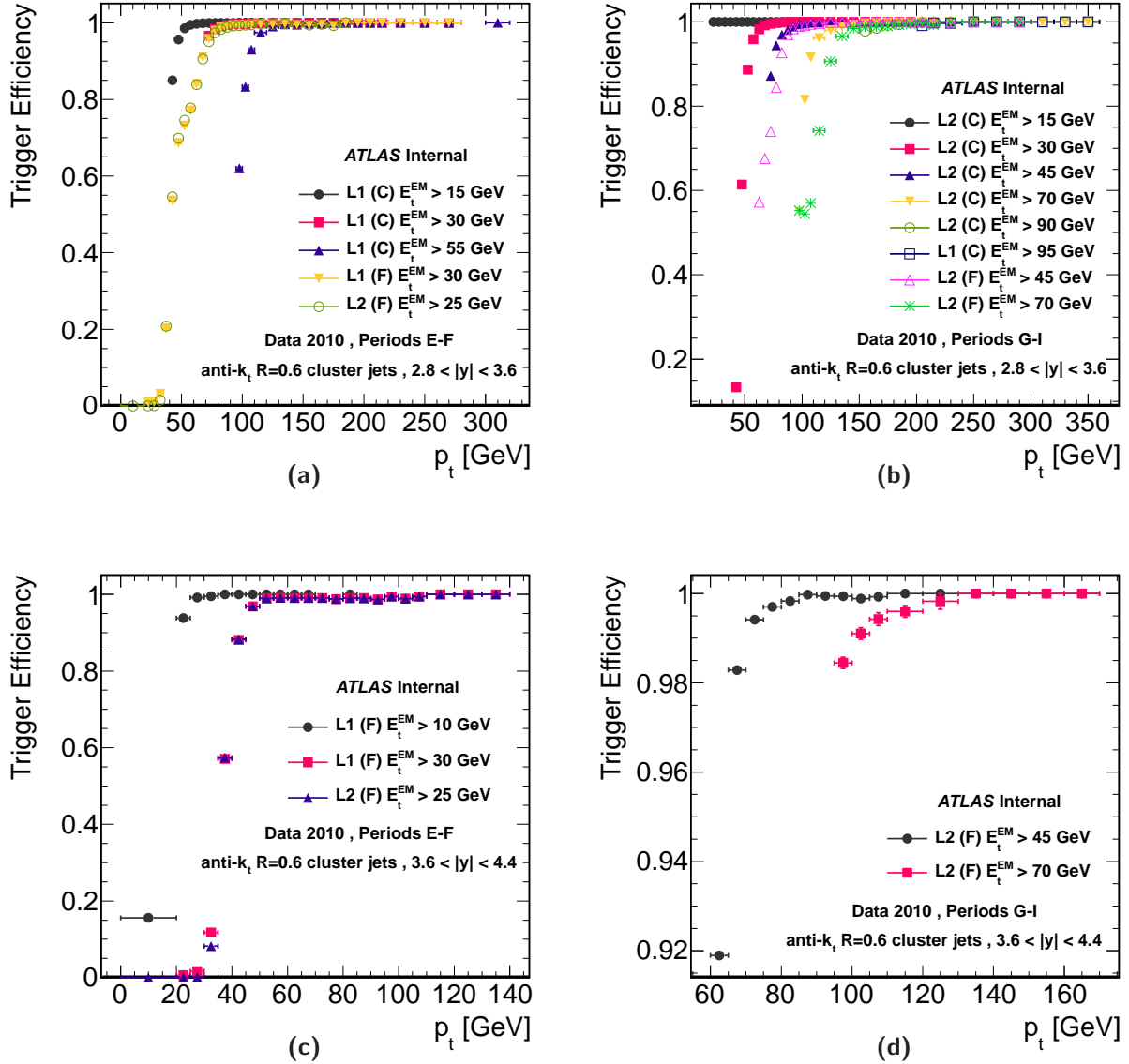


Figure A.2. Trigger efficiency curves for various Level 1 (L1) and Level 2 (L2) triggers. Several 2010 data taking periods are represented, as indicated in the figures. The triggers are associated with jets within rapidity $2.8 < |y| < 3.6$ ((a) and (b)) and within rapidity $3.6 < |y| < 4.4$ ((c) and (d)), belonging to either the central (C) or the forward (F) jet trigger systems. Trigger thresholds are denoted by E_t^{EM} , signifying the minimal transverse energy at the electromagnetic scale, of a jet which is required to fire the trigger. (See also [chapter 6](#), [figure 6.1](#) and accompanying text.)

p_t [GeV]	Per-jet trigger efficiency			
	Period A Run < 152777	Periods A-D (Run \geq 152777)	Periods E-F (excl. E1-E4)	Periods G-I

$1.3 < y < 1.6$				
$20 < p_t \leq 42.5$	1	1	1	1
$42.5 < p_t \leq 70$	1	0.89	0.89	0.96
$70 < p_t \leq 97.5$	1	0.88	0.88	0.87
$97.5 < p_t \leq 152.5$	1	0.81	0.81	0.83
$152.5 < p_t \leq 197.5$	1	0.83	0.83	0.82
$197.5 < p_t \leq 217.5$	1	0.83	0.83	0.80
$p_t \geq 217.5$	1	0.83	0.83	0.81

$2.8 < y < 3.6$				
$20 < p_t \leq 42.5$	1	1	1	1
$42.5 < p_t \leq 62.5$	1	1	1	1
$62.5 < p_t \leq 72.5$	1	1	1	0.99
$72.5 < p_t \leq 95$	1	1	0.97	0.99
$95 < p_t \leq 160$	1	1	0.97	0.99
$p_t \geq 160$	1	1	0.97	1

$3.6 < y < 4.4$				
$20 < p_t \leq 42.5$	1	1	0.95	1
$42.5 < p_t \leq 50$	1	1	0.95	0.99
$50 < p_t \leq 67.5$	1	1	0.95	0.99
$67.5 < p_t \leq 100$	1	1	0.95	0.97
$p_t \geq 100$	1	1	0.95	0.97

Table A.2. The plateau per-jet trigger efficiency for the 2010 data as a function of jet transverse momentum, p_t , and rapidity, y , in various data taking periods, as indicated in the table. Trigger inefficiencies in the crack region, within rapidity $1.3 < |y| < 1.6$, arise due to inhomogeneities in the calorimeter, while those in the forward region, $2.8 < |y| < 4.4$, arise due to a dead FCAL tower. (See [section 6.2.2](#) for details.)

10. Summary

2010 Period A , Run < 152777	
Trigger name	L1_MBTS
L1_MBTS	$1.84 \cdot 10^{-4}$

2010 Periods A-D (Run \geq 152777)					
Trigger name	L1_MBTS	L1_J5	L1_J15	L1_J30	L1_J55
L1_MBTS	$5.62 \cdot 10^{-4}$	$2.53 \cdot 10^{-2}$	$2.62 \cdot 10^{-1}$	$2.62 \cdot 10^{-1}$	$2.62 \cdot 10^{-1}$
L1_J5		$2.53 \cdot 10^{-2}$	$2.62 \cdot 10^{-1}$	$2.62 \cdot 10^{-1}$	$2.62 \cdot 10^{-1}$
L1_J15			$2.62 \cdot 10^{-1}$	$2.62 \cdot 10^{-1}$	$2.62 \cdot 10^{-1}$
L1_J30				$2.62 \cdot 10^{-1}$	$2.62 \cdot 10^{-1}$
L1_J55					$2.62 \cdot 10^{-1}$

2010 Periods E-F (excl. E1-E4)							
Trigger name	L1_MBTS	L1_J5	L1_J15	L1_J30	L1_J55	L1_FJ10	L1_FJ10
L1_MBTS	$7.93 \cdot 10^{-5}$	$2.46 \cdot 10^{-3}$	$2.40 \cdot 10^{-2}$	$1.10 \cdot 10^0$	$2.17 \cdot 10^0$	$1.55 \cdot 10^{-2}$	$2.17 \cdot 10^0$
L1_J5		$2.38 \cdot 10^{-3}$	$2.63 \cdot 10^{-2}$	$1.10 \cdot 10^0$	$2.17 \cdot 10^0$	$1.78 \cdot 10^{-2}$	$2.17 \cdot 10^0$
L1_J15			$2.40 \cdot 10^{-2}$	$1.10 \cdot 10^0$	$2.17 \cdot 10^0$	$3.87 \cdot 10^{-2}$	$2.17 \cdot 10^0$
L1_J30				$1.10 \cdot 10^0$	$2.17 \cdot 10^0$	$1.10 \cdot 10^0$	$2.17 \cdot 10^0$
L1_J55					$2.17 \cdot 10^0$	$2.17 \cdot 10^0$	$2.17 \cdot 10^0$
L1_FJ10						$1.54 \cdot 10^{-2}$	$2.17 \cdot 10^0$
L1_FJ30							$2.17 \cdot 10^0$

Table A.3. Integrated luminosity in pb^{-1} for different trigger combinations used in several data taking periods in 2010. Data taken up to period F are included. The uncertainty on the luminosity is 3.4%. (See [section 6.2.3](#) for details.)

2010 Periods G-I							
Trigger name	EF_MBTS	L2_J15	L2_J30	L2_J45	L2_J70	L2_J90	L1_J95
EF_MBTS	$9.84 \cdot 10^{-5}$	$2.41 \cdot 10^{-3}$	$5.03 \cdot 10^{-2}$	$2.45 \cdot 10^{-1}$	$6.27 \cdot 10^0$	$6.00 \cdot 10^0$	$3.44 \cdot 10^1$
L2_J15		$2.33 \cdot 10^{-3}$	$5.24 \cdot 10^{-2}$	$2.49 \cdot 10^{-1}$	$6.27 \cdot 10^0$	$6.00 \cdot 10^0$	$3.44 \cdot 10^1$
L2_J30			$5.02 \cdot 10^{-2}$	$2.68 \cdot 10^{-1}$	$6.29 \cdot 10^0$	$6.02 \cdot 10^0$	$3.44 \cdot 10^1$
L2_J45				$2.46 \cdot 10^{-1}$	$6.33 \cdot 10^0$	$6.06 \cdot 10^0$	$3.44 \cdot 10^1$
L2_J70					$6.27 \cdot 10^0$	$7.72 \cdot 10^0$	$3.44 \cdot 10^1$
L2_J90						$6.00 \cdot 10^0$	$3.44 \cdot 10^1$
L1_J95							$3.44 \cdot 10^1$

2010 Periods G-I			
Trigger name	L2_FJ25	L2_FJ45	L2_FJ70
EF_MBTS	$1.58 \cdot 10^{-1}$	$3.73 \cdot 10^0$	$3.44 \cdot 10^1$
L2_J15	$1.61 \cdot 10^{-1}$	$3.73 \cdot 10^0$	$3.44 \cdot 10^1$
L2_J30	$1.82 \cdot 10^{-1}$	$3.75 \cdot 10^0$	$3.44 \cdot 10^1$
L2_J45	$3.30 \cdot 10^{-1}$	$3.81 \cdot 10^0$	$3.44 \cdot 10^1$
L2_J70	$6.32 \cdot 10^0$	$7.62 \cdot 10^0$	$3.44 \cdot 10^1$
L2_J90	$6.05 \cdot 10^0$	$7.43 \cdot 10^0$	$3.44 \cdot 10^1$
L1_J95	$3.44 \cdot 10^1$	$3.44 \cdot 10^1$	$3.44 \cdot 10^1$
L2_FJ25	$1.58 \cdot 10^{-1}$	$3.80 \cdot 10^0$	$3.44 \cdot 10^1$
L2_FJ45		$3.73 \cdot 10^0$	$3.44 \cdot 10^1$
L2_FJ70			$3.44 \cdot 10^1$

Table A.4. Integrated luminosity in pb^{-1} for the different trigger combinations used during periods G-I in 2010. The uncertainty on the luminosity is 3.4%. (See [section 6.2.3](#) for details.)

10. Summary

2011 Periods D,I-M						
Trigger name	EF_rd0	EF_J10	EF_J15	EF_J20	EF_J30	EF_J40
EF_rd0	$1.48 \cdot 10^{-3}$	$3.22 \cdot 10^{-3}$	$9.34 \cdot 10^{-3}$	$2.58 \cdot 10^{-2}$	$2.65 \cdot 10^{-1}$	$2.96 \cdot 10^{-1}$
EF_J10		$1.74 \cdot 10^{-3}$	$9.57 \cdot 10^{-3}$	$2.60 \cdot 10^{-2}$	$2.64 \cdot 10^{-1}$	$2.96 \cdot 10^{-1}$
EF_J15			$7.83 \cdot 10^{-3}$	$3.21 \cdot 10^{-2}$	$2.70 \cdot 10^{-1}$	$3.02 \cdot 10^{-1}$
EF_J20				$2.43 \cdot 10^{-2}$	$2.87 \cdot 10^{-1}$	$3.18 \cdot 10^{-1}$
EF_J30					$2.62 \cdot 10^{-1}$	$5.56 \cdot 10^{-1}$
EF_J40						$2.94 \cdot 10^{-1}$

2011 Periods D,I-M						
Trigger name	EF_J55	EF_J75	EF_J100	EF_J135	EF_J180	EF_J240
EF_rd0	$1.05 \cdot 10^0$	$3.88 \cdot 10^0$	$1.34 \cdot 10^1$	$1.24 \cdot 10^2$	$3.26 \cdot 10^2$	$3.83 \cdot 10^3$
EF_J10	$1.05 \cdot 10^0$	$3.87 \cdot 10^0$	$1.34 \cdot 10^1$	$1.24 \cdot 10^2$	$3.25 \cdot 10^2$	$3.82 \cdot 10^3$
EF_J15	$1.06 \cdot 10^0$	$3.87 \cdot 10^0$	$1.34 \cdot 10^1$	$1.24 \cdot 10^2$	$3.25 \cdot 10^2$	$3.82 \cdot 10^3$
EF_J20	$1.07 \cdot 10^0$	$3.89 \cdot 10^0$	$1.34 \cdot 10^1$	$1.24 \cdot 10^2$	$3.25 \cdot 10^2$	$3.82 \cdot 10^3$
EF_J30	$1.31 \cdot 10^0$	$4.12 \cdot 10^0$	$1.36 \cdot 10^1$	$1.24 \cdot 10^2$	$3.25 \cdot 10^2$	$3.82 \cdot 10^3$
EF_J40	$1.34 \cdot 10^0$	$4.16 \cdot 10^0$	$1.37 \cdot 10^1$	$1.24 \cdot 10^2$	$3.26 \cdot 10^2$	$3.82 \cdot 10^3$
EF_J55	$1.05 \cdot 10^0$	$4.91 \cdot 10^0$	$1.44 \cdot 10^1$	$1.25 \cdot 10^2$	$3.26 \cdot 10^2$	$3.82 \cdot 10^3$
EF_J75		$3.86 \cdot 10^0$	$1.72 \cdot 10^1$	$1.27 \cdot 10^2$	$3.28 \cdot 10^2$	$3.82 \cdot 10^3$
EF_J100			$1.34 \cdot 10^1$	$1.35 \cdot 10^2$	$3.35 \cdot 10^2$	$3.82 \cdot 10^3$
EF_J135				$1.24 \cdot 10^2$	$3.61 \cdot 10^2$	$3.82 \cdot 10^3$
EF_J180					$3.25 \cdot 10^2$	$3.82 \cdot 10^3$
EF_J240						$3.82 \cdot 10^3$

Table A.5. Integrated luminosity in pb^{-1} for the different trigger combinations used throughout 2011 (Periods D,I-M). The uncertainty on the luminosity is 3.9%. (See [section 6.2.3](#) for details.)

A.3. The jet area/median method for pile-up subtraction

Additional figures pertaining to [chapter 7](#) are presented in the following; the dependence of the average median of the transverse momentum density of jets on the number of reconstructed vertices and on the average number of interactions is shown in [figures A.3 - A.4](#); the dependence of the quality criteria for the median pile-up correction on the transverse momentum of truth jets is shown in [figure A.5](#); the *in-situ* performance qualifiers for the median pile-up correction are shown in [figures A.6 - A.7](#).

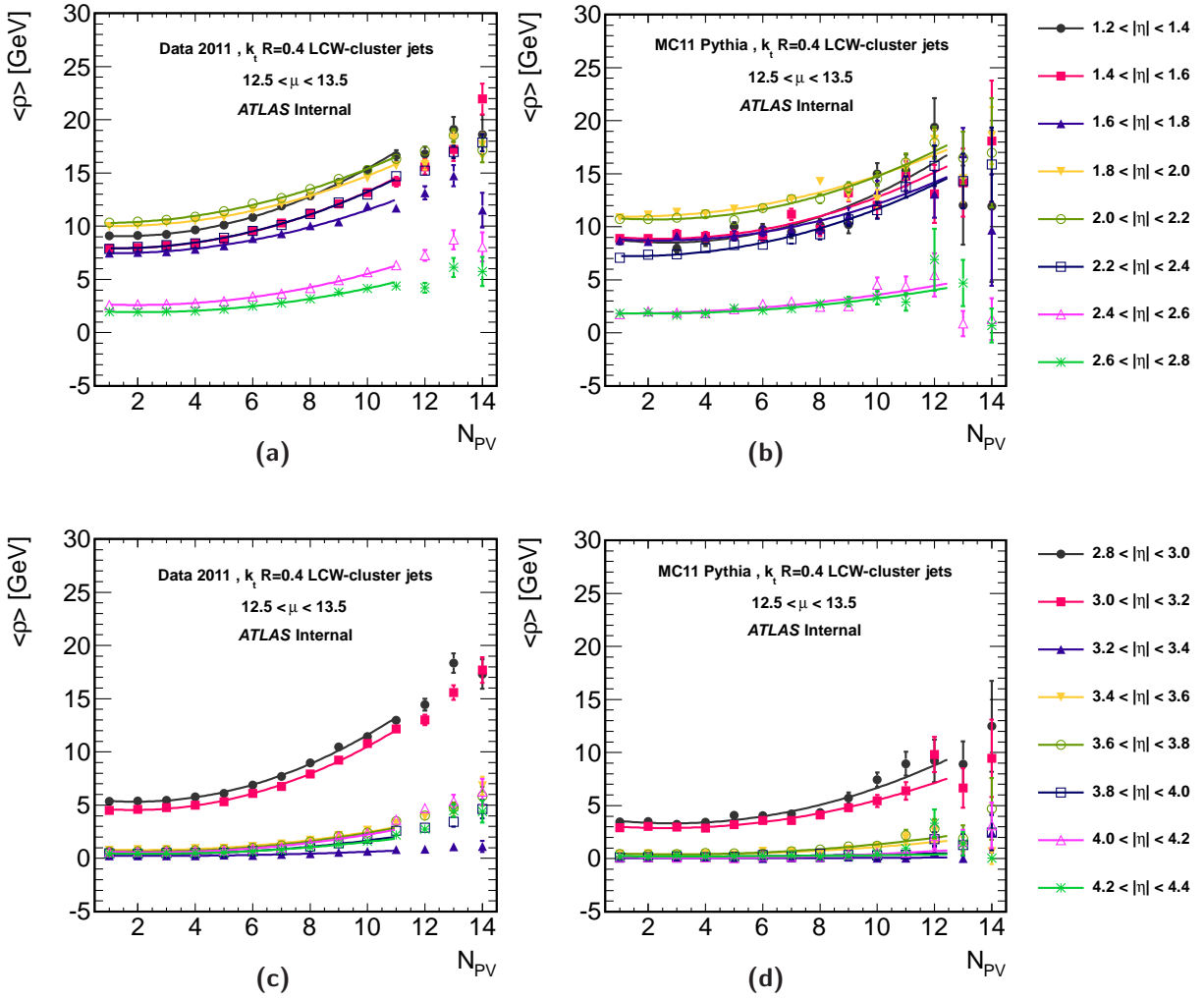


Figure A.3. Dependence of the average median, $\langle \rho \rangle$, on the number of reconstructed vertices, N_{PV} , for a fixed range of the average number of interactions, μ . Several pseudo-rapidity bins within $1.2 < \eta < 2.8$ ((a), (b)) and $2.8 < \eta < 4.4$ ((c), (d)) are shown, using data and MC, as indicated in the figures. The lines represent polynomial fits to the points. (See also [chapter 7](#), [figure 7.7](#) and accompanying text.)

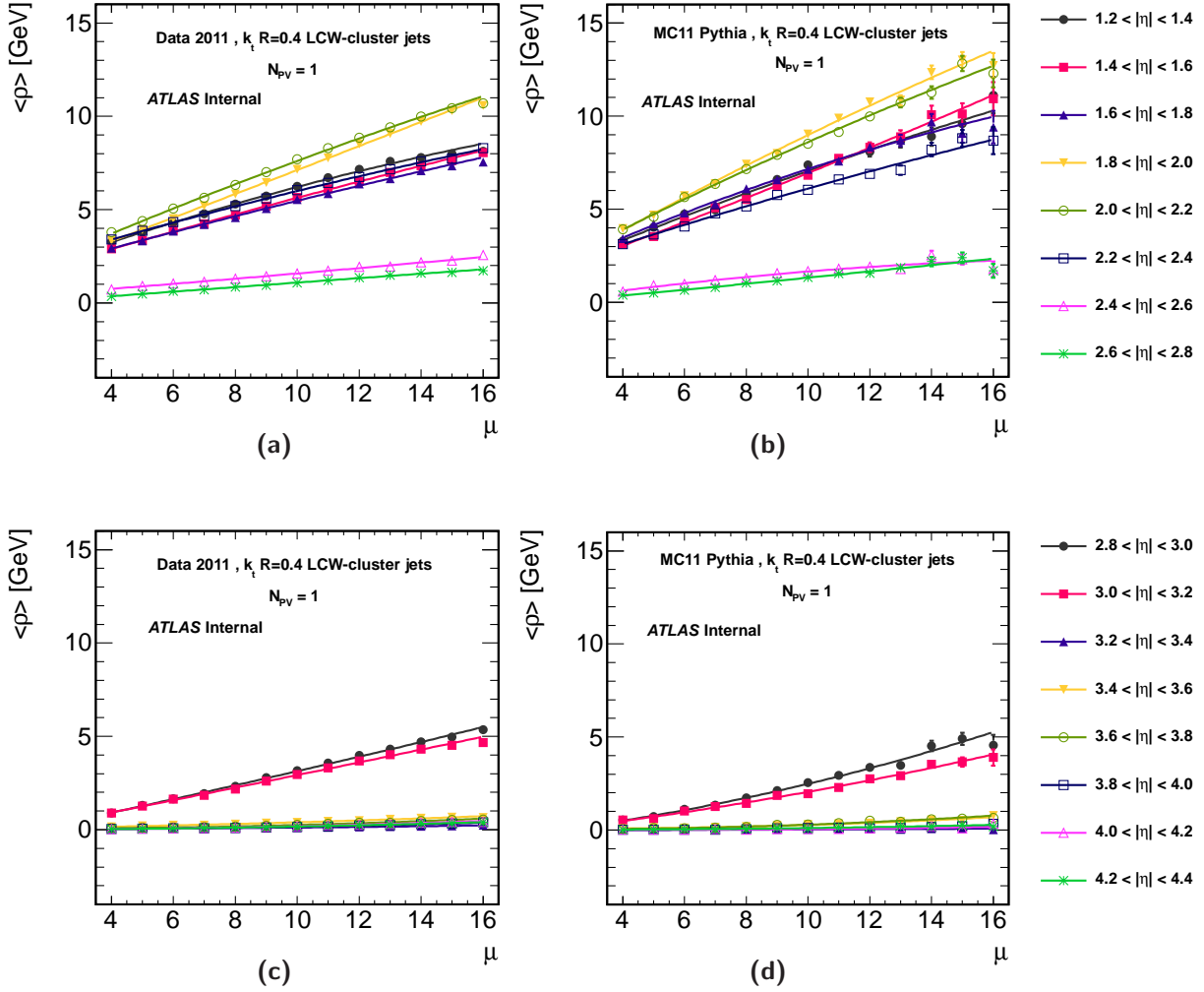


Figure A.4. Dependence of the average median, $\langle p \rangle$, on the average number of interactions, μ , for events with a single reconstructed vertex, N_{PV} . Several pseudo-rapidity bins within $1.2 < \eta < 2.8$ ((a), (b)) and $2.8 < \eta < 4.4$ ((c), (d)) are shown, using data and MC, as indicated in the figures. The lines represent polynomial fits to the points. (See also [chapter 7](#), [figure 7.7](#) and accompanying text.)

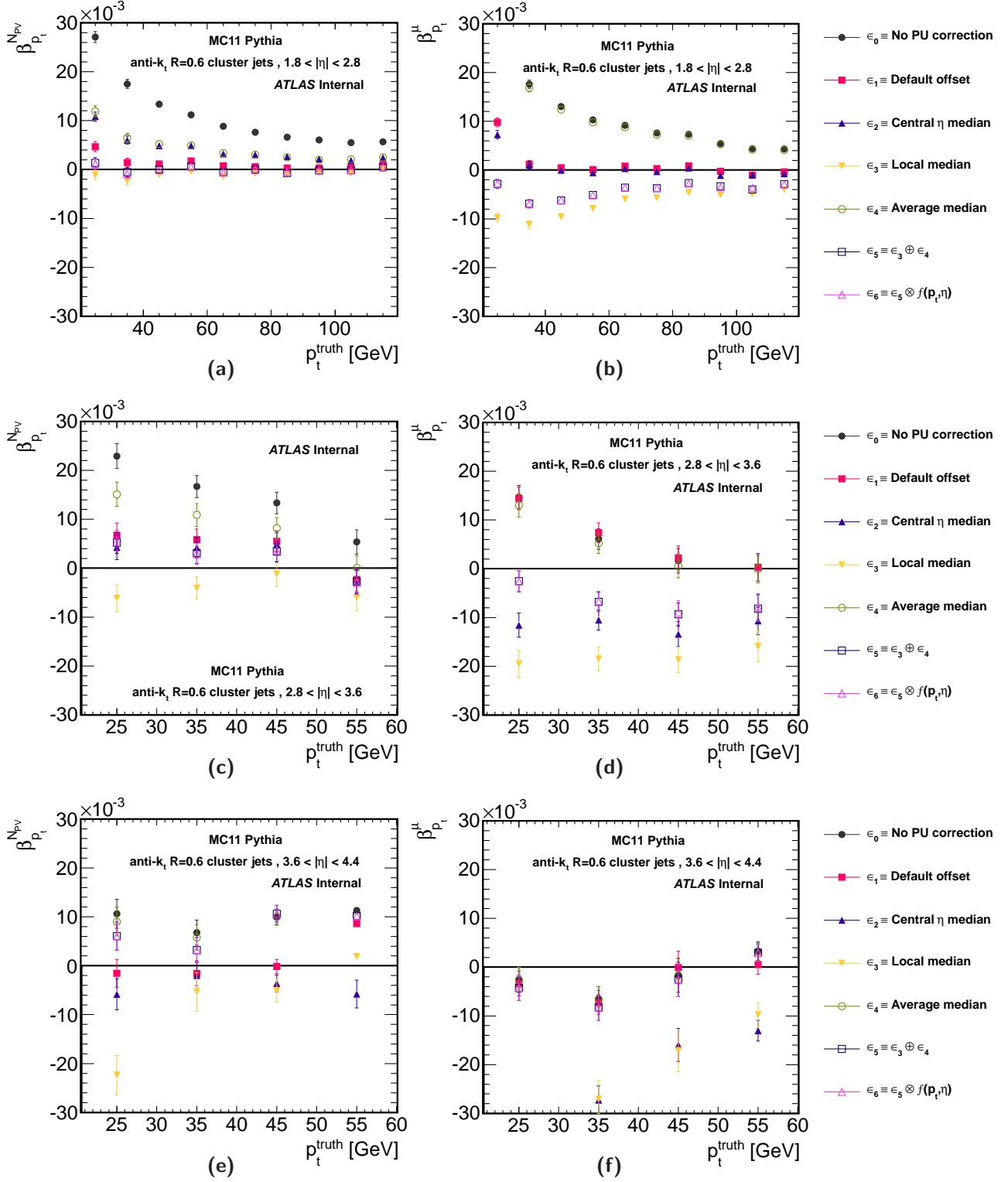


Figure A.5. Dependence on truth jet transverse momentum, p_t^{truth} , of the parameters defined in chapter 7, equation (7.13), $\beta_{p_t}^{N_{PV}}$ ((a), (c) and (e)) and $\beta_{p_t}^{\mu}$ ((b), (d) and (f)), using jets corrected for pile-up with ϵ_0 - ϵ_6 , within several pseudo-rapidity, η , regions, as indicated in the figures. (See also chapter 7, figure 7.10 and accompanying text.)

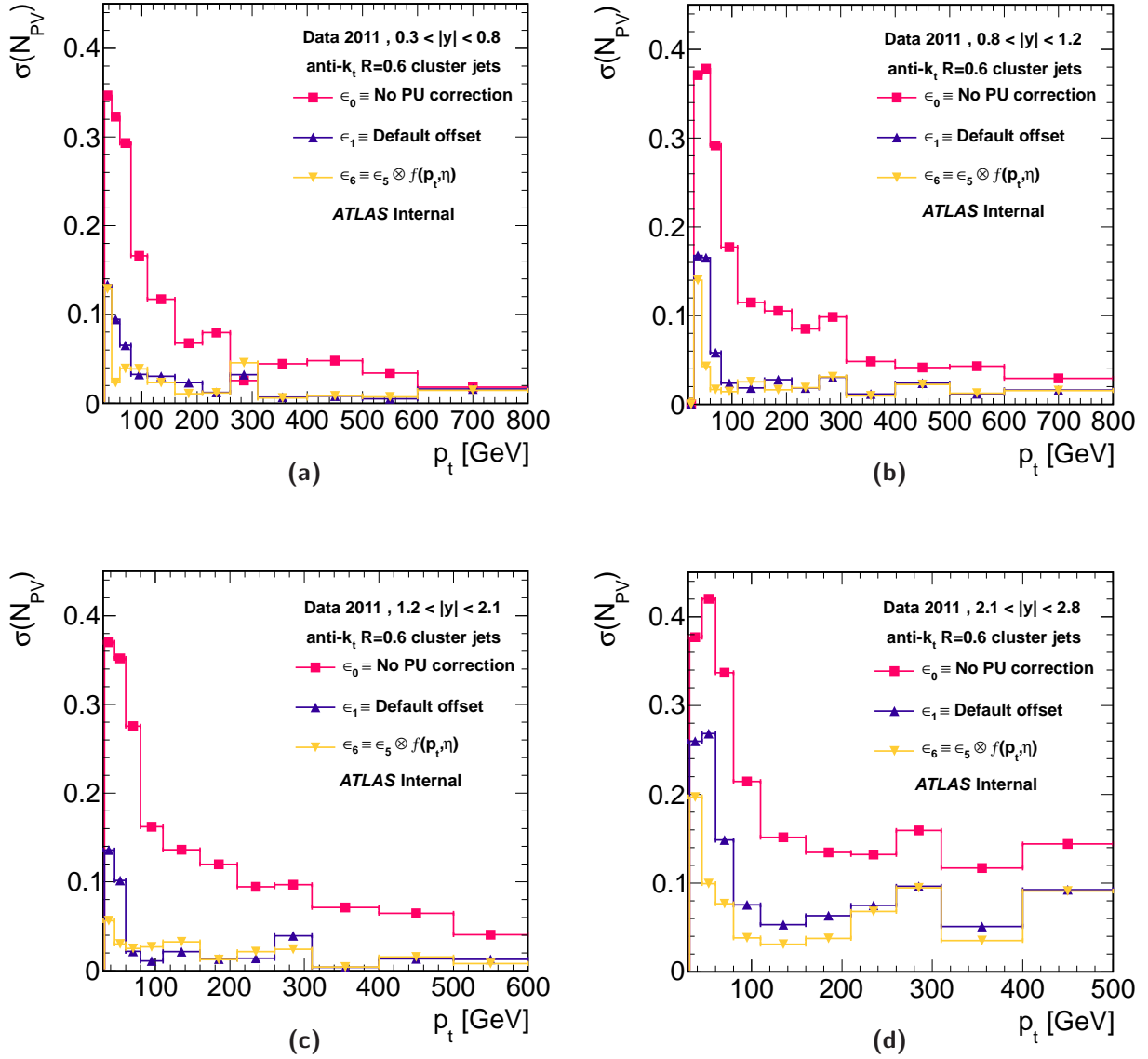


Figure A.6. Standard deviation with regard to single-vertex events, $\sigma(N_{PV})$, of the differential transverse momentum, p_t , spectrum of the highest- p_t jet in an event, for jets within several rapidity, y , regions, corrected for pile-up by ϵ_0 , ϵ_1 and ϵ_6 , as indicated in the figures. (See also [chapter 7](#), [equation \(7.18\)](#), [figure 7.25](#) and accompanying text.)

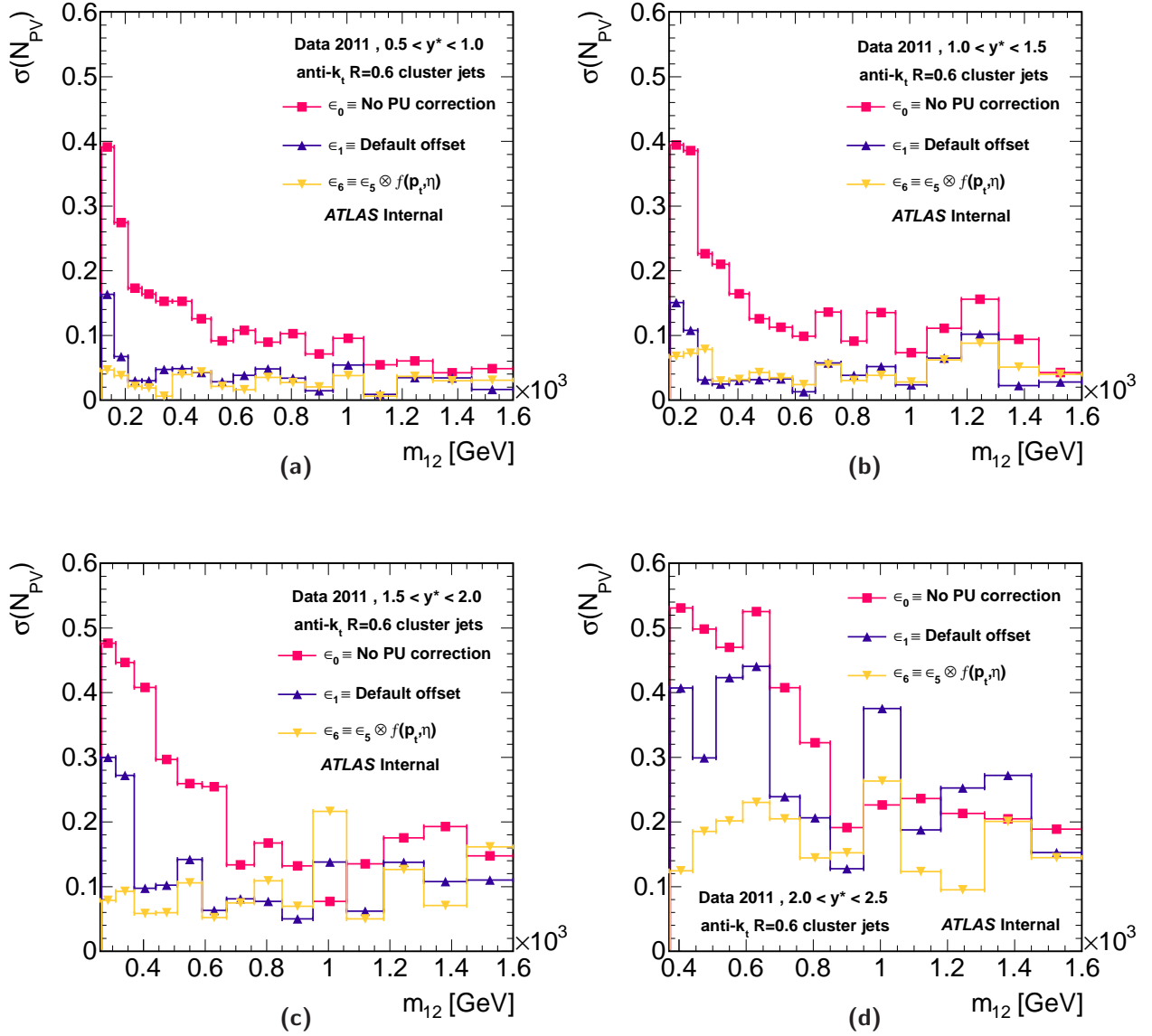


Figure A.7. Standard deviation with regard to single-vertex events, $\sigma(N_{PV})$, of the invariant mass distribution, m_{12} , of the two jets with the highest transverse momentum in an event, for several center-of-mass jet rapidities, y^* , using jets corrected for pile-up by ϵ_0 , ϵ_1 and ϵ_6 , as indicated. (See also chapter 7, equation (7.18), figure 7.25 and accompanying text.)

A.4. Dijet mass distribution

Additional figures pertaining to [chapter 8](#) are presented in the following; non-perturbative correction factors for the theoretical calculation of the dijet invariant mass distributions are shown in [figure A.8](#); the uncertainties on the theoretical calculation and the systematic uncertainties on the data for the invariant mass measurement may be inferred from [figures A.9 - A.14](#);

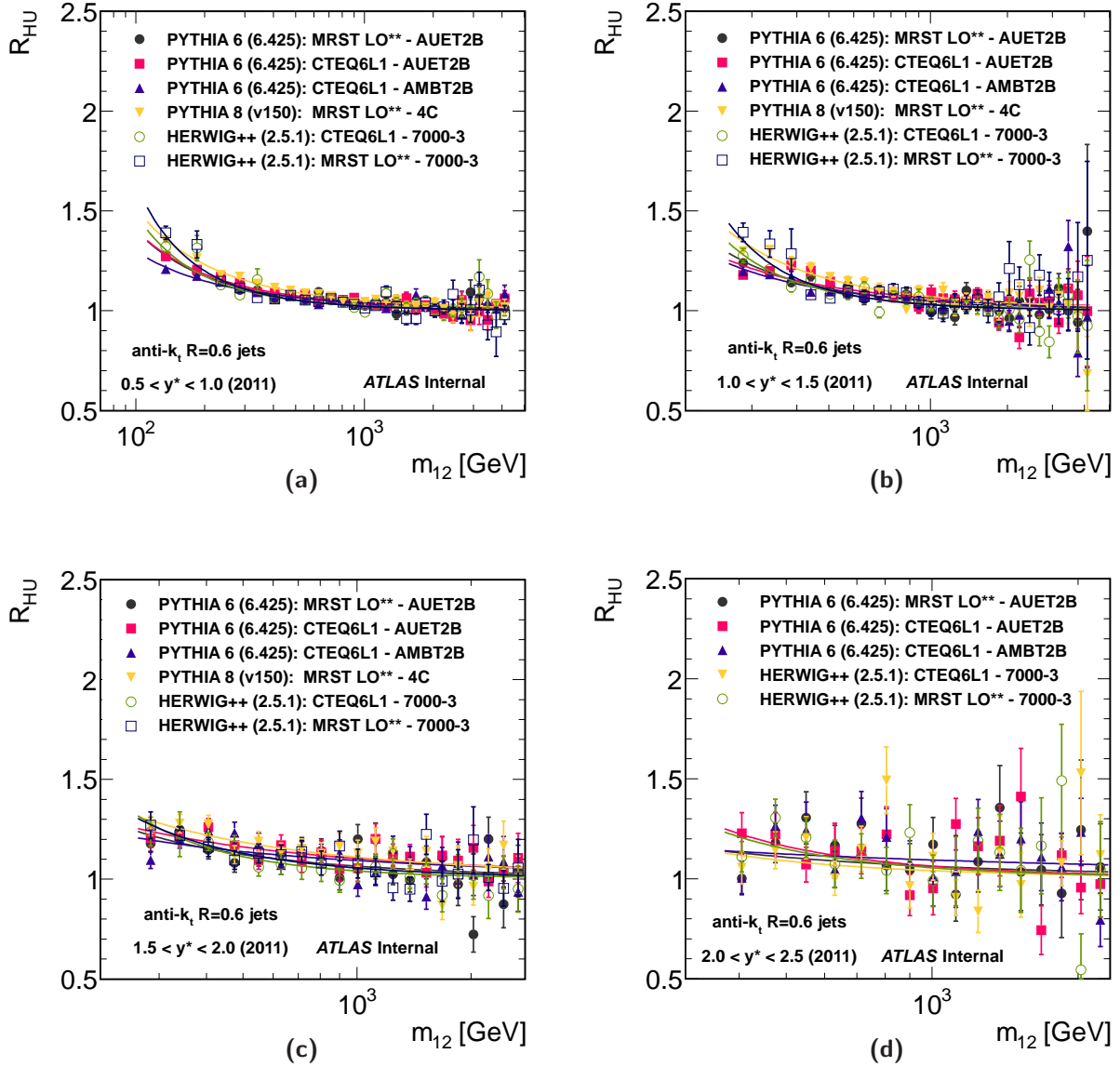


Figure A.8. Non-perturbative correction factors, \mathcal{R}_{HU} , for the invariant mass, m_{12} , spectrum of the two jets with the highest transverse momentum in an event, as a function of m_{12} , for different center-of-mass jet rapidities, y^* , for several combinations of generators, PDF sets, and underlying event tunes, as indicated in the figure and explained in [section 8.2.2](#). The lines represent fits to the various MC samples, using the 2011 phase-space definition of the measurement. (See also [chapter 8](#), [figure 8.3](#).)

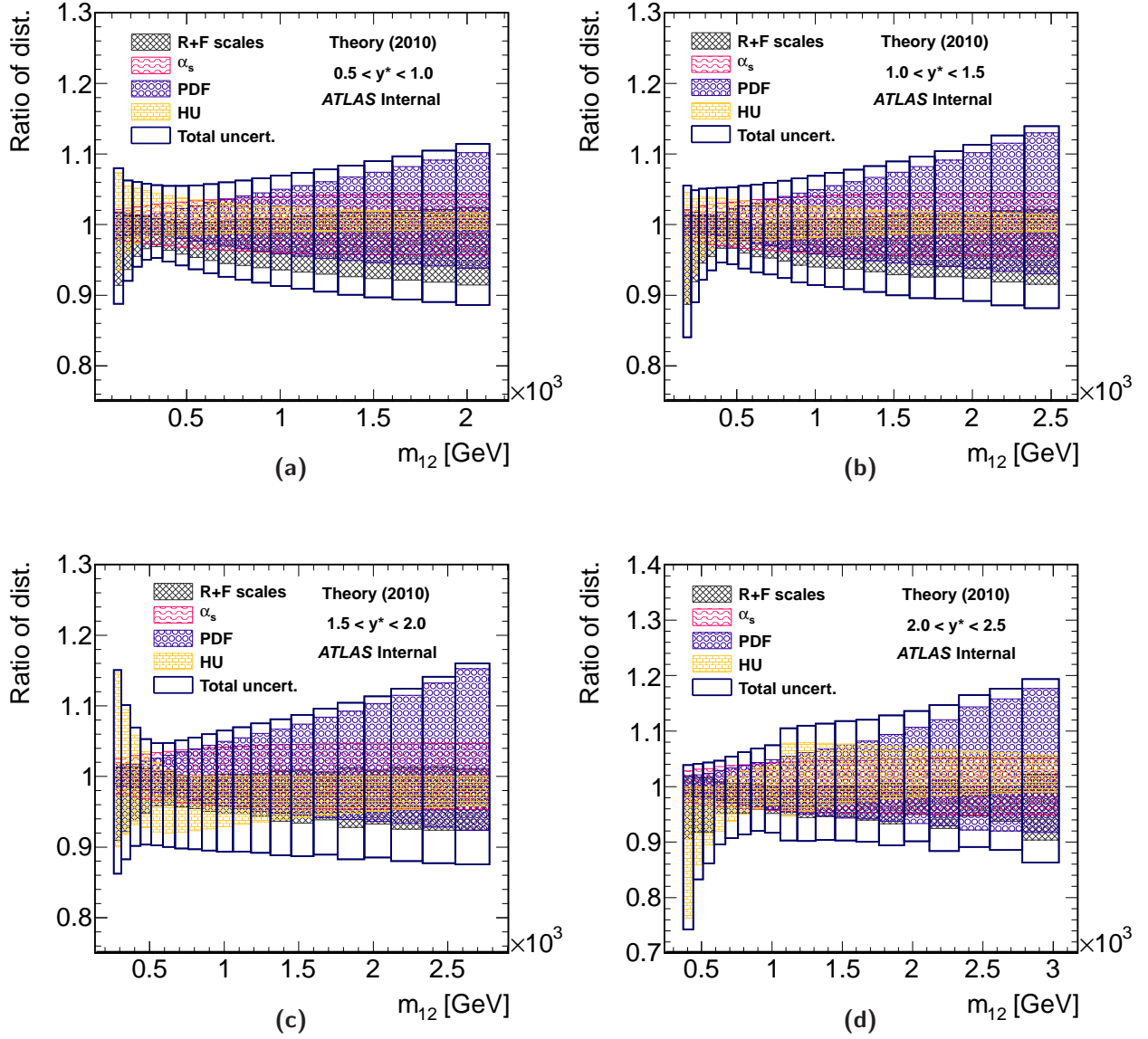


Figure A.9. The ratio of NLOJET++ expectations obtained under different assumptions relative to the nominal calculation, as a function of the invariant mass, m_{12} , of the two hadron-level jets with the highest transverse momentum, for different center-of-mass jet rapidities, y^* , for the 2010 measurement. The variations on the nominal expectation include the uncertainty on the renormalization and factorisation scales (R+F scales), the uncertainty on the value of the strong coupling constant (α_s), use of different parton density functions (PDF), the uncertainty on the hadronization and UE corrections (HU) and the total uncertainty on all the latter (total uncert.). (See also [chapter 8](#), [figure 8.4](#) and accompanying text.)

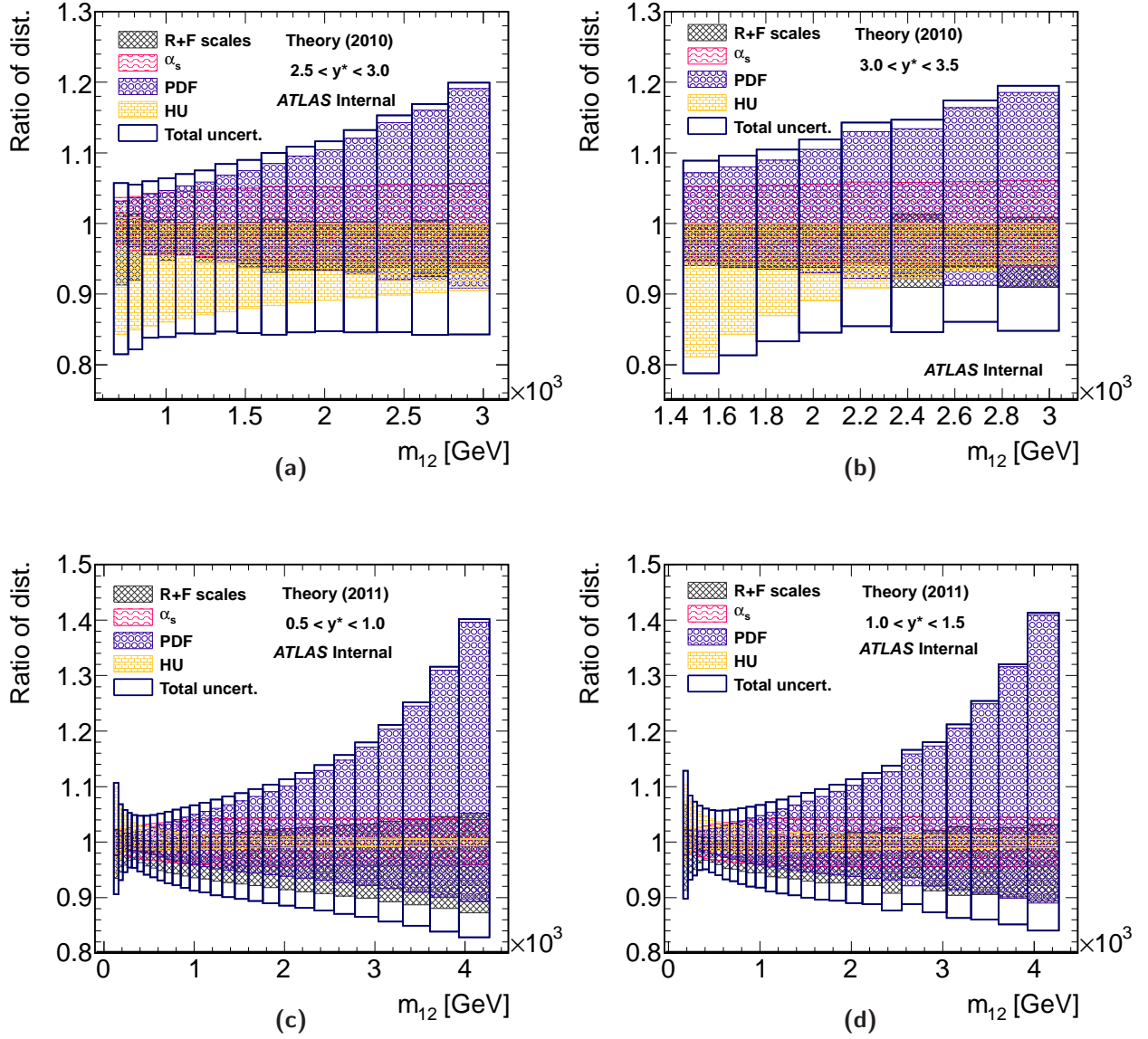


Figure A.10. The ratio of NLOJET++ expectations obtained under different assumptions relative to the nominal calculation, as a function of the invariant mass, m_{12} , of the two hadron-level jets with the highest transverse momentum, for different center-of-mass jet rapidities, y^* , for the 2010 ((a),(b)) and for the 2011 ((c) and (d)) measurements. The variations on the nominal expectation include the uncertainty on the renormalization and factorisation scales (R+F scales), the uncertainty on the value of the strong coupling constant (α_s), use of different parton density functions (PDF), the uncertainty on the hadronization and UE corrections (HU) and the total uncertainty on all the latter (total uncert.). (See also [chapter 8](#), [figure 8.4](#) and accompanying text.)

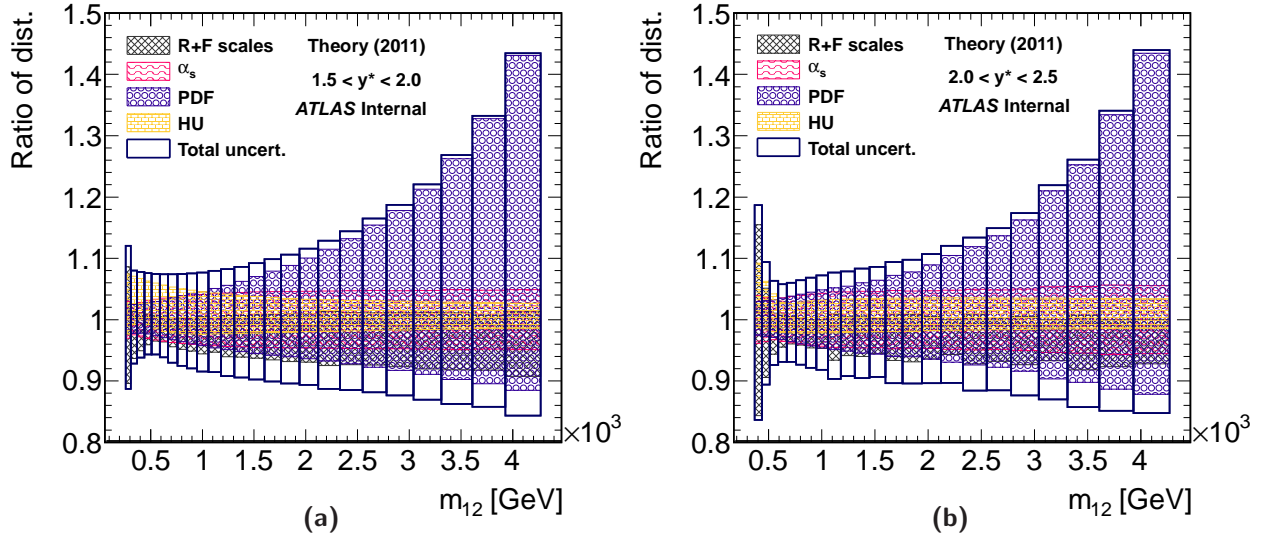


Figure A.11. The ratio of NLOJET++ expectations obtained under different assumptions relative to the nominal calculation, as a function of the invariant mass, m_{12} , of the two hadron-level jets with the highest transverse momentum, for different center-of-mass jet rapidities, y^* , for the 2011 measurement. The variations on the nominal expectation include the uncertainty on the renormalization and factorisation scales (R+F scales), the uncertainty on the value of the strong coupling constant (α_s), use of different parton density functions (PDF), the uncertainty on the hadronization and UE corrections (HU) and the total uncertainty on all the latter (total uncert.). (See also [chapter 8](#), [figure 8.4](#) and accompanying text.)

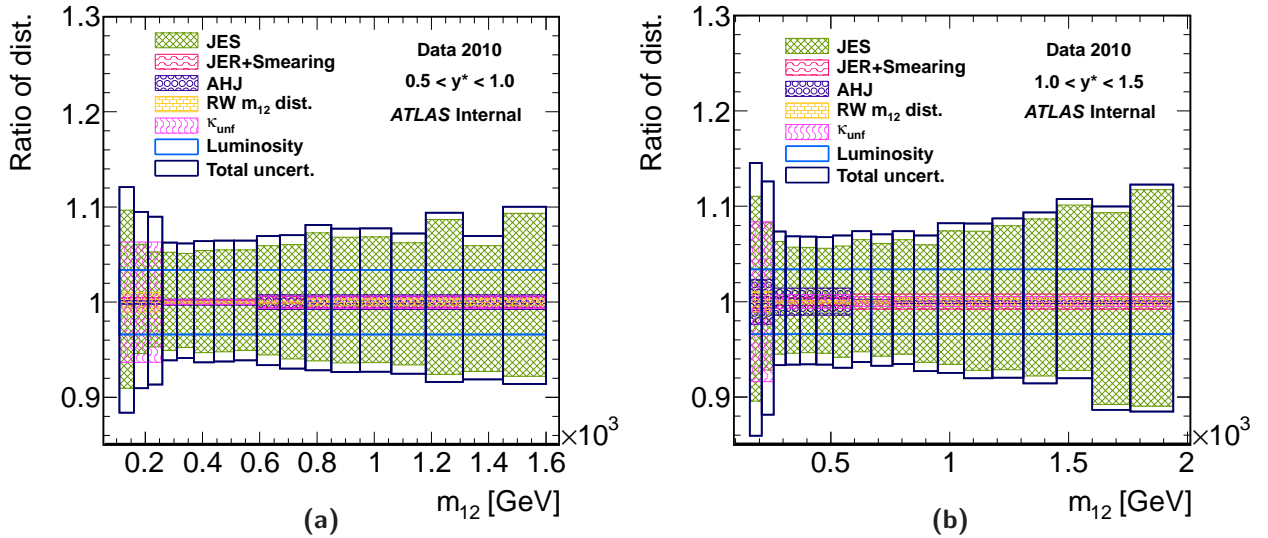


Figure A.12. Dependence on the invariant mass, m_{12} , of the two jets with the highest transverse momentum in an event, of the ratio between the m_{12} distributions with and without systematic variations (described in the text), for center-of-mass jet rapidity, $y^* < 0.5$, in the 2010 measurement, including the uncertainty on the jet energy scale (JES); the uncertainty on the jet energy and angular resolutions (JES + smearing); the uncertainty associated with the choice of physics generator (AHJ); the uncertainty associated with variation in the simulated shape of the m_{12} spectrum (RW m_{12} dist.); the choice of the number of iterations used in the unfolding procedure (κ_{unf}); the uncertainty on the luminosity (luminosity); and the total uncertainty on all the latter (total uncert.). (See also [chapter 8](#), [figure 8.12](#) and accompanying text.)

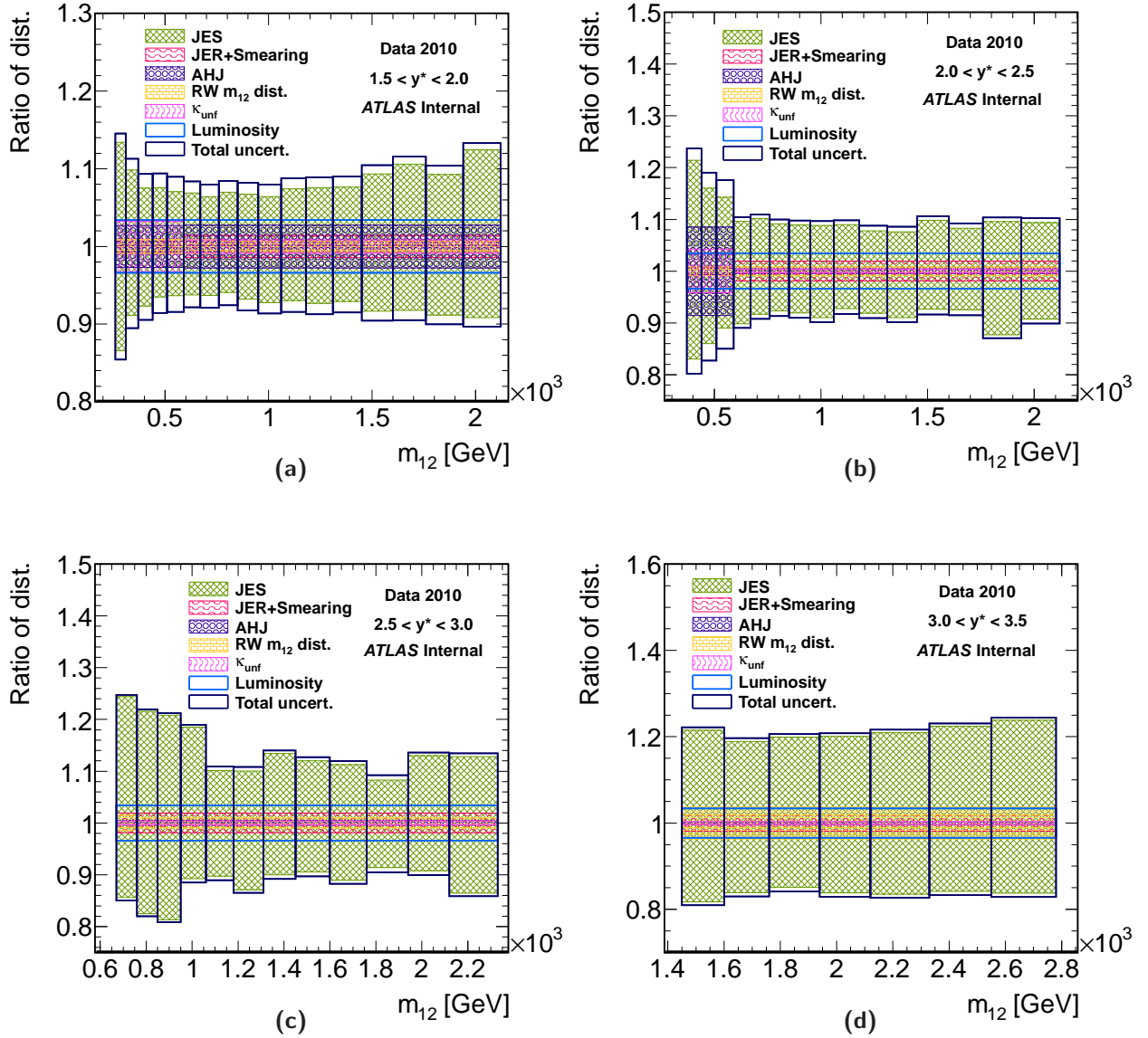


Figure A.13. Dependence on the invariant mass, m_{12} , of the two jets with the highest transverse momentum in an event, of the ratio between the m_{12} distributions with and without systematic variations (described in the text), for different center-of-mass jet rapidities, y^* , in the 2010 measurement, including the uncertainty on the jet energy scale (JES); the uncertainty on the jet energy and angular resolutions (JES + smearing); the uncertainty associated with the choice of physics generator (AHJ); the uncertainty associated with variation in the simulated shape of the m_{12} spectrum (RW m_{12} dist.); the choice of the number of iterations used in the unfolding procedure (κ_{unf}); the uncertainty on the luminosity (luminosity); and the total uncertainty on all the latter (total uncert.). (See also [chapter 8](#), [figure 8.12](#) and accompanying text.)

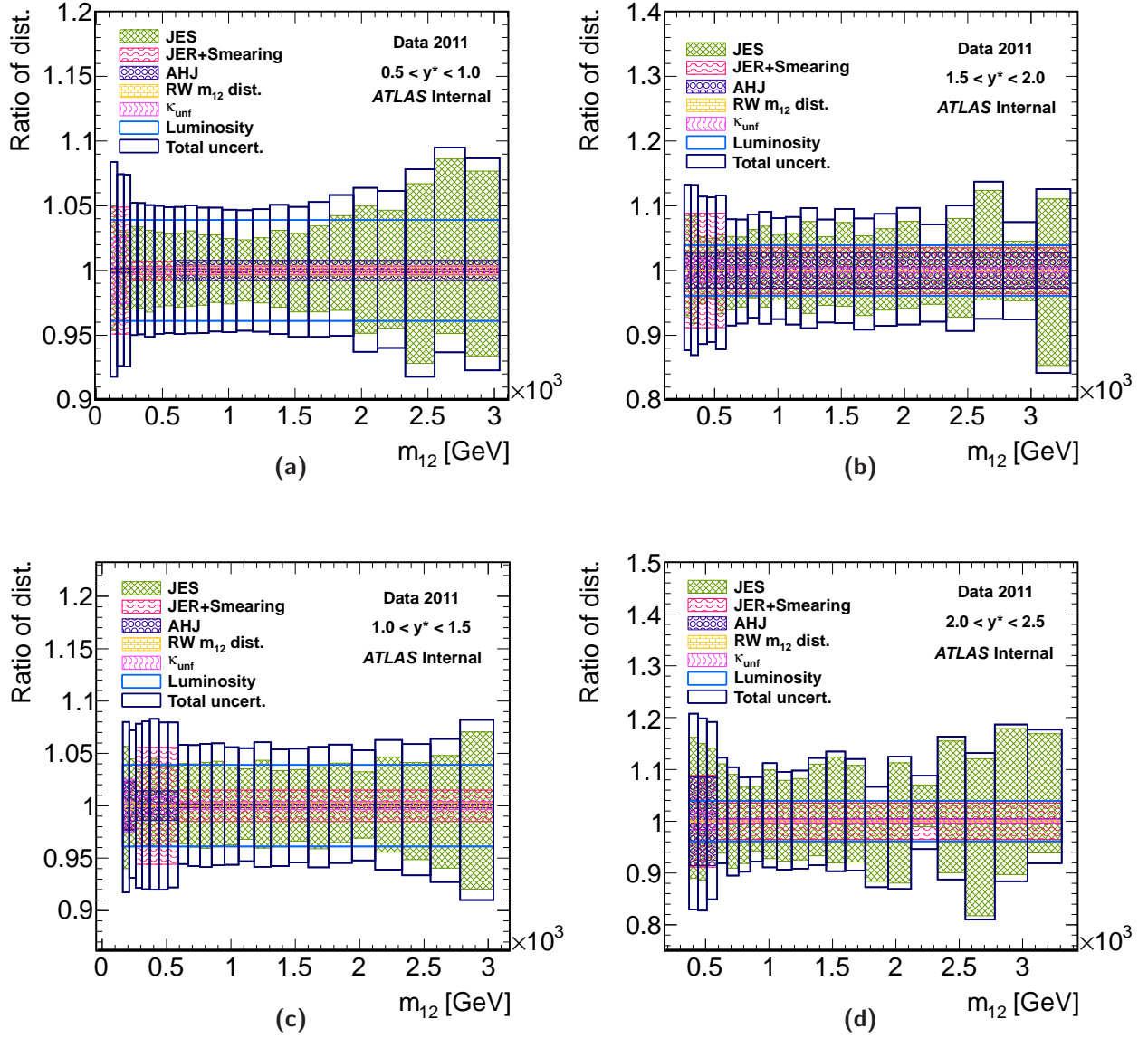


Figure A.14. Dependence on the invariant mass, m_{12} , of the two jets with the highest transverse momentum in an event, of the ratio between the m_{12} distributions with and without systematic variations (described in the text), for different center-of-mass jet rapidities, y^* , in the 2011 measurement, including the uncertainty on the jet energy scale (JES); the uncertainty on the jet energy and angular resolutions (JES + smearing); the uncertainty associated with the choice of physics generator (AHJ); the uncertainty associated with variation in the simulated shape of the m_{12} spectrum (RW m_{12} dist.); the choice of the number of iterations used in the unfolding procedure (κ_{unf}); the uncertainty on the luminosity (luminosity); and the total uncertainty on all the latter (total uncert.). (See also [chapter 8](#), [figure 8.12](#) and accompanying text.)

A.5. Hard double parton scattering in four-jet events

Additional figures pertaining to [chapter 9](#) are presented in the following; normalized distributions of the input variables to the NN (defined in [equation \(9.14\)](#)) are used in [figures A.15 - A.17](#) to compare the data to the expectation. The latter refers to a combination of the signal and background samples, normalized in proportion according to the fitted value of the fraction of DPS events, $f_{\text{DPS}} = 8.1\%$.

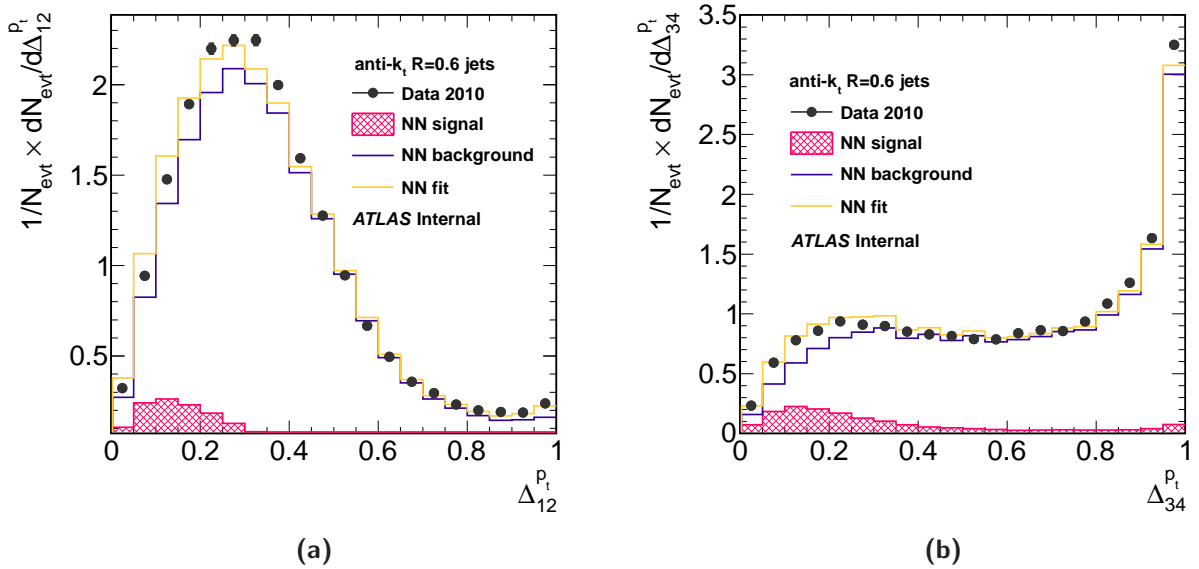


Figure A.15. Differential distributions of the variables, $\Delta_{12}^{p_t}$ (a) and $\Delta_{34}^{p_t}$ (b), which are defined in [chapter 9, equation \(9.14\)](#), for four-jet events in the 2010 data, for the signal and background input samples of the NN and for the sum of the two NN inputs (denoted by “NN fit”), where the signal and background samples are each normalized according to the fit to the fraction of DPS events, as explained in [section 9.3.3](#).

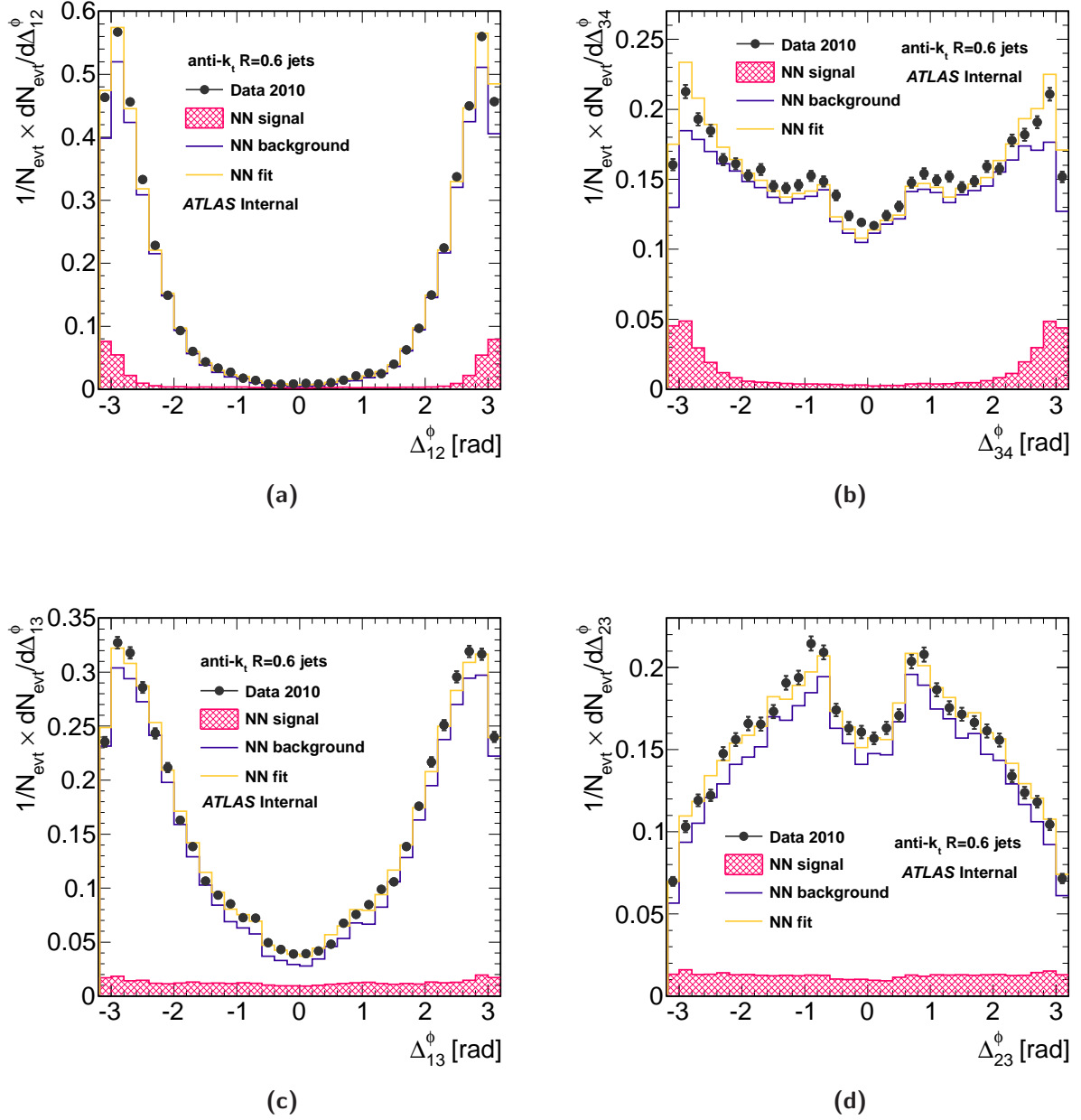


Figure A.16. Differential distributions of the variables, Δ_{12}^{ϕ} (a), Δ_{34}^{ϕ} (b), Δ_{13}^{ϕ} (c) and Δ_{23}^{ϕ} (d), which are defined in [chapter 9, equation \(9.14\)](#), for four-jet events in the 2010 data, for the signal and background input samples of the NN and for the sum of the two NN inputs (denoted by “NN fit”), where the signal and background samples are each normalized according to the fit to the fraction of DPS events, as explained in [section 9.3.3](#).

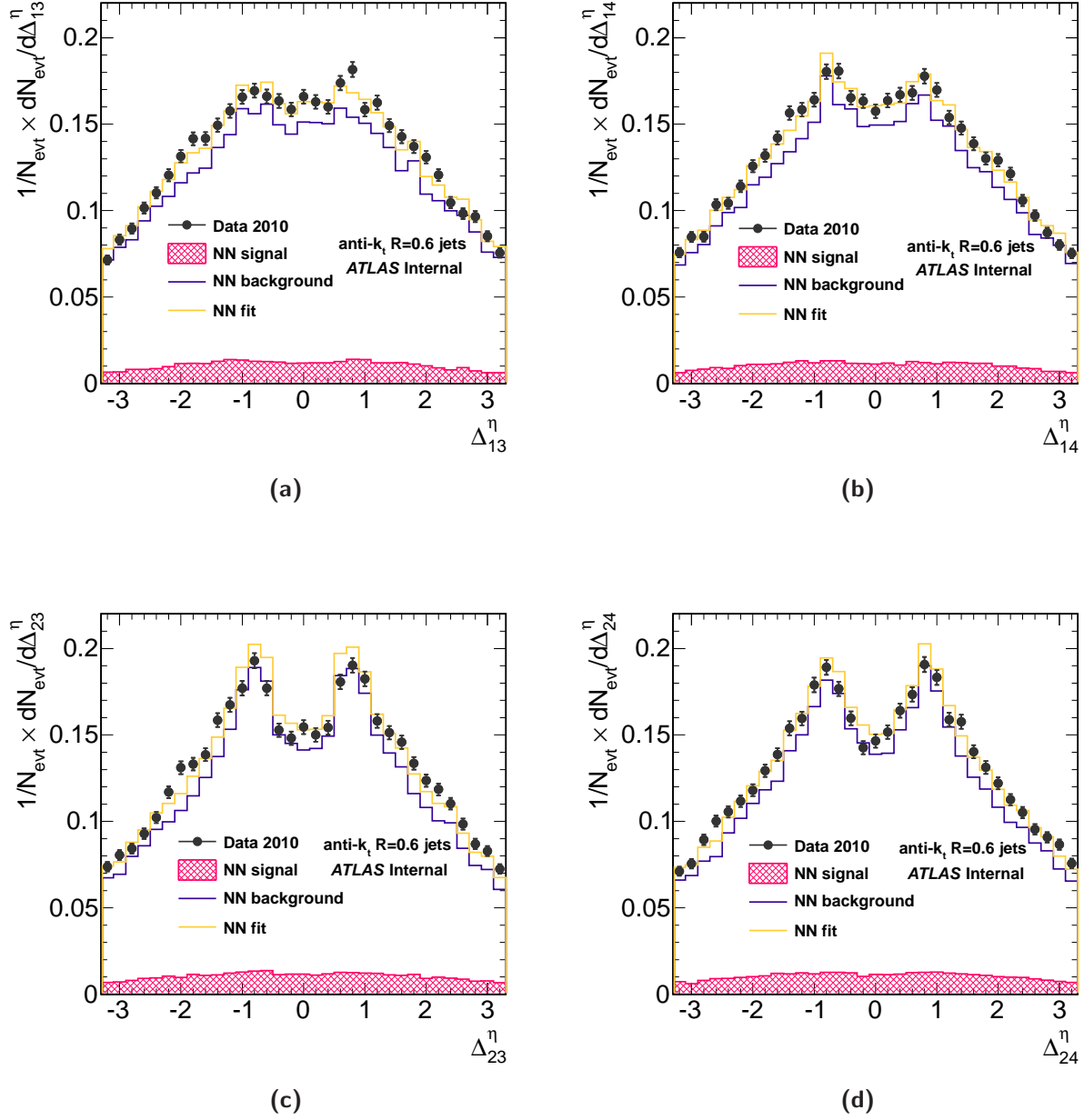


Figure A.17. Differential distributions of the variables, Δ_{13}^η (a), Δ_{14}^η (b), Δ_{23}^η (c) and Δ_{24}^η (d), which are defined in [chapter 9, equation \(9.14\)](#), for four-jet events in the 2010 data, for the signal and background input samples of the NN and for the sum of the two NN inputs (denoted by “NN fit”), where the signal and background samples are each normalized according to the fit to the fraction of DPS events, as explained in [section 9.3.3](#).

Bibliography

- [1] O. Nachtmann, *Elementary particle physics: concepts and phenomena*. Theoretical and Mathematical Physics. Springer-Verlag, 1990. <http://books.google.co.il/books?id=wMPvAAAAAAAJ>.
- [2] ATLAS Collaboration, G. Aad et al., *Observation of a new particle in the search for the Standard Model Higgs boson with the ATLAS detector at the LHC*, *Phys.Lett.* **B716** (2012) 1–29, [arXiv:1207.7214](https://arxiv.org/abs/1207.7214) [hep-ex].
- [3] CMS Collaboration, S. Chatrchyan et al., *Observation of a new boson at a mass of 125 GeV with the CMS experiment at the LHC*, *Phys.Lett.* **B716** (2012) 30–61, [arXiv:1207.7235](https://arxiv.org/abs/1207.7235) [hep-ex].
- [4] P. Ramond, *Journeys Beyond the Standard Model*. Frontiers in Physics, V. 101. Perseus Books Group, 2004. <http://books.google.co.il/books?id=RCd0IGTfQysC>.
- [5] G. P. Salam, *Towards Jetography*, [arXiv:arXiv:0906.1833](https://arxiv.org/abs/hep-ph/0906.1833) [hep-ph].
- [6] D. Stump et al., *Inclusive jet production, parton distributions, and the search for new physics*, *JHEP* **10** (2003) 046, [arXiv:hep-ph/0303013](https://arxiv.org/abs/hep-ph/0303013).
- [7] A. Sherstnev and R. S. Thorne, *Parton distributions for LO generators*, *Eur. Phys. J.* **C 55** (2008) 553–575, [arXiv:0711.2473](https://arxiv.org/abs/hep-ph/0711.2473) [hep-ph].
- [8] J. Pumplin et al., *New generation of parton distributions with uncertainties from global QCD analysis*, *JHEP* **07** (2002) 012, [arXiv:0201195](https://arxiv.org/abs/hep-ph/0201195) [hep-ph].
- [9] J. Pumplin et al., *New generation of parton distributions with uncertainties from global QCD analysis*, *JHEP* **07** (2002) 012, [arXiv:hep-ph/0201195](https://arxiv.org/abs/hep-ph/0201195).
- [10] ATLAS Collaboration, G. Aad et al., *Search for New Particles in Two-Jet Final States in 7 TeV Proton-Proton Collisions with the ATLAS Detector at the LHC*, *Phys.Rev.Lett.* **105** (2010) 161801, [arXiv:1008.2461](https://arxiv.org/abs/1008.2461) [hep-ex].
- [11] ATLAS Collaboration, G. Aad et al., *Search for Quark Contact Interactions in Dijet Angular Distributions in pp Collisions at $\sqrt{s} = 7$ TeV Measured with the ATLAS Detector*, *Phys.Lett.* **B694** (2011) 327–345, [arXiv:1009.5069](https://arxiv.org/abs/1009.5069) [hep-ex].
- [12] ATLAS Collaboration, G. Aad et al., *Search for New Physics in Dijet Mass and Angular Distributions in pp Collisions at $\sqrt{s} = 7$ TeV Measured with the ATLAS Detector*, *New J.Phys.* **13** (2011) 053044, [arXiv:1103.3864](https://arxiv.org/abs/1103.3864) [hep-ex].
- [13] E. L. Berger, C. Jackson, and G. Shaughnessy, *Characteristics and Estimates of Double Parton Scattering at the Large Hadron Collider*, *Phys.Rev.* **D81** (2010) 014014, [arXiv:0911.5348](https://arxiv.org/abs/hep-ph/0911.5348) [hep-ph].
- [14] A. Del Fabbro and D. Treleani, *A Double parton scattering background to Higgs boson production at the LHC*, *Phys.Rev.* **D61** (2000) 077502, [arXiv:hep-ph/9911358](https://arxiv.org/abs/hep-ph/9911358) [hep-ph].

- [15] E. Levin and J. Miller, *Two parton shower background for associate W Higgs production*, *Eur.Phys.J.* **C61** (2009) 1–31, [arXiv:0803.0646 \[hep-ph\]](#).
- [16] G. Calucci and D. Treleani, *Double parton scatterings in high-energy hadronic collisions*, *Nucl.Phys.Proc.Suppl.* **71** (1999) 392, [arXiv:hep-ph/9711225 \[hep-ph\]](#).
- [17] J. R. Gaunt and W. J. Stirling, *Double Parton Distributions Incorporating Perturbative QCD Evolution and Momentum and Quark Number Sum Rules*, *JHEP* **03** (2010) 005, [arXiv:0910.4347 \[hep-ph\]](#).
- [18] G. Calucci and D. Treleani, *Proton structure in transverse space and the effective cross-section*, *Phys.Rev.* **D60** (1999) 054023, [arXiv:hep-ph/9902479 \[hep-ph\]](#).
- [19] J. R. Gaunt, *The GS09 double parton distribution functions*, *PoS DIS2010* (2010) 030, [arXiv:1006.1118 \[hep-ph\]](#).
- [20] J. R. Gaunt and W. J. Stirling, *Single and Double Perturbative Splitting Diagrams in Double Parton Scattering*, [arXiv:1202.3056 \[hep-ph\]](#).
- [21] B. Humpert, *The production of gauge boson pairs by p anti-p colliders*, *Phys.Lett.* **B135** (1984) 179.
- [22] L. Ametller, N. Paver, and D. Treleani, *POSSIBLE SIGNATURE OF MULTIPLE PARTON INTERACTIONS IN COLLIDER FOUR JET EVENTS*, *Phys.Lett.* **B169** (1986) 289.
- [23] T. Akesson et al., *Double parton scattering in pp collisions at $\sqrt{s} = 63$ GeV*, *Z. Phys. C* **34** (1986) 163.
- [24] J. Alitti et al., *A study of multi-jet events at the CERN pp collider and a search for double parton scattering*, *Phys. Lett. B* **268** (1991) no. 1, 145.
- [25] CDF Collaboration, F. Abe et al., *Study of four-jet events and evidence for double parton interactions in $p\bar{p}$ collisions at $\sqrt{s} = 1.8$ TeV*, *Phys. Rev.* **D47** (1993) 4857.
- [26] CDF Collaboration, F. Abe et al., *Double parton scattering in $p\bar{p}$ collisions at $\sqrt{s} = 1.8$ TeV*, *Phys. Rev.* **D56** (1997) 3811.
- [27] D0 Collaboration, V. Abazov et al., *Double parton interactions in photon+3 jet events in p-p collisions $\sqrt{s} = 1.96$ TeV*, *Phys.Rev.* **D81** (2010) 052012, [arXiv:0912.5104 \[hep-ex\]](#).
- [28] I. Sadeh, *Direct Measurement of DPS at ATLAS*, . <https://indico.cern.ch/conference0therViews.py?view=standard&confId=184925>. Talk given at the MPI@LHC 2012 Workshop, CERN, Geneva, Nov 2012.
- [29] D. Griffiths, *Introduction to Elementary Particles*. John Wiley & Sons, New York, USA, 1987.
- [30] R. K. Ellis, W. J. Stirling, and B. R. Webber, *QCD and Collider Physics*, vol. 8. Cambridge University Press, 1996.
- [31] H. Yukawa, *On the Interaction of Elementary Particles. I**, *Progress of Theoretical Physics Supplement* **1** (1955) 1–10. <http://ptp.ipap.jp/link?PTPS/1/1/>.
- [32] C. N. Yang and R. L. Mills, *Conservation of Isotopic Spin and Isotopic Gauge Invariance*, *Phys. Rev.* **96** (Oct, 1954) 191–195. <http://link.aps.org/doi/10.1103/PhysRev.96.191>.
- [33] Y. N. M. Gell-Mann, *The Eight Fold Way*,. Benjamin, New York, 1964.

- [34] R. P. Feynman, *The behavior of hadron collisions at extreme energies*, in *High Energy Collisions*, C. N. Yang et al., eds., pp. 237–256. 1969.
- [35] D. J. Gross, *The discovery of asymptotic freedom and the emergence of QCD*, *Proceedings of the National Academy of Sciences of the United States of America* **102** (2005) no. 26, 9099–9108, <http://www.pnas.org/content/102/26/9099.full.pdf+html>.
<http://www.pnas.org/content/102/26/9099.short>.
- [36] T. Sjostrand and P. Z. Skands, *Multiple interactions and the structure of beam remnants*, *JHEP* **03** (2004) 053, [arXiv:hep-ph/0402078](https://arxiv.org/abs/hep-ph/0402078).
- [37] T. Sjostrand, S. Mrenna, and P. Skands, *PYTHIA 6.4 Physics and Manual*, *JHEP* **05** (2006) 026, [arXiv:hep-ph/0603175](https://arxiv.org/abs/hep-ph/0603175).
- [38] F. W. Bopp, R. Engel, and J. Ranft, *Rapidity gaps and the PHOJET Monte Carlo*, [arXiv:hep-ph/9803437](https://arxiv.org/abs/hep-ph/9803437).
- [39] G. Corcella et al., *HERWIG 6.5 release note*, [arXiv:hep-ph/0210213](https://arxiv.org/abs/hep-ph/0210213).
- [40] J. R. Gaunt, C.-H. Kom, A. Kulesza, and W. J. Stirling, *Same-sign W pair production as a probe of double parton scattering at the LHC*, [arXiv:1003.3953](https://arxiv.org/abs/1003.3953) [[hep-ph](#)].
- [41] F. E. Paige, S. D. Protopopescu, H. Baer, and X. Tata, *ISAJET 7.69: A Monte Carlo event generator for $p p$, anti- $p p$, and $e^+ e^-$ reactions*, [arXiv:hep-ph/0312045](https://arxiv.org/abs/hep-ph/0312045).
- [42] D. J. Gross and F. Wilczek, *Asymptotically Free Gauge Theories. I*, *Phys. Rev. D* **8** (Nov, 1973) 3633–3652. <http://link.aps.org/doi/10.1103/PhysRevD.8.3633>.
- [43] D. J. Gross and F. Wilczek, *Asymptotically free gauge theories. II*, *Phys. Rev. D* **9** (Feb, 1974) 980–993. <http://link.aps.org/doi/10.1103/PhysRevD.9.980>.
- [44] H. D. Politzer, *Reliable Perturbative Results for Strong Interactions?*, *Phys. Rev. Lett.* **30** (Jun, 1973) 1346–1349. <http://link.aps.org/doi/10.1103/PhysRevLett.30.1346>.
- [45] Particle Data Group Collaboration, J. Beringer et al., *Review of Particle Physics (RPP)*, *Phys.Rev.* **D86** (2012) 010001.
- [46] G. Proserpi, M. Raciti, and C. Simolo, *On the running coupling constant in QCD*, *Prog.Part.Nucl.Phys.* **58** (2007) 387–438, [arXiv:hep-ph/0607209](https://arxiv.org/abs/hep-ph/0607209) [[hep-ph](#)].
- [47] M. Breidenbach et al., *Observed Behavior of Highly Inelastic Electron-Proton Scattering*, *Physical Review Letters* **23** (Oct., 1969) 935–939. <http://slac.stanford.edu/spires/find/hep/www?j=PRLTA,23,935>.
- [48] J. C. Collins, D. E. Soper, and G. F. Sterman, *Factorization of Hard Processes in QCD*, *Adv.Ser.Direct.High Energy Phys.* **5** (1988) 1–91, [arXiv:hep-ph/0409313](https://arxiv.org/abs/hep-ph/0409313) [[hep-ph](#)].
- [49] A. V. Manohar, *An Introduction to spin dependent deep inelastic scattering*, [arXiv:hep-ph/9204208](https://arxiv.org/abs/hep-ph/9204208) [[hep-ph](#)].
- [50] H1 and ZEUS Collaboration, F. Aaron et al., *Combined Measurement and QCD Analysis of the Inclusive $e^+ p$ Scattering Cross Sections at HERA*, *JHEP* **1001** (2010) 109, [arXiv:0911.0884](https://arxiv.org/abs/0911.0884) [[hep-ex](#)].
- [51] Y. L. Dokshitzer, *Calculation of the Structure Functions for Deep Inelastic Scattering and $e^+ e^-$ Annihilation by Perturbation Theory in Quantum Chromodynamics.*, *Sov.Phys.JETP* **46** (1977) 641–653.

- [52] V. Gribov and L. Lipatov, *Deep inelastic $e p$ scattering in perturbation theory*, Sov.J.Nucl.Phys. **15** (1972) 438–450.
- [53] G. Altarelli and G. Parisi, *Asymptotic Freedom in Parton Language*, Nucl. Phys. **B126** (1977) 298. <http://www.slac.stanford.edu/spires/find/hep/www?key=224570&FORMAT=WWWBRIEFBIBTEX>.
- [54] S. J. Brodsky and G. R. Farrar, *Scaling Laws for Large Momentum Transfer Processes*, Phys.Rev. **D11** (1975) 1309.
- [55] H. Abarbanel, M. Goldberger, and S. Treiman, *Asymptotic properties of electroproduction structure functions*, Phys.Rev.Lett. **22** (1969) 500–502.
- [56] J. C. Collins and D. E. Soper, *The Theorems of Perturbative QCD*, Annual Review of Nuclear and Particle Science **37** (1987) 383–409.
- [57] H1 Collaboration, A. Aktas et al., *Dijet Cross Sections and Parton Densities in Diffractive DIS at HERA*, JHEP **10** (2007) 042, [arXiv:0708.3217](https://arxiv.org/abs/0708.3217) [hep-ex].
- [58] G. Watt, *Parton distribution function dependence of benchmark Standard Model total cross sections at the 7 TeV LHC*, JHEP **1109** (2011) 069, [arXiv:1106.5788](https://arxiv.org/abs/1106.5788) [hep-ph].
- [59] ZEUS Collaboration, S. Chekanov et al., *Forward-jet production in deep inelastic ep scattering at HERA*, Eur. Phys. J. **C52** (2007) 515–530, [arXiv:0707.3093](https://arxiv.org/abs/0707.3093) [hep-ex].
- [60] H1 Collaboration Collaboration, A. Aktas et al., *Forward jet production in deep inelastic scattering at HERA*, Eur.Phys.J. **C46** (2006) 27–42, [arXiv:hep-ex/0508055](https://arxiv.org/abs/hep-ex/0508055) [hep-ex].
- [61] H. Abramowicz, *The HERA challenges for LHC*, Acta Phys. Polon. **B40** (2009) 1791–1808, [arXiv:0906.0694](https://arxiv.org/abs/0906.0694) [hep-ex].
- [62] L. Lipatov, *Reggeization of the Vector Meson and the Vacuum Singularity in Nonabelian Gauge Theories*, Sov.J.Nucl.Phys. **23** (1976) 338–345.
- [63] E. Kuraev, L. Lipatov, and V. S. Fadin, *The Pomeranchuk Singularity in Nonabelian Gauge Theories*, Sov.Phys.JETP **45** (1977) 199–204.
- [64] I. Balitsky and L. Lipatov, *The Pomeranchuk Singularity in Quantum Chromodynamics*, Sov.J.Nucl.Phys. **28** (1978) 822–829.
- [65] Z. Nagy, *Next-to-leading order calculation of three jet observables in hadron hadron collision*, Phys. Rev. **D68** (2003) 094002, [arXiv:hep-ph/0307268](https://arxiv.org/abs/hep-ph/0307268). <http://www.desy.de/~znagy/Site/NLOJet++.html>.
- [66] ATLAS Collaboration, M. Leyton, *Minimum Bias and Underlying Event Measurements with ATLAS*, [arXiv:1202.2090](https://arxiv.org/abs/1202.2090) [hep-ex].
- [67] V. Sudakov, *Vertex parts at very high-energies in quantum electrodynamics*, Sov.Phys.JETP **3** (1956) 65–71.
- [68] Yu. L. Dokshitzer, V. A. Khoze, A. H. Mueller, S. I. Troyan, *Basics of Perturbative QCD*. Basics of. Éditions Frontières, 1991.
- [69] B. Andersson et al., *Parton fragmentation and string dynamics*, Phys. Rep. **97** (1983) 31–145.
- [70] B. R. Webber, *A QCD model for jet fragmentation including soft gluon interference*, Nucl. Phys. **B 238** (1984) 492.
- [71] D. Amati and G. Veneziano, *Preconfinement as a Property of Perturbative QCD*, Phys.Lett. **B83** (1979) 87.

- [72] M. Bahr, S. Gieseke, and M. H. Seymour, *Simulation of multiple partonic interactions in Herwig++*, JHEP **07** (2008) 076, [arXiv:0803.3633 \[hep-ph\]](#).
- [73] S. Eckweiler, *Measurement of the Inelastic Proton-Proton Cross-Section at $\sqrt{s} = 7$ TeV with the ATLAS Detector*, .
- [74] G. Antchev, P. Aspell, I. Atanassov, V. Avati, J. Baechler, et al., *First measurement of the total proton-proton cross section at the LHC energy of $\sqrt{s} = 7$ TeV*, Europhys.Lett. **96** (2011) 21002, [arXiv:1110.1395 \[hep-ex\]](#).
- [75] L. Frankfurt, M. Strikman, and C. Weiss, *Dijet production as a centrality trigger for pp collisions at CERN LHC*, Phys.Rev. **D69** (2004) 114010, [arXiv:hep-ph/0311231 \[hep-ph\]](#).
- [76] E. Levin and L. Frankfurt, *The Quark hypothesis and relations between cross-sections at high-energies*, JETP Lett. **2** (1965) 65–70.
- [77] H. Lipkin and F. Scheck, *Quark model for forward scattering amplitudes*, Phys.Rev.Lett. **16** (1966) 71–75.
- [78] S. Bondarenko, E. Levin, and J. Nyiri, *Recent experimental data and the size of the quark in the constituent quark model*, Eur.Phys.J. **C25** (2002) 277–286, [arXiv:hep-ph/0204156 \[hep-ph\]](#).
- [79] M. Ryskin and A. Snigirev, *A Fresh look at double parton scattering*, Phys.Rev. **D83** (2011) 114047, [arXiv:1103.3495 \[hep-ph\]](#).
- [80] M. G. Ryskin and A. M. Snigirev, *Double parton scattering in double logarithm approximation of perturbative QCD*, Phys. Rev. D **86** (Jul, 2012) 014018. <http://link.aps.org/doi/10.1103/PhysRevD.86.014018>.
- [81] B. Blok, Y. Dokshitzer, L. Frankfurt, and M. Strikman, *Origins of Parton Correlations in Nucleon and Multi-Parton Collisions*, [arXiv:1206.5594 \[hep-ph\]](#).
- [82] ATLAS Collaboration, G. Aad et al., *Luminosity determination in ATLAS*, . <https://twiki.cern.ch/twiki/bin/view/AtlasPublic/LuminosityPublicResults>.
- [83] ATLAS Collaboration, G. Aad et al., *The ATLAS Experiment at the CERN Large Hadron Collider*, JINST **3** (2008) S08003.
- [84] ATLAS Collaboration, G. Aad et al., *Expected Performance of the ATLAS Experiment - Detector, Trigger and Physics*, [arXiv:0901.0512 \[hep-ex\]](#).
- [85] ATLAS Collaboration, G. Aad et al., *Luminosity Determination in pp Collisions at $\sqrt{s} = 7$ TeV using the ATLAS Detector in 2011*, Tech. Rep. ATLAS-CONF-2011-116, 2011.
- [86] ATLAS Collaboration, G. Aad et al., *Luminosity Determination in pp Collisions at $\sqrt{s} = 7$ TeV Using the ATLAS Detector at the LHC*, Eur.Phys.J. **C71** (2011) 1630, [arXiv:1101.2185 \[hep-ex\]](#).
- [87] W. Kozanecki, *Precision of the absolute luminosity calibration at the LHC in 2011, 2012*. <https://indico.cern.ch/conferenceDisplay.py?confId=156433>. Talk given in an internal ATLAS weekly meeting.
- [88] A. Buckley et al., *General-purpose event generators for LHC physics*, Phys. Rept. **504** (2011) 145–233, [arXiv:1101.2599 \[hep-ph\]](#).
- [89] T. Sjostrand, S. Mrenna, and P. Z. Skands, *PYTHIA 6.4 physics and manual*, JHEP **0605** (2006) 026, [arXiv:0603175 \[hep-ph\]](#).

- [90] R. Corke and T. Sjostrand, *Improved Parton Showers at Large Transverse Momenta*, Eur. Phys. J. C **69** (2010) 1–18, [arXiv:1003.2384 \[hep-ph\]](#).
- [91] T. Sjostrand and P. Z. Skands, *Transverse-momentum-ordered showers and interleaved multiple interactions*, Eur. Phys. J. C **39** (2005) 129–154, [arXiv:0408302 \[hep-ph\]](#).
- [92] ATLAS Collaboration, *Charged particle multiplicities in pp interactions at $\sqrt{s} = 0.9$ and 7 TeV in a diffractive limited phase-space measured with the ATLAS detector at the LHC and new PYTHIA6 tune*, Tech. Rep. [ATLAS-CONF-2010-031](#), May, 2010.
- [93] ATLAS Collaboration, *Charged particle multiplicities in p - p interactions for track $p_T > 100$ MeV at $\sqrt{s} = 0.9$ and 7 TeV measured with the ATLAS detector at the LHC*, Tech. Rep. [ATLAS-CONF-2010-046](#), July, 2010.
- [94] ATLAS Collaboration, *ATLAS tunes of PYTHIA 6 and Pythia 8 for MC11*, Tech. Rep. ATL-PHYS-PUB-2011-009, CERN, Geneva, Jul, 2011.
- [95] T. Sjostrand, S. Mrenna, and P. Z. Skands, *A Brief Introduction to PYTHIA 8.1*, Comput.Phys.Comm. **178** (2008) 852–867, [arXiv:0710.3820 \[hep-ph\]](#).
- [96] R. Corke and T. Sjostrand, *Interleaved Parton Showers and Tuning Prospects*, JHEP **1103** (2011) 032, [arXiv:1011.1759 \[hep-ph\]](#).
- [97] G. Marchesini et al., *Monte Carlo simulation of general hard processes with coherent QCD radiation*, Nucl. Phys. B **310** (1988) 461.
- [98] G. Marchesini et al., *A Monte Carlo event generator for simulating hadron emission reactions with interfering gluons*, Comput. Phys. Commun. **67** (1991) 465–508.
- [99] G. Corcella et al., *HERWIG 6.5 release note*, [arXiv:0210213 \[hep-ph\]](#).
- [100] J. M. Butterworth, J. R. Forshaw, and M. H. Seymour, *Multiparton interactions in photoproduction at HERA*, Z. Phys. C **72** (1996) 637–646, [arXiv:9601371 \[hep-ph\]](#).
- [101] ATLAS Collaboration, *First tuning of HERWIG/JIMMY to ATLAS data*, Tech. Rep. [ATL-PHYS-PUB-2010-014](#), October, 2010.
- [102] M. Bahr et al., *Herwig++ physics and manual*, Eur. Phys. J. C **58** (2008) 639–707, [arXiv:0803.0883 \[hep-ph\]](#).
- [103] M. L. Mangano, M. Moretti, F. Piccinini, R. Pittau, and A. D. Polosa, *ALPGEN, a generator for hard multiparton processes in hadronic collisions*, JHEP **07** (2003) 001, [arXiv:0206293 \[hep-ph\]](#).
- [104] M. L. Mangano, M. Moretti, and R. Pittau, *Multijet matrix elements and shower evolution in hadronic collisions: $Wb\bar{b} + n$ jets as a case study*, Nucl. Phys. B **632** (2002) 343–362, [arXiv:0108069 \[hep-ph\]](#).
- [105] T. Gleisberg, S. Hoeche, F. Krauss, M. Schonherr, S. Schumann, et al., *Event generation with SHERPA 1.1*, JHEP **0902** (2009) 007, [arXiv:0811.4622 \[hep-ph\]](#).
- [106] F. Krauss, A. Schaliche, and G. Soff, *APACIC++ 2.0: A Parton cascade in C++*, Comput.Phys.Comm. **174** (2006) 876–902, [arXiv:hep-ph/0503087 \[hep-ph\]](#).
- [107] J.-C. Winter, F. Krauss, and G. Soff, *A Modified cluster hadronization model*, Eur.Phys.J. **C36** (2004) 381–395, [arXiv:hep-ph/0311085 \[hep-ph\]](#).
- [108] D. R. Yennie, S. C. Frautschi, and H. Suura, *The infrared divergence phenomena and high-energy processes*, Annals of Physics **13** (June, 1961) 379–452.

- [109] GEANT4 Collaboration, S. Agostinelli et al., *GEANT4: A simulation toolkit*, Nucl. Instrum. Meth. **A 506** (2003) 250–303.
- [110] ATLAS Collaboration, *The ATLAS simulation infrastructure*, Eur. Phys. J. **C 70** (2010) 823–874, [arXiv:1005.4568 \[physics.ins-det\]](#).
- [111] A. Ribon et al., *Status of Geant4 hadronic physics for the simulation of LHC experiments at the start of the LHC physics program*, Tech. Rep. [CERN-LCGAPP-2010-02](#), May, 2010.
- [112] G. Folger and J. Wellisch, *String parton models in GEANT4*, [arXiv:0306007 \[nucl-th\]](#).
- [113] N. S. Amelin et al., *Transverse flow and collectivity in ultrarelativistic heavy ion collisions*, Phys. Rev. Lett. **67** (1991) 1523–1526.
- [114] N. S. Amelin, L. P. Csernai, E. F. Staubo, and D. Strottman, *Collectivity in ultrarelativistic heavy ion collisions*, Nucl. Phys. **A 544** (1992) 463–466.
- [115] L. V. Bravina, L. P. Csernai, P. Levai, N. S. Amelin, and D. Strottman, *Fluid dynamics and quark gluon string model: What we can expect for Au + Au collisions at 11.6-A/GeV/c*, Nucl. Phys. **A 566** (1994) 461–464.
- [116] L. V. Bravina, *Scaling violation of transverse flow in heavy ion collisions at AGS energies*, Phys. Lett. **B 344** (1995) 49–54.
- [117] H. W. Bertini, *Intranuclear-cascade calculation of the secondary nucleon spectra from nucleon-nucleus interactions in the energy range 340 to 2900 MeV and comparisons with experiment*, Phys. Rev. **A 188** (1969) 1711–1730.
- [118] M. P. Guthrie, R. G. Alsmiller, and H. W. Bertini, *Calculation of the capture of negative pions in light elements and comparison with experiments pertaining to cancer radiotherapy*, Nucl. Instrum. Meth. **66** (1968) 29–36.
- [119] M. P. Guthrie and H. W. Bertini, *News item results from medium-energy intranuclear-cascade calculation*, Nucl. Phys. **A 169** (1971) 670–672.
- [120] N. V. Stepanov, *Statistical modeling of fission of excited atomic nuclei. 2. calculation and comparison with experiment*, Tech. Rep. In Russian, ITEP, Moscow, 1988.
[Preprint:ITEP-88-55](#).
- [121] P. Adragna et al., *Testbeam studies of production modules of the ATLAS Tile calorimeter*, Nucl. Instrum. Meth. **A 606** (2009) 362–394.
- [122] P. Adragna et al., *Measurement of pion and proton response and longitudinal shower profiles up to 20 nuclear interaction lengths with the ATLAS Tile calorimeter*, Nucl. Instrum. Meth. **A 615** (2010) 158–181.
- [123] E. Abat et al., *Response and shower topology of 2 to 180 GeV pions measured with the ATLAS barrel calorimeter at the CERN test-beam and comparison to Monte Carlo simulations*, Tech. Rep. [ATL-CAL-PUB-2010-001](#), May, 2010.
- [124] E. Abat et al., *Study of energy response and resolution of the ATLAS barrel calorimeter to hadrons of energies from 20 GeV to 350 GeV*, Nucl. Instrum. Meth. **A 621** (2010) 134–150.
- [125] E. Abat et al., *Study of the response of the ATLAS central calorimeter to pions of energies from 3 to 9 GeV*, Nucl. Instrum. Meth. **A 607** (2009) 372–386.
- [126] C. Cojocaru et al., *Hadronic calibration of the ATLAS liquid argon end-cap calorimeter in the pseudorapidity region $1.6 < |\eta| < 1.8$ in beam tests*, Nucl. Instrum. Meth. **A 531** (2004) 481–514.

- [127] J. Pinfold et al., *Performance of the ATLAS liquid argon endcap calorimeter in the pseudorapidity region $2.5 < |\eta| < 4.0$ in beam tests*, Nucl. Instrum. Meth. **A 593** (2008) 324–342.
- [128] A. E. Kiryunin, H. Oberlack, D. Salihagic, P. Schacht, and P. Strizenec, *GEANT4 physics evaluation with testbeam data of the ATLAS hadronic end-cap calorimeter*, Nucl. Instrum. Meth. **A 560** (2006) 278–290.
- [129] ATLAS Collaboration, *Response of the ATLAS calorimeter to single isolated hadrons produced in proton proton collisions at centre-of-mass energy of $\sqrt{s} = 900$ GeV*, Tech. Rep. [ATLAS-CONF-2010-017](#), March, 2010.
- [130] ATLAS Collaboration, *ATLAS calorimeter response to single isolated hadrons and estimation of the calorimeter jet scale uncertainty*, Tech. Rep. [ATLAS-CONF-2011-028](#), March, 2011.
- [131] ATLAS Collaboration, *A measurement of the material in the ATLAS inner detector using secondary hadronic interactions*, [arXiv:1110.6191 \[hep-ex\]](#).
- [132] ATLAS Collaboration, *Photon conversions at $\sqrt{s} = 900$ GeV measured with the ATLAS detector*, Tech. Rep. [ATLAS-CONF-2010-007](#), June, 2010.
- [133] ATLAS Collaboration, *Probing the material in front of the ATLAS electromagnetic calorimeter with energy flow from $\sqrt{s}=7$ TeV minimum bias events*, Tech. Rep. [ATLAS-CONF-2010-037](#), July, 2010.
- [134] C. Buttar, J. D’Hondt, M. Kramer, G. Salam, M. Wobisch, et al., *Standard Model Handles and Candles Working Group: Tools and Jets Summary Report*, [arXiv:0803.0678 \[hep-ph\]](#).
- [135] M. Cacciari, G. Salam, and G. Soyez, *The anti- k_t jet clustering algorithm*, JHEP **0804** (2008) 063, [arXiv:arXiv:0802.1189](#).
- [136] S. D. Ellis and D. E. Soper, *Successive combination jet algorithm for hadron collisions*, Phys. Rev. **D48** (1993) 3160–3166, [hep-ph/9305266](#).
- [137] Y. L. Dokshitzer, G. D. Leder, S. Moretti, and B. R. Webber, *Better jet clustering algorithms*, JHEP **08** (1997) 001, [hep-ph/9707323](#).
- [138] M. Wobisch and T. Wengler, *Hadronization corrections to jet cross sections in deep-inelastic scattering*, [hep-ph/9907280](#).
- [139] G. P. Salam, M. Cacciari, and G. Soyez. <http://www.lpthe.jussieu.fr/salam/fastjet/>.
- [140] W. Lampl et al., *Calorimeter clustering algorithms: description and performance*, Tech. Rep. [ATL-LARG-PUB-2008-002](#), April, 2008.
- [141] *Pile-up corrections for jets from proton-proton collisions at $\sqrt{s} = 7$ TeV in ATLAS in 2011*, Tech. Rep. [ATLAS-CONF-2012-064](#), CERN, Geneva, Jul, 2012.
- [142] E. Abat et al., *Combined performance studies for electrons at the 2004 ATLAS combined test-beam*, JINST **5** (2010) P11006.
- [143] M. Aharrouché et al., *Measurement of the response of the ATLAS liquid argon barrel calorimeter to electrons at the 2004 combined test-beam*, Nucl. Instrum. Meth. **A 614** (2010) 400–432.
- [144] J. Colas et al., *Response uniformity of the ATLAS liquid argon electromagnetic calorimeter*, Nucl. Instrum. Meth. **A 582** (2007) 429–455, [arXiv:0709.1094 \[physics.ins-det\]](#).

- [145] M. Aharrouche et al., *Energy linearity and resolution of the ATLAS electromagnetic barrel calorimeter in an electron test-beam*, Nucl. Instrum. Meth. **A 568** (2006) 601–623.
- [146] M. Aharrouche et al., *Study of the response of ATLAS electromagnetic liquid argon calorimeters to muons*, Nucl. Instrum. Meth. **A 606** (2009) 419–431.
- [147] ATLAS Collaboration, *Readiness of the ATLAS Tile calorimeter for LHC collisions*, Eur. Phys. J. **C 70** (2010) 1193–1236, [arXiv:1007.5423 \[physics.ins-det\]](#).
- [148] ATLAS Collaboration, *Electron performance measurements with the ATLAS detector using the 2010 LHC proton-proton collision data*, submitted to Eur. Phys. J. (2011) , [arXiv:1110.3174 \[hep-ex\]](#).
- [149] Guennadi, *The overview of the ATLAS local hadronic calibration*, J. Phys.: Conf. Ser. **160** (2009) no. 1, 012079+. <http://dx.doi.org/10.1088/1742-6596/160/1/012079>.
- [150] ATLAS Collaboration, G. Aad et al., *Jet energy measurement with the ATLAS detector in proton-proton collisions at $\sqrt{s} = 7$ TeV*, [arXiv:1112.6426 \[hep-ex\]](#).
- [151] S. Adomeit, F. Balli, T. Carli, C. Doglioni, D. Gillberg, G. Halladjian, B. Malaescu, L. Mijovic, C. Meyer, A. Picazio, S. Schramm, A. Schwartzman, J. Taenzer, and K. Terashi, *Jet energy scale and its systematic uncertainty in proton-proton collisions at $\sqrt{s}=7$ TeV with ATLAS 2011 data*, Tech. Rep. ATLAS-COM-CONF-2012-171, CERN, Geneva, Aug, 2012.
- [152] M. Begel et al., *Jet energy scale and its systematic uncertainty in proton-proton collisions at $\sqrt{s}=7$ TeV in ATLAS 2010 data*, Tech. Rep. ATLAS-COM-CONF-2011-053, CERN, Geneva, Mar, 2011.
- [153] ATLAS Collaboration, *Jet energy resolution in proton-proton collisions at $\sqrt{s} = 7$ TeV recorded in 2010 with the ATLAS detector*, [arXiv:1210.6210 \[hep-ex\]](#).
- [154] ATLAS Collaboration, G. Aad et al., *Charged-particle multiplicities in pp interactions at $\sqrt{s} = 900$ GeV measured with the ATLAS detector at the LHC*, Phys.Lett. **B688** (2010) 21–42, [arXiv:1003.3124 \[hep-ex\]](#).
- [155] S. Baker et al., *Measurement of inclusive jet and dijet production in pp collisions at $\sqrt{s}=7$ TeV using the ATLAS detector*, Tech. Rep. ATL-COM-PHYS-2011-738, CERN, Geneva, Jun, 2011. Supporting documentation for the inclusive jet and dijet publication using the full 2010 dataset.
- [156] ATLAS Collaboration, G. Aad et al., *Measurement of inclusive jet and dijet production in pp collisions at $\sqrt{s} = 7$ TeV using the ATLAS detector*, Phys. Rev. **D86** (2012) 014022, [arXiv:1112.6297 \[hep-ex\]](#).
- [157] V. Lendermann, J. Haller, M. Herbst, K. Kruger, H.-C. Schultz-Coulon, et al., *Combining Triggers in HEP Data Analysis*, Nucl.Instrum.Meth. **A604** (2009) 707–718, [arXiv:0901.4118 \[hep-ex\]](#).
- [158] *ATLAS liquid-argon calorimeter: Technical Design Report*. Technical Design Report ATLAS. CERN, Geneva, 1996.
- [159] ATLAS Collaboration, G. Aad et al., *Measurement of the Inelastic Proton-Proton Cross-Section at $\sqrt{s} = 7$ TeV with the ATLAS Detector*, Nature Commun. **2** (2011) 463, [arXiv:1104.0326 \[hep-ex\]](#).
- [160] ATLAS Collaboration, *Performance of large-R jets and jet substructure reconstruction with the ATLAS detector*, .

- [161] M. Cacciari, G. P. Salam, and G. Soyez, *The Catchment Area of Jets*, **JHEP** **04** (2008) 005, [arXiv:0802.1188 \[hep-ph\]](#).
- [162] M. Cacciari and G. P. Salam, *Pileup subtraction using jet areas*, **Phys. Lett.** **B659** (2008) 119–126, [arXiv:0707.1378 \[hep-ph\]](#).
- [163] S. Catani, Y. L. Dokshitzer, M. H. Seymour, and B. R. Webber, *Longitudinally invariant $K(t)$ clustering algorithms for hadron hadron collisions*, **Nucl. Phys.** **B406** (1993) 187–224.
- [164] G. P. Salam and G. Soyez, *A practical Seedless Infrared-Safe Cone jet algorithm*, **JHEP** **05** (2007) 086, [arXiv:0704.0292](#).
- [165] ATLAS Collaboration, G. Aad et al., *Underlying event characteristics and their dependence on jet size of charged-particle jet events in pp collisions at $\sqrt{s} = 7$ TeV with the ATLAS detector*, [arXiv:1208.0563 \[hep-ex\]](#).
- [166] S. Frixione and G. Ridolfi, *Jet photoproduction at HERA*, **Nucl.Phys.** **B507** (1997) 315–333, [arXiv:hep-ph/9707345 \[hep-ph\]](#).
- [167] H.-L. Lai, M. Guzzi, J. Huston, Z. Li, P. M. Nadolsky, et al., *New parton distributions for collider physics*, **Phys.Rev.** **D82** (2010) 074024, [arXiv:1007.2241 \[hep-ph\]](#).
- [168] S. D. Ellis, Z. Kunszt, and D. E. Soper, *Two jet production in hadron collisions at order α_s^3 in QCD*, **Phys.Rev.Lett.** **69** (1992) 1496–1499.
- [169] T. Carli, D. Clements, A. Cooper-Sarkar, C. Gwenlan, G. P. Salam, et al., *A posteriori inclusion of parton density functions in NLO QCD final-state calculations at hadron colliders: The APPLGRID Project*, **Eur.Phys.J.** **C66** (2010) 503–524, [arXiv:0911.2985 \[hep-ph\]](#).
- [170] H.-L. Lai, J. Huston, Z. Li, P. Nadolsky, J. Pumplin, et al., *Uncertainty induced by QCD coupling in the CTEQ global analysis of parton distributions*, **Phys.Rev.** **D82** (2010) 054021, [arXiv:1004.4624 \[hep-ph\]](#).
- [171] S. Moretti, M. Nolten, and D. Ross, *Weak corrections to four-parton processes*, **Nucl.Phys.** **B759** (2006) 50–82, [arXiv:hep-ph/0606201 \[hep-ph\]](#).
- [172] T. Adye, *Unfolding algorithms and tests using RooUnfold*, 2011. Proceedings of the PHYSTAT 2011 Workshop, **CERN-2011-006** (2011) 313–318, <http://arxiv.org/abs/1105.1160>. [arxiv:1105.1160](#).
- [173] G. D’Agostini, *A multidimensional unfolding method based on Bayes’ theorem*, **Nuclear Instruments and Methods in Physics Research Section A: Accelerators, Spectrometers, Detectors and Associated Equipment** **362** (1995) no. 23, 487 – 498. <http://www.sciencedirect.com/science/article/pii/016890029500274X>.
- [174] ATLAS Collaboration, G. Aad et al., *Measurement of the jet fragmentation function and transverse profile in proton-proton collisions at a center-of-mass energy of 7 TeV with the ATLAS detector*, **Eur.Phys.J.** **C71** (2011) 1795, [arXiv:1109.5816 \[hep-ex\]](#).
- [175] C. M. Bishop, *Neural Networks for Pattern Recognition*. Oxford University Press, USA, 1 ed., Jan., 1996. <http://www.amazon.com/exec/obidos/redirect?tag=citeulike07-20&path=ASIN/0198538642>.
- [176] D. E. Rumelhart, G. E. Hinton, and R. J. Williams, *Neurocomputing: foundations of research*, ch. Learning representations by back-propagating errors, pp. 696–699. MIT Press, Cambridge, MA, USA, 1988. <http://dl.acm.org/citation.cfm?id=65669.104451>.